VIDE. TEHNOLOĢIJA. RESURSI

IX starptautiskās zinātniski praktiskās konferences materiāli
2013.gada 20.-22.jūnijs

2. SĒJUMS

ENVIRONMENT. TECHNOLOGY. RESOURCES

Proceedings of the 9th International Scientific and Practical Conference
June 20-22, 2013

VOLUME II

Rēzekne
2013

Zinātnisko rakstu krājumā iekļauti IX starptautiskās zinātniski praktiskās konferences "Vide. Tehnoloģija. Resursi" raksti.
Rakstu tematika saistīta ar vides kvalitāti un monitoringu, piesārņojuma novēršanas tehnoloģijām, tīrāku ražošanu, ilgtspējīgo lauksaimniecību, vides izglītību un ekonomiku. Rakstu krājumā pārstāvēti referāti, kas ir saistīti ar datorzinātnes, matemātikas, mehānikas, elektrotehnikas, elektronikas un mehatronikas pielietošanu vides zinātnē, metālapstrādē un citu nozaru problēmu risināšanā.
Proceedings include papers presented at the 9th International Conference "Environment. Technology. Resources."
The themes of the papers are – the environmental quality and monitoring, pollution prevention technologies, cleaner production, sustainable agriculture, environmental education and economics.The conference includes papers on applications of computer science, mathematics, mechanics, electrical engineering, electronics and mechatronics for solution of environmental, metal industry and other problems.

CONTENT

IV COMPUTER SCIENCE

V MECHANICS, MECHANICS OF MATERIALS

VI ELECTRICAL DRIVE, ELECTROTECHNICS, ELECTRONICS AND MECHATRONICS

IV

COMPUTER SCIENCE

Offer Opportunities of Levelling Online Courses for Latvia

Vita Balikova

Riga Technical University, Azenes iela 12, Riga, LV1048, Latvia, vita.balikova@rtk.lv

Abstract. **Currently, all European countries, including Latvian, there is a decrease of students' mathematical knowledge. As a result, universities and high schools face the challenge of filling the knowledge in mathematics among students. This has resulted in increasing the level of knowledge disparity in study groups. And experience shows that many students need extra - levelling courses. One of solution of such courses would be a free on-line levelling courses.**

Key words: **levelling course, e-learning, open educational resources, online education, massive open online course (MOOC).**

I INTRODUCTION

Study in the first year is a period of adaptation of the students in the new educational environment. A significant increase in the amount of information students need to learn in one session is a serious problem for first-year students. In a lesson in school pupils usually study new material for an average of twenty minutes, the new information in the university student should take during the whole session. Problems encountered by students learning new material also due to the high level of abstraction inherent in the concepts, terms, for example, in higher mathematics. Most of the terms and claims sections of higher mathematics can not to be found in the interpretation of the world. But they are necessary for the internal needs of mathematics, as they will be used in future for the theory, and the solution of practical problems to be used indirectly. In recent years to these difficulties added one more problem: occurrence of students with insufficient knowledge of basic mathematics. The number of students who can not add fractions, disclose brackets, deal with integers, each year gets bigger. . This has resulted in increasing the level of knowledge disparity in study groups. This leads to a need for a extra – levelling course in mathematics.

In addition, at this time we live in a reform in the system of secondary and higher education, which is associated with the correction of educational programs. This leads to a greater diversity of quality and depth of mathematical training graduates.

II MATERIALS AND METHODS

Situation in Latvia

Latvian students' average achievement in mathematics (482 points) is below the OECD (Organisation for Economic Co-operation and Development - Organisation for Economic Co-operation and Development - OECD) country average performance (496 points) and below the EU average performance (491), only a few EU countries (Lithuania, Greece, Bulgaria, Romania) achievements were even lower. Latvian overall progress of all students of mathematics competence since 2003 practically unchanged.

OECD PISA (Programme for International Student Assessment of the OECD) in 2006 and PISA 2009 will no longer show the Latvian education quality average growth, as demonstrated by the OECD program for the first cycles and other international comparative studies of education quality, such as the IEA TIMSS. Latvian is a relatively small primary school with good and outstanding achievement in reading, mathematics and science, and their number continues to decline. It would seriously hamper national development documents, the goals of science, technology and other areas. More there is a tendency to accelerate work with weaker students, which, of course, are also important primary in the final period. Our old schoolchildren's performance dependency on family welfare, home access to educational and cultural resources, compared to many other countries, is not big and it has a tendency to decrease. So the Latvian educational institutions in some extent able to compensate the negative factors. [6], [7], [8].

14th December 2012 on Faculty of Physics and Mathematics (FPM) of Latvian University (LU) was found Natural Science and Mathematics Education Centre of FPM LU established to provide a bridge between the University and the school, working with the talented students of science and mathematics teachers as well as finding new talent. It was created within project "Science and Mathematics". The newly established center tasks is to encourage young people's interest in science and math, to encourage innovation to enter the mainstream education system, continuity and collaboration between general education and higher education, promote science students and the general public, but also in strengthening the research activities in general education. [3], [4]

The Natural Science and Mathematics Education Centre of FPM LU is founded for work with gifted children, so there's no work with unsuccessful in mathematics.

At website "macibuvideo.lv" is available explanations and analysis of previous year school

exams in video. In "Macibuvideo.lv" are placed short movies, where are simply explains of the laws and tasks solving. Students, teachers, parents and other interested peoples for free are available in nearly 200 training videos in mathematics, physics and chemistry for the secondary school classes. Movies stock is added regularly, gradually covering the entire content of the school curriculum in physics, chemistry and mathematics.

"Everyone in the school, teaching their subjects, we arrived at the need for a resource that allows you to be in several places at the same time. It also started to develop an educational video that has gained popularity in our and other students as well as teachers. Towards Mathematics and Physics 12th class exams this year, we are happy to see that "macibuvideo.lv 'attendance increased sharply. past week the number of unique users per day has doubled from 200 to 400 and has tripled in the time that visitors spend on average on our site., we aim to benefit materials many people as possible, so try to keep them available for free in the future, "says actor and Mathematics video creator Kalis.

"Macibuvideo.lv" has created in 2011 by three members of the "Mission Possible" - Martins Kalis, Gatis Narvaišs and Karl Kravis. "Macibuvideo.lv" goal is to help students understand mathematics and natural relationships, with high-quality video and task inventories in Latvian language appropriate for mathematics, physics and chemistry content in Latvian schools. [9]

The website "Macibuvideo.lv" has great explanatory videos, but there's no option to perform the tasks.

Internet - portal Skolas.lv is a multifunctional working environment for students and their parents, teachers, school administration and the education system as a whole. It helps to realize the high-quality and modern educational process, improves the availability of digital learning content, allows teachers to work more interesting and easier, but the administration of educational institutions to effectively manage these processes.

On Skolas.lv single electronic repository of training materials, which are nearly 2,500 different teaching materials and teaching aids printed bibliographic data are available. It is intended for all Latvian teachers and students (according to access rights). It is possible to search, select and insert learning tasks and learning resources, which can later easily be used in teaching.

Catalog is compiled in digital educational materials originating from other projects, such as "Natural Sciences and Mathematics Project", as well as valuable materials and LEIS SEDA project "Innovation in education 'new teaching materials and annotations Ministry of Education approved textbooks. [10]

This year eBig3 project was started. EBig3 is a synergetic approach with eLearning, TV and mobile technologies to promote new business developments.

Project aims to create a network for cross-border research cooperation in technology enhanced learning (TEL) and to develop a strategy for educational business promotion service. Project will begin implementing the strategy and pilot a set of innovative learning solutions for inclusive human resource development and to promote the spirit of entrepreneurship in border regions.

The project will combine three kinds of TEL in a complementary way:

- eLearning–mainly computer and/or internet-based learning;
- tLearning–TV based learning;
- mLearning–learning with a use of mobile devices; to produce an effective & innovative cross-media learning delivery system (eBig3) that goes beyond traditional web-based learning approaches.

The system will combine a wide coverage of TV technology and a wide accessibility of mobile technology with the capacity and flexibility of broadband. This will allow a learner to use a single delivery channel at a particular time (depending on availability and preferences) or a complementary combination of two or three delivery channels thus supporting learning anywhere any time paradigm. The work on the project solution includes integration of technical issues for cross-media learning content delivery, refinement of pedagogic considerations, development of shared understanding of target user learning contexts in border areas, production of learning content & organizing course pilots. [11], [12], [13], [14]

Latvian most popular platform called e-learning environment Moodle is. Moodle is an open source software designed course management system. Moodle software itself is free and requires a standard server configuration, the installation can be performed by any server administrator. Another issue is the Moodle platform customization specific needs of the organization and technical support. Also, think about the Moodle user training, user support and administration. [15]

Some of universities of Latvia, for example, LU offer leveling course for own students. This courses are available in e-learning form to. [18]

The situation outside the Latvia

A massive open online course (MOOC) is an online course aiming at large-scale participation and open access via the web. MOOCs are a recent development in distance education and often use open educational resources. Typically they do not offer academic credit or charge tuition fees. Only about 10% of the tens of thousands of students who may sign up complete the course. [24]

MOOCs originated about 2008 within the open educational resources (or OER) movement. Many of the original courses were based on connectives' theory, emphasizing that learning and knowledge emerge from a network of connections. 2012 became "the year of the MOOC" as several well-financed

providers, associated with top universities, emerged, including Coursera, Udacity, and edX.[25] Other universities scrambled to join in, as did more established online education providers such as Blackboard Inc, in what has been called a "stampede." Dozens of universities in Canada, Mexico, Europe and Asia have announced partnerships with the large American MOOC providers. [24][26]

Features associated with early MOOCs, such as open licensing of content, open structure and learning goals, and connectivism may not be present in all MOOC projects.

The short lecture format used by many MOOCs developed from "Khan Academy's free archive of snappy instructional videos. The website supplies a free online collection of more than 4,000 micro lectures via video tutorials stored on YouTube teaching mathematics, history, healthcare, medicine, finance, physics, chemistry, biology, astronomy, economics, cosmology, and organic chemistry, American civics, art history, macroeconomics, microeconomics, and computer science. [17] Khan Academy launched a computer science module in September 2012. Khan Academy has delivered over 240 million lessons. [16]

Analysts in the UK conducted a study of the state of the level of mathematics for first year students (over 10 years) and found steady downward trend of their level of knowledge and the establishment of the center responded to support students with poor school preparation. Here, students can fill in the gaps of school knowledge, previously ascertained exactly which topics they need to repeat. This is - a kind of diagnostic and rehabilitation center 0.

Almost every major world university has its own leveling courses in several subjects, including mathematics. [19]

The Khan Academy is a non-profit educational website created in 2006 by American educator Salman Khan, a graduate of MIT and Harvard Business School. With the stated mission of "providing a high quality education for anyone, anywhere".

III Conclusions

Currently, all European countries, including Latvian, there is a decrease of students' mathematical knowledge. As a result, universities and high schools face the challenge of filling the knowledge in mathematics among students. This has resulted in increasing the level of knowledge disparity in study groups. And experience shows that many students need extra - leveling courses. Latvian, European and American universities offers such courses only for oun students, often at an additional cost.

Furthermore, most universities tend to offer the same courses to the same group of academically best-qualified young students and fail to open up to other types of learning and learners, e.g. non-degree retraining courses for adults or gap courses for students not coming through the traditional routes. This has not only impeded access for disadvantaged social groups and prevented higher enrolment rates but has also slowed down innovation in curricula and teaching methods, hindered the provision of training/retraining opportunities to increase skills and competency levels in the workforce and led to persistent mismatches between graduate qualifications and labour market needs. Graduate unemployment in many Member States is unacceptably high. [19]

Either way, Massive Open Online Courses (MOOC) is now widely discussed innovation in higher education offer in the world.

Course offerings are varied. However, in these projects courses are mostly in English, but some of them are already available for content translation into other languages.

Compared to traditional courses in MOOC courses is very high student dropout, only about 4-10% of the participants completed MOOC to the end. None of the distance learning courses free of charge has yet found a sustainable business model.

Currently MOOC is free of charge. The vendors is still looking and check for the options to make a profit with the help of this course - continuing to offer courses for free or at a relatively lower cost than the "classroom" courses.

Course accreditation is very slow and it is not clear how separate courses will be part of the overall process of obtaining qualifications. Most vendors currently MOOC not be granted credits or qualifications.

Latvia already has a joint course development experience – working together Riga Technical University, University of Liepaja, Latvian University of Agriculture, Daugavpils University, Kaunas University of Technology, the University of Siauliai and Utena labor market training center, a free access to distance education system eBig3 was established. [27] There are offered already 11 courses. The project manager Atis Kapenieks emphasizes that eBig3 model is used not only internet technologies, but also used TV and mobile phones. LTV7, regional television, on Saturdays, demonstrates eBig3 style movie. movie characters appear in different situations, which is an in-depth understanding of eBig3 film invites eBig3 rates, sending SMS from your mobile phone. SMS technology is also used to enrich the learning support and significantly reduce the high dropout of students.

Thus, the problem diversity of level of mathematical preparation of students can be solved by the introduction of a leveling course. One of solution of such courses would be a free on-line leveling courses. In the case of Latvia, the courses can be offered in the project eBig3.

It is many levelling courses. However, data on the use and effectiveness of those courses are not sufficiently. This leads to the need for research on the use and effectiveness of the course.

IV References

[1] The Centre for Innovation in Mathematics Teaching [Online]. Available: http://www.cimt.plymouth.ac.uk/default.htm [Accessed: Feb. 27, 2013].

[2] Имас О.Н.. Пахомова Е.Г. Выравнивающий курс – одно из средств повышения качества образования (статья). Известия ТПУ. – 2004. –Том 307. – №7. – С. 159–161. - [Online]. Available: http://cyberleninka.ru/article/n/vyravnivayuschiy-kurs-odno-iz-sredstv-povysheniya-kachestva-obrazovaniya [Accessed: Feb. 27, 2013]

[3] Ķīlis R. Informatīvais ziņojums „Par situāciju skolēnu sekmībā vispārējā izglītībā” – 16.04.2012. - [Online]. http://izm.izm.gov.lv/upload_file/Normativie_akti/info_zinoju mi/2012/IZMizino_160412_sekmiba.539.pdf [Accessed: Feb. 27, 2013]

[4] Fizmat.lv – [Online]. http://fizmati.lv/skoleniem/ [Accessed: Feb. 27, 2013]

[5] Fizikas un matemātikas fakultātē tiks atklāts Dabaszinātņu un matemātikas izglītības centrs – [Online] http://www.lu.lv/zinas/t/9664/ [Accessed: Feb. 27, 2013]

[6] OECD Programme for International Student Assessment (PISA) [Online]. http://www.oecd.org/pisa/ [Accessed: Feb. 27, 2013].

[7] PISA data Alalysis Manual. SPSS second edition, 2009 [Online] – http://browse.oecdbookshop.org/oecd/pdfs/free/9809031e.pdf [Accessed: Feb. 27, 2013].

[8] PISA 2006 Technical Report, 2006.

[9] Macību video [Online] – http://macibuvideo.lv/ [Accessed: Feb. 27, 2013].

[10] Skolas.lv [Online] – https://www.skolas.lv/Lapas/sakums.aspx [Accessed: Feb. 27, 2013].

[11] eBig3 - [Online] http://www.latlit.eu/eng/running_projects/lliii183_ebig3/_gv/p rint_1 [Accessed: Feb. 27, 2013].

[12] LATLIT - [Online] – http://www.latlit.eu/eng/running_projects/lliii183_ebig3 [Accessed: Feb. 27, 2013].

[13] Kapenieks A., Zuga B., Stale G., Kapenieks J. Jr., Jirgensons M., Ozolina A., Apinis B., Vitolina I., Gorbunovs A., Kudina I., Kapenieks J. Sn., Gulbis R., Treijere M., Slaidins I., Jakobsone-Snepste G., Gibze S., Kapenieks K., Tomsons D., Ulmane-Ozoliņa L., Letinskis J., Cakula S., Balode A., Blija T., Vilkonis R., Cibulskis G., Rutkauskiene D.. "eBig3": a new triple screen approach for the next generation of lifelong learning experience – [to be published]

[14] Kapenieks A., Zuga B., Stale G., Jirgensons M. An E-ecosystem Driven Next Generation Life Long Learning Approach. IIMC International Information Management Corporation, 2012. ISBN: 978-1-905824-34-2, IST-Africa 2012 Conference & Exhibition

[15] Balikova V., Ulmane I. The computer-based methods of training used in educational process. Balikova V., Ulmane I. Mācību procesā lietojamās datorizētās apmācību metodes, //

[16] Khan Academy - [Online] – http://www.khanacademy.org/contribute [Accessed: Feb. 27, 2013].

[17] Michels, Spencer (2010-02-22). "Khan Academy: How to Calculate the Unemployment Rate". *PBS NewsHour*. PBS. – [Online] – http://www.pbs.org/newshour/rundown/2010/02/khan-academy-how-to-calculate-the-unemployment-rate.html. [Accessed: Feb. 27, 2013].

[18] Metakurss: Izlīdzinošais kurss vidusskolas matemātikā. – [Online] – http://estudijas.lu.lv/course/info.php?id=818 [Accessed: Feb. 27, 2013].

[19] Delivering On The Modernisation Agenda For Universities: Education, Research And Innovation. Communication from the Commission to the Council and the European Parliament, Commission Of The European Communities, Brussels, 10.5.2006 – [Online] – http://eur-lex.europa.eu/LexUriServ/LexUriServ.do?uri=COM:2006:020 8:FIN:en:PDF [Accessed: Feb. 27, 2013].

[20] Некряч Е.Н., Пахомова Е.Г., Подберезина Е.И. Выравнивающий курс как способ повышения эффективности образовательного процесса, Научно-методическая конференция, Томск 2011 – [Online] – http://www.lib.tpu.ru/fulltext/c/2011/C09/111.pdf [Accessed: Feb. 27, 2013].

[21] Norises statistika un rezultātu raksturojums – [Online] – http://visc.gov.lv/vispizglitiba/eksameni/statistika.shtml [Accessed: Feb. 27, 2013].

[22] Kamerāde D. Mācīšanās internetā par brīvu - kā tā ietekmēs augstskolas Latvijā?, 2013 – [Online] – http://politika.lv/article/macisanas-interneta-par-brivu-ka-ta-ietekmes-augstskolas-latvija [Accessed: Feb. 27, 2013].

[23] MOOCs at Edinburgh – [Online] – http://www.ed.ac.uk/studying/postgraduate/online-distance-learning/programmes/mooc-edinburgh [Accessed: Feb. 27, 2013].

[24] Lewin T. Universities Abroad Join Partnerships on the Web. New York Times, 2013 – [Online] – http://www.nytimes.com/2013/02/21/education/universities-abroad-join-mooc-course-projects.html?_r=0 [Accessed: Feb. 27, 2013].

[25] Smith L. 5 education providers offering MOOCs now or in the future, 2012. – [Online] – http://www.educationdive.com/news/5-mooc-providers/44506/ [Accessed: Feb. 27, 2013].

[26] Laura Pappano. The Year of the MOOC - The New York Times, 2012. – [Online] – http://www.nytimes.com/2012/11/04/education/edlife/massive-open-online-courses-are-multiplying-at-a-rapid-pace.html?pagewanted=1 [Accessed: Feb. 27, 2013].

[27] EBig3 – [Online] – http://ebig3.eu [Accessed: Feb. 27, 2013].

Rīgas Tehniskās koledžas zinātniskie raksti „Augstākā profesionālā izglītība teorijā un praksē", 10. sējums, izdevniecība „RTU", Rīga, 2012 – 95. – 100. lpp.

The Concept of Ontology for Numerical Data Clustering

Peter Grabusts

Rezekne Higher Educational Institution, Research Institute for Regional Studies,
Atbrivoshanas alley 76, Rezekne, LV-4601, Latvia, peter@ru.lv

Abstract. **Classical clustering algorithms have been studied quite well, they are used for the numerical data grouping in similar structures - clusters. Similar objects are placed in the same cluster, different objects – in another cluster. All classical clustering algorithms have common characteristics, their successful choice defines the clustering results. The most important clustering parameters are following: clustering algorithms, metrics, the initial number of clusters, clustering validation criteria. In recent years there is a strong tendency of the possibility to get the rules from clusters. Semantic knowledge is not used in classical clustering algorithms. This creates difficulties in interpreting the results of clustering. Currently, the possibilities to use ontology increase rapidly, that allows to get knowledge of a specific data model. In the frames of this work the ontology concept, prototype development for numerical data clustering, which includes the most important characteristics of clustering performance have been analyzed.**

Keywords – clustering, cluster analysis, ontology.

I INTRODUCTION

Cluster analysis as one of the intelligent data analysis tasks is searching for independent groups (clusters), their attributes and performance in the test data [1, 4, 15]. Resolving such a task allows better understand the data, because clustering can be used practically in any application area where data analysis is required.

The author's research interests are related to the cluster analysis and its aspects: application of clustering algorithms, fuzzy clustering, rule extraction from clustered data etc. [6, 7]. Therefore, there is logical desire to pursue the research in ontology inclusion into cluster analysis [5].

To evaluate the clustering performance aspects the following aim was put forward - to analyze and summarize the options of clustering algorithms in order to create an ontology prototype for numerical data clustering. The research tasks are subordinated to the target aim:

- to review clustering algorithms;
- carry out the evaluation of the eligibility of the metrics selection;
- characterize the impact of changes in the number of clusters;
- evaluate the reliability of the results of clustering (clusters validity);
- evaluate the possibility to get rules from clusters;
- develop the ontology concept for numerical data clustering.

II AN OUTLINE OF CLASSICAL CLUSTERING APPROACH

Clustering differs from classification in following: for performing the analysis in clustering process there is no need to distribute a separate variable group. From this point of view, clustering is considered as a "learning without a teacher" and is used in the initial stage of the study.

Cluster analysis is characterized by two features that distinguish it from other methods [4]:

- the result depends on the object or the kind of attributes, they can be clearly
- certain objects, or objects with fuzzy description;
- the result depends on the potential of the cluster and the object relations, that is, we should take into account the possible object belonging to multiple clusters and detection the ownership of the object(strict or fuzzy membership).

Given an important role for clustering in data analysis, object ownership concept was generalized to a class function that defines the belonging of object classes to that particular class. Two classes of characteristic functions were distinguished:

- discrete function that accepts one of two possible values - belong / do not belong to the class (classical clustering);
- a function that accepts values from the interval [0,1]. The closer the values of the function are to 1, the "more" the subject belongs to a certain class (fuzzy clustering).

Clustering algorithms are mainly designed for multi-dimensional data sampling processing, when the data are given in tabular form "object-quality". They allow you to group objects into certain groups, where objects related to each other by a specific rule. It does not matter, how these groups are called – taxons, clusters or classes, the main thing is that it with sufficient precision reflects the characteristics of this object. After clustering the data for further analysis are used with other intelligent data analysis techniques to determine the nature of the resulting regularities and for future uses.

Clustering is typically used during data processing as a first step in the analysis. It identifies groups with similar data that can later be used for the exploration of relationships between the data. Cluster analysis

process formally consists of the following steps (see Fig. 1):

- collecting data necessary for the analysis;
- classes data (clusters) characterizing size and borderline;
- data grouping in clusters;
- definition of classes hierarchy and analysis of the results.
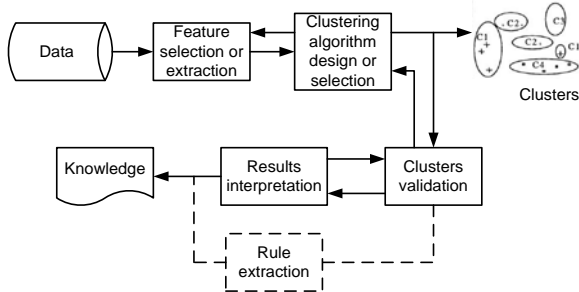
Fig. 1. Clustering procedure [15]

All clustering algorithms have common characteristics, the choice of which characterize the efficiency of clustering (see Fig. 2).
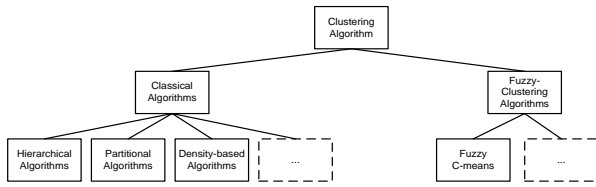
Fig. 2. Hierarchical view of the clustering algorithm class

The most important clustering parameters are following: metric (the distance of cluster element to the cluster center), the number of clusters k, clustering validity, the opportunity to get rules [2, 9, 10].

Metrics. The main purpose of metrics learning in a specific problem is to learn an appropriate distance/similarity function. A metrics or distance function is a function which defines a distance between elements of a set [4, 8, 14]. A set with a metric is called a metric space. In many data retrieval and data mining applications, such as clustering, measuring similarity between objects has become an important part. In general, the task is to define a function Sim(X,Y), where X and Y are two objects or sets of a certain class, and the value of the function represents the degree of "similarity" between the two. Formally, a distance is a function D with nonnegative real values, defined on the Cartesian product X x X of a set X. It is called a metrics on X if for every x, y, z ∈ X:

- $D(x,y)=0$ if x=y (the identity axiom);
- $D(x,y) + D(y,z) \geq D(x,z)$ (the triangle inequality);
- $D(x,y)=D(y,x)$ (the symmetry axiom).

A set X provided with a metric is called a metric space.

Euclidean distance is the most common use of distance – it computes the root of square differences between coordinates of a pair of objects:

$$D_{XY} = \sqrt{\sum_{k=1}^{m}(x_{ik} - x_{jk})^2} \; . \qquad (1)$$

Manhattan distance or city block distance represents distance between points in a city road grid. It computes the absolute differences between coordinates of a pair of objects:

$$D_{XY} = \sum_{k=1}^{d}| x_{ik} - x_{jk} | . \qquad (2)$$

Minkowski distance is the generalized metric distance:

$$D_{XY} = (\sum_{k=1}^{d}| x_{ik} - x_{jk} |^{p})^{1/p} \; . \qquad (3)$$

Note that when p=2, the distance becomes the Euclidean distance. When p=1, it becomes city block distance.

Cosine distance is the angular difference between two vectors:

$$D_{XY} = \cos(\theta) = \frac{X \bullet Y}{\|X\|\|Y\|} = \frac{\sum_{i=1}^{n} X_i \times Y_i}{\sqrt{\sum_{i=1}^{n}(X_i)^2} \times \sqrt{\sum_{i=1}^{n}(Y_i)^2}}$$

(4)

The distance measure can also be derived from the correlation coefficient, such as the Pearson correlation coefficient. Correlation coefficient is standardized angular separation by centering the coordinates to its mean value. It measures similarity rather than distance or dissimilarity:

$$r_{ij} = \frac{\sum_{k=1}^{d}(x_{ik} - \overline{x}_i)(x_{jk} - \overline{x}_j)}{\sqrt{\sum_{k=1}^{d}(x_{ik} - \overline{x}_i)^2 \sum_{k=1}^{d}(x_{jk} - \overline{x}_j)^2}} , \qquad (5)$$

where $\overline{x}_i = \dfrac{1}{d}\sum_{k=1}^{d} x_{ik}$.

Noticing that the correlation coefficient is in the range of [-1,1], with 1 and -1 indicating the strongest positive and negative correlation respectively, we can define the distance measure as

$$D_{XY} = (1 - r_{ij})/2 . \qquad (6$$

When using correlation coefficients for distance measures, it should be taken into consideration that they tend to detect the difference in shapes rather than determining the magnitude of differences between two objects.

The summary of the metrics is shown in the Figure 3 and Table I.
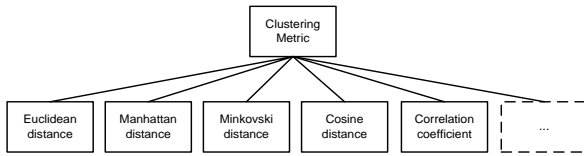
Fig. 3. Hierarchical view of the clustering metrics class

TABLE I
DISTANCE MEASURES AND THEIR APPLICATIONS

Measure	Examples and applications
Euclidean distance	K-means with its variations
Manhattan distance	Fuzzy ART, clustering algorithms
Cosine distance	Text Mining, document clustering
Pearson correlation	Widely used as the measure for microarray gene expression data analysis

Traditionally Euclidean distance is used in clustering algorithms, the choice of other metric in definite cases may be disputable. It depends on the task, the amount of data and on the complexity of the task.

Cluster numbers. An important role in the realization of clustering algorithms is the number of clusters and initial centers determination. Generally is assumed that it is priori known the number of clusters and as values of the initial cluster centers m are offered to take the first points of training set m.

Clustering validity. Cluster validity is a method to find a set of clusters that best fits natural partitions (number of clusters) without any class information. There are three fundamental criteria to investigate the cluster validity: external criteria, internal criteria, and relative criteria [4]. In this case only external cluster validity index was analyzed.

Given a data set X and a clustering structure C derived from the application of a certain clustering algorithm on X, external criteria compare the obtained clustering structure C to a pre-specified structure, which reflects *apriori* information on the clustering structure of X. For example, an external criterion can be used to examine the match between the cluster labels with the category labels based on a priori information.

Based on the external criteria, there is the following approach: comparing the resulting clustering structure C to an independent partition of the data P, which was built according to intuition about the clustering structure of the data set.

If P is a pre-specified partition of data set X with N data points and is independent of the clustering structure C resulting from a clustering algorithm, then the evaluation of C by external criteria is achieved by comparing C to P. Considering a pair of data points x_i and x_j of X, there are four different cases based on how x_i and x_j are placed in C and P.

- Case 1: x_i and x_j belong to the same clusters of C and the same category of P.
- Case 2: x_i and x_j belong to the same clusters of C but different categories of P.
- Case 3: x_i and x_j belong to different clusters of C but the same category of P.
- Case 4: x_i and x_j belong to different clusters of C and different category of P.

Correspondingly, the numbers of pairs of points for the four cases are denoted as a, b, c and d. Because the total number of pairs of points is N(N-1)/2, denoted as M, we have:

$$M = a + b + c + d = \frac{n(n-1)}{2}, \qquad (7)$$

where n is the number of data points in the data set. When C and P are defined, one can choose one of the many clustering quality criteria. Some popular clustering quality criteria are following (see also Fig. 4) [4].

Rand index is calculated by using the following formula:

$$R = \frac{a+d}{M}.$$

(8)

Rand index suggests an objective criterion for comparing two arbitrary clusterings based on how pairs of data points are clustered. Given two clusterings, for any two data points there are two cases:

- The first case is that the two points are placed together in a cluster in each of two clusterings or they are assigned to different clusters in both clusterings.
- The second case is that the two points are placed together in a cluster in one clustering and they are assigned to different clusters in the other.

Hubert index is calculated by using the following formula:

$$\Gamma = \frac{1}{M} \sum_{i=1}^{n-1} \sum_{j=i+1}^{n} X_{ij} Y_{ij}.$$

(9)

The value of both index ranges between 0 and 1. A higher index value indicates greater similarity between C and P.

Jaccard coefficient:

$$J = \frac{a}{a+b+c}. \qquad (10)$$

Fowlkes and Mallows index:

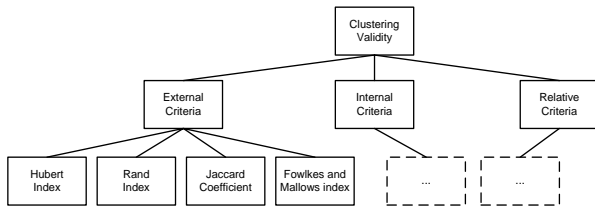$$FM = \sqrt{\frac{a}{a+b} \frac{a}{a+c}}. \qquad (11)$$

Fig. 4. Hierarchical view of the clustering validity class

Rule extract. The possibility to convert clustering information directly into symbolic knowledge form is through the rules (rule extraction). These assumptions are formulated as IF ... THEN ... rules [3]. The benefits of the mining rules are as follows:

- the opportunity to verify the rules on different variants of the input data is given;
- failures of training data can be identified, thus clustering operation can be improved by introducing new or removing additional clusters;
- determination of a previously unknown regularities in the data that currently have a growing importance in Data Mining industry;
- the resulting rules can be set up in a base of rules, which might also be used for similar types of applications.

Several artificial neural network algorithms use clustering during learning process, that leads to a hidden neurons (hidden units) deriving, which are actually centers of clusters [9, 13].

The nature of each hidden unit enables a simple translation into a single rule:

IF Feature$_1$ is TRUE AND IF Feature$_2$ is TRUE ...
AND IF Feature$_n$ is TRUE THEN Class$_x$. (12)

where a *Feature* is composed of upper and lower bounds calculated by the center μ_n positions, width σ and feature steepness S. The value of the steepness was discovered empirically to be about 0.6 and is related to the value of the width parameter. The values of μ and σ are determined by the training algorithm. The upper and lower bounds are calculated as follows:

$$X_{lower} = \mu_i - \sigma_i + S \text{ and } X_{upper} = \mu_i + \sigma_i - S. \quad (13)$$

Then rule extraction RULEX process can be seen below in Table II [9].

TABLE II

RULE EXTRACTION ALGORITHM

Procedure:
For each hidden unit:
For each μ_i
$X_{lower} = \mu_i - \sigma_i + S$
$X_{upper} = \mu_i + \sigma_i - S$
Build rule by:
antecedent=[X_{lower}, X_{upper}]
Join antecedents with AND
Add class label
Write rule

Consequently, a base for the rules has been obtained.

III PossIBILITIES OF ONTOLOGY

In recent years the development of ontologies is formal description of the terms in the domain and the relationships between them that moves from the world of artificial intelligence laboratories to desktops of domain experts [5]. In the World Wide Web ontologies have become common things. Ontologies on the net range from large taxonomies, categorizing Web sites, to categorizations of products sold and their characteristics. In many disciplines nowadays standardized ontologies are being developed that can be used by domain experts to share and annotate information in their fields.

Informally, an ontology is a description of the view of the world in relation to a particular area of interest. This description consists of the terms and rules for the use of these terms, limiting their roles within a specific area. Formally, ontology is a system consisting of a set of concepts and a set of statements about the concepts on the base of which you can build up classes, objects, relations, functions, and theories.

The main components of the ontology are: classes or concepts, relationships, functions, axioms, examples.

There are various definitions of ontology, but recently the generally recognized is the following definition: "An ontology is a formal explicit specification of a shared conceptualization" [11]. Ontologies are often equated with taxonomic hierarchies of classes. Thus, the aim of ontology is to accumulate knowledge in general and formal way.

Ontologies can be classified in different forms. One of the most popular types of classification is proposed by Guarino, who classified types of ontologies according to their level of dependence on a particular task or point of view [12]:

- *Top-level ontologies*: describe general concepts like space, time, event, which are independent of a particular problem or domain.
- *Domain-ontologies*: describe the vocabulary related to a generic domain by specializing the concepts introduced in the top-level ontology.
- *Task ontologies*: describe the vocabulary related to a generic task or activity by specializing the top-level ontologies.
- *Application ontologies*: they are the most specific ones. Concepts often correspond to roles played by domain entities. They have a limited reusability as they depend on the particular scope and requirements of a specific application.

Ontologies are widely used in Semantic Web and document clustering, but there is very little information about the use of ontology in numerical data clustering.

Thus, an ontology is an explicit representation of knowledge. It is a formal, explicit specification of shared conceptualizations, representing the concepts and their relations that are relevant for a given domain of discourse [11].

Worked out numerical data clustering ontology concept is composed of the following classes:

Clustering Task. It is an abstract class. It is connected with the clustering algorithm class. Depending on the purpose and the clustering area (domain) clustering algorithm, the number of clusters and the data sample are chosen.

Clustering_Algorithm. This class represents a list of available clustering algorithms and their features (see Fig. 1).

Clustering_Metric. This class represents a list of available distance metrics for clustering algorithms (see Fig. 2).

Clustering_Validity. This class represents a list of cluster validity methods (see Fig. 3).

Clustering_Rule. This class represents a list of rule extraction methods from clusters (if it is possible).

Based on such analysis of classes the following approach is offered for ontology-based clustering, as shown in Fig. 5.
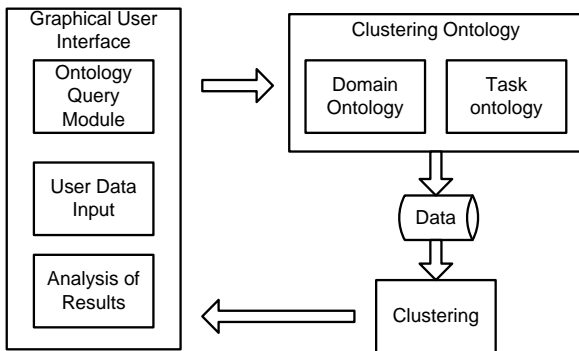
Fig. 5. The framework concept of ontology-based numerical data clustering

Developing framework Protégé OWL tool is used for construct this prototype [16].

Protégé is a special tool, which is thought to create and edit ontology, but OWL (Web Ontology Language) is a language through which it is possible to define the ontology. OWL ontology may include descriptions of classes, their characteristics and their instances. OWL formal semantics describes how, using these data get information which was not openly described in ontology, but which follows from the data semantics. Protégé is a free open-source platform, which contains special tool kit which makes it possible to construct domain models and knowledge-based applications based on ontologies. In Protégé environment a number of knowledge-modeling structures and actions that support ontology creation, visualization and editing of different display formats are implemented.

Protégé is an extensible knowledge model. The internal representational primitive in Protégé can be redefined declaratively. Protégé's primitive - the component of its knowledge model - provide classes, instances of these classes, frame representing attributes of classes and instances.

Ontology development with the help of Protégé starts with the definition and description of classes hierarchy, and then instances of these classes and different types of relationships (properties in Protege) in order to put more meaningful information within the ontology are assigned.

For demonstration ontology development two classes are chosen: *Clustering_Algorithm* and *Clustering_Metric* (see Fig. 6 and Fig. 7).
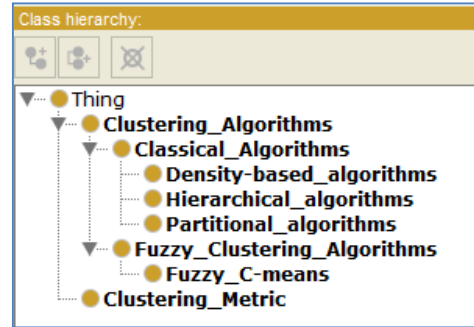
Fig. 6. Clustering domain subclasses in the "Class hierachy" tab of Protégé
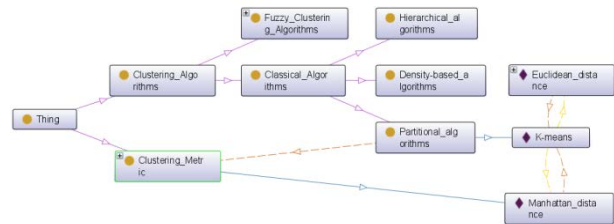
Fig. 7. A visualization of the domain Clustering subclasses in OntoGraf tab

Since clustering algorithm relates to partitional algorithms class, then in class *Partitional_algorithms* was included member *K_means*. K-Means algorithm can use metrics Euclidean distance or Manhattan distance, then in class *Clustering_Metric* were included members: *Euclidean_distance* and *Manhattan_distance*.

K_means member was defined by following characteristics (properties):

K_Means – use -> Euclidean_distance
K_Means – use -> Manhattan_distance

In turn, *Clustering_Metric* object *Euclidean_distance* was assigned following property:

Euclidean_distance - isUsedBy -> K_means (see Fig. 8).
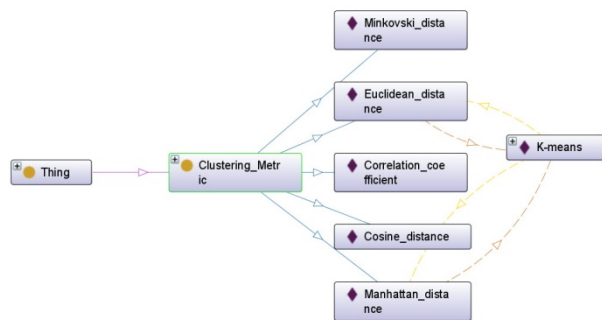
Fig. 8. K-means property visualization in *Clustering_Metric* class

The demonstration example clearly shows that with a help of Protégé we can create an effective description of the ontology, but it is sufficiently laborious process. Author will continue his work on numerical data clustering ontology and its further improvement.

V CONCLUSION

There are no directly formalized criteria in cluster analysis, so different clustering parameters are chosen in subjective assessment. This refers to the clustering algorithm selection, the choice of number of clusters in each case, the cluster validation criteria determination. Also very important is the knowledge extracted from clusters in the form of rules. All this leads to problems in interpreting the results of clustering. In recent decades, cluster analysis has evolved from one of the data analysis section into a separate direction, which is closely related to knowledge support systems. Partly, this happened due to the introduction of the ontology concepts in the description of clustering characteristics. The use of clustering ontology in documents and semantic web applications is developing very rapidly, but the numerical data clustering is undeservedly neglected. The author has taken the attempt to define and develop an ontology-based prototype for numerical data clustering. This conception contains several concept classes: clustering algorithms, cluster numbers, cluster validity and other characteristics features. In further studies these classes refinement and a real model development according to data clustering purpose will be carried out.

VI REFERENCES

[1] B. S. Everitt, *Cluster analysis*. John Viley and Sons, London, 1993, 170 p.
[2] L. Kaufman and P. J. Rousseeuw, Finding groups in data. An introduction to cluster analysis. John Wiley & Sons, 2005.
[3] S. Russel and P. Norvig, *Artificial Intelligence: A Modern Approach*. Prentice Hall, 2010, 1132 p.
[4] R. Xu and D. C. Wunch, *Clustering*. John Wiley & Sons,2010, pp. 263-278.
[5] D. Gašević, D. Djurić and V. Devedžić, Model driven architecture and ontology development. Springer-Verlag, 2006.
[6] F. Hoppner, F. Klawonn, R. Kruse and T. Runkler, *Fuzzy Cluster Analysis*. John Whiley and Sons, New York, 1999,289 p.
[7] M. Crawen and J. Shavlik, Using sampling and queries to extract rules from trained neural networks. Machine Learning: Proceedings of the Eleventh International Conference, San Francisco, CA, 1994.
[8] P. Vitanyi, *Universal similarity*. *ITW2005*, Rotorua, New Zealand, 2005.
[9] R. Andrews and S. Gewa, "RULEX and CEBP networks as the basis for a rule refinement system," in *J. Hallam et al, editor, Hybrid Problems, Hybrid Solutions*. IOS Press, 1995.
[10] G. Gan, C. Ma and J. Wu, "Data clustering: Theory, algorithms and applications," ASA-SIAM series on Statistics and Applied Probability, SIAM, Philadelphia, ASA, Alexandria, VA, 2007.
[11] T. R. Gruber, "A translation approach to portable ontologies," Knowledge Acquisition, 5(2),199-220, 1993.
[12] N. Guarino, "Formal Ontology in Information Systems," 1st International Conference on Formal Ontology in Information Systems, FOIS, Trento, Italy, IOS Press, 3-15, 1998.
[13] D. R. Hush and B. G. Horne, "Progress in Supervised Neural Networks. What's new since Lippmann?" IEEE Signal Processing Magazine, vol.10, No 1.,p.8-39, 1993.
[14] M. Li, X. Chen, B. Ma and P. Vitanyi, "The similarity metric," IEEE Transactions on Information Theory, vol.50, No. 12, pp.3250-3264, 2004.
[15] X. Rui and D. Wunsch II, "Survey of clustering algorithms," Neural Networks, IEEE Transactions on, 16(3):645–678, May 2005.
[16] "Protégé project homepage," [Online]. Available: http://protege.stanford.edu/index.html [Accessed: March 13, 2013].

A System for Input of 3D Objects into Computing Environment

Raycho Ilarionov, Krasimir Krastev

TU – Gabrovo

Abstract. **This paper proposes an approach for design and implementation of automated 3D scanner used for input of mechanical 3D objects into computing environment. The presented model of 3D scanner is based on kinematic diagram of positioning system with 5 degree of freedom – 3 linear and 2 rotational, each driven by servo motors. For distance measuring is used laser scanning head with rotational triangulation. The paper describes also algorithms for functional control of the scanning process, obtaining of point cloud, object reconstruction and export to standard CAD format.**

Keywords - **3D scanning, CAD/CAM, Laser measuring, Positioning System, Point Cloud, 3D object reconstruction.**

I Introduction

Nowadays, the design of new products in mechanical engineering becomes impossible without the use of CAD software for three dimensional modeling. In this relation more topical become the question for direct entry of finished parts into computing environment in order to create theirs models, parameters measurement or just for quality control [9]. This process is known also, as reverse engineering. For its needs are used specialized devices called under common name - 3D scanners. Today this class of devices are a necessary component in each one modern CAD/CAM system in machine building, as they help to improve efficiency in the design and maintenance of new machine elements, as well as such that are out of productions.

Due to its relevance, the systems for 3D scanning are subject of continuous development and improvement [7]. Could be divided into three main directions of development:

- – Automation of the scanning process;
- – Resolution and scanning speed;
- – Detailed scanning;

In this paper is presented an approach for design of system for 3D object scanning with higher level of automation and possibility for many sides scanning of objects with complex geometrical shape with presence of multiple holes, slots and edges.

II Exposition

In the classical scanners, scanning is a process of digitalization of a given object with the purpose of entering a two dimensional graphic information from it into computing environment. Unlike them the 3D scanners captures the surface shells of given object – i.e. his relief [4]. The process of entering of three dimensional bodies into computing environment consists of two basic steps – 3D scanning and object reconstruction (Fig. 1.).

The information, which is collected by a 3D scanner, represents a set of points in three-dimensional space, also called 'point cloud'. Each point from the cloud lying on the object surface and is represented by its three-dimensional coordinates - x, y and z. In this way can be get a clear picture for relief and shape of the object, and subsequently by using suitable CAD product to be created a model, measurement or analyzing of parameters. As output information from 3D scanning is obtained a file containing the three coordinates of each point from the object surface. The reconstruction of the scanned objects is made by CAD programs which implement specialized algorithms for generation of polygonal mesh and export of the results to standard CAD formats [8].

As input data for the reconstruction of an object is a file generated by 3D scanner, which contains the set of three-dimensional points describing the scanned object.
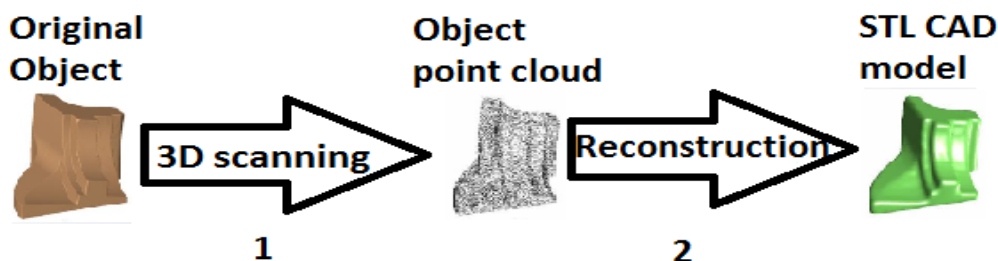

Fig. 1. 3D object input into computing environment

In general, a 3D scanner consists of a scanning measuring head and positioning electro-mechanical system [4]. The scanning head measures relative coordinates from its current position to the object surface and the positioning system is used to move the head around the object (or vice versa), taking into account the absolute coordinates, compared to defined reference point. By accurate juxtaposing of the relative coordinates from the scanning head with the absolute coordinates from the positioning system, can be obtain a set of 3D points describing a scanned object [5].

In designing of systems for 3D scanning it is necessary to be defined two main points:

Maximum dimensions of the scanned objects;

Scanning method and optimal resolution;

The overall dimensions of the scanned objects can vary in very wide range. In the machine building, however most of the components, which are usually subjected to 3D scanning, fall within the range of up to 300mm in height and up to 500mm in diameter.

The classical method for 3D scanning uses contact measurement probe to measure the distance to the object surface. This method gives the most accurate results, but is relatively slow and there is a prerequisite of scratching the scanned surface. Modern 3D scanning devices used mainly noncontact scanning methods, as these are more preferred in this type of systems. The principle of their work consists in the emission of light toward the object and calculating the angular offset or the time for receiving of the reflected light. The resolution and accuracy of the scanning heads depends largely on their measuring range and is selected depending on the required accuracy of scanning. In common case this range is up to 100mm measurement range, 0.025mm resolution and +/- 0.005mm repeatability.

This paper considers the following key points related to the design of a system for 3D scanning:

Selection of kinematic model for positioning system of the 3D scanner;

Selection of scanning head;

Selection of elements for drive and control of the positioning system;

Structural and functional model of the 3D scanner;

Reconstruction of scanned 3D object and exporting to standard CAD format;

III DEVELOPMENT OF KINEMATIC MODEL FOR POSITIONING SYSTEM

Desktop 2D scanners use two-dimensional coordinate positioning system for perambulating the scanned image. However, for collecting of three-dimensional information this is not enough - it is necessary at least one more, third coordinate.

When scanning 3D objects can be considered two main aspects - the movement of the scanning head around and along the object or vice versa - moving the object around and under scanning head [10]. The first option is more appropriate, because of the significantly lower mass and dimensions of the scanning head compared to some parts that may be subjected to scanning.

To unify the very kinematic model of the scanning system it is necessary to approximate every part which should undergo scanning to an object of regular shape. Regular shaped 3D bodies in Cartesian space can be divided into two large groups:

– rotational bodies – they are obtained through rotating a curve around one of the axes;
– plane bodies – they are obtained through linear motion of a curve along one of the axis;

It follows, that are necessary at least four degrees of freedom - three linear for horizontal and vertical motion of the scanning head and one more to rotate the object. In practice, however, the actual three-dimensional objects are irregularly shaped with many edges, holes and slots. This entails the necessity of an additional degree of freedom to rotate the scanning head at different angles toward the scanned surface.

A model covering these primitives should possess at least five degree of freedom - three linear and two rotational movements.

The selected kinematical model of positioning system is a five axis coordinate system of portal type for moving scanning head and rotation of the scanned object (Fig. 2.). There are three linear axes 'X', 'Y', 'Z' and two rotational axes – 'A' and 'B'.

Table 1 shows the nominal parameters of the presented kinematic model for positioning system of the 3D scanner.
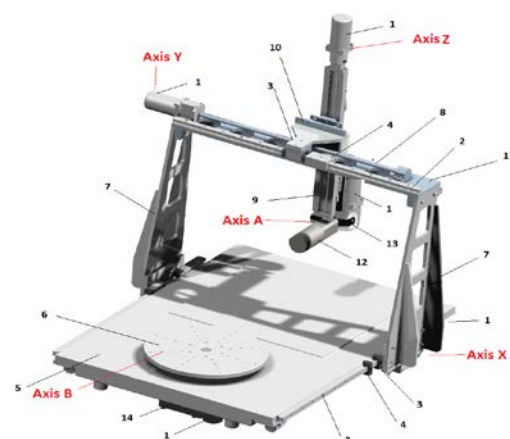

Fig.2. Kinematic model of the positioning system

Elements of the positioning system:

Driving servo motors for 'X', 'Y', 'Z', 'A' and 'B' axes;

2. Guiding rails;
3. Sliding carriage;
4. Linear encoder;
5. Basis;
6. Rotational table (axis 'B');
7. Vertical support;

8. Ball-screw - axis 'Y';
9. Ball-screw - axis 'Z';
10. Carrier – axis 'Z';
11. Horizontal support;

12. Scanning head;
13. Reducer – axis 'A';
14. Reducer – axis 'B';

TABLE. 1.

Axis	Working range	Work Speed	Max. Speed	Nom. Torque	Min. Step
X	550 mm	5000 mm/min	10000mm/min	0,25Nm	0,001mm
Y	550 mm	5000 mm/min	10000mm/min	0,18Nm	0,001mm
Z	350 mm	5000 mm/min	10000mm/min	0,19Nm	0,001mm
A	+/-90°	1800 °/min	3600 °/min	0,23 Nm	0,01 °
B	0 – 360°	3600 °/min	7200 °/min	0,32 Nm	0,01 °

NOMINAL PARAMETERS OF THE POSITIONING SYSTEM

*The presented torque of axis 'X' is for one of the driving axis at full load.

The position accuracy is achieved by incremental linear encoders with resolution of 1000inc per mm, which allows position accuracy of 1μm. The kinematic scheme is comparatively light without any major inertial moments. The portal type provides stability of the system to the vibrations of the measuring Z coordinate. Synchronous drive of the portal prevents twisting and guarantees the perpendicularity of axis 'Y' to axis 'X'. For driving of the linear axes are used precise ball-screws with 2mm pitch and driving of the rotary axes is through reducers. Reduction factor for axis 'A' is i = 10, and for axis 'B' is i = 100. Presented in the table nominal torques are calculated from the nominal weight of the elements in corresponding axis, maximal positioning speed and permissible acceleration – up to 20000mm/s2 for linear axes and 3000°/s2 for rotational axes. Maximum allowed mass of the scanned objects placed on the rotary table is 20kg.

Fig. 3. Laser scanning head OTM 3A

IV SELECTION OF SCANNING HEAD

The selection of scanning head usually is individual depending of the specific group of three-dimensional objects, which has to be scanned.

For this selection are necessary to be observed the following main criterions:
Scanning head working principle;
Measurement range ;
Resolution;
Repeatability of measurement;
Time to measure;

Type of the communication interface;

At the moment most spread measurement methods [6] used in scanning heads are:

- Structured light – projecting of light patterns over the object surface with using of DLP projector and image capturing by CCD camera;

- Laser triangulation – projecting of laser light formed as spot or line over the object surface with using of laser source and capturing of the reflected light by CCD sensor;

Both methods use triangulation principle to measure the distance to the object surface (emitter, object and receiver form a triangl) Because of their small masses, scanning heads which operate on the laser triangulation principle are most appropriate for 3D scanning systems, with motion of the scanning head. Highest scanning speed can be achieved by the laser section method – the projected laser light is line shaped, as by this way are simultaneously scanned up to 10000 points from the object surface. The disadvantage, however, is the strongly expressed shadow effect due to the large angle of triangulation. Rotational triangulation is a kind of laser triangulation, which works at very small base angle between emitter and receiver, as in this way shadowing effect is minimal.

Due to the necessity for scanning of complex geometrical objects with presence of multiple sharp edges and deep slots is selected laser scanning head of Wolf&Beck GmbH type OTM 3A-50 (Fig. 3) operating on the rotational triangulation method [3]. The scanning head is controlled by PCI controller, which is mounted in PC slot, communication between them is through digital serial interface - RS422 (Fig. 3.). PCI controller is supplied with drivers for Windows. Key features of OTM 3A-50:

– Work distance: 140 mm;
– Measurement range: 50 mm;
– Resolution: 0.005 mm;
– Repeatability: 0.025 mm;
– Time to measure: 500μs

Max. slope of the scanned surface: 60°;

PCI controller of the scanning head provides digital I/O interface for control and synchronization with external systems. Due to its direct action this interface is suitable for synchronization the measurements with the positioning system of the scanner.

V SELECTION OF DRIVE AND CONTROL ELEMENTS

For driving of the positioning system are necessary executive electrical motors, these are stepper motors, DC servo motors and AC servo motors. AC servo motors are preferred choice due to their wide control capabilities, high dynamic, overload capacity and lack of maintenance (in fact, they are eternal).

The selection of driving motors is made on two main criterions:

Necessary torque to drive the positioning system;

Maximal positioning speed;

To unify the model of positioning system it is preferred a selection of same kind servo motors for all axes. Table 1 show, that highest drive torque is needed for axis 'B' – 0,32Nm. When choosing the right servo motor it is necessary to provide 25% of stock. The nominal speed which must provide selected servo motor type is calculated from the maximal positioning speed and pitch of the screw for linear axes and reduction factor for the rotational axes. In this case is derived that, for driving of all linear axes is required nominal speed > 5000min-1, for axis 'A' >100 min-1 and for axis 'B' >2000 min-1.

For the concrete application are selected synchronous servo motors type DT3 of the German company AMK GmbH [2] (may be used and the servo motors of different manufacturer). In Table 2 are presented technical parameters of this kind of servomotors.

The total number of servo motors is six. Two of them are used to drive the portal part along 'X' axis and by one to drive of axes 'Y','Z','A' and 'B'.

For control of the selected servo motors are used double servo inverter type KWD with nominal power of 2x1kV. This selection is made based on servo motors nominal current, as is provided 25% stock. The power supply of the servo inverters is by common module type KEN10 with nominal power of 10kVA. Control plates for each axis are KW-R06 type with integrated EtherCAT control interface, working in real time.

For positioning system control is selected PC based industrial controller (PLC) of AMK GmbH Company – type A5S-ECO with EtherCAT digital interface.

TABLE. 2.

TECHNICAL PARAMETERS OF SELECTED DT3 SERVO MOTOR BY AMK GMBH

Motor type	MO [Nm]	MN [Nm]	PN [kW]	I_N (A)	n_N [U/min]	n_{max} [1/min]	M_{max} [Nm]	Imax[A]
DT3-0,5-10-RxO-9000	0,64	0,5	0,31	0,9	6000	10000	1,9	4

VI STRUCTURAL AND FUNCTIONAL MODEL OF THE 3D SCANNER

Structural model

The structural model of the 3D scanner (Fig. 4.) represents all connections between the elements in the control system. It consists of two control subsystems:

PC-CAD work station with Windows based operation system. Include:

Program for 3D scanner control, as Windows application;

PCI controller for the scanning head PCI OTM3A – mounted in slot of PC;

Driver for scanning head control;

CAD software for edit and reconstruction of the scanned objects;

System for driving and control of the positioning system. Include:

Industrial controller for real time motion control;

Application program, which implements motion control functionality;

6 servo motors for driving of axes 'X', 'Y', 'Z', 'A' и 'B';

3 double servo inverter modules for controlling each of the 6 servo motors;

Linear encoders for position measurement by axes 'X', 'Y', 'Z' and rotational encoder for position measurement by axis 'B'.

All motion control functions of the positioning system are executed by Motion Controller AMK A5-ECO, as is guaranteed real time operation with higher accuracy of synchronization between all servo axes at fixed transmitting cycle of 500μs and minimal dissipation of 500ns. The connection between motion control and the servo drives is through digital EtherCAT interface. The connection between the two subsystems is through Ethernet (LAN) interface.

Synchronization between scanning head measurements and actual coordinates from the positioning system is through a clock signal, generated at each measurement from a digital output of the OTM3A PCI controller [5]. This clock signal is send to trigger input for position measurement of each servo drive, which cause immediate record of the current axis position with corresponding sequential number in the PLC memory. In the same time measured data by the scanning head are recorded in the memory of the work station (PC) with corresponding sequential number. Buffer length is up to 125000 records organized as FIFO structure, at overflow it starts from the beginning. Buffer structure

and data format, which are recorded by the scanning head for each captured point are presented in Table 3

and the data format from the positioning system in Table 4.
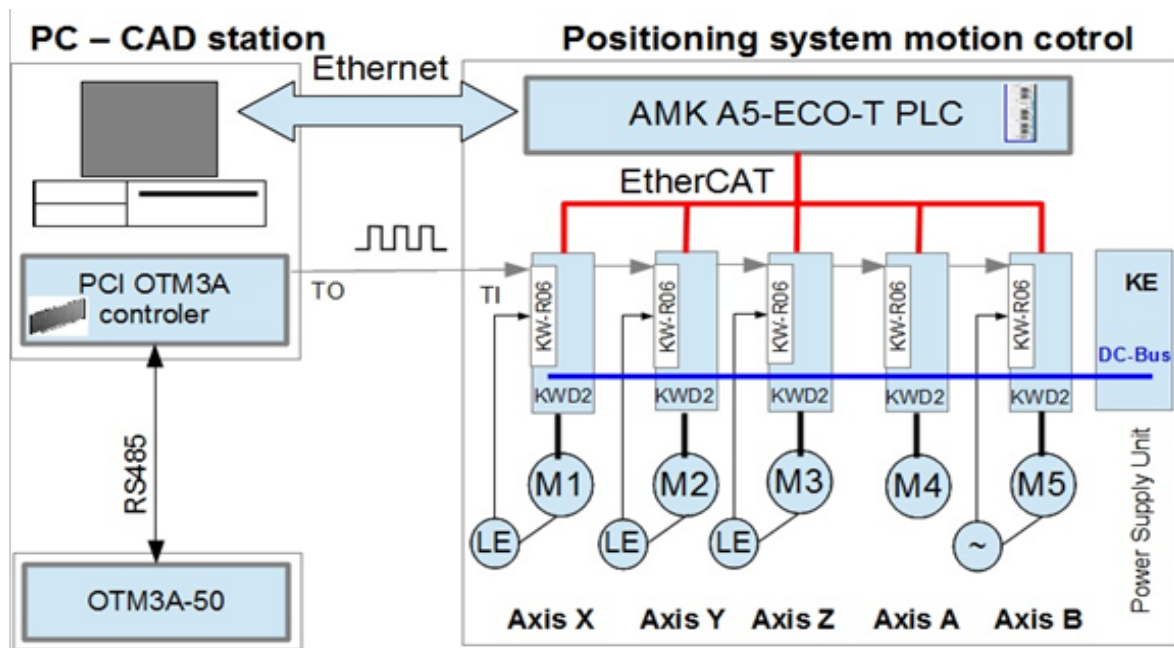
Fig. 4. Structural model of the 3D scanner

TABLE. 3.

SCANNING HEAD – STRUCTURE OF THE DATA BUFFER

Distance[0]	Angle[0]	Intensity[0]	Status[0]	Tan[0]
Distance[1]	Angle[1]	Intensity[1]	Status[1]	Tan[1]
Distance[n]	Angle[n]	Intensity[n]	Status[n]	Tan[n]

TABLE. 4.

POSITIONING SYSTEM – STRUCTURE OF THE DATA BUFFER

X [0]	Y [0]	Z [0]	A [0]	B [0]
X [1]	Y [1]	Z [1]	A [1]	B [1]
X [n]	Y [n]	Z [n]	A [n]	B [n]

A minimal scanning step of 0,041mm is calculated at maximal scanning speed of OTM 3A-50 up to 2000p/s and maximal moving speed of the positioning system up to 5000mm/min.

Functional model

The functional model of the 3D scanner (Fig. 3.) considers the functionality and the tasks of the control software. The software is divided into two main control programs, which must work together:

Control program of the 3D scanner. Developed with QT Creator and MinGW compiler. Provides the following functionality:

Interactive graphical interface to the operator for working with the 3D scanner;

Control of the laser scanning head;

Control of the positioning system with sending of commands to the PLC;

Maintain communication with the PLC;

Control of the 3D scanner operating modes;

Collecting and recording of data from the scanning;

Application program for motion control. Developed with CoDeSys V2.3 [1]. Provides the following functionality:

Control and diagnostic of all servo motors;

Referencing of axes 'X', 'Y', 'Z', 'A' and 'B';

Manual positioning of all axes – continuous and in step mode;

Input of settings for scanning;

Automatic scanning by surface primitive presented by the control program;

Record of measured coordinates in memory buffer and their transfer to a PC;

Automatic monitoring and maintenance in the measuring range of the scanning head;

The graphical user interface (Fig. 5.) of the program for control the scanner, provides opportunity to work in two operating modes:
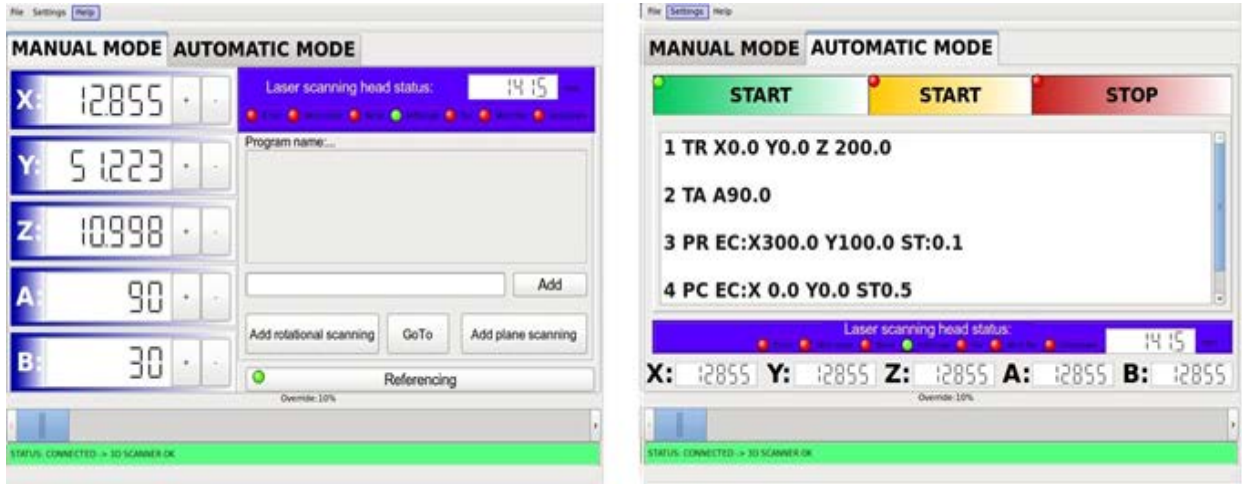
Fig. 5. Graphical user interface of the 3D scanner control program

Manual mode – in this operating mode the user interface provides:

Manual positioning with buttons of each selected axes in continuous motion control or in stepping motion control and sending of commands for axes referencing;

Indication of current position and measured distance by the scanning head;

Menu for system settings – for scanning head and the positioning system;

Command interpreter and program editor;

Wizard with graphical user interface for entering of scanning cycles;

Status information of the positioning system and laser scanning head;

Automatic mode – this operating mode is responsible for the automatic scanning by preselected input program. In automatic mode the user interface provides:

Start of preselected scanning program;

Buttons for start, stop and pause of started automatic cycle;

Visualization of actual coordinates of the positioning system and the measured distance from the scanning head;

System status information;

To scanning of 3D objects is developed an approach for surface division into primitive areas, which are processed by pre-programed cycles. These scanning cycles can be grouped into separate programs and stored on non-volatile device for future use. The commands which are set for execution to the positioning system controller represent scanning cycles in which the scanning head is moved over predefined areas from the object surface. For the convenience of the operator and to accelerate the time for system setup, a wizard is designed with a graphical interface for setting and entering of each program scanning cycle - Fig. 6 shows the graphical interface of the wizard for entering of cycle for cylindrical scanning. Descriptions of the scanning cycles and the commands for them are presented in Table 5.

Format of the commands:

CC __ E:_ separator _ O: _ separator _R:_ separator _ST: __%

TABLE. 5.

SET OF PROGRAM CYCLES FOR SCANNING OF SURFACE PRIMITIVES FROM 3D OBJECT

| Command	Meaning
TA	Absolute positioning , target coordinates are set with E:
TR	Relative positioning, target coordinates are set with E:
PR	Plain rectangle area scanning, O: set the origin point, E: end point – by diagonal
PC	Plain circle scanning, O: set the point of circle center, E: end point – from lying on the circle
PA	Plain scanning as part of circle O: set the arc origin point, E: end point, R-radius of the arc
PT	Plain triangle area scanning (isosceles), O: set first corner - origin point, E: set second corner
CL	Cilindrical scanning, O: set the origin point , E: set the end point
CS	Cilindrical scanning with offset center * - O: set origin point, E: set end point, R: set the offset
SF	Spherical scanning, O: set the origin point, E: set end point, R set the radius
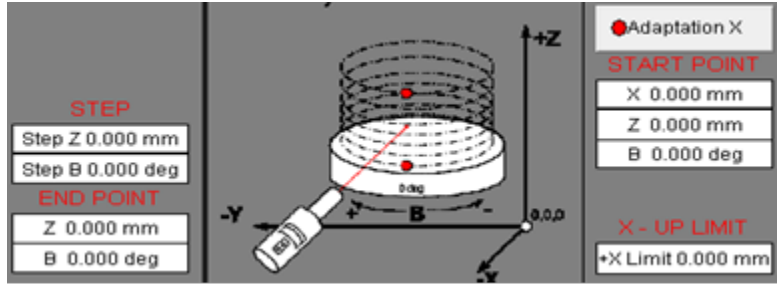
Fig. 6. Window of the wizard for input of cylindrical scanning cycle

Each command for scanning cycle begins with two-letter mnemonic code – 'CC'. The command is followed by parameters for the scanning – end coordinates (End) 'E:', start coordinates (Origin) 'O:', optional parameter 'R:', scanning step 'ST:' and speed override '%', as percent of the nominal.

For example: PR E: X100.0 Y20.0 A90.0 # O:X0.0 Y0.0 A90.0 # ST:0.01 %100 – plane scanning in XY plane from 0.0, 0.0 to 100.0, 20.0 with step of 0.01mm, at full speed. Required for each parameter group is to be separated with sign for separation – '#'. The format of each parameter is up to three coordinates. The scanning plane is selected depending of the first two coordinates, stored after 'E:' – end point parameter. The first coordinates stored after 'E:' define the master axis for the cycle and the second coordinate is an auxiliary – slave axis is controlled in stepping mode depending of the scan step. Depending of the difference between first and last coordinates, third axis is interpolated together with the master axis – if exists a record. The origin coordinates are not mandatory, if they are missing, as point of origin is accepted the current position of the scanner. Setting of scanning step is required only at the first command in the program – it is modal. If no speed is set, the system runs at maximum speed.

During the scanning process the two data flows are combined together in a common file by the control program – the data are shown in Table 3 and Table 4. This file is stored in the same folder on PC, where is placed the control program. After end of the scanning a coordinate transformation is applied over the recorded data, with purpose to convert the measured distance data and the captured positions of the positioning system in three-dimensional Cartesian coordinates.

Full coordinate transformation of the 3D scanner is presented with dependence (1) and it is universal for all methods for scanning of three dimensional objects with the presented prototype.

Where:

θ_i – is the angle of rotation of the scanning head(axis 'A');

α_i - is the angle of the rotational table (axis 'B');

r_i – is the difference between 'X' axis position and the measured distance by the scanning head in sequential point of measurement, taking into account 'A' axis position;

j_i – is the distance from the axis of symmetry of axis 'B' to the object surface in the point of measurement;

$$P = \begin{bmatrix} x_1 & y_1 & z_1 \\ x_2 & y_2 & z_2 \\ \dots & \dots & \dots \\ x_n & y_n & z_n \end{bmatrix} = \begin{bmatrix} r_1\cos(\alpha_1 + \arctan\frac{j_1}{Y_1}) & r_1\sin(\alpha_1 + \arctan\frac{j_1}{Y_1}) & Z_1 - (l_1\sin\theta_1) \\ r_2\cos(\alpha_2 + \arctan\frac{j_2}{Y_2}) & r_2\sin(\alpha_2 + \arctan\frac{j_2}{Y_2}) & Z_2 - (l_2\sin\theta_2) \\ \dots & \dots & \dots \\ r_n\cos(\alpha_n + \arctan\frac{j_n}{Y_n}) & r_n\sin(\alpha_n + \arctan\frac{j_n}{Y_n}) & Z_n - (l_n\sin\theta_n) \end{bmatrix} \quad (1)$$

As output data from the scanning is obtained standard file in *.xyz or *.pcd format, which contains the point cloud and fully describe the scanned 3D object.

VII RECONSTRUCTION OF SCANNED 3D OBJECTS

For reconstruction of the scanned objects with proposed prototype of 3D scanner has been chosen the program 'MeshLab' - developed by Computing Lab IST CNR [8]. MeshLab supports multiple of functions for editing and processing of point clouds with 3D points as end large scale of algorithms for generating of polygonal meshes, rendering and finally export of the models into STL or DXF CAD file formats.
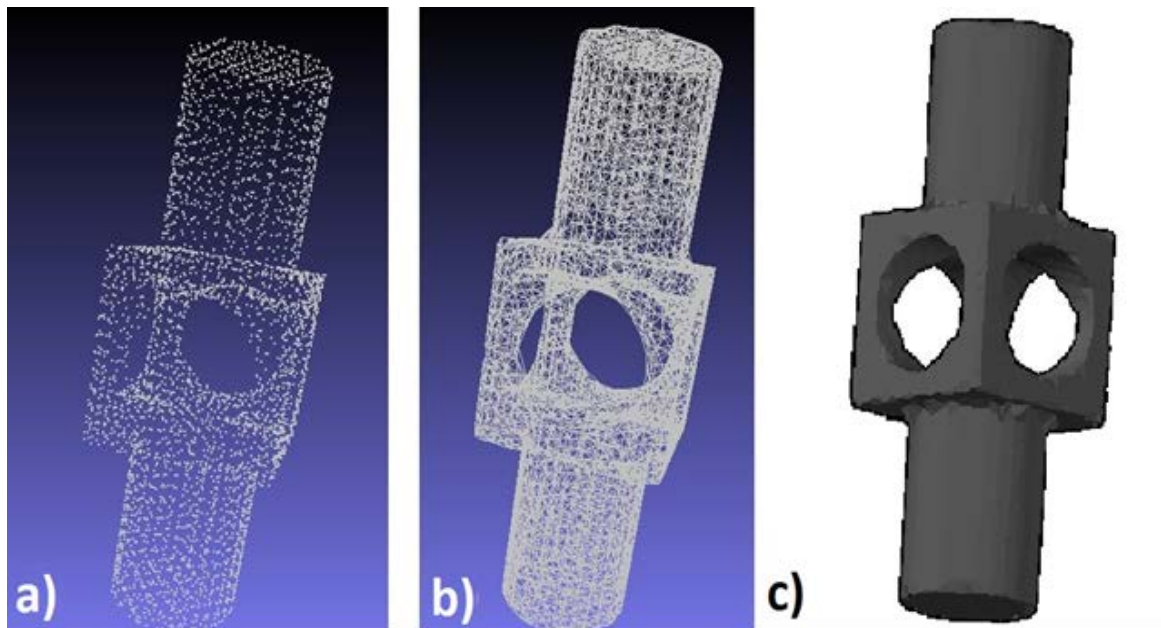
Fig. 7. a) Point cloud of scanned mechanical detail, b) Triangulated model, c) Solid model in AutoCAD

The process of reconstruction passes through the following steps:

Import and editing of the point cloud – includes basic operations, as shifting, rotation, grouping, scaling, as well as noise reduction and the excess point in the cloud.

Construction of polygons – includes polygonal meshes generation, editing, optimization and smoothing. Some of the most used algorithms are:
Alfa Complex/Shape;
Delaunay Triangulation;
Surface Reconstruction –Ball-Pivoting;
Surface Reconstruction – Poisson;
Voronoi Filtering;

Creation of NURBS surfaces – includes processing and creation of NURBS surfaces, surfaces grouping, editing and finishing.

Exportation of the models into standard CAD file format – most used are STL and DXF file formats.

On Fig.7 consistently are shown the stages of reconstruction of scanned object with the proposed model of 3D scanner.

As reconstruction input data has imported a *.xyz file into MeshLab, which contains the point cloud of the scanned object. The scanning has made with resolution of 0.075mm. For creating of polygonal mesh has used the algorithm "Voronoi Filtering" with maximum poles threshold of 100.

Good results are obtained also with algorithms "Alfa Complex/Shape" and "BallPivoting". For smoothing of the created surfaces and detailing of the object has applied algorithm with the method of "Catmull-Clark". Finally the obtained polygonal model has exported into AutoCAD, where is presented as a solid body.

VIII CONCLUSION

The proposed in this paper approach for designing of 3D laser scanning device has been realized, as prototype in AMK LLT Company, Bulgaria, together with the support of Technical University of Gabrovo.

In the design process have been consistently considered the criteria for selection of suitable kinematic scheme, choice of scanning head, drive and control elements.

The presented prototype of 3D scanner is intended mainly for scanning of three-dimensional solid bodies in machine building, which have complicated form with multiple edges and slots. This has been obtained by using a 5-axis positioning system that provides linear motion and rotation of the measuring element as well vertical rotation of the scanned object. The selected laser scanning head works on the principle of rotational triangulation and allows scanning of surfaces at slope up to 60° and presence of transparent and highly reflective areas.

Proposed is a method for separation of the object surface shell into primitives for scanning as separate from it areas, which are then combined.

The maximal dimensions of the scanned objects are up to 300mm in height and 500mm in diameter, the maximum weight of the parts is 20kg. A satisfactory accuracy of 0.025mm of the scanning and minimal positioning step of 1μm for the linear axes and 0.01 ° for the rotational axis, has been achieved.

As output data from the scanning have been obtained standard files in *.xyz or *.pcd formats containing the set of the scanned points lying on the object surface.

Also has been proposed methodology for reconstruction of 3D objects by theirs point clouds and export of them as standard file formats into CAD environment, with using of the program MeshLab.

IX REFERENCES

[1]   [1] 3S-Smart Software Solutions GmbH. User Manual for PLC Programming with CoDeSys 2.3 . 2007.
[2]   [2] AMK GmbH. Servo drives user manuals. 2005.
[3]   [3] Dr. Wolf&Beck GmbH. Integration Handbook for Optoelectronic Distance Measuring System, 2005.
[4]   [4] Ilarionov, R., Model approach in the design of device for 3D information input into computing environment, CompSyst Tech 09, ACM, New York, USA
[5]   [5] Ilarionov.,R., K. Krastev, Flexible control of positioning system and laser scanning probe with data flow synchronization, Unitech 12, Gabrovo , Bulgaria
[6]   [6] Shell, R., Hall, E. (2000). Handbook of Industrial Automation, Marcel Dekker Inc, New York, USA.
[7]   [7] Schäfter + Kirchhoff. Applications: Measuring and Process Control in 3D using Laser Lines, Laser Spots and Laser Patterns, 2011.
[8]   [8]   MeshLab   –   online   documentation. http://sourceforge.net/apps/mediawiki/meshlab/index.php?title =Main_Page
[9]   [9] Benefits   of   3D   scanning. http://www.applications3d.com/Blog/?paged=3
[10]   Six   axis   motion   control   aparatus. http://www.freepatentsonline.com/8249823.pdf

Urban Objects Segmentation Using Edge Detection

Sergejs Kodors, Imants Zarembo

Rezekne Higher Educational Institution

Abstract. **This manuscript describes urban objects segmentation using edge detection methods. The goal of this research was to compare an efficiency of edge detection methods for orthophoto and LiDAR data segmentation. The following edge detection methods were used: Sobel, Prewitt and Laplacian, with and without Gaussian kernel. The results have shown, that LiDAR data is better, because it does not contain shadows, which produce a noise.**

Keywords – **edge detection, remote sensing, segmentation.**

I INTRODUCTION

Remote sensing is the science of obtaining and interpreting information from a distance. Remote sensing observes the surfaces and atmosphere of the planets using aerial, ground, satellite and spacecraft observations [7].

The main object of the observations is Earth with purposes: making and updating maps, geospatial databases creation, environmental monitoring, city planning, weather forecasting, etc. [1], [6]-[7].

All remote sensing systems designed to monitor the surface of Earth are based on the reflection and emission of the energy from surface features. Therefore the sensing systems are divided into 3 groups by their information acquisition principles [7]:

- Reflected solar radiation sensors;
- Thermal infrared sensors;
- Imaging radar sensors.

The interpretation of information is connected with image analysis: land use assessment [8], individual trees segmentation [2], etc.

There is a problem that the obtained images contain information about the scene – different objects at once. Therefore there is need to separate these objects before the classification process.

Image segmentation is used to separate the objects and to divide them from a background. Image segmentation is the process of partitioning digital image into multiple regions which have the similar features [3]-[5].

One of the techniques to segment digital images is edge detection.

This manuscript includes information about orthophoto and LiDAR data segmentation using edge detection methods. The Sobel, Prewitt and Laplacian kernels with Gaussian filter were used in the experiment to segment digital image with urban objects.

II EDGE DETECTION PROCESS

Edge detection process consists of 3 steps [3], [5]:

1) Filtering: this stage goal is to reduce an image noise. The often types of the noise are the salt and pepper noise, the impulse noise and Gaussian noise;

2) Enhancement: this stage goal is to detect changes of intensity in a neighbourhood of a point (pixel). The gradient magnitude are computed to indicate the changes of intensity;

3) Detection: this stage goal is to group all elements into 2 sets: black and white pixels. It is attached by thresholding.

III ENHANCEMENT

The boundaries between different surfaces of the scene in digital image are called edges. The edge is a significant change of image intensity.

One of approaches to estimate the edges is gradient-based methods, where the gradient of 2D function is calculated by the formula (1).

$$\nabla f(x, y) = \frac{\partial f(x, y)}{\partial x} \bar{i} + \frac{\partial f(x, y)}{\partial y} \bar{k}, \text{ (1)}$$

where $\bar{i}$ and $\bar{k}$ are unit vectors.

So a point of the significant gradient magnitude (2) is defined as the edge, if the significance is determined by the predefined threshold.

$$\left| \nabla f \right| = \sqrt{(\partial f / \partial x)^2 + (\partial f / \partial y)^2}, \quad \text{(2)}$$

where $\left| \nabla f \right|$ - the gradient magnitude.

The computation of the partial derivation in the gradient may be approximated in digital image by using masks (see Fig. 1-2) [4].

Fig. 1. Sobel masks.

Fig. 2. Prewitt masks.

The computation using masks is founded on the convolution (3).

$$y(n,m) = \sum_{k=-\infty}^{\infty} \sum_{t=-\infty}^{\infty} x(k,t)*h(n-k,m-t), \quad (3)$$

where h is kernel or mask with the central element $h(0,0)$.

The results of convolution using Sobel or Prewitt masks must be summed by formula (4) or (5) to get the gradient magnitude.

$$\left|\nabla f\right| = \sqrt{G_x^2 + G_y^2}. \quad (4)$$

$$\left|\nabla f\right| = \left|G_x\right| + \left|G_y\right|. \quad (5)$$

The Laplacian mask (see Fig. 3) is digital implementation of the second order derivative (6).

$$\nabla^2 f = \frac{\partial^2 f}{\partial x^2} + \frac{\partial^2 f}{\partial y^2}. \quad (6)$$

And Laplacian mask 5x5 in Fig. 4.

Fig. 3. Laplacian mask.

Fig. 4. Laplacian mask 5x5.

IV FILTERING

The Gaussian filter is one of the methods to reduce the noise.

Gaussian kernel is calculated by the formula (7).

$$G(x,y) = \frac{1}{2\pi\sigma^2} \exp(-\frac{x^2 + y^2}{2\pi\sigma^2}), \quad (7)$$

where σ - standard deviation and $G(0,0)$ is the central point of the mask (kernel). Then the image is convolved by Gaussian kernel using the formula (3).

The illustration of 2D Gaussian function is shown in Fig. 5 and Gaussian function shape dependence on the standard deviation in Fig. 6.

V POINT CLOUD TRANSFORMATION INTO 2D

LiDAR data is 3D point cloud, therefore to process it by edge detection, it must be transformed into 2D image.

Every point of the point cloud has its 3D coordinates XYZ, so it can be transformed into 2D by the point height (see in Fig. 7).
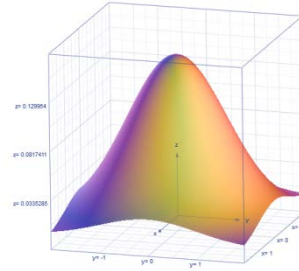
Fig. 5. Gaussian function, if $\sigma = 1$.
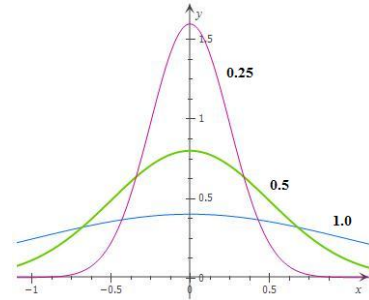
Fig. 6. Shapes of Gaussian function, where bold numbers are standard deviations.
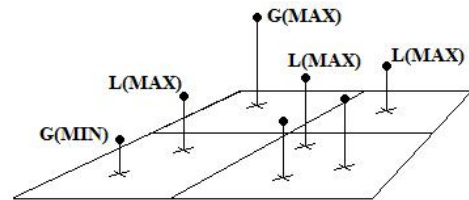
Fig. 7. Point cloud transformation into 2D by point height, where G are global min & max points and L are local min & max points.

Firstly the surface XY is divided into sectors, then the local maximum is found to every sector. After that the sectors are colored in gray colors, where white and black colors are specified by the global minimum and maximum.

VI MATERIALS AND METHODS

27

The process can be generalized by the following sequence:

1) Image is converted into grayscale format;
2) Gaussian filter (15x15, 3.0) is applied;
3) Sobel, Prewitt, Laplacian 3x3 and 5x5 filters are applied;
4) Min-max normalization is applied;
5) Thresholding by mean value is applied.

The special patterns have been prepared for the experiment, which simulate orthophoto and transformed LiDAR data into 2D. These patterns are illustrated in Fig. 8.
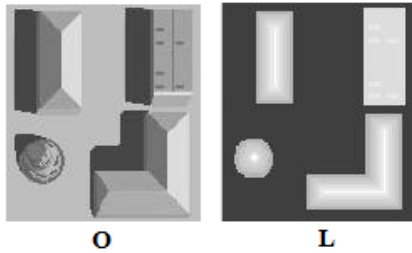
Fig. 8. Patterns for experiment, where *O* – simulates orthophoto, but *L* – simulates transformed LiDAR data.

VII RESULTS AND DISCUSSION

The results of edge detection are illustrated in Fig. 9-16, where the alphabetic symbols are the first symbols of the kernels names.
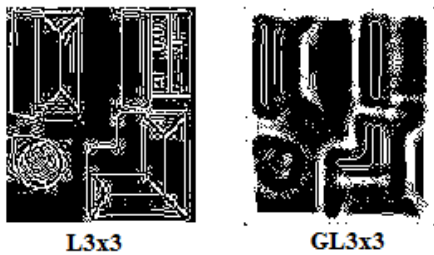
Fig. 9. Laplacian 3x3, pseudo-orthophoto case.
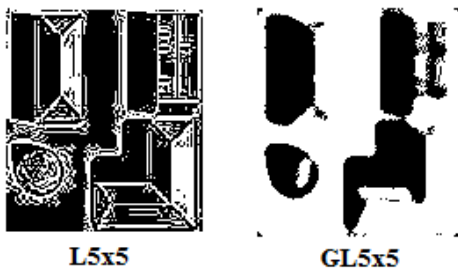
Fig. 10. Laplacian 5x5, pseudo-orthophoto case.

Fig. 11. Sobel, pseudo-orthophoto case.
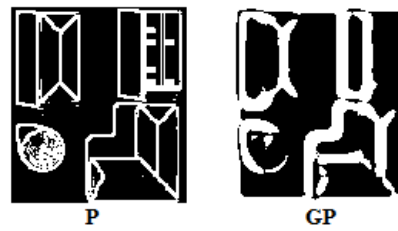
Fig. 12. Prewitt, pseudo-orthophoto case.
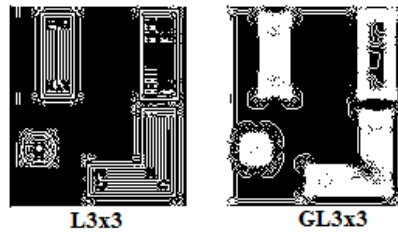
Fig. 13. Laplacian 3x3, pseudo-LiDAR data case.
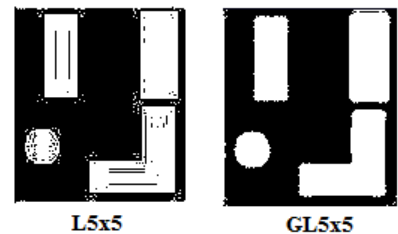
Fig. 14. Laplacian 5x5, pseudo-LiDAR data case.
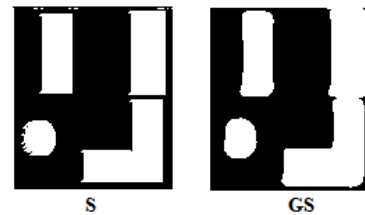
Fig. 15. Sobel, pseudo-LiDAR data case.
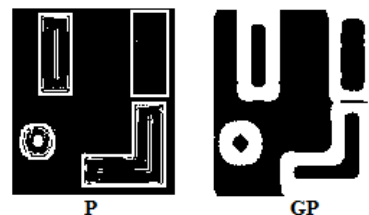
Fig. 16. Prewitt, pseudo-LiDAR data case.

VIII CONCLUSIONS

The results of the experiment have shown, that transformed LiDAR data is more efficient for the urban objects segmentation, because it does not contain shadows (see in Fig. 9-16). In Fig. 9-12 one can see, that edge detection is sensitive to shadows, it separates light and dark parts of image.

IX REFERENCES

[1] I. Dowman, *Integration of LiDAR and IfSAR for Mapping*: *XXth ISPRS Congress Technical Commission II*, July 12-23, 2004, Turkey, Istanbul.
[2] W. Li, Q. Guo, M. K. Jakubowski and M. Kelly, "A New Method for Segmenting Individual Trees from the Lidar Point

Cloud," Photogrammetric Engineering & Remote Sensing, vol. 78, pp. 75-84, January 2012.

[3] N. Senthilkumaran and R. Rajesh, "Edge Detection Techniques for Image Segmentation – A Survey of Soft Computing Approaches," International Journal of Recent Trends in Engineering, vol. 1, pp. 250-254, May 2009.

[4] S. S. Al-amri, N. V. Kalyankar and S. D. Khamitkar, "Image Segmentation by using Edge Detection," International Journal on Computer Science and Engineering, vol. 2, pp. 804-807, 2010.

[5] Y. Ramadevi, T. Sridevi, B. Poornima and B. Kalyani, "Segmentation and Object Recognition using Edge Detection Techniques," *International Journal of Computer Science & Information Technology*, vol. 2, pp. 153-160, December 2010.

[6] J.-Y. Rau, N.-Y. Chen and L.-C. Chen, "True Orthophoto Generation of Built-Up Areas Using Multi-View Images," Photogrammetric Engineering & Remote Sensing, vol. 68, pp. 581-588, June 2002.

[7] R. B. Smith, "Introduction to Remote Sensing of Environment (RSE),"*MicroImages*, 2012. [Online]. Available: MicroImages, http://www.microimages.com/documentation/ [Accessed March 7, 2013].

[8] S. Martinez and D. Mollicone, "From Land Cover to Land Use: A Methodology to Assess Land Use from Remote Sensing Data," *Remote Sensing*, vol. 4, no. 4, p. 1024, April 2012. Available: http://www.mdpi.com/journal/remotesensing [Accessed March 7, 2013].

Development of Information Model of Forming Basic Educational Programs in the Light of Professional Competencies

Lilia Motaylenko, Olga Poletayeva, Sergey Lyokhin

FSG-fEIHPE "Pskov State University», Faculty of Informatics. Adress: pl. Lenin 2, Pskov, 180000, Russia

Abstract. **This paper describes the process of forming the basic educational programs to the professional competence of the proposed model based on a competency areas.**

Keywords – **information technologies, model, professional competencies.**

Introduction of Federal State Educational Standards (GEF) causes the need for new approaches in the planning and organizing the educational process at a university. When developing the curriculum for particular training the higher educational institution faces the problem of its qualitative assessment.

Figure 1 shows a standard model of the educational process at the university (Higher Educational Institution – HEI). Based on the recommendations of the GEF the university forms the Main Educational Program (MEP), which includes the Base of Disciplines (BD) with a Set of Competences Recommended (SRC) and the Variable part of Disciplines with disciplines to be chosen (VD). The university independently chooses variable the sets of disciplines, and puts them into line with the set of competencies proposed by GEF; it may also introduce additional Competences (CVD).

Fig. 1.   The model of educational process without feedback

The competencies being acquired by the students in the course of learning disciplines from variable part are formed by the university so that they can correspond to the content of the discipline being studied. As a result a list of competences of particular training is formed which meets the requirements of GEF. On the based of MEP, developed by Teaching Staff University (TSU), Working Programs of Disciplines (WPD) are developed. The Educational Process (EP) will be organized on these programs. In this situation, the Student (St) is a consumer of education services offered by the university, without any affecting the course of the educational process.

General cultural and professional competences of future specialists are finally formed at the end of training and can't be corrected. At the same time, rapidly changing situation in the labor market requires constant monitoring and upgrading the curriculum. Therefore one should be able to change a set of competencies in subjects so that the graduate could meet the requirements both of labor market and the requirements of professional standards. [1]

To obtain practically significant result when realizing this approach a number of issues must be solved:

– having learned a particular discipline students differently as for quality and quantity master competences formed by the university (the subjectivity of students);

– TSU from different universities teaching the same disciplines may put qualitatively and quantitatively different competences in their courses (the subjectivity of the teacher);

– the employer, when recruiting specialist, expects him/her to know how to use competencies required for a particular class of problems (the subjectivity of the employer). At the same time, the employer can not practically influence the majority of competencies obtained by the graduate, as some of them are hard-coded in the GEF, and the rest are introduced during developing the curriculum, that is, in the early phase of training the future specialist [2];

– due to the possibility to introduce a variety of disciplines and competencies respectively divergent part of the cycles, different higher educational institutions can graduate specialists with slightly different skills and knowledge in the same fields (subjectivity of HEI).

The solution to these problems is possible through the implementation of upgraded models of the educational process in the institution, in particular the introduction of a feedback model and modules of competency areas. The latter are sets of expert assessments that take into account the contributions of

competencies to the final result due to weighting coefficients. Experts can act both as developers of MED and WPD and as consumers.

It is proposed to rate competencies not only qualitatively (if a graduate holds this competence at least a little) but quantitatively (what part of educational process is dedicated to the development of competence and how well graduates hold it in general).

Figure 2 shows an educational process model that takes into account the subjectivity of a student. Based on expert assessments, competences are assigned the appropriate weight and teachers form Competence Areas (CA TSU) in their subjects. After studying the discipline the student gives expert assessment – weight to competencies mastered. This results in a student's area of competence (CA St). Based on the analysis of these areas TSU make recommendations for correcting WPD both as for changing labor intensivity and as for competences being formed. The implementation of this model in the educational process may reduce the impact of subjectivity of teacher / student and increase the interest of students in obtaining of a set of knowledge and competences.
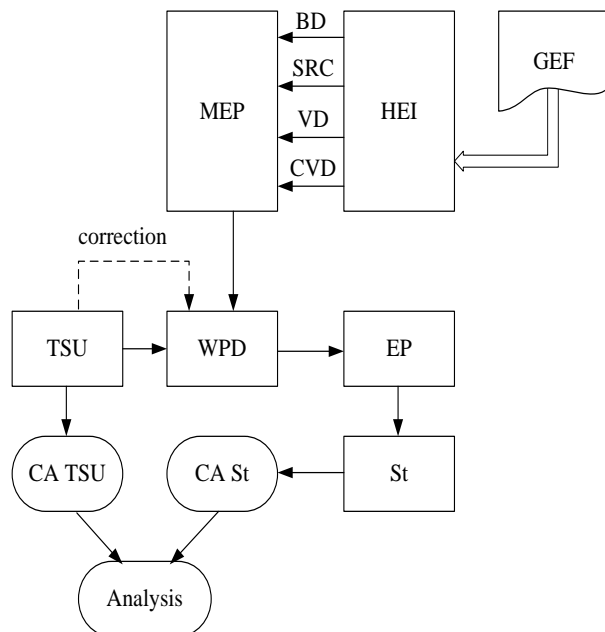
Fig. 2. Model of the educational process that takes into account the subjectivity of the student

Figure 3 shows an educational process model that takes into account the subjectivity of the Employer (Em). By analyzing either the content of the set of competencies and WPD, or MED in general, the employer creates his/her competency area (CA Em), being able to edit competences given in the GEF as well as reasonably recommend new competencies.

As it was in previous model recommendations on updating the WPD and the whole MED if there are a lot of differences and made. In the first case to make recommendations to adjust the working discipline programs, employers of different profiles may be involved. In the second case, which provides for correcting MED, the model given may be affective only when there are employers from large enterprises being competent in relevant field of training.
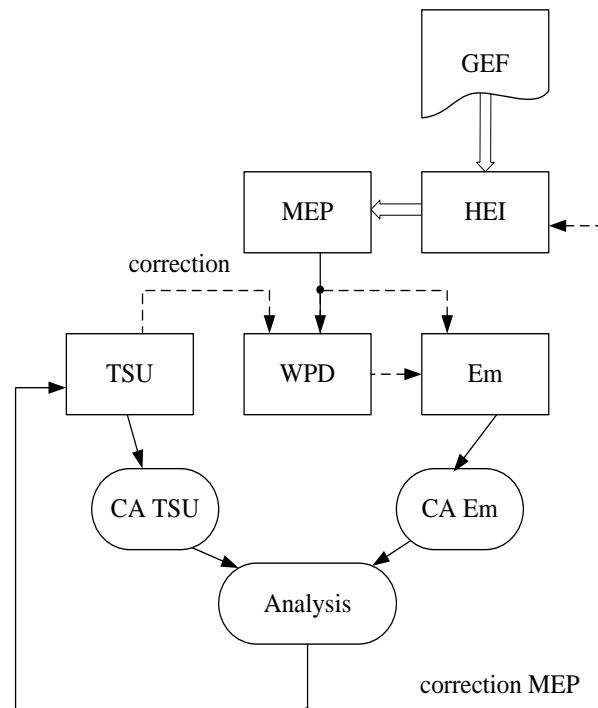
Fig. 3. Model of the educational process, taking into account the requirements of professional standards

Figure 4 shows an educational process model, which takes into account the requirements of Professional Standards (PS) for industries. In this case, the employer creates CA Em on base of professional standards and the university in it's turn creates a competence area CA based on GEF. When analyzing the differences in the requirements of the parties for competences being formed certain correction is possible in the competence area of both the employer and the university. The implementation of this model enhances the role of the employer in selecting and developing of appropriate skills.

In practice, an integrated approach is possible, that is the development of combined variants of teaching based on the model proposed.

Implementation of the proposed models of the educational process with proposed models competency areas, will provide criteria to optimize training plans and working programs while maintaining their individuality for various universities, as requirements analysis is carried out at the level of competency areas, and not of the MED, or WPD. Competency areas can be built separately for different cycles of disciplines or parts of cycles. The involvement of the employer to work at the educational process will take into account the possibility of his/her vision for the future specialist.
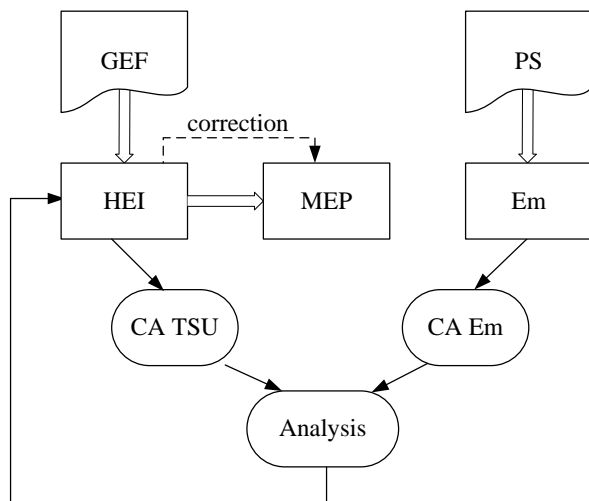
Fig. 4. Model of the educational process, taking into account the requirements of professional standards

However, practical implementation of the proposed models starting with "zero" may face a number of difficulties:

– to produce areas of competency it is necessary to gain sufficient statistical data;

– indifferentness to implementation of models In general, changes in the working program will be implemented only in the next academic year;

– the objective of forming competency areas by employers;

– and other difficulties.

At the same time, a number of leading universities have some achievements and positive results in implementing competence-based approach.
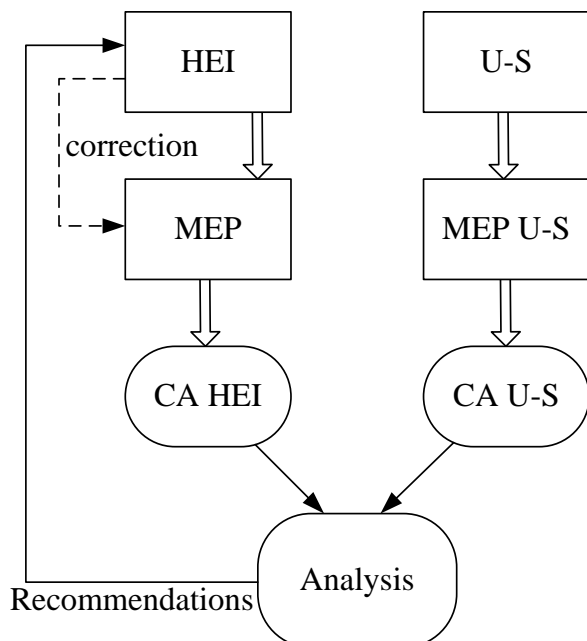
Fig. 5. Model the educational process based on the experience of leading universities

This allows on the first stage to use their findings and recommendations, that is as shown in Figure 5, to use the model, which analyzes competence areas of University-Standard (CA U-S) and a university

developing and correcting MED (CA HEI), and then after accumulating necessary information to carry out the current correction of relevant documents and processes.

The implementation of the proposed models in the technology of the information system of education will decrease the effects of subjectivity when developing basic educational programs and thus increase the demand for future specialist.

To implement these models it is necessary to have a powerful tool to collect information from students, teachers and employers about competencies' weights. To satisfy this requirement, the software system was created [3].

The system consists of database (MySQL), client web application ("the client app") and desktop administration application ("the admin app") (fig. 6).
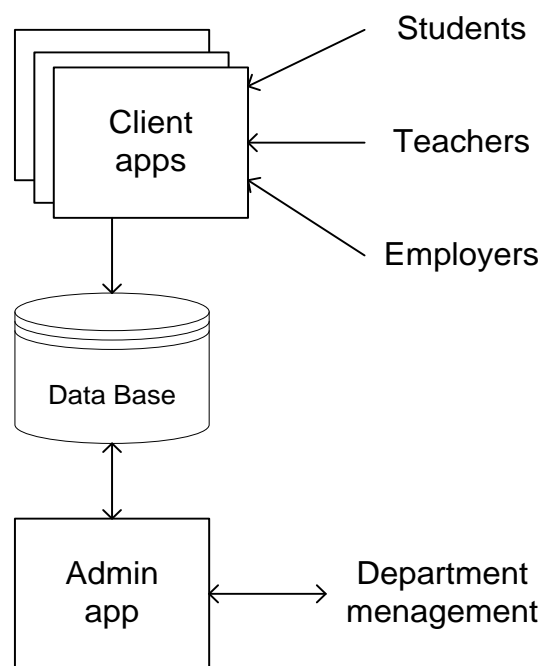
Fig. 6. Architecture of the software system

An administrator fulfills the system with lists of users, specializations, disciplines and competencies. There is an ability to automatically generate passwords. Users are grouped by roles, faculties and study years. This application created with C# language.

To enter the client app user have to enter a password. Three roles are set: student, teacher and employer. Teacher role allows user to set list and weights of competencies of disciplines he/she teaches. Student role allows setting weights of competencies of disciplines he/she have learned. If student suggests that more competencies was purchased by him than stated in teacher's list, he can add them into his own list and rate them. Employee role allows user to set weights of competencies without separation by disciplines. Links between users and disciplines are created by administrator. This application created with PHP language and running on Apache Server.

Collected data is performed in Admin App as 2D polar graph where angle is competence number and radius is it's weight in curriculum (fig. 7).
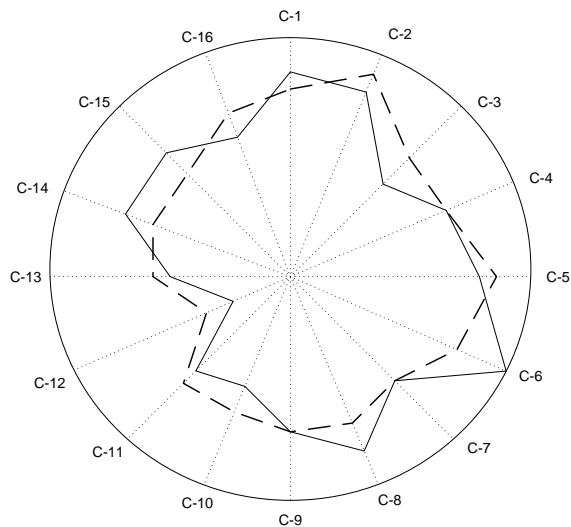
Fig. 7.   Representation of CA

Solid line shows CA TCU, dot line shows CA U-S or CA Em User can select data selects from separate discipline or from curriculum in general. Competencies weights data collected from students are averaged. When user select curriculum in general, data from separate disciplines are summarized.

After data collected and results analyzed department management make decision of curriculum correction using models described above.

In models fig. 3 – fig. 5 such correction have to be make relying on desired curriculum data in general. And it is difficult with no automation. Creation of the algorithm of automation curriculum correction is one of tasks of future research.

REFERENCES

[1] Lehin S.N., Motaylenko L.V., Poletaeva O.A. MEP development in areas related to information technology to meet the requirements of professional standards for IT-industry. Education in the Russian Federation to the ten open-Russian Conference (16-18 May 2012). Moscow: Moscow State University. MV University, 2012, pp. 404 - 405.

[2] Motaylenko L.V., Poletayeva O.A., Sof'ina V.N. Problem of matching the competence model of higher educational institution graduates and professional competence of the IT industry. Basic research and innovation in national research universities: Proceedings of the Scientific and Technical Conference. Vol. 4. SPb.: Izd Polytechnic. University Press, 2012. pp. 64

[3] Poletaev D.I., Poletaeva O.A., The first phase of the development of an automated information system for recording the distribution of competences // Bulletin of the Pskov State University Economic and technic since Vol.2. Pskov: Izd. Pskov SU, 2013, pp. 107 -112

The Prospects of Using Fuzzy Approaches to Ecological Risk Assessment

Oleg Uzhga-Rebrov, *Rezekne Higher Education Institution,*
Galina Kuleshova, *Riga Technical University*

Abstract. **The issue of environmental quality improvement has been receiving much attention in the developed countries in recent years. Due to that, the role of assessment of ecological risks associated both with natural events and technogene activity of humans is increasing. Previous approaches to the assessment of ecological risks were fully based on statistical data and expert evaluation of potential losses and probabilities of unfavourable consequences. When this kind of assessment is carried out, it is assumed explicitly that experts are able to evaluate point probabilities. However, such assumptions are far from being true. As a result, fuzzy approaches to ecological risk assessment became popular lately. This paper focuses on two practical approaches of that kind. The paper is aimed at attracting practical attention to new up-to-date techniques that could be successfully applied to assess ecological risks in Latvia.**

Keywords –linguistic categories, safety analysis, fuzzy numbers, fuzzy representation of knowledge, fuzzy rules.

I INTRODUCTION

A great deal of attention has been paid lately to the problem of environment protection in the developed countries. The quality of environment may be negatively affected by several nature factors: earthquakes, volcano eruption, hurricanes, floods, draught, etc. These factors have existed during the whole history of the Earth evolution, so ecosystems have sufficient and strong enough protection mechanisms to resist to the action of different unfavourable nature factors. Even greater negative impact on the environment is made by technogene human activity. All the negative effects associated with different kinds of such activity can be divided into two large groups: (1) irrational use of the existing nature resources, which might cause large problems for further generations (externalities between the generations) and (2) different kinds of environment pollution occurring as a result of economic activity. The necessity of avoiding or lessening negative effects of the second group has been recognised long ago and important measures are undertaken to reach the goals stated. The actions aimed at lessening these effects are planned and accomplished on the basis of the respective measurements and monitoring of relevant factors. This kind of approach can be quite validated when dealing with already existing deviations in the functioning of ecosystems that can be evaluated directly but real causes of these deviations can be discovered and proper corrective actions can be developed. It is more difficult to assess ecological risks. The problem is that the risks are related to the potential negative effects on the environment which might occur due to different natural and technogene reasons. For example, what consequences might follow potential long-term period of the draught in the region or potential accident at a chemical enterprise? In such situations it is necessary to evaluate possible losses at different levels of the negative impact and chances of occurrence of such losses. During a long period, the chances of occurrence of different kind of losses were commonly evaluated by probabilities assuming that all possible levels of losses constitute a complete group of random events. Thus, the assessment of ecological risks within standard approach includes two dimensions: possible losses and probabilities of occurrence of losses at different levels of possible influence.

A question then arises: how to obtain the necessary initial data for evaluating ecological risks? If sufficient statistical material is available, the task is not difficult. A visual example can be the assessment of fire risk in a building of a certain type. Rich statistical material allows one to justly evaluate the relative frequency of fire occurrence in this kind of buildings. This frequency can be correctly assumed as the probability of fire occurrence in a certain building. Estimated losses caused by the fire can be easily calculated as average losses related to previous fires. Based on the obtained evaluations, the risk can be easily evaluated and the cost of insurance police can be determined.

Unfortunately, the presence of sufficient statistical material in the assessment of ecological risks is the exception rather than the rule. The uniqueness of such situations and their rear occurrence do not allow one to use efficient apparatus of statistics to obtain necessary evaluations. To cope with the lack of objective information, expert evaluation is frequently used. Experts-specialists based on their professional knowledge, experience and, sometimes, intuition can provide the necessary data. However, the problem of confidence degree evaluation for the data obtained appears. Practically, there are no suitable methods for solving that task if objective initial information is completely unavailable; though methods exist that

allow one to a priori evaluate potential non-objectivities of the expert in the planned evaluation but these techniques might provide only little help as regards the confidence of evaluations of the particular expert, whereas the use of group expert evaluation may only make the task even more complicated in the case when the evaluations of separate experts turn to be sufficiently contradictive.

A lot of techniques are developed for obtaining and using uncertain probabilistic evaluations; these include interval probabilities, second order probabilities etc. The shortcomings of these techniques are their complexity and poor interpretability of the uncertain results obtained.

In 1965, L.Zadeh [6] proposed a principally new conceptual basis for dealing with vague, imprecise information – fuzzy set theory. The theory was widely developed during the past years. Nowadays, fuzziness is used practically in all fields of scientific and practical activity. This paper considers two practical examples of using fuzzy sets and fuzzy rules in ecological risk assessment. Based on the analysis of the considered examples some generalized conclusions are drawn and recommendations on applying fuzzy techniques for ecological risk assessment are given.

II Basic Concepts of Fuzzy Set Theory

Nowadays there are a large number of textbooks and reference guides available on fuzzy set theory. As an example of a textbook, we can mention [1]; while a more detailed and thorough description of the theory can be found in [3].

Fuzzy set theory has been developed to cope with vague and imprecise categories having no sharp boarders. As an example let us consider the variable *Age of individuals*. Let us assume that the value of that variable may be within the interval [0,100] years. Let us distinguish separate categories in that interval, say, children, young people, middle age people and older people. These categories can be distinguished by fixing boundaries between separate categories. Let us assume that the value of boarder between young people and middle aged people is set as 35 years. Then a person at the age of 34 years 11.5 months will be ascribed to the category of young people but a person at the age of 35 years 0.5 months will be ascribed to the category of middle aged people. A slight difference in the age makes one to ascribe these persons to different age categories, which is not justified. Now, let us assume that the age of an individual is determined approximately. According to the above-mentioned age classification, this individual can be ascribed to a single category only. But what can be done if, based on his look, it is possible to ascribe him both to the category of young people and the category of middle-aged people? A great deal of similar examples can be offered: classification of individuals according to weight, classification of temperature etc.

To ensure a more flexible and convenient operation of different kind of classification categories, the boundaries between the categories can be somehow made vague. This idea is implemented in the concept of *linguistic category* (alternatively, *linguistic term*). Different values of relevant variable may belong to a certain linguistic category with different extent (strength). Moreover, some values of the variable may belong to different linguistic categories with equal or different extents.

Let us consider a case study. Assume that as a result of accident, a harmful substance has entered the environment, which might cause unfavourable effects of different extent. It is clear that the degree of unfavourable influence will depend on the concentration of that substance in the external environment. Let us distinguish these fuzzy linguistic categories of the degree of the unfavourable effect at the scale of harmful substance concentration: low, medium and high. These categories are conditionally represented as membership function graphs in Fig. 1.

As can be seen from Fig. 1, at the concentration values less than c_1, the extent of pollution will definitely be low. At the values of concentration $c_1 \leq C \leq c_4$ the extent of membership of pollution to the fuzzy category *low* decreases in succession from 1 to 0. At the values of concentration $c_2 \leq C \leq c_5$, the extent of pollution membership in a fuzzy category *medium* increases in succession from 0 to 1. At the values of concentration $c_2 \leq C \leq c_4$ actual pollution can also be ascribed to both fuzzy category *low* and fuzzy category *medium* with different degrees of membership. At the concentration equal to c_3, the degrees of membership in both categories will be similar. Degrees of membership to other fuzzy categories can be interpreted in the same way.

In practical applications, fuzzy numbers are of great importance. A *fuzzy number* is a fuzzy subset defined in a set of real numbers **R**. As an example, two triangular fuzzy numbers A_1 and A_2 are shown in Fig.2. These numbers have received their name because of the form of membership function graphs. There also exist other types of fuzzy numbers. Arithmetic operations on fuzzy numbers can be performed according to the rules of fuzzy arithmetic.

A set of interconnected variables describing a certain set of the real world is often called a system. If the states of variable values are expressed by means of fuzzy sets and/or other fuzzy operators, this kind of system is called *a fuzzy system*. In the most general case, fuzzy systems can be classified as model-based, knowledge-based and also hybrid [2]. Fuzzy systems that are based on knowledge are the result of traditional modelling of systems; they employ appropriate fields of fuzzy mathematics (fuzzy analysis, fuzzy mathematic operations, fuzzy relations etc.). In knowledge-based fuzzy systems, the correlations among variables are described by means of a set of fuzzy rules.
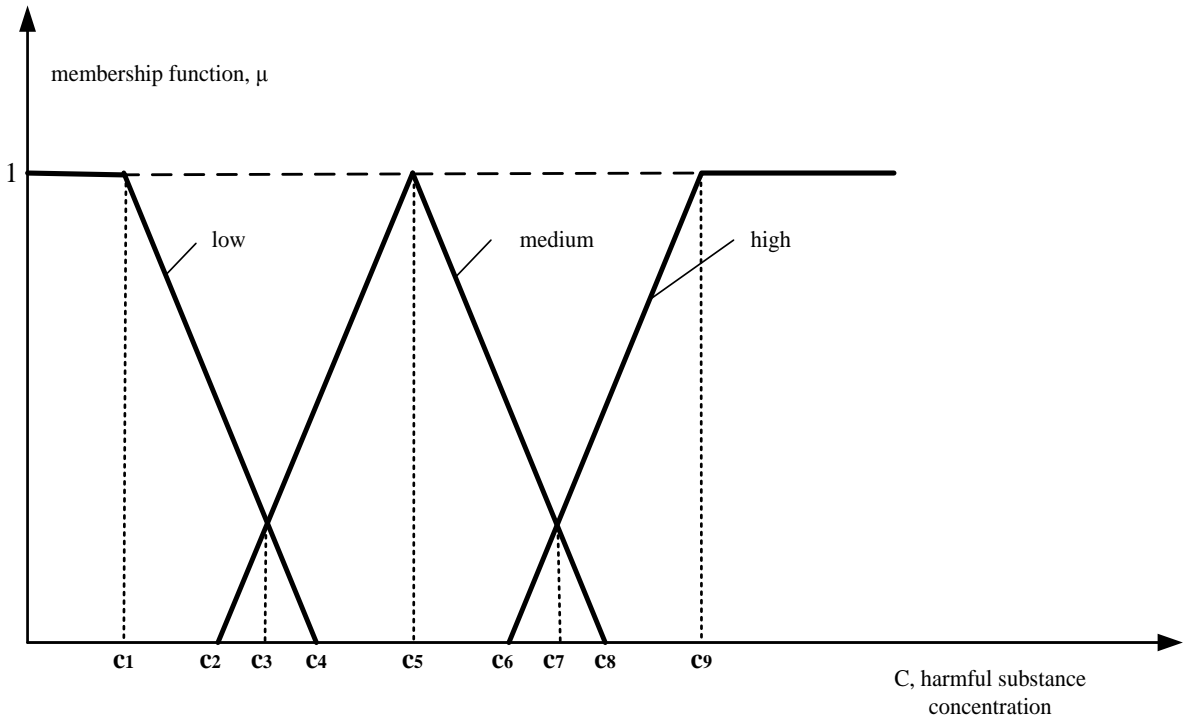
Fig.1. Graphs of membership functions of fuzzy categories of the degree of unfavourable impact on the environment at the scale of harmful substance concentration
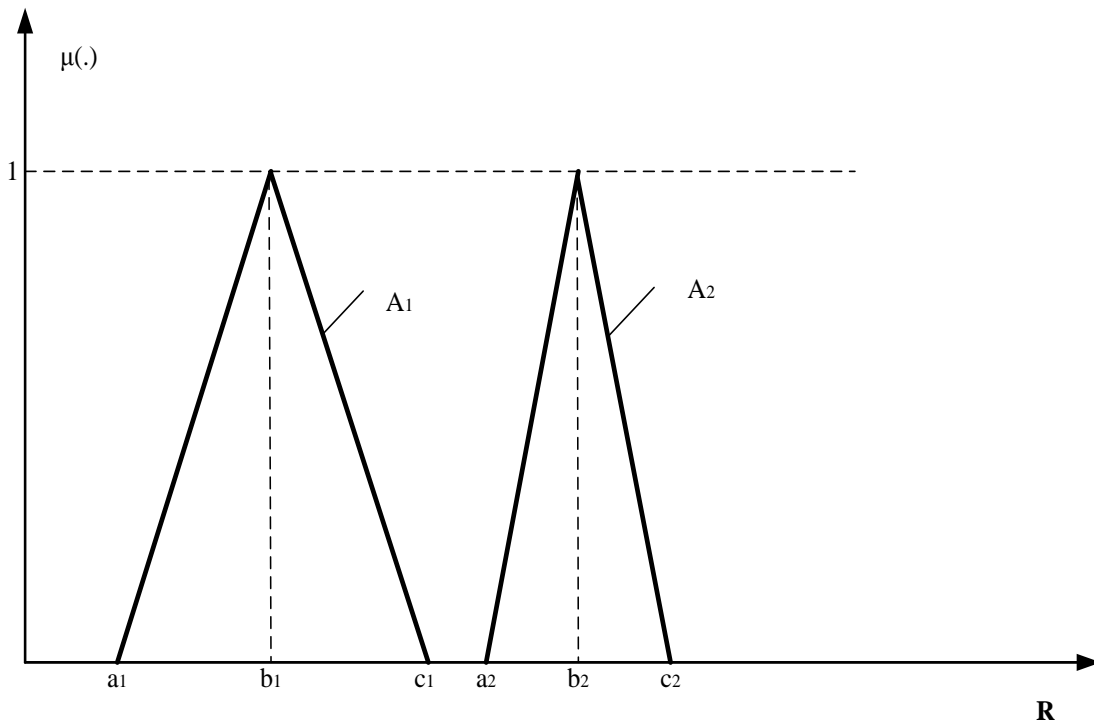

Fig.2. Sample representation of triangular fuzzy numbers

These rules are formed using experts' opinions and evaluations that represent their knowledge in the subject area.

This knowledge can be initially expressed in the terms of natural language and then formally transformed into the fuzzy forms.

III AN EXAMPLE OF TECHNICAL RISK ASSESSMENT USING A FUZZY MODEL-BASED SYSTEM

To illustrate the above-mentioned technique, let us use the data shown in [5]. The paper provides a detailed analysis of fuzzy evaluation of technical system safety. It is clear that ecological risk is inversely proportional to the safety of relevant technical system activity. The matter is that the lower the safety of, say, equipment for manufacturing dangerous chemical substance, the higher the probability of its breakage and the higher the risk that during the accident the environment will heavily suffer. Thus, the assessment of technical risks is actually equivalent to the assessment of ecological risks.

The event of technical system breaking or degradation is a fundamental element of safety analysis, and the main problem is how to model damage events with complicated possible states. The qualitative analysis of safety has to assess not the chances of real damage of system element, but the chances of occurring such element state at which the element is still functioning but its parameters have changed in such way that the chance of damage is growing. In this sense, the discussion is about different kinds of damage.

Standard statistical approach to the assessment of technical system safety suffers from a shortcoming that quite frequently initial data are not sufficient to induce reliable evaluations. The fuzzy set-based approach helps to take into consideration the insufficiency of the initial data. In the considered variant of the approach, it is assumed that relevant initial data are represented as triangular fuzzy numbers and operations on them are carried out by the rules of fuzzy arithmetic.

Technical system safety analysis can be performed in two variants [5]: (1) in the form of structure function synthesis and (2) in the form of damage tree analysis. The first variant is used at the stage of system development but the second one – at the stage of system exploitation. In any case, the major factors of system safety are fuzzy reliability of normal functioning of the i-th component, $\widetilde{\mathrm{Re}}l(i)$, fuzzy average number of damages of the i-th component at time unit $\tilde{\lambda}(i)$ and fuzzy average time between damages of the i-th component $1/\tilde{\lambda}(i)$.

In parallel fragments of the system, components are included in parallel; one of the components is in working state while the other components are in the standby state. When the functioning component is out of order, the next component is turned on and so on. Thus, a complete abandoning of the fragment will only occur when all its components are damaged.

Fuzzy likelihood of the normal functioning of the fragment at time moment t is calculated by this expression:

$$\widetilde{\mathrm{Re}}l(fr) = \prod_{i=1}^{n} \widetilde{\mathrm{Re}}l(i) = \prod_{i=1}^{n} e^{-\tilde{\lambda}(i)t} = e^{-n\tilde{\lambda}t}, \quad (1)$$

where n – number of the components that are connected in parallel;

$\tilde{\lambda}$ - average number of damages of the component.

In [5] it is shown that in the case of n in parallel connected components with constant value $\tilde{\lambda}$, that are represented in the form of triangular fuzzy numbers (a, b, c) (see Fig.2) the resulting triangular number for $\widetilde{\mathrm{Re}}l(fr)$ in expression (1) can be represented as

$$\widetilde{\mathrm{Re}}l(fr) = (e^{-an}, b^{-bn}, c^{-cn}). \quad (2)$$

This kind of approximation brings a small error but significantly simplifies the calculations.

For a fragment of technical system with n connected in sequence elements we have

$$\tilde{\lambda}(fr) = \sum_{i=1}^{n} \tilde{\lambda}(i). \quad (3)$$

If the values of $\tilde{\lambda}(i)$ are represented in the form of triangular fuzzy numbers (a_i, b_i, c_i), the calculation of the value $\tilde{\lambda}(fr)$ is reduced to a simple addition of these numbers according to the rules of fuzzy arithmetic.

After the value of $\tilde{\lambda}(fr)$ is calculated, it is possible to calculate in sequence the value of $\tilde{\lambda}(system)$ for the existing connections of the fragments.

What is the advantage of the considered fuzzy approach to the calculation of technical system safety as compared to the standard probabilistic approach? The probabilistic approach foresees point evaluations of the probabilities of fuzzy events – damages of system's components. Under the conditions of the shortage of the initial information, the confidence of the obtained evaluations can be extremely low. In the considered approach, the incompleteness and insufficiency of the initial information is explicitly modelled by means of triangular fuzzy numbers. It is natural that the fuzziness of the initial evaluations is translated into the fuzziness of the result. However this kind of fuzziness is better than point evaluations with unknown level of confidence. At least, under the fuzzy results it can be clearly seen in which limits and with which confidence the real value of the factor under evaluation can be expected. To lessen the degree of imprecision of the results, the worst values of the evaluations can be used as a basis and conclusions can be drawn on the basis of such pessimistic evaluation. Besides, defuzzification techniques can be used that enable making more narrow intervals of fuzzy resulting evaluations.

IV An Example of Technical Risk Assessment Using a Fuzzy Knowledge-Based System

In [4], the authors describe a technique for evaluating the ecological risk that is connected to mercury emissions when mining gold in Canada. The level of mercury in sediments, water and biota is the basis for making political and technical decisions on making correcting procedures. It is clear that the chemical analysis is the major source of information for the evaluation of potential harmful impact on the environment. To obtain data reliable by many points of evaluation, large financial resources and numerous educated staff is required. The authors point out that when similar task was solved in Sweden, mercury content was evaluated in 1836 lakes. However, when forecasting the development of situation evolution in the future at so numerous initial data, prediction error was within 50%. This gives evidence that to receive reliable results, even larger amount of initial data is required.

Based on the analysis of the state of the art, the authors [4] have suggested a simple heuristic approach to the evaluation of ecological risks in the area of gold mining. The evaluation of mercury content in the water, sediments and live organisms is made using terms of linguistic categories high, medium and low. For all relevant factors of the task, the identification of linguistic categories and construction of membership function graphs is made. In their work the authors treat the values of membership functions as the Degree of Belief (DoB).

Sediments are both carriers and sources of contaminants in aquatic systems. The possibility of Hg bioaccumulation is influenced by the contamination level of sediment. The Index of Geoaccumulation (I_{geo}) as a quantitative measure of metal pollution in aquatic sediments [4] uses the relationship between concentration C of the element in the sediment and background in fossil argillaceous sediment (B):

$$I_{geo} = \frac{\log_2 C}{1,5B.} \tag{4}$$

For making a fuzzy evaluation of the extent of presence of Hg in sediments, the authors have classified these types of sediments:

Type 1: Comprises gravels, white or light grey clay or sand, limestone, sandstones;

Type 2: comprises any reddish clayey or sand sediment;

Type3: comprises organic-rich sediments.

Using the knowledge and experience of experts, a set of rules connecting the type of sediments and fuzzy values of other relevant factors with the fuzzy amount of hydrargyrum at the point of measurement, is constructed. All the rules are shaped as an expert system HgEx. As the authors point, "HgEx is heuristic system, which accommodates imprecise data input for many variables, such as pH, Eh, water conductivity, biomass productivity, water transparency and contamination factor. The system does not replace the monitoring programs because all data are obtained in field trip, but rather reduces the need for accurate results to provide a preliminary but conclusive risk assessment report".

V Results and Conclusions

This paper considered two practical approaches to the fuzzy evaluation of ecological risks. One of the approaches is based on fuzzy models, while the other one employs a fuzzy representation of knowledge. Fuzzy evaluation of technical risks has already found practical application. Its advantages are in the opportunity to use vague, imprecise initial Information, which is not possible when using standard statistical approach. In no case it means the rejection to use this kind of approach. In the case, when sufficient statistical data are available (e.g. in case of fires or aviation accidents), the statistical approach has undoubted advantages. However, in practical tasks of ecological risks evaluation, the lack of sufficient initial data is the rule rather than the exception; so here fuzzy techniques are preferable.

As shown in Section 3, fuzzy evaluation of technical risks requires only fuzzy evaluations of initial factors. By regulating the basis of relevant triangular fuzzy numbers, practically any degree of non-knowledge regarding the factors to be evaluated can be modelled. It is natural that the fuzzier the initial data are, the fuzzier the results will be. However, even at the sufficient fuzziness of the results, practically there is no alternative to the fuzzy approach. In this kind of state, it is simply impossible to get more or less reliable probabilistic evaluations.

The practical method for the assessment of technical risks presented in Section 3, can be successfully employed in numerous other situations. A logically validated requirement for such application is a tight functional relation between the initial data and the resulting evaluations.

Another practical approach to assessing ecological risks that is discussed in Section 4 is completely based on the use of the knowledge and experience of experts. Different versions of that technique might also find a wide application in other fields where it is possible to determine heuristic dependencies between the initial data and the resulting evaluations. Fuzzy rules are excellent tool for expressing relevant dependencies.

Other conceptual approaches to the assessment of ecological risks at the imprecise initial information also exist; one of such approaches is based on the theory of possibilities. The consideration of alternative approaches is, however, beyond the scope of this paper, first due to the limited paper size and second due to numerous advantages of fuzzy techniques.

VI REFERENCES

[1] M. Ganesh, *Introduction to Fuzzy Sets and Fuzzy Logic*. PHI Learning Pvt. Ltd, 2006, 256 p.

[2] G.J. Klir, *Uncertainty and Information. Foundation of Generalized Information Theory*. John Wiley&Sons, Inc., 2004.

[3] G.J. Klir and Yuan Bo, *Fuzzy Sets and Fuzzy Logic. Prentice Hall,* 1995, 592 p.

[4] M.M. Veiga and J.A. Meech, "Application of Fuzzy Logic to Environmental Risk Assessment", Department of Mining and Mineral Process Engineering, University of British Columbia, Vancouver, Canada, http://www.mining.ubc.ca/faculty/meech/fuzchile.htm.

[5] L. Warren, "On Modeling Hybrid Uncertainty in Information", Australian Department of Defense. http://www.dtic.mil/cgi-bin/GetTRDoc?AD=ADa467752.

[6] L. Zadeh, "Fuzzy Sets", *Information Control*, 1965, 8, pp. 338 – 353.

Path Planning Usage for Autonomous Agents

Edvards Valbahs, Peter Grabusts

Rezekne Higher Educational Institution, Faculty of Engineering, Atbrivoshanas alley 76,
Rezekne, LV-4601, Latvia.

Abstract. In order to achieve the wide range of the robotic application it is necessary to provide iterative motions among points of the goals. For instance, in the industry mobile robots can replace any components between a storehouse and an assembly department. Ammunition replacement is widely used in military services. Working place is possible in ports, airports, waste site and etc. Mobile agents can be used for monitoring if it is necessary to observe control points in the secret place. The paper deals with path planning programme for mobile robots. The aim of the research paper is to analyse motion-planning algorithms that contain the design of modelling programme. The programme is needed as environment modelling to obtain the simulation data. The simulation data give the possibility to conduct the wide analyses for selected algorithm. Analysis means the simulation data interpretation and comparison with other data obtained using the motion-planning. The results of the careful analysis were considered for optimal path planning algorithms. The experimental evidence was proposed to demonstrate the effectiveness of the algorithm for steady covered space. The results described in this work can be extended in a number of directions, and applied to other algorithms.

Keywords – robotic, Simulated Annealing, path planning.

I Introduction

The article is connected to the travelling salesman problem (TSP), but with some exceptions and conditions. In the case when the TSP is envisaged the following approximate path planning algorithms are used [2, 3, 4]:

- The closest neighbour algorithm;
- Simulated Annealing (SA);
- Genetic Algorithm (GA);
- Ant colony optimization.

The closest neighbour approach is the simplest and straightforward TSP one [10]. The way to this approach to always visit the closest city. The polynomial complexity of the approach is $O(n^2)$. The algorithm is relatively simple:

1 – Choose a random city;
2 – Find out the nearest city unvisited and visit it;
3 – Are there any unvisited cities left? If yes, repeat step 2;
4 – Return to the first city.

SA is successfully used and adapted to get an approximate solutions for the TSP [10]. SA is basically a randomized local search algorithm similar to *Tabu Search* but do not allow path exchange that deteriorates the solution. The polynomial complexity of the approach is $O(n^2)$ accordingly.

```
Input: ProblemSize, iterations_max, temp_max
Output: S_best
1.    S_current ← CreateInitialSolution(ProblemSize)
2.    S_best ← S_current
3.    for i = 1 to iterations_max do
4.        S_i ← CreateNeighborSolution(S_current)
5.        temp_curr ← CalculateTemperature(i, temp_max)
6.        if Cost(S_i) ≤ Cost(S_current) then
7.            S_current ← S_i
8.            if Cost(S_i) ≤ Cost(S_best) then
9.                S_best ← S_i
10.           end
11.       else if Exp((Cost(S_current)-Cost(S_i))/temp_curr) > Rand() then
12.           S_current ← S_i
13.       end
14.   end
15.   return S_best
```

Fig. 1.   Pseudocode for SA

The SA method [1, 5, 16] is widely used in applied science (Fig. 1). The well-known traveling salesman problem has effectively solved by means of this method. For instance, the arrangement of many circuit elements on a silicon substrate is considerably improved to reduce interference among the elements [15, 18].

GA conducts in a way similar to the nature [3]. A basic GA starts working with a randomly generated population of potential solution. The candidates are then mated to produce offspring and only some of them go through a mutating process. Each candidate has an optimal value demonstrating us how go it is. Choosing the most optimal candidates for mating and mutation the overall optimality of the candidate solutions increases. Using GA to the TSP involves implementing a crossover procedure, a measure of optimality and mutation as well. Optimality of the solution is a length of the solution.

Ant colony optimization is the algorithm that is inspired by the nature [9]. It is based on ant colony

moving behaviour. Good results can be achieved by means of the algorithm but not for complex problems.

We managed to use SA algorithm rather successfully in our previous work [17] taking into account the specific side of this work (it will be discussed in detail further). Therefore, it is necessary to discuss some principles of SA realization in detail. In order to calculate the total path it is necessary to know the shortest route among all the cities. As we do not know the distance, we must apply one of the algorithms to define the shortest route among all the cities. It is Dijkstra's algorithm [14] that gives the possibility to get the shortest path tree. The polynomial complexity of the Dijkstra's algorithm is $O(n^2)$.

II GOALS

The aim of the research paper is to analyze motion-planning algorithms that contain the design of modelling programme. The programme is needed as environment modelling to obtain the simulation data. The simulation data give the possibility to conduct the wide analyses for selected algorithm. Analysis means the simulation data interpretation and comparison with other data obtained using the motion-planning.

The use in practice and the necessity of it is greatly connected to optimal algorithm and methodological work out for autonomous agents that move in the space and are able to plan route on their own [6, 7, 8, 11, 12, 13]. One of such agent-samples exiting in our everyday life is autonomous vacuum cleaner. Autonomous vacuum cleaners do not usually use the motion-planning algorithm. They are based on some simple algorithms, for example cleaning in a spiral, crossing the premises avoiding the walls and their moving is casual after touching the walls. The philosophy of this design was offered by the scientists of Massachusetts Institute of Technology. Agents must behave as insects having primitive controlling devices in accordance to the environment. As a result, though an autonomous vacuum cleaner is very effective in cleaning premises, it is required much more time as compared with work made by a human. There is a drawback, the autonomous vacuum cleans some spaces many times but other spaces only once. The use of motion-planning algorithms can raise the effectiveness of an autonomous vacuum cleaner.

III ASSUMPTIONS

In order to fulfill the aim of the research paper the following conditions are introduced for:
- premises where an object moves;
- robot (or object) moves around the premises;
- path the robot moves on in the premises.

The premises are presented as two-dimensional plane. The plane of premises is equally divided into the cells. The cell dimensions are equal to agent dimension that moves in the premises. The space can be represented as a graph with two kinds of edges (see Fig. 2).

Horizontal and vertical edges are marked with unbroken lines they are of similar length, but others are longer and marked with dash lines. It is linked with agent movement possibilities.
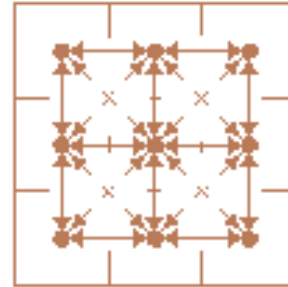
Fig. 2.   The example of the graph and 3 x 3 space

The object moves only one cell forward and back i.e. during one motion the object can move to the one cell from empty eight ones (eight cells around one cell) paying attention to that cell is not occupied by the obstacle but if it is occupied, the graph will not have the relevant vertex (see Fig. 3).
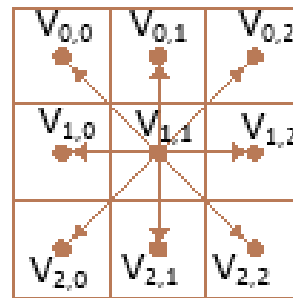
Fig. 3.   The example of agent's motion (where $v_{i,j}$ is relevant vertex)

As opposed to classical TSP we take a number of additional rules and it means that the agent can cross the one the same cell several times in succession (it must cross any cell one time obligatory). Thus, the agent's initial vertex does not coincide with its final vertex of total route.

In this research paper both algorithms were compared practically using and combining different placement of obstacles in the unchangeable two-dimensional space. All the results were obtained on one and the same computer (2.66 GHz processor and 2GB RAM), operating systems (Ubuntu 12.04.1 LST Linux were used). The following information was collected about:
- the number of covering for each cell;
- the time which was necessary for both algorithms to plan the route.

The given illustrations (see Fig. 4) show coverage density (it is an example that was obtained in our previous work [17]).
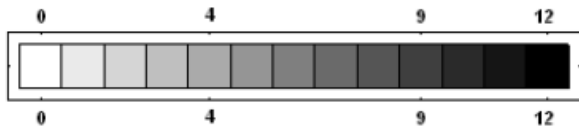
Fig. 4.   Density scale (white - uncovered; black - covered the most)
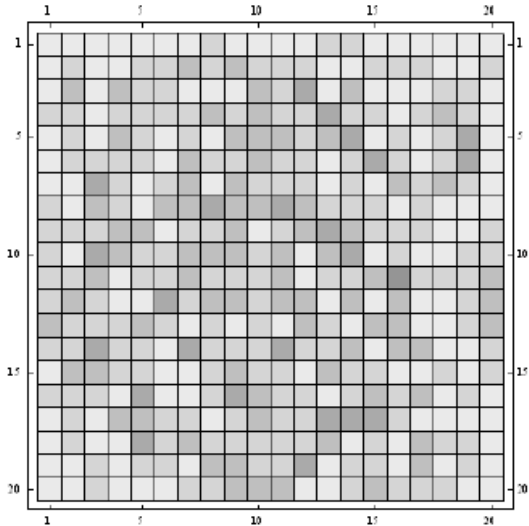
Fig. 5.   Coverage density for the space without obstacles for SA
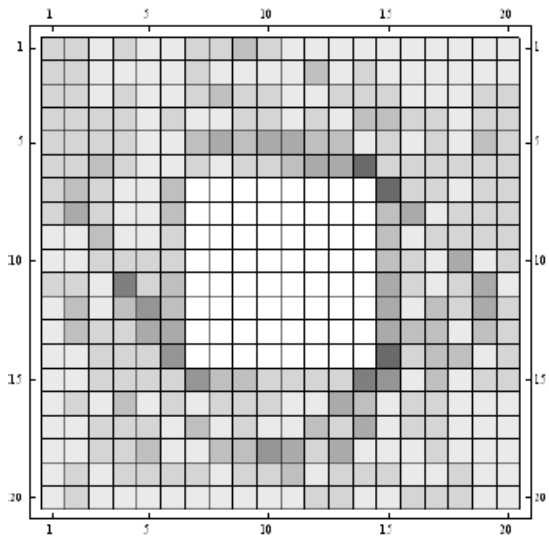
Fig. 6.   Coverage density with the obstacle consisting of 64 cells (the obstacle is in the middle of the premises) for SA
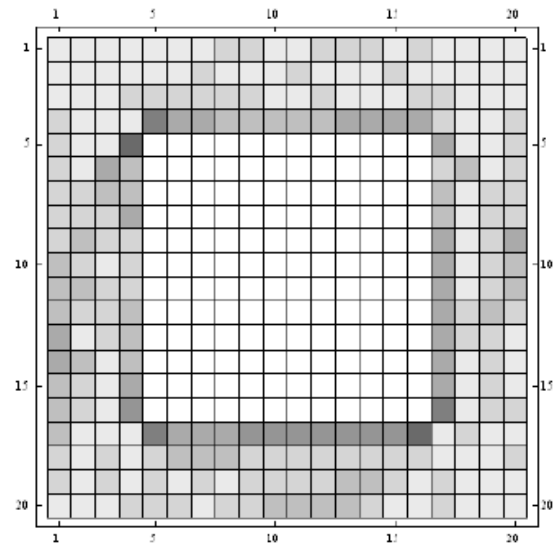
Fig. 7.   Coverage density with the obstacle consisting of 144 cells (the obstacle is in the middle of the premises) for SA
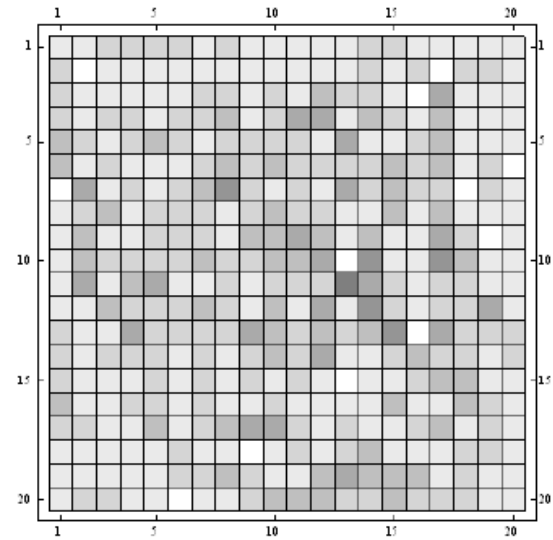
Fig. 8.   Coverage density with the 12 random obstacles for SA
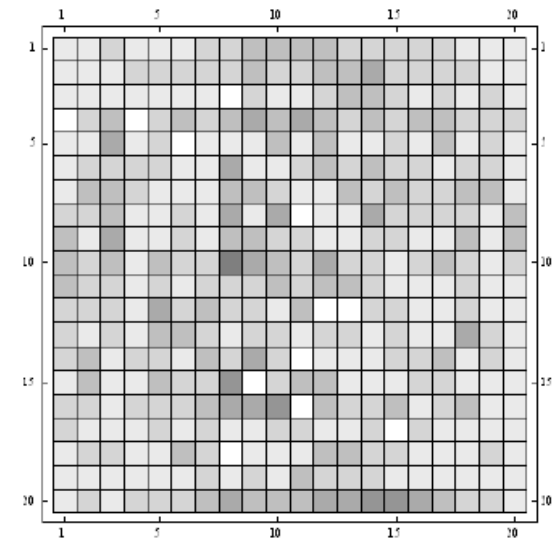
Fig. 9.   Coverage density with another set of the 12 random obstacles for SA
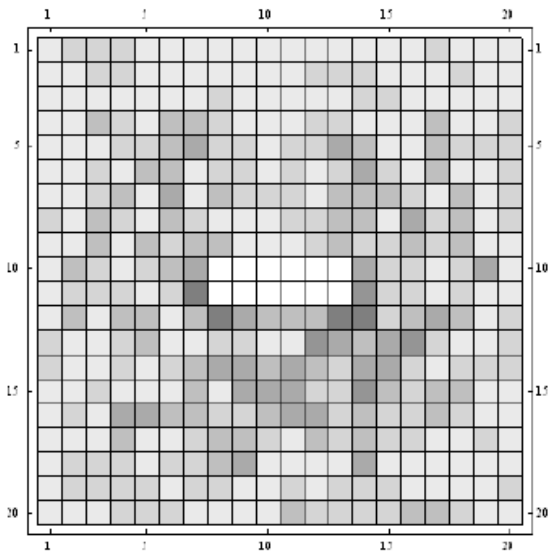
Fig. 10. Coverage density with the obstacle consisting of 12 cells (the obstacle is in the middle of the premises) for SA
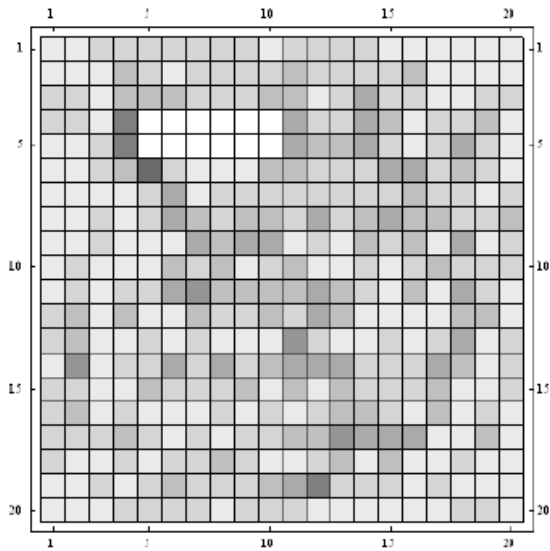
Fig. 11. Coverage density with the obstacle consisting of 12 cells for SA

The density scale (see Fig. 4) is the same for all coverage densities. Coverage density shows how often the robot covers each cell.

IV RESULTS

Taking into account the fact that the distance among all the vertexes (cities) are unknown in the beginning, it is necessary to define the shortest paths among those vertexes mentioned above. Dijkstra's algorithm can be used but increasing the measures of the premises, the time is proportionally increases accordingly that is necessary for evaluating path tree. Therefore, it is needed to simplify the calculation of the shortest path, which is possible, provided the peculiarities and nuances of the task are taken into consideration. In addition, the empty premises should be observed. If all the mentioned above remains valid, the simple algorithm can be worked out to define the shortest paths.

Let us consider the agent's general moving paths. If there are no vertexes between the current initial and goal vertexes, the agent can move only to eight possible positions (cells) depending on goal vertex (see Fig. 3). Admitting that first vertex index i defines the vertical position and the second vertex j defines the horizontal position we can draw a line either horizontally or vertically. And one of the vertexes will have the index with common value (see Fig. 12).

Fig. 12. The example of agent moving horizontally (where i index value is common for both vertexes)

Another situation can be seen if the current initial and goal vertexes are neither on the horizontal nor vertical lines (see Fig. 13-15).

a.)
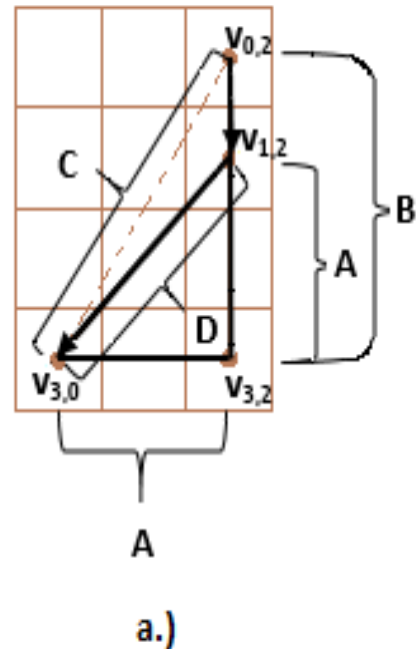
Fig. 13. Three examples of agent moving (where A, B and C are sections among the vertexes): agent moves from $v_{0,2}$ to $v_{3,0}$ crossing $v_{1,2}$

43
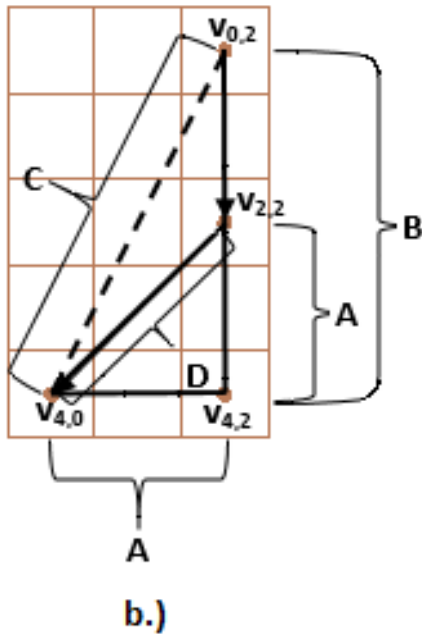
Fig. 14.   Three examples of agent moving (where A, B and C are sections among the vertexes): agent moves from $v_{0,2}$ to $v_{4,0}$ crossing $v_{2,2}$
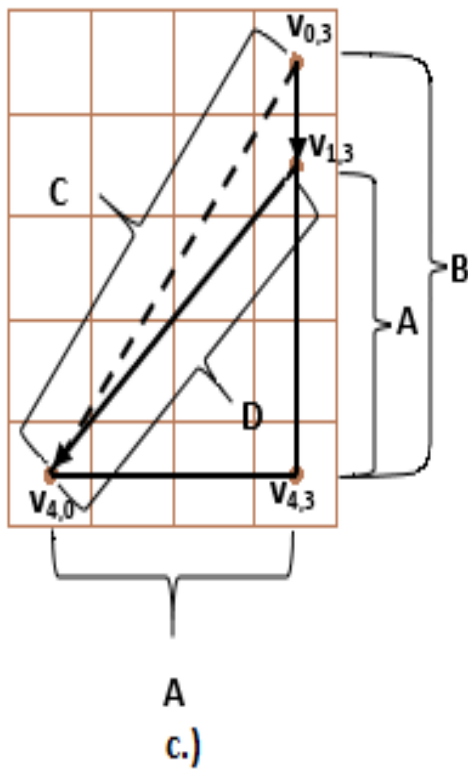
Fig. 15.   Three examples of agent moving (where A, B and C are sections among the vertexes agent moves from $v_{0,3}$ to $v_{4,0}$ crossing $v_{1,3}$)

All cases of Fig. 13-15 have common characteristics that unites them. The shortest path from initial vertex to goal vertex is section C but for the agent this path is unavailable because of current task conditions and peculiarities. These cases can be described by the right-angled triangle where C is a side of the triangle. In addition, side B is longer than side A. One of the shortest paths among the relevant (corresponding) vertexes:

- the agent moves along the longest side B of the right-angled triangle until the gap between the covered path and side B is equal to side A;
- if gap between the covered path and side B is equal to side A, then the agent moves along the angle allowed (along the section D) to the goal vertex (let us mark that this action corresponds to the case when side B is equal to side A i.e. the right-angled triangle is the isosceles triangle, too (see Fig. 13) in case initial vertex is $v_{1,2}$, 4, (see Fig. 14) in case initial vertex is $v_{2,2}$ and (see Fig. 15) in case initial vertex is $v_{1,3}$)).

We can follow that the path is longer than optimal side C. And it can be calculated by the use of following formulae: $L = B-A+2^{0.5}*A$, where L is the length of the path from initial vertex to goal vertex. By turn, C can be calculated from $C = (A^2+B^2)^{0.5}$. It is possible to calculate how match percent L is longer than C (if L is equal to 100 %), then the final result is equal to $P=((L-C)*100)/L$. Our goal premises are 100 x 100 cells. The value of P is reflected with contour line for the given premises depending on A and B (see Fig. 16).
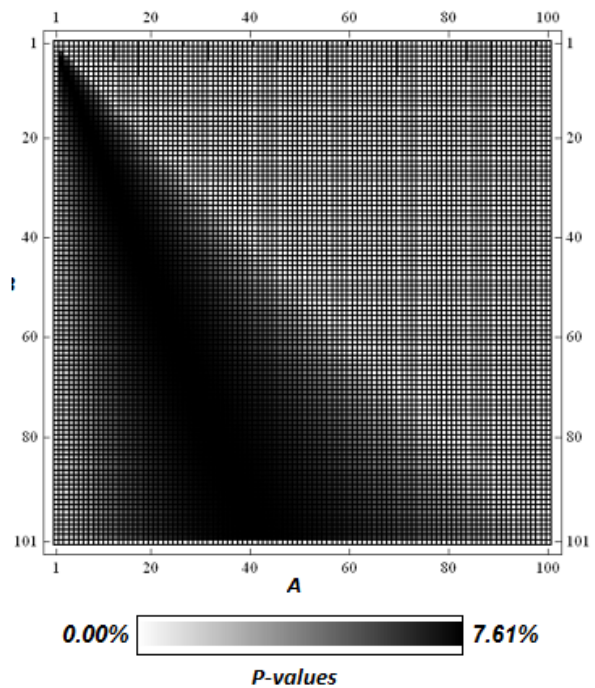
Fig. 16.   P value depending on B and A, if A > 1 and B > A

It is possible to calculate maximum P value for 100 x 100 cells big premises (see Fig. 16) that is equal to 7.61 %. The method/algorithm mentioned was applied instead of Dijkstra's algorithm to calculate total path or covering of 100 x 100 cells big premises and it is obstacles free (see Fig. 17).

44
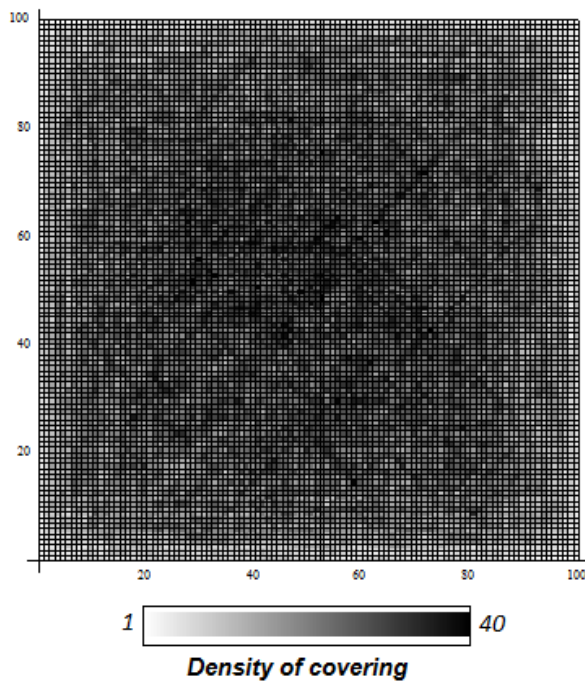
Fig. 17.   The density of covering for 100 x 100 cells big premises (it is obstacles free)

Density of covering changes from 1 up to 40 (there are the cells which were covered only once and there are the cells covered maximum 40 times). Totally, the agent performed 192666 steps in order to cross each cell of the premises.

V CONCLUSION

It can be concluded that the algorithm offered is rather simple and it replaced Dijkstra's algorithm effectively according to the task. The algorithm allows decreasing the time of calculation, which is necessary to define the shortest route among graph vertexes.

The shortest path can be defined in a simple way (even in such cases mentioned in Fig. 13-15), provided that it is necessary to know the gap between the indexes of initial and goal vertexes. For instance, if initial vertex is $v_{i1,j1}$ and goal vertex is $v_{i2,j2}$, the first gap is $\Delta_1=|i_1-i_2|$ and the second gap is $\Delta_2=|j_1-j_2|$. As to the next step, it is needed to calculate the biggest gap between both the gaps. The shortest path is equal to the biggest gap. For instance, Fig. 13 reflects the shortest path which occupies 4 cells, but in other cases (see Fig. 14-15) it is 5 cells big.

It must be marked that total path can be a bit longer it is connected to the specific task which was envisaged in the chapters "Assumptions" and "Results" in detail. The worst case can be evaluated theoretically for the premises of 100 x 100 cells. If we take into consideration that the total route will consist of path pieces, which are longer than 7.61 % in comparison with C value (see Fig. 16), the total path will be longer than optimal 7.61 % (actually, it is the worst maximal variant. We must pay attention to the fact that SA provides only approximate solution).

The algorithm can be successfully used e.g. in autonomous public transport restricted by means of rules, technical requirements in autonomous robots and military equipment. In addition, the algorithm can be used in various computer games where a path planning is done in dynamic environment.

It is possible to conclude that the algorithm offered can be used in the different application areas not only for path planning of a robot.

VI REFERENCES

[1]   E. Aarts and J. Korst. Simulated annealing and Boltzman machines: A stochastic approach to combinatorial optimization and neural computing. John Wiley and Sons, 1989.
[2]   D. L. Applegate, R. E. Bixby, V. Chvátal and W.J. Cook, The Traveling Salesman Problem, Princeton University Press, Princeton, USA, 2007.
[3]   W. J. Cook, *In Pursuit of the Traveling Salesman*. Princeton University Press, Princeton, USA 2011.
[4]   D. Davendra, *Traveling Salesman Problem, Theory and Applications*. InTech, Rijeka, Croatia, 2010.
[5]   R.H.J.M. Otten and L.P.P.P. Ginneken, *The Annealing Algorithm*. Kluwer Academic Publishers, 1989.
[6]   R. Siegwart, I. R. Nourbakhsh and D. Scaramuzza, *Introduction to Autonomous Mobile Robots*. A Bradford Book The MIT Press Cambridge, Massachusetts London, England, 2011.
[7]   P. H. Batavia and I. Nourbakhsh, *Path planning for the Cye personal robot, IEEE/RSJ International Conference on Intelligent Robots and Systems(IROS),* 2000.
[8]   R. Biswas, B. Limketaki, S. Sanner and S. Thrun, *Towards Object Mapping in Dynamic Environments with Mobile Robots, Proceedings of the Conference on Intelligent Robots and Systems (IROS)*, Lausanne, Switzerland, 2002.
[9]   M. Dorigo and L. M. Gambardella, "Ant Colonies for the Traveling Salesman Problem," University Libre de Bruxelles, Belgium, 1996.
[10] D. S. Johnson and L. A. McGeoch, "The Traveling Salesman Problem: A Case Study in Local Optimization." in E. H. L. Aarts and J. K. Lenstra (editors), John Wiley and Sons, Ltd., 1997, pp. 215-310.
[11] V. Ashkenazi, D. Park and M. Dumville, "Robot Positioning and the Global Navigation Satellite System," Industrial Robots: An International Journal, 27(6), pp. 419-426, 2000.
[12] J. Buhmann, W. Burgard, A. B. Cremers, D. Fox, T. Hofmann, F. Schneider, J. Strikos and S. Thrun, "The Mobile Robot Rhino," AI Magazine, 16(1), 1995.
[13] H. Choset, "Coverage of Known Spaces: The Boustrophedon Cellular Decomposition, in Autonomous Robots," 9:247-253, Kluwer, 2000.
[14] E. W. Dijkstra, "A note on two problems in connexion with graphs," Numerische Mathematik, v. 1, p. 269-271, 1959.
[15] S. Kirkpatrick, "Optimization by Simulated Annealing: Quantitative Studies," Journal of Statistical Physics, 34, pp. 975-986, 1984.
[16] S. Kirkpatrick, C. D. Gelatt and M. P. Vecchi, "Optimization by Simulated Annealing," Science, 220, pp. 671-680, 1983.
[17] E. Valbahs and P. Grabusts, "Motion Planning of an Autonomous Robot in Closed Space with Obstacles," Scientific Journal of RTU. 5. series., Datorzinatne. - 15. vol., pp. 52-57, 2012.
[18] M. P. Vecchi and S. Kirkpatrick, "Global Wiring by Simulated Annealing," IEEE Transaction on Computer Aided Design, CAD-2, pp. 215-222, 1983.

Pathfinding Algorithm Efficiency Analysis in 2D Grid

Imants Zarembo, Sergejs Kodors

Rezekne Higher Education Institution

Abstract. **The main goal of this paper is to collect information about pathfinding algorithms A*, BFS, Dijkstra's algorithm, HPA* and LPA*, and compare them on different criteria, including execution time and memory requirements. Work has two parts, the first being theoretical and the second practical. The theoretical part details the comparison of pathfinding algorithms. The practical part includes implementation of specific algorithms and series of experiments using algorithms implemented.**

Such factors as various size two dimensional grids and choice of heuristics were taken into account while conducting experiments.

Keywords – **A*, BFS, Dijkstra's algorithm, HPA*, LPA*, shortest path problem.**

I INTRODUCTION

Pathfinding theory describes a process of finding a path between two points in a certain environment. In the most cases the goal is to find the specific shortest path, which would be optimal, i.e., the shortest, the cheapest or the simplest. Criteria such as, a path, which imitates path chosen by a person, a path, that requires the lowest amount of fuel, or a path from point A to point B through point C is often found relevant in many pathfinding tasks.

The shortest path problem is a pressing issue in many fields, starting with navigation systems, artificial intelligence and ending with computer simulations and games. Although all of these fields have their own specific algorithms, there are many general purpose pathfinding algorithms which can be successfully applied. But it is not always clear what advantages certain algorithm has in comparison to its alternatives.

As a part of this paper pathfinding algorithms A*, BFS, Dijkstra's algorithm, HPA* and LPA* were implemented to analyze their efficiency in an environment based on two dimensional grid. Such factors as grid size, traversed node count and execution time were taken into consideration conducting series of experiments.

II MATERIALS AND METHODS

To assess algorithm efficiency in two dimensional grids experiments were conducted using A*, BFS, Dijkstra's algorithm, HPA* and LPA* to find the shortest path between two randomly placed nodes. Algorithm execution times and traversed node count were measured.

Two dimensional grids used in experiments contained two types of nodes: passable and blocked. 20% of grid was randomly filled with blocked nodes. To assess algorithm efficiency experiments were conducted on various size grids: 64x64, 128x128, 256x256, 512x512 and 1024x1024 nodes.

In case of HPA* three level hierarchy was chosen and initial grid was divided into 4x4 clusters. These parameters were chosen because any smaller division of base grid (64x64 in this case) would lead to incorrect search results while executing preprocessing phase.

Manhattan distance was chosen as heuristic function, because it is strictly grid based distance:

$$H = |x_1 - x_2| + |y_1 - y_2|. \tag{1}$$

Every experiment was repeated 100 times to reduce the amount of random errors. Algorithms were implemented assuming that pathfinding may only occur horizontally or vertically, with no diagonal movement. Every transition between two neighboring nodes costs 1.

All experiments were conducted on the computer with CPU running at a frequency of 2.8 GHz.

III ALGORITHM A*

A* is a pathfinding algorithm used for finding optimal path between two points called nodes. Algorithm A* uses best-first search to find the lowest cost path between start and goal nodes. Algorithm uses heuristic function, to determine the order in which to traverse nodes. This heuristic is sum of two functions:

G — exact cost of the path from initial node to the current node;

H — admissible (not overestimated) cost of reaching the goal from current node;

$F = G + H$ — cost to reach goal, if the current node is chosen as next node in the path.

Estimated heuristic cost is considered admissible, if it does not overestimate the cost to reach the goal [3].

Selection of heuristic function is an important part of ensuring the best A* performance. Ideally H is equal to the cost necessary to reach the goal node. In this case A* would always follow perfect path, and would not waste time traversing unnecessary nodes. If

overestimated value of H is chosen, the goal node is found faster, but at a cost of optimality. In some cases that may lead to situations where the algorithm fails to find path at all, despite the fact, that path exists. If underestimated value of H is chosen, A* will always find the best possible path. The smaller H is chosen, the longer it will take for algorithm to find path. In the worst-case scenario, $H = 0$, A* provides the same performance as Dijkstra's algorithm [2].

A* starts its work by creating two node lists: a closed list containing all traversed nodes and an open list of nodes that are being considered for inclusion in the path. Every node contains three values: F, G and H. In addition to these three values every node needs to contain information about which node precedes it to determine path by which this node can be reached.

IV ALGORITHM BREADTH-FIRST SEARCH

Breadth-first search (BFS) is one of the simplest graph search algorithms and is a prototype for several more advanced algorithms. Prim's minimal spanning tree algorithm and Dijkstra's single-source graph search algorithm uses principles similar to BFS [1].

Given a graph $G = (V, E)$ and the starting node s, BFS will systematically traverse edges of G, to find all nodes, that are reachable from node s. It calculates distance (the smallest number of edges) from node s to every reachable node and creates breadth-first tree, which contains all reachable nodes. The root of this tree is node s. Every node v reachable from node s in breadth-first tree makes the shortest path from s to v in graph G, i.e., path which contains the smallest number of edges. The algorithm is applicable to directed and undirected graphs.

To follow search progress, breadth-first search algorithm marks all nodes in white, gray or black. All nodes are white in the beginning. When during the search node is encountered for the first time it becomes gray or black. Gray and black nodes are considered visited. BFS sorts these nodes to ensure that search is progressing breadth-first. If $(u, v) \in E$ and node u is black, then node v is gray or black i.e. all black node neighbors have been visited. Gray nodes can have white neighbors, they represent border between visited and not visited nodes.

The algorithms complexity in time can be expressed as $O(|E| + |V|)$, in the worst case scenario every edge and every node is visited. $O(|E| + |V|)$ can fluctuate between $O(|V|)$ and $O(|V|^2)$ depending on graph edge evaluation.

V DIJKSTRA'S ALGORITHM

Dijkstra's algorithm deals with single-source the shortest path problems in directed, weighted graphs $G = (V, E)$ with non-negative edge costs ($w(u, v) \geq 0$ for every edge $(u, v) \in E$) [2]. Dijkstra's algorithm maintains set of nodes S, whose final shortest-path weights from source s have already been determined. The algorithm repeatedly selects nodes $u \in V - S$

with the minimum shortest-path estimate, sums u and S, and relaxes all edges leaving u.

Dijkstra's algorithm is called "greedy" algorithm, because it always chooses "the lightest" and "the nearest" node $V - S$ to add to the set S.

The simplest implementation of Dijkstra's algorithm holds the set of nodes Q in simple linked list and finding node with minimal weight is linear search in set Q. In this case algorithm execution time is $O(|E| + |V|^2)$. The algorithm worst case performance can be expressed as $O(|E| + |V|\log|V|)$ [5].

VI ALGORITHM HPA*

Hierarchical pathfinding A* was developed by Adi Botea and his colleagues in 2004. HPA* is a near-optimal pathfinding algorithm, it finds paths which are within 1% of optimal [7]. It is combination of pathfinding and clusterization algorithms, which works by creating an abstract graph on the basis of two dimensional grids. The main HPA* principle is based on dividing search problem into several smaller sub problems, and caching results for every path segment [8].

Clusterization, used in this algorithm, is relatively simple: a low resolution two dimensional grid $s \times s$ is created, where s is a size of new grid. New grid is placed directly above the initial grid. Every node in new grid becomes a cluster. All initial grid nodes that are located under according cluster are considered members of that cluster. Each cluster is considered separate graph. The abstract graph is then created to connect all separate graphs. To achieve that, border nodes needs to be found between neighboring clusters - nodes that are on cluster outer sides are checked. If node has a passable neighbor in an adjacent cluster, it is considered connected, and connection between two graphs representing clusters are added to abstract graph. In cases where there are many adjacent connections between two clusters, they are combined into one entrance. Then entrances are added to abstract graph and connected. Abstract graph still lacks internal edges (paths between entrances inside one cluster). These edges are created by running A* algorithm through every node in each separate cluster. If A* finds path, its cost becomes costs of found abstract edge, else edge is not added to abstract graph. Inter-cluster edges inherit their costs from initial graph edge cost. Finally abstract graph is ready for pathfinding using A* [9].

HPA* pathfinding phase consists of two parts called preprocessing and online search. During preprocessing start and goal nodes are inserted into abstract graph, and inter-cluster edges are added. Then A* is used on abstract graph to find the shortest route. During online search the shortest route found in abstract graph is refined to full path in initial graph using A*. To find full path from start to goal node A* is used in every cluster on nodes that connect clusters. Finally partial results from every cluster are combined into full path [10].

VII Algorithm Lifelong Planning A*

Lifelong Planning A* (LPA*) is an algorithm intended for solving the shortest-path problems on known finite graphs whose edge cost increase or decrease over time [5]. S denotes the finite set of nodes of the graph. $succ(s) \subseteq S$ denotes the set of successors of node $s \in S$. Similarly, $pred(s) \subseteq S$ denotes the set of predecessors of node $s \in S$. $0 < c(s,s') \leq \infty$ denotes the cost of moving from node s to node $s' \in succ(s)$. LPA* always determines the shortest path from a given start node s_{start} to a given goal node $s_{goal} \in S$, knowing both the topology of the graph and the current edge costs. The start distances satisfy the following relationship:

$$g^*(s) = \begin{cases} 0 & if \ s = s_{start} \\ min_{s' \in pred(s)}\big(g^*(s') + c(s',s)\big) \ otherwise. \end{cases} \quad (2)$$

$g^*(s)$ denotes the start distance to node $s \in S$, i.e., the cost of the shortest path from s_{start} to s.

LPA* is an incremental version of A* that applies to the same finite path-planning problems as A*. It shares with A* the fact that it uses nonnegative and consistent heuristics $h(s)$ that approximate the goal distance of the node s to focus its search. Consistent heuristics obey the triangle inequality $h(s_{goal}) = 0$ and $h(s) \leq c(s,s') + h(s')$ for all nodes $s \in S$ and $s' \in succ(s)$ with $s \neq s_{goal}$. LPA* reduces to a version of A* that breaks ties among vertices with the same F value in favor of smaller G values when LPA* is used to search from scratch and to a version of DynamicsSWSF-FP that applies to path-planning problems and terminates earlier than the original version of DynamicsSWSF-FP when LPA* is used with uninformed heuristics [6].

VIII Results and discussion

Algorithm execution time

Breadth-first search is brute-force search algorithm; its results differ noticeably in comparison with informed search algorithms. Table I shows, that the algorithm execution time increases exponentially with search area size increase.

TABLE I
ALGORITHM BFS EXECUTION TIME

Grid size (nodes)	Execution time (ms)
64x64	150
128x128	2803
256x256	48313
512x512	821598
1024x1024	13962457

To find the shortest path in 512x512 node grid, the algorithm took 821 seconds and in 1024x1024 node grid — 13962 seconds. This considerable execution time shows that the algorithm is the most likely not applicable to real-time search problems in large grids.

Increasing the search problem size Dijkstra's algorithm execution time increases linearly. On average in 1024x1024 grid the algorithm finds the shortest path in 2,3 seconds. Table II shows the algorithm execution times for different grid sizes.

TABLE II
DIJKSTRA'S ALGORITHM EXECUTION TIME

Grid size (nodes)	Execution time (ms)
64x64	6
128x128	25
256x256	120
512x512	515
1024x1024	2362

Algorithm A* performance was greater in comparison with Dijkstra's algorithm in every grid size selected for experiments. The algorithms execution time increases linearly with grid size. Table III shows the algorithm execution times for different grid sizes.

TABLE III
ALGORITHM A* EXECUTION TIME

Grid size (nodes)	Execution time (ms)
64x64	4
128x128	16
256x256	77
512x512	265
1024x1024	1148

Lifelong Planning A* performance is higher than Dijkstra's algorithms in all grid sizes, but it is lower than A* performance in 512x512 and 1024x1024 node grids. The algorithms execution time increases linearly with grid size. Table IV shows the algorithm execution times for different grid sizes.

TABLE IV
ALGORITHM LPA* EXECUTION TIME

Grid size (nodes)	Execution time (ms)
64x64	4
128x128	11
256x256	57
512x512	319
1024x1024	1490

Algorithm HPA* execution time, using 4x4 clusters and 3 level hierarchy, is lower than any other algorithm in this experiment. The algorithms execution time increases linearly with grid size. Table V shows the algorithm execution times for different grid sizes.

TABLE V

ALGORITHM HPA* EXECUTION TIME

Grid size (nodes)	Execution time (ms)
64x64	3
128x128	14
256x256	52
512x512	190
1024x1024	775

The experimental data shows, that the fastest execution times belong to HPA* in almost all grid sizes, only dropping behind LPA* in 128x128 grid by 3 ms. The slowest execution times were shown by BFS, which was considerably slower than the second slowest algorithm — Dijkstra's. All algorithm execution times are shown in Table VI and graphically in Fig. 1.

TABLE VI

ALGORITHM EXECUTION TIME

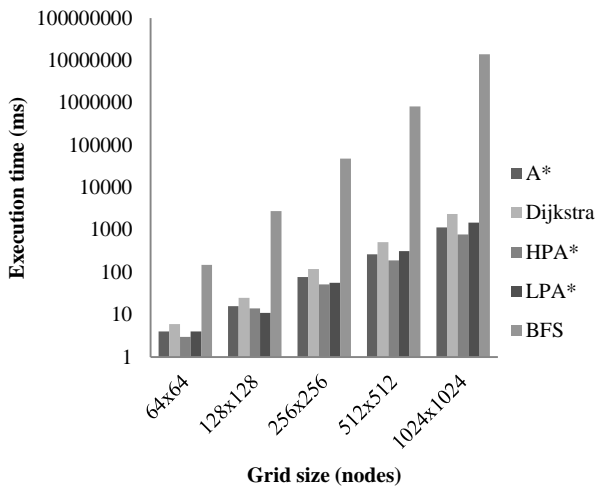| Algorithm	Grid size (nodes)				
	64x64	128x128	256x256	512x512	1024x1024
BFS	150	2803	48313	821598	13962457
Dijkstra	6	25	120	515	2362
A*	4	16	77	265	1148
LPA*	4	11	57	319	1490
HPA*	3	14	52	190	775

Fig. 1. Algorithm execution time

Traversed nodes

Breadth-first search traverses the most nodes from all the algorithms discussed. Table VII shows the algorithm traversed node count for the different grid sizes.

TABLE VII

ALGORITHM BREADTH-FIRST SEARCH TRAVERSED NODES

Grid size (nodes)	Traversed nodes
64x64	3155
128x128	12887
256x256	52367
512x512	213648
1024x1024	1159255

While searching for a path Dijkstra's algorithm traversed slightly less nodes than BFS. Similar amount of visited nodes for Dijkstra's algorithm and BFS can be explained by the fact, that both algorithms use similar node traversal principles. Table VIII shows the algorithm traversed node count for different grid sizes.

TABLE VIII

DIJKSTRA'S ALGORITHM TRAVERSED NODES

Grid size (nodes)	Traversed nodes
64x64	3173
128x128	13058
256x256	52068
512x512	209251
1024x1024	836977

Algorithm A* traversed less nodes than BFS, Dijkstra's algorithm or LPA* while searching for the shortest path. The algorithm uses heuristics to expand nodes in the direction of the goal thus minimizing traversed node count. Table IX shows the algorithm traversed node count for different grid sizes.

TABLE IX

ALGORITHM A* TRAVERSED NODES

Grid size (nodes)	Traversed nodes
64x64	623
128x128	1576
256x256	8071
512x512	40333
1024x1024	104109

Lifelong Planning A* traversed node count increases linearly with grid size increase. On average LPA* traverses half as much nodes as Dijkstra's algorithm. Table X shows LPA* algorithm traversed node count for different grid sizes.

TABLE X

ALGORITHM LPA* TRAVERSED NODES

Grid size (nodes)	Traversed nodes
64x64	994
128x128	6163
256x256	25004
512x512	115973
1024x1024	460318

Hierarchical Pathfinding A* traversed the least nodes from all selected algorithms in all grid sizes. This can be explained by the fact, HPA* only searches paths within selected clusters, which were chosen in preprocessing phase. Table XI shows the algorithm traversed node count for different grid sizes.

TABLE XI

ALGORITHM HPA* TRAVERSED NODES

Grid size (nodes)	Traversed nodes
64x64	454
128x128	1334
256x256	3551
512x512	10629
1024x1024	41491

Comparing algorithms by nodes traversed, Breadth-first has traversed the most nodes and Hierarchical Pathfinding A* - the least nodes. All algorithms traversed node counts are shown in Table XII and graphically in Fig. 2.

TABLE XII

ALGORITHM TRAVERSED NODES

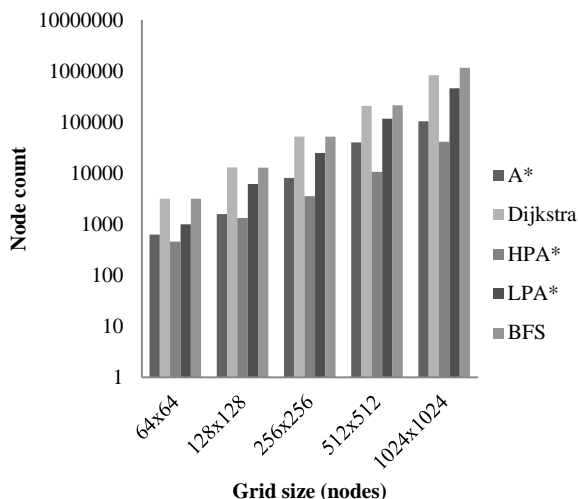| Algorithm	Grid size (nodes)				
	64x 64	128x 128	256x 256	512x 512	1024x 1024
A*	623	1576	8071	40333	104109
Dijkstra	3173	13058	52068	209251	836977
HPA*	454	1334	3551	10629	41491
LPA*	994	6163	25004	115973	460318
BFS	3155	12887	52367	213648	1159255

Fig. 2. Algorithm traversed nodes

Breadth-first search results overall are similar to Dijkstra's in 64, 128, 256 and 512 nodes grids, but falls behind in 1024 node grid.

IX CONCLUSIONS

Comparing A*, Breadth-first search, Dijkstra, HPA* and LPA* algorithms execution times in different size two dimensional grids, the slowest was BFS. This result can be explained by the fact, that the algorithm operation principle is very simple and it does not use any heuristics. Dijkstra's algorithm was faster than BFS, but slower than all other algorithms. A* and LPA* performance was similar: LPA* was faster in smaller grids (64, 128, 256), but A* in larger (512, 1024). Which leads to conclusion, that LPA* is better suitable for smaller pathfinding problems, while A* is better used for solving larger problems. Algorithm HPA* was the fastest in searching path between 2 points, primarily because of hierarchical problem division into smaller parts.

Breadth-first search traversed the most nodes, closely followed by Dijkstra's algorithm. LPA* traverses node count was larger than A* in all grid sizes. A* traversed node count was the second best amon discussed algorithms. HPA* traversed the least nodes.

X REFERENCES

[1] T. H. Cormen, C. E. Leiserson, R. L. Rivest and S. Clifford, *Introduction to Algorithms (3rd ed.).* MIT Press and McGraw-Hill, 2009. pp. 658.
[2] E. W. Dijkstra, "A note on two problems in connexion with graphs," Numerische Mathematik, vol. 1, 1959, pp. 269-271.
[3] P. E. Hart, N. J. Nilsson and B. Raphael, "A Formal Basis for the Heuristic Determination of Minimum Cost Paths," in *IEEE Transactions of Systems Science and Cybernetics*, vol. 4, 1968, pp. 100-107.
[4] D. Wagner, T. Willhalm, "Geometric Speed-Up Techniques for Finding Shortest Paths in Large Sparse Graphs". 2003.
[5] S. Koenig, M. Likhachev, D. Furcy. "Lifelong Planning A*". Artificial Intelligence, Vol. 155 Issue 1-2, 2004, pp. 93 - 146.
[6] L. Sangeorzan, K. Kiss-Iakab, M. Sirbu, "Comparison of 3 implementations of the A* algorithm". North University of Baia Mare. 2007.
[7] A. Botea, M. Muller, J. Schaeffer, "Near, Optimal Hierarchical Path-Finding," Journal of Game Development, 1(1): 2004, pp. 7-28.
[8] M. R. Jansen, M. Buro, *HPA* Enhancements. Proceedings of the Third Artificial Intelligence and Interactive Digital Entertainment Conference*, Stanford, California, USA. 2007.
[9] N. Sturtevant, M. Buro, *Partial Pathfinding Using Map Abstraction and Refinement. AAAI 05 Proceedings of the 20th national conference on Artificial intelligence*, vol. 3. 2005. pp. 1392 – 1397.
[10] R. C. Holte, M. B. Holte, R. M. Zimmer, A. J. MacDonald, *Hierarchical A*: Searching Abstraction Hierarchies Efficiently. AAAI 96 Proceedings of the thirteenth national conference on Artificial intelligence*, vol. 1, 1996. pp. 530 – 535.

V

MECHANICS, MECHANICS OF MATERIALS

Force-in-Chain Study of Chain-Electric Hoist with Periodical Variable Angular Rotational Velocity of Chain-Wheel

Ivan Balashev, Silviu Macuta

Technical University of Gabrovo, Bulgaria, Dunarea de jos University of Galati, Romania

Abstract. **Lifting mechanism of chain electric hoist with periodical variable angular velocity of chain-wheel has been studied in this paper. The non-uniform movement of chain is considerably decreased and from where the dynamic load is also decreased. The experimental studies of the lifting mechanism have been carried out at different operation modes. The results from these studies have been graphically presented and conclusions have been done.**

Key words: **chain electric hoist, experimental studies, force-in-chain.**

I INTRODUCTION

Lifting mechanism of chain electric hoist with periodical variable angular velocity of chain-wheel has been developed and studied. This leads to compensation in large degree of the non-uniformity of the load movement and also the dynamics is improved.

II THEORETICAL AND EXPERIMENTAL STUDIES

The mechanical diagram of lifting mechanism of chain electric hoist with periodical variable angular velocity of chain-wheel is shown in Figure 1 [1, 2]. It is driven by asynchronous electric motor with conic rotor and built-in brake connected with a planetary gear 2 which is contacted to the other one with periodical variable gear ratio from 2KH-KA type. It is consisted of central gears 3 and 4 in which planet gears 5 put on a carrier 6 are engaged.

The carrier is put on the output shaft of the gear where the chain-wheel 8 is mounted. The gear 10, engaged with gear 11 and bearing supported on the fixed axis 12, is put on the driving shaft 9. An elbow 13, entering in a radial canal of the strip 14 fixed on gear 4 with internal teeth, is mounted on one side of the gear 11.

During the rotation of the driving shaft 9 with constant angular velocity ω_9, one basic rotation motion of the output shaft 7 with angular velocity $\omega_{7,0}$ is received. The second reciprocal-rotation motion with angular velocity $\tilde{\omega_7}$ is added to the first one. The second motion is formed by closing kinematic chain (link gear) [1] which is consists of gears 10 and 11, eccentric 13 and strip with canal 14.
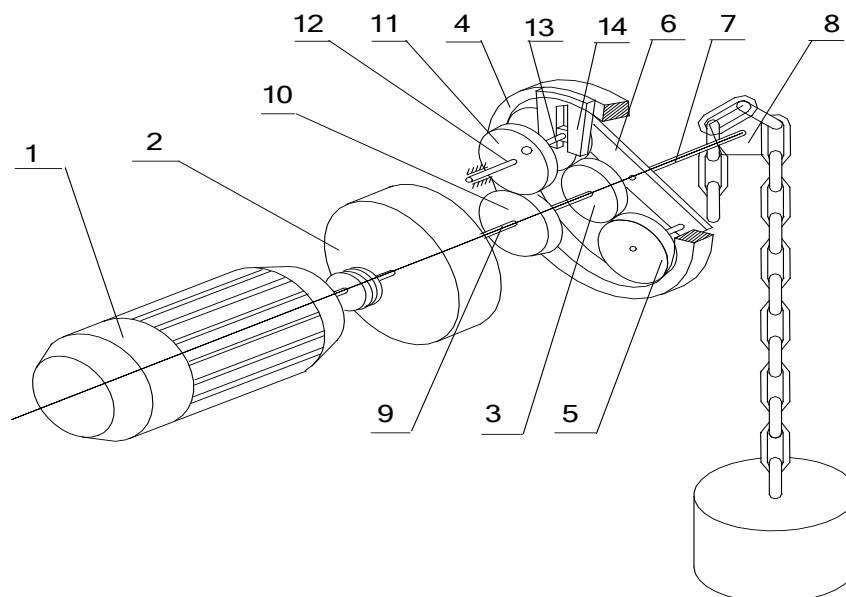

Fig 1. Scheme of lifting mechanism

The periodical variable angular velocity ω_{kz} of the chain-wheel is determined as follows [1]:

$$\omega_{kz} = \omega_{7,0} + \tilde{\omega_7} = \frac{1 + \dfrac{a.e.\cos(\varphi_9/i_o) - e^2}{e^2 + a^2 - 2.a.e.\cos(\varphi_9/i_o)} \cdot \dfrac{z}{i_o}}{1 - z}.\omega_9$$
(1)

where φ_9 is the rotation angle of shaft 9;

a and $i_0=z_{11}/z_{10}$ are center distance and gear ratio of the closing gear with gears 10 and 11 respectively;

e is an eccentricity of the elbow 13;

$z=-z_4/z_3$ is a parameter of the planetary gear.

The variation of angular velocity ω_{kz} of rotation of the chain-wheel is shown in Figure 2. It is determined at different values of the eccentricity e according to angle $\omega 9$ of driving shaft 9. The other parameters are accepted as follows: z=-4; number of teeth of the chain-wheel zk=5 and a=67.5 mm.
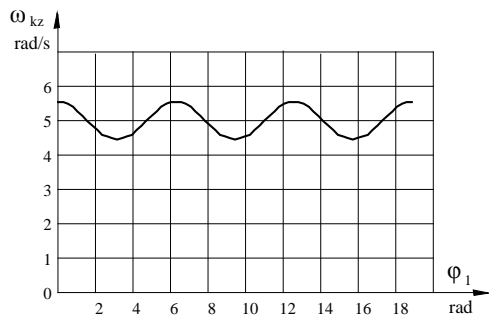

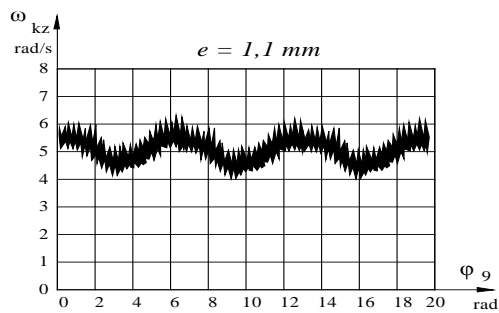Fig 2. Theoretical determinate variation of the angular velocity

Fig 3. Experimental determinate variation of the angular velocity

The experimental studies of laboratory model of chain electric hoist with periodical variable angular velocity of chain-wheel have been carried out. This model has been developed in Technical University of Gabrovo. The following records have been made for the variation of the angular velocity ω_{kz} of rotation of the chain-wheel (Figure 3), for the variation of force-in-chain at rotation of the chain-wheel with periodical variable angular velocity (Figure 4) as well as for the variation of force-in-chain at rotation of the chain-wheel with constant angular velocity (Figure 5) at condition of load lifting.

Force-in-chain at lifting from the ground with rotation of the chain-wheel
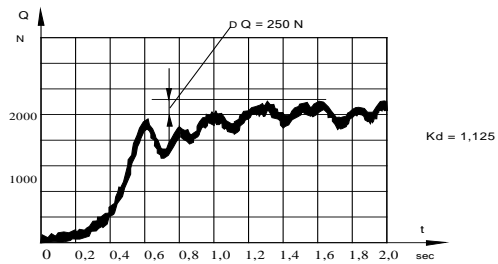
Fig 4. With periodical variable angular velocity
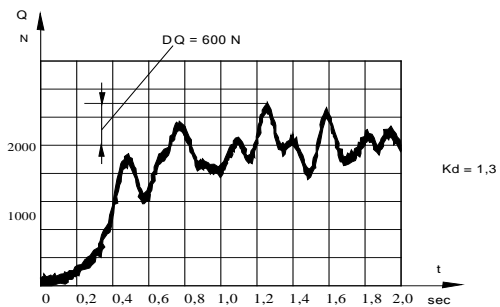
Fig 5. With constant angular velocity

Experimental studies at the other operation modes of the chain electric hoist with "polygon effect" compensation of the chain drive have been carried out. The results have been compared with these ones of the existing constructions of chain electric hoist with rotation of the chain-wheel with constant angular velocity.

Oscillograms of variance of the force-in-chain at condition – stopping at the end of load lifting are shown in Figure 6 and Figure 7. Oscillograms of variance of the force-in-chain at condition – lifting of suspended load are shown in Figure 8 and Figure 9.

Force-in-chain at stopping at the end of load lifting with rotation of the chain-wheel

Fig 6 With periodical variable angular velocity

Fig 7   With constant angular velocity

Force-in-chain at lifting of suspended load with rotation of the chain-wheel

Fig 8   With periodical variable angular velocity
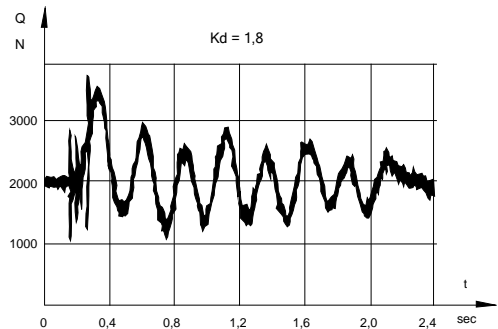
Fig 9.   With constant angular velocity

Oscillograms of variance of the force-in-chain at condition – lowering of suspended load are shown in Figure 10 and Figure 11. Oscillograms of variance of the force-in-chain at condition – stopping of suspended load are shown in Figure 12 and Figure 13.

The coefficients for dynamism have been determined for each operation mode of two lifting mechanisms of chain electric hoists. They are given in the tables and also are determined by means of the following relationship:

$$k_d = \frac{Q + \Delta Q}{Q} \qquad (2)$$

Force-in-chain at lowering of suspended load with rotation of the chain-wheel
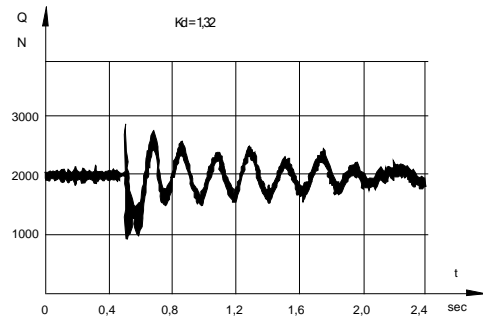
Fig 10. With periodical variable angular velocity
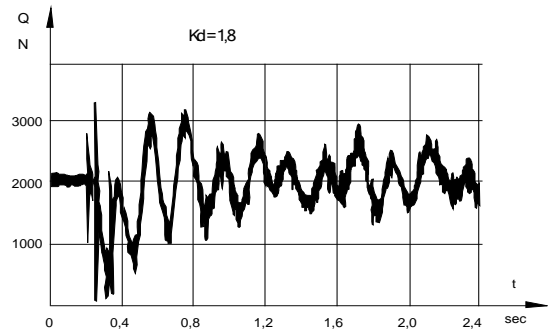
Fig 11. With constant angular velocity

Force-in-chain at stopping of suspended load with rotation of the chain-wheel
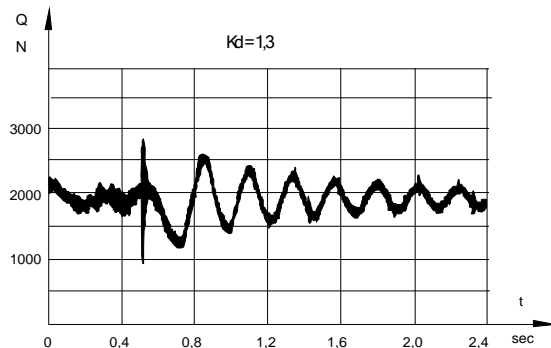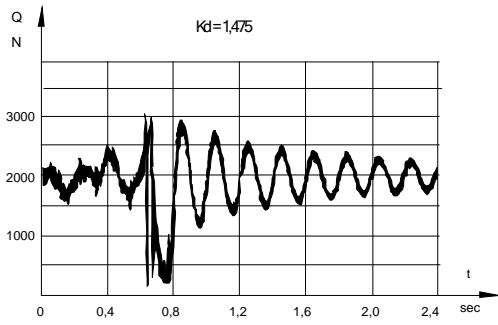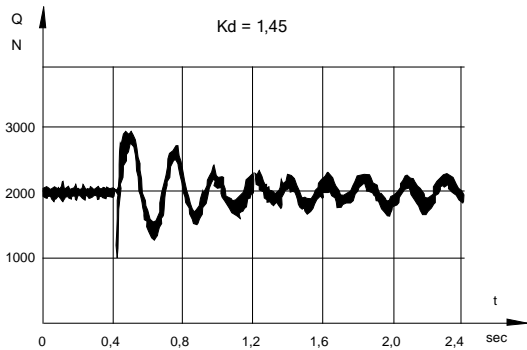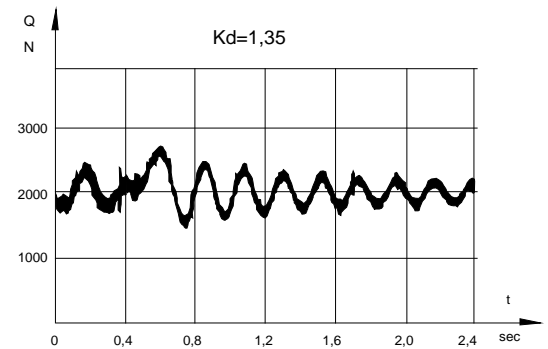

Fig 12. With periodical variable angular velocity
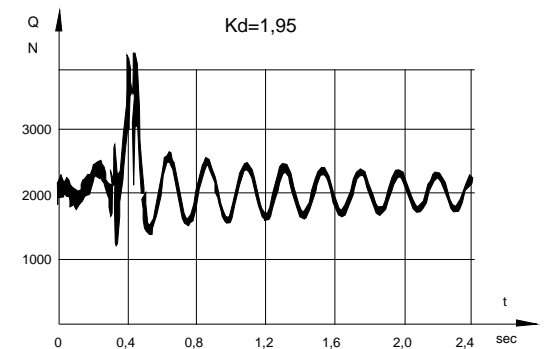
Fig 13. With constant angular velocity

III CONCLUSIONS

The following conclusions have been drawn by means of the carried-out theoretical and experimental studies of lifting mechanism of chain electric hoist which are connected with an application of the planetary gear 2KH-KA type with periodical variable gear ratio:

- An original construction of lifting mechanism of chain electric hoist with an application of the planetary gear 2KH-KA type with periodical variable gear ratio has been developed. The "polygon effect" of the chain drive is compensated at this design.

- The non-uniform movement of the chain (load) is decreased at the suggested construction of chain electric hoist because of the compensation of the "polygon effect" of chain drive as well as this one of the dynamic loads.

- The coefficient of dynamism k_d at the suggested construction is decreased with 15,5% at the condition of load lifting from the ground during the carried-out dynamic experimental studies of lifting mechanism of chain electric hoist with an application of the planetary gear 2KH-KA type with periodical variable gear ratio.

IV REFERENCES

[1] Балашев, И. Л., Планетарные передачи с циклическим переменым передаточным отношение, International Congress Gear Transmissions, vol. II, 1995.

[2] Balashev, I. L., L. Stoyanov, Planetary gear, Inventor's certificate No 51647, MPK F 11 H3 / 44,1996.

Analysis of Dynamic Parameters of Observation Towers in Latvia

Liga Gaile

Riga Technical University, Department of Structural Analysis. Address: Azenes Street 16, Riga, LV-1048, Latvia.

Abstract. The purpose of this research is to experimentally identify the performance of most of the light-weight observation towers open for public in Latvia. It analyzes the structure of towers, technical condition, dynamic parameters and dynamic response to human movement along the tower height. During the experiment there were measured and recorded the vibration accelerations of 18 observation towers' upper platform. Further dynamic parameters were extracted using the spectral analysis. There was performed the sensitivity analysis to establish parameters that most influences the dynamic response amplitudes due to human movement. All experimentally obtained fundamental frequencies of the inspected towers are in the typical range of human walking frequencies. It is found that the main parameter that denotes the response level (acceleration amplitude) of the tower due to human movement is a tower self-weight.

Keywords – acceleration, frequency, human induced vibrations, observation tower.

I INTRODUCTION

Historically the free standing towers primarily were used by military to provide a good observation of the surrounding area. The era of observation towers as a sightseeing symbol probably started in Paris during the 1889 with the Eiffel rise at the World's Fair. Observation towers located in cities usually are tall structures and serve as an architectural symbol but towers located in the countryside are designed to allow viewers an unobstructed view of the landscape and tend to have a design mostly driven by economic aspects.

Latvia has around 20 light-weight observation towers accessible for general public with height more than 20m (Fig. 1). Mostly they are located in countryside of Latgale and Kurzeme region. Almost half of them are responsibility of the state company JSC "Latvia's State Forests" that continuously develops environmental infrastructure objects. As an example serves recently opened for public (October, 2012) 28,5m high timber observation tower "Ančupānu skatu tornis" near Rezekne city. Although construction of such towers is rather expensive it is a great way to increase tourist flow to the area otherwise not very popular.

Most of the towers in Latvia have set rules to limit the number of visitors from 5 to 10 people however this limit is not based on any research information and construction is purely based on the previous experience. In 2010 a light-weight eccentric steel structure observation tower was opened for public in Jurmala and most of the visitors experience vibration amplitudes causing uncomfortable feeling. This structure highlights the lack of understanding and inadequate design information of the building codes, regarding the slender tower dynamic response to human induced loads [1]. It demonstrates that in areas with low seismicity and relatively low wind loads the human induced dynamic loads could be determinative in a slender and light-weight observation tower design because it is important to meet acceptable comfort level for tower visitors.
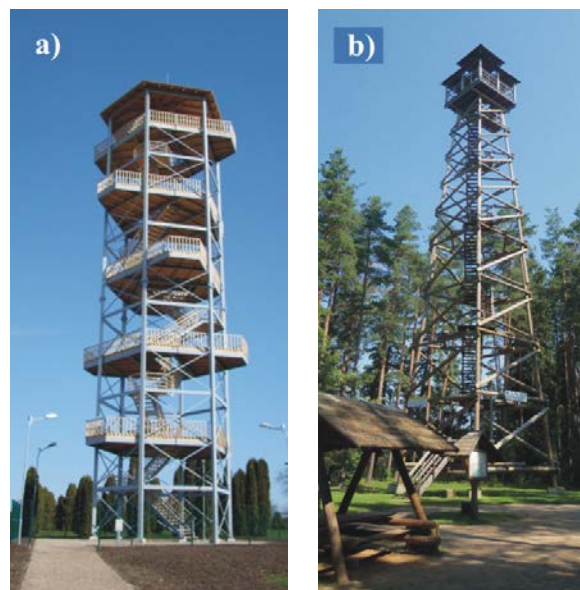
Fig. 1.   Observation towers: a) steel, b) timber

From the extensive experimental and numerical researches in last decade regarding the light-weight footbridge vibrations induced by human dynamic loads it is known that slightly damped bridges become susceptible to vibrations when structures natural frequencies are in the range of human step frequencies [2]-[5]. In the case of bridge pedestrian density greatly influences the step frequency [6]. The mean step frequency for the low density (0.2-0.5 Persons/m2) pedestrian stream is 1.8-1.9Hz according to [6].

In the case of stairs that is essential component of any lattice observation tower there is a wide variation of walking speeds and therefore the wide variation of step frequencies can be found in literature. The study

[7] presents the measured walking speeds of 485 individuals on "the long stairs" during the event Expo 2000 in Hannover. It was found that in case of small or no visible influence among individuals the mean footfall frequency is 1.416 Hz with standard deviation of 0.277 Hz. The observed minimum frequency was 0.48 Hz and maximum (corresponds to running) was 4.25 Hz.

To assess the existing observation towers dynamic performance in this study there were experimentally measured and recorded data of 18 observation tower's top platform vibration acceleration under an operational conditions. There were obtained the natural frequencies exited by human movement up and down along the towers' height, dynamic response levels (acceleration amplitudes) and damping ratios for the most of observation towers in Latvia. Additionally there were theoretically analyzed parameters that most influences the response level (vibration acceleration and displacement amplitudes) under the human induced typical walking load.

II MATERIALS AND METHODS

A. Experimental programme

During the experiments there were measured and recorded the vibration accelerations of 18 observation towers (Fig. 2.)

Fig. 2. Location of observation towers in Latvia.

There were used five 3-axis light-weight (55g) USB accelerometers (Model X6-1A) to record the accelerations. Devices were located on the upper platform of towers. The measurement sample rate is 160 Hz. Each accelerometer simultaneously records vibration accelerations in three directions. The typical arrangement of accelerometers is presented in Fig. 3.
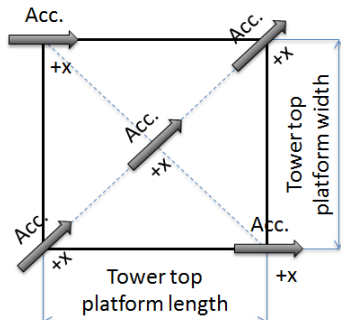
Fig. 3. Accelerometers arrangement scheme

The acceleration amplitudes were measured under the following conditions: very mild wind and no visitors on the tower, two visitors moving upstairs and afterwards downstairs the tower and free decay of vibrations. Additionally, there were measured the geometry of structures and weather conditions during the experiments.

B. Processing technique of experimental data

The structural dynamic behavior denotes the modal parameters of structure (natural frequencies, damping ratios and mode shapes). The field of research so called "modal analysis" is dealing with identification of those parameters.

The branch of modal analysis is operational modal analysis that aims to determine the dynamic characteristics of structure under operational conditions.

Excitation force of two person movement along tower's height is weak compared to observation tower's self-weight and stiffness therefore peaks in the output spectrum will be responses in the structural modes.

There was performed spectral analysis using software package ME'scopeVES to determine the exited frequency content of simultaneously recorded time traces of observation tower's top platform accelerations.

There were obtained the autocorrelation functions (1) of the time traces that show how the mean power in a signal is distributed over frequency. It is also a very handy tool to detect the harmonic signals buried in the noise [8].

$$G_{AA}(f) = A(f) \cdot A^*(f), \tag{1}$$

where A(f) is the Fourier transform of the time trace a(t) defined as:

$$A(f) = \int_{-\infty}^{\infty} a(t)e^{-ift} dt, \tag{2}$$

The "*" indicates the complex conjugate and:

$$e^{ift} = \cos(ft) + i\sin(ft), \tag{3}$$

where i is a unity imaginary number.

To reduce the leakage effects due to non-periodicity of the time signal records the "Hanning window" was applied to each sampling window before the FFT (Fast Fourier Transform) was applied. In the ME'scopeVES the modal parameters are extracted from the cross channel measurement functions using FRF-based curve fitting methods. The DeConvolution window was applied to remove the "second half" of the time domain correlation function associated with the measurement.

To check the reliability of obtained natural frequencies there was used the stabilization diagram that subsequently assumes an increasing number of poles.
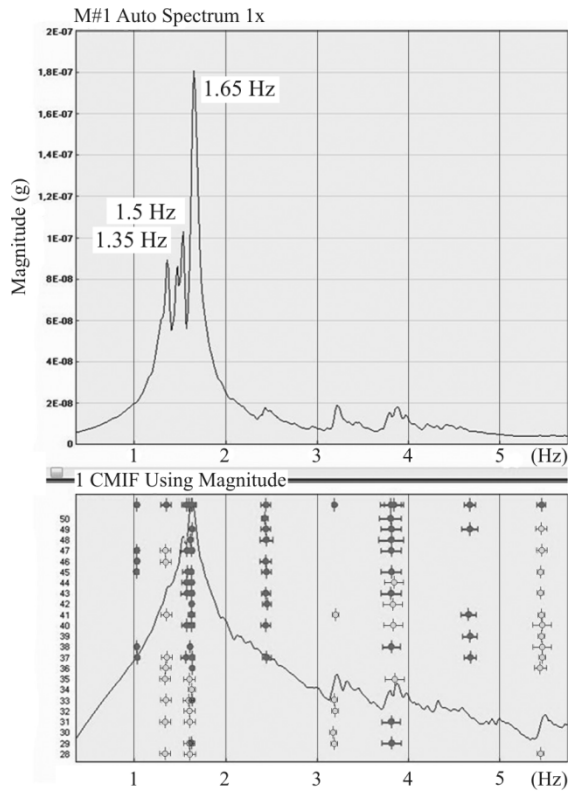
Fig. 4.   Response spectrum and stabilization diagram of Ligatne tower due to 2 persons ascending
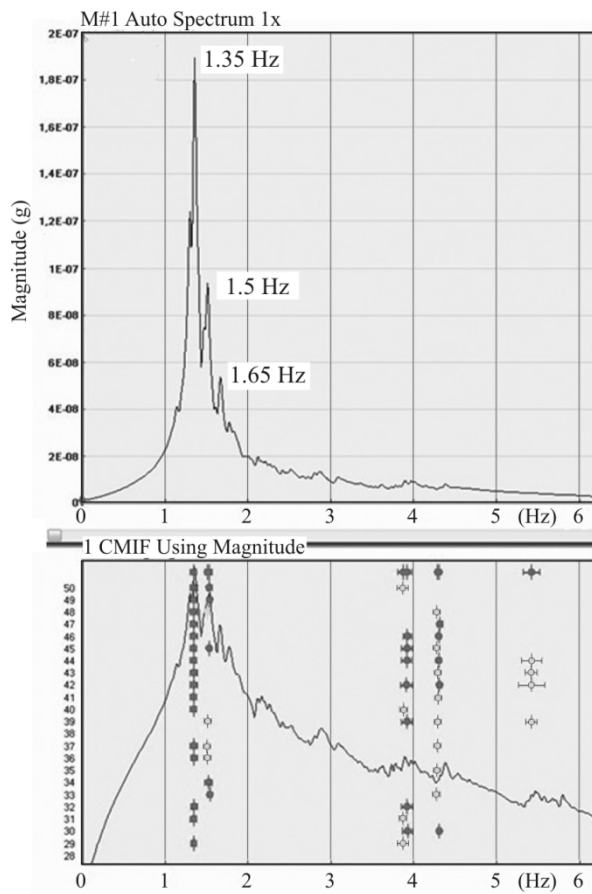
Fig. 5.   Response spectrum and stabilization diagram of Ligatne tower due to 2 persons descending

The physical poles (exited frequencies) always appear as "stable poles" consequently the unrealistic poles are filtered out. Examples of obtained auto spectrum and stabilization diagrams presented in Fig. 4 and 5.

Damping ratios of the towers were obtained from free decay time histories using formula (4) [9]:

$$\xi = \frac{1}{2\pi n} \ln \frac{a_0}{a_n} \qquad (4)$$

where,

n – number of relevant periods in time history;
a_0 - max amplitude;
a_n - min amplitude.

C.   Theoretical Background

Slender sightseeing towers are the line - like structure and for the purpose of response analysis it was modeled as the cantilever with uniformly distributed mass along the height. The foundation stiffness was not taken into account. The observation tower's loading scheme for analytical investigation of different parameters (mass, stiffness and tower height) influence on the structures dynamic response is presented in Fig. 6.
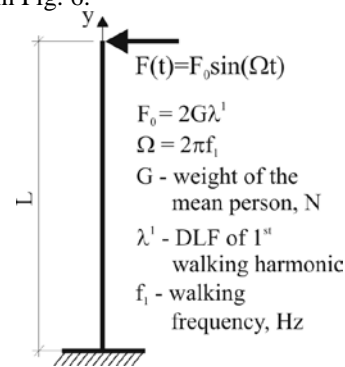
Fig. 6.   Calculation scheme

According to generally accepted design processes for low frequency structures it is convenient to consider the maximum level of the resonant response that can be induced by person under repeated footfall. It was previously found that tower would not reach "the steady state vibration" due to inconsistent periodicity of applied loading [10]. Thus for the sensitivity analysis purpose the load is applied in the horizontal direction with magnitude of two persons' typical first walking harmonic (longitudinal direction) at cantilever tip. The weight of one person is assumed 740N and dynamic load factor (DLF) is assumed 0.12.

The sensitivity analysis was performed in the following parameter range:

Height of the tower: 20m … 40m;
Self-weight of the tower: 4kN/m … 1500kN/m;
Stiffness of the structure (EI):
$1.4 \cdot 10^9 Nm^2$ … $1.6 10^{10} Nm^2$.

The reference tower parameters are following:
Height of the tower: L_{av}=30m;

Self-weight of the tower: $m_{av}=9.5$kN/m
Stiffness of the structure: $EI_{av}=9.04\cdot10^9$Nm^2 ;
Damping ratio: $\xi=2.5\%$.

In calculations it was considered that 4 repeated footfalls in a row coincide with the fundamental frequency of the structure.

The methodology for obtaining the analytical solution (displacements and accelerations) of equation of motion (5) is taken from [10].

$$\frac{\delta^2}{\delta y^2}\left[EI(y)\frac{\delta^2 x}{\delta y^2}\right]+m(y)\frac{\delta^2 x}{\delta t^2}+$$
$$+c(y)\frac{\delta x}{\delta t}=G\lambda^1\sin(\Omega t), \quad (5)$$

where,
 EI – stiffness;
 x – displacement;
 c – damping;
 m – mass.

III RESULTS AND DISCUSSION

There were experimentally measured and recorded data of 18 observation tower's top platform vibration acceleration under a mild wind and two persons movement along the tower's height to obtain the exited natural frequencies, damping ratios and acceleration amplitudes for the light-weight lattice towers made of different materials.

There were some examples of mixed structures e.g. timber structure (columns, beams, and cladding) with a steel rod lateral resisting system. Mostly observation towers can be divided in timber (70% of the inspected towers) and steel structures. The slope of the observation towers' stairs was in the range of 30^0 to 70^0 but most of the observation towers' slop of the stairs was around 45^0. Although the most of observation towers are less than ten years old their technical condition widely varies. Only the timber towers less than five years old with a treated timber are in good technical condition.

The recorded time histories and corresponding frequency spectrums with stabilisation diagrams of the observation tower in Ligatne are presented in Fig 7. The recorded peak accelerations under mild wind conditions are about 20 times less than from two person movement upstairs and downstairs. Most of this tower's height was sheltered by surrounding trees. In this case response spectra show that ascending and descending excite the same frequencies. In ascending case higher magnitude has the fundamental frequency of the tower (1.35Hz) but in descending case higher magnitude has higher frequency (1.65Hz).
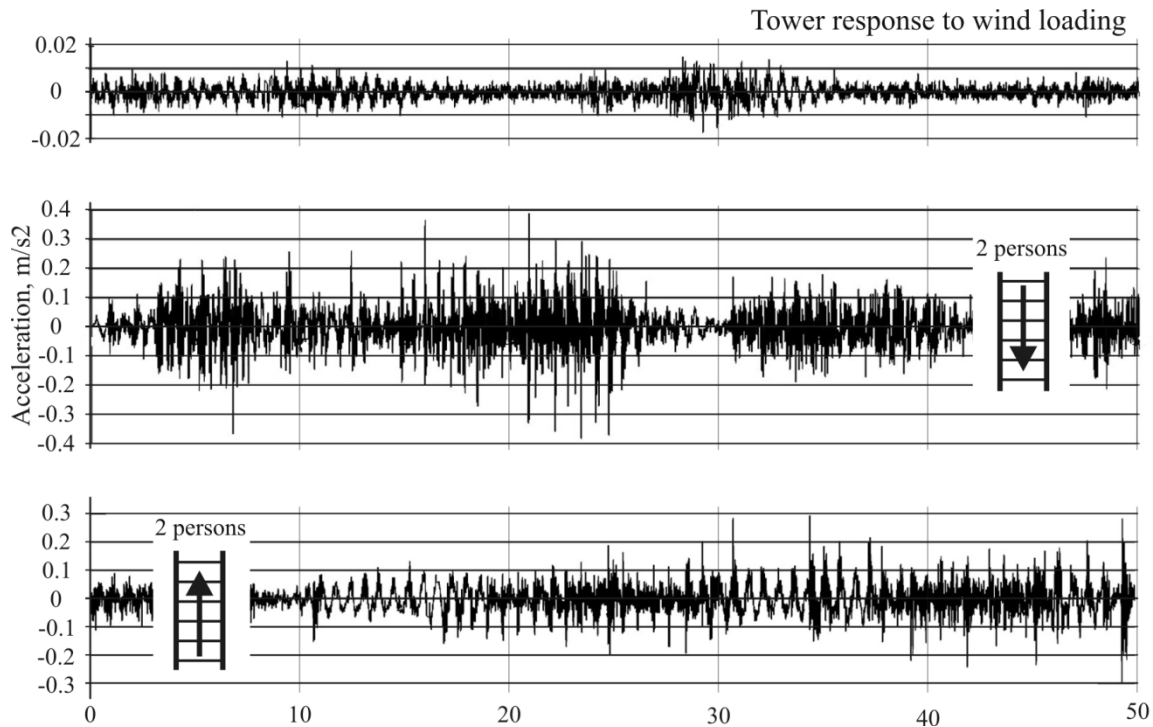
Fig. 7.   Acceleration time history of observation tower in Ligatne

Table 1 presents the three main exited natural frequencies of observation towers and maximum accelerations observed due to two persons movement up and down the tower stair as well as presented damping ratios in such were obtained.

The Table 1 excludes the inspected towers that were in unsatisfactory technical condition.

The lowest exited frequencies of human movement are generally the fundamental frequencies of the observation towers. To recognize it, there was analysed frequency spectrum of each tower obtained from ambient response data where as an input force was considered the wind loading.

60

TABLE 1.

OBSERVATION TOWER DYNAMIC RESPONSE TO HUMAN INDUCED LOADING

Tower name and height of the top platform above the ground level	Structural material	Exited frequencies of two persons movement, Hz						A_{max}, m/s²	x, %
		Ascending			Descending				
Krustkalnu tower (25m)	Steel	2.6	2.8	-	2.6	2.8	-	0.47	0.8
Kalsnava tower (25m)	Steel	1.7	-	-	1.6	1.7	2.2	0.33	1.7
Jurmala tower (34m)	Steel	0.75	0.8	1.15	0.8	3.3	-	0.35	2.3
Eglu kalns (26.5m)	Timber	1.3	4.2	-	1.3	2.5	4.2	0.3	4
Priedaine (32m)	Timber	1.2	2	3.1	1.1	2	2.2	0.26	-
Kamparkalns (26.5m)	Timber	1.35	1.45	-	1.45	2.85	-	0.3	3.1
Udru kalns (26.5m)	Timber	1.35	2.6	-	1.35	1.55	2.6	0.25	3.85
Ventspils tower (12m)	Steel	Excitement is negligible; fundamental frequency is 3.4Hz							-
Kuldiga tower (16.3m)	Mixed	0.8	1.1, 1.2	2.6	0.8	1.2	2.6	0.26	-
Lielais liepu tower (34m)	Timber	1.1	1.3	2.1	1.1	1.5	4.7	0.13	-
Ligatne tower (22m)	Timber	1.35	1.5	1.65	1.35	1.5	1.65	0.25	5.4
Lozmeteju tower (28.5)	Timber	1	1.1	2.2	1	1.1	-	0.3	-

All fundamental frequencies of the inspected towers are in the typical human walking range as given in the [10]. It is noticed that generally during the stair ascend case with highest acceleration amplitude exited the lowest natural frequency but in descending case there could be different dominant natural frequency. It corresponds well with the observations during the experiment that visitors move downstairs faster than upstairs. The differences in the exited natural frequencies of the towers with very similar structure and the same fundamental frequency due to human movement (Kamparkals tower and Udru kalns tower) indicate the stochastic nature of human dynamic loading.

Although the inspected towers varies in the structural arrangements and materials the maximum response level (acceleration amplitude) of two persons movement are close to 0.3m/s² . The exception are two steel towers (Krustkalns and Jurmala) that are considerably lighter and have higher acceleration amplitudes and tower in Ventspils that is very short with no visible effect from human movement.

To analyse the different parameter (tower's self-weight, height and stiffness (EI)) influence theoretically on the dynamic response level due to two persons movement was performed the sensitivity analysis for the range of parameters as given in the previous section of the paper. The Fig. 8 presents tower tip displacement amplitude changes if one of the considered parameters is changed but others are fixed. The Fig.9 shows acceleration amplitude changes in a similar manner.

The perception of vibration depends on vibration frequency and the acceleration amplitudes are directly related to pedestrian comfort [11]. Therefore there is a specific interest in amplitude values of accelerations.

Results of the sensitivity analysis reveal that a change in tower stiffness does not influence the acceleration amplitudes. The most important parameter is mass of the structure that does not influence the displacement amplitudes but significantly influences the acceleration amplitudes.

Basically, stiffer structure has higher frequency however displacements are smaller and as a result there is no significant change in the acceleration amplitude. This well correspond with the experimental results where the acceleration levels are approximately the same for towers with similar self-weight.

In reality there is impossible the situation when changes of the stiffness or height of tower would not influence the self-weight of structure. Nevertheless the sensitivity analysis confirms that lighter towers made of stronger materials such as steel compared to timber ones will be more prone to human movement induced vibrations and could reach higher acceleration values. This corresponds well with the experimental results in the Table 1.

Experimentally determined peak acceleration of Lielais liepu kalns tower $A_{max} = 0.13$m/s² (Table 1) is considerably smaller than other timber towers have, although the fundamental frequency is quite low (1.1Hz).
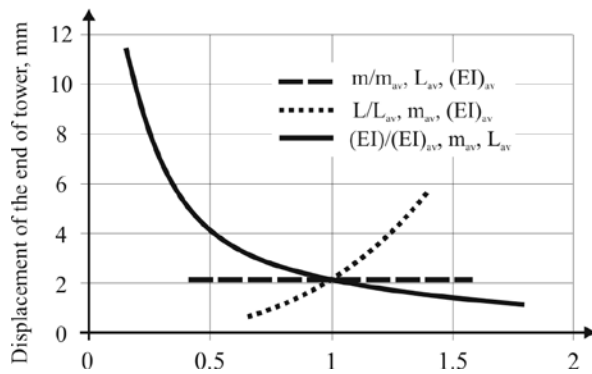
Fig. 8.   Displacement amplitude of tower tip due to geometrical parameter change
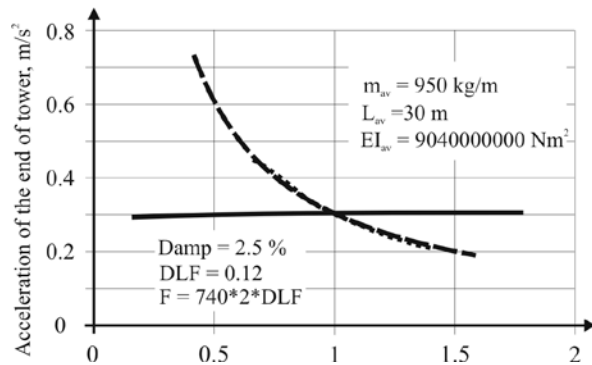

Fig.9.   Acceleration amplitude of tower tip due to geometrical parameter change

The structure of this particular tower has additional structural elements that increases the tower self-weight but do not increase significantly the stiffness of the structure and the tower visitors did not have any discomfort feeling compared to other towers with peak acceleration more than 0.25 m/s^2. This corresponds well with the carried out theoretical sensitivity analysis.

IV CONCLUSIONS

The experimental data presented in this paper are based on measurements of 12 light – weight lattice observation towers' (with different structural assembly and used materials) responses (acceleration amplitudes) to human induced dynamic loading. In theoretical part of the paper particular attention is paid to find the parameters of the structure that mostly influence the dynamic response level (displacements and accelerations) to this loading. The main conclusions from the study can be summarized as follows:

1. Observation towers are sensitive to the human induced loads. Human movement along the tower height induces vibration with frequencies that are natural frequencies of the structure.

2. The experimental results reveal the different natural frequencies with different magnitude redistribution of towers with a similar geometry and same fundamental frequency were exited. This indicates the stochastic nature of human induced loading. In all cases there were exited several natural

frequencies with comparable magnitudes. Generally, ascending the tower stairs excites the lowest natural frequencies of the structure with highest acceleration amplitudes. When descending the tower stairs the acceleration magnitude distribution over frequencies differs from the ascending case. Then the higher amplitudes have exited frequencies closer to 2Hz. This correlates with observation that tower visitors descend the tower stairs at higher speed than ascend.

3. The damping ratios of timber observation towers are roughly twice (x≈4%) of steel ones.

4. The parameter that mostly influences the tower acceleration amplitudes due to human movement induced loads are the self-weight of the structure.

5. The good correlation between the experimental results and theoretical analysis predicting the acceleration amplitudes induced by human movement indicates that the made assumption of considered 4 repeated footfalls in a row coincides with the fundamental frequency of the structure is adequate.

V ACKNOWLEDGMENTS

VI REFERENCES

[1] L. Gaile. and I. Radinsh, *Eccentric lattice tower response to human induced dynamic loads. Proceedings of 19th International Congress on Sound and Vibration*, July 8-12, 2012, Vilnius, Lithuania, CD-ROM, pp. 560-567, 2012.

[2] E. T. Ingolfsson and C.T. Georgakis, "A stochastic load model for pedestrian – induced lateral forces on footbridges", Engineering Structures, 33, pp. 3454-3470, 2011.

[3] F. Venuti and L. Bruno, "Crowd – structure interaction in lively footbridges under synchronous lateral excitation: A literature review", Physics of Life Reviews, 6, pp. 176–206, 2009.

[4] S. Zivanovic, A. Pavic and P. Reynolds "Vibration Serviceability of Footbridges under Human – Induced Exitation: A Literature Review", Journal of Sound and Vibration, 279 (1-2), pp. 1–74, 2004.

[5] S. Zivanovic and A. Pavic, "Probabilistic assessment of human response to footbridge vibration", Journal of Low Frequency Noise, Vibration and Active Control, Vol. 28(4), pp. 255-268, 2009.

[6] C. Butz, M. Feldmann and et.al., "Advanced load models for synchronous pedestrian excitation and optimised design guidelines for steel footbridges," European Commission, Research Fund for Coal and Steel, European Communities, Tech. Rep., 2008.

[7] T. Kretz, A. Grunebohm, and et. al., "Upstairs Walking Speed Distributions on a Long Stair-way", Safety Science, 46, pp. 72-78, 2008.

[8] W. Heylen, S. Lammens and P. Sas, *Modal analysis theory and testing.* Leuven: Katholieke Universiteit Leuven, 2007.

[9] H. A. Büchholdt and S. E. M. Nejad, *Structural Dynamics for Engineers.* ICE Publishing: UK, 2011.

[10] L. Gaile. and I. Radinsh, *Lattice tower dynamic performance under human induced loading. Proceedings of 11th International Conference on Recent Advances in Structural Dynamics*, July 1-3, 2013, Pizza, Italy, accepted for publishing, 2012.

[11] M. J. Griffin, *Handbook of Human Vibration.* Elsevier Ltd., 2004.

Formwork with Variable Geometry for Concrete Shells Production Technology

Vitalijs Lusis

Riga Technical University,
Faculty of Civil Engineering, Concrete mechanics laboratory
Address: 1 Kalku Street, Riga, LV-1658, Latvia

Abstract – **One of the main constructive materials in the building sphere is a precast concrete and fiber concrete. It is well influenced by scientific research basis, development and implementation of progressive technologies. The fiber concrete it is an ideal material with practically unlimited number of shapes. A nomenclature of concrete articles increases, it is working on different shape formation and processing. While preparation for this document started with the concept fabrication, it is necessary to understand the methods of construction variable geometry formwork of concrete thin-shell surfaces, both past and present as a point of departure. An understanding of this background helps provide an essential foundation for the exploration of new potential advances in the field of thin-shell construction. Obviously that is the reason for fiber concrete to be the most widespread constructive building material all over the world. In the article are considered shell development technology features and is evaluated technical and economical effectiveness of concrete shells with thin walls. Now variable geometry systems from flexible materials are developing and improving, there is a great potential followed by modern events in concrete technology. The results of laboratory experiments have proved that the technology can be used for fibro concrete shell production and construction.**

Keywords – **concrete shells, shells production technology, glass fibers, fiberconcrete.**

I INTRODUCTION

Recent developments in concrete technology have led to ultra-high performance fibre reinforced concrete with revolutionary performance in tension and compression. In fact, ultra high performance fibre reinforced concrete can be seen as a completely new construction material and its possibilities are still to be revealed. Fibre reinforced concrete use leads itself to a variety of innovative designs as a result of its many desirable properties. Not only the higher quality contemporary construction materials capable of resisting tension forces contributed to this development, but also the theoretical knowledge gained from the late 19th century up to the present day. Earlier the engineers were restricted by constructional possibilities. The modern era of shell construction is recognized by the trend towards greater spans and thinner shells.

Modern shell structures span larger column-free areas from 100 m and more and, more important, with thinner thicknesses than the traditional domes. Thin concrete shell structures can cover the roofs of various buildings efficiently and aesthetically. The search for new spatial structures resulted in widespread pioneering with new types of shells.

Architecture form has got a thin concrete shell created in the form of circles, hyperboloids and paraboloids and of double curved shapes with undefined free-form shapes (Deconstructivism). In order to achieve required geometrically complicated forms and surfaces of textured concrete is necessary a flexible and adjustable formwork system [1,2,3]. The desire to reduce the thickness is understandable as the dead weight of the shell represents the major portion of the total load.

Figure 1. L'Oceanogràfic in Valencia, Spain — an open-air oceanographic park, architect Félix Candela

Figure 2. Los Manantiales Restaurant (1957) in Xochimilco, Mexico by Felix Candela

Most shells are constructed in a conventional manner: pouring concrete on a formwork. Other possibilities are the use of airform moulds or stressed membranes combined with sprayed concrete. Although the number of repetition is often not very high, prefabricated elements may be used.

If one shell has to be chosen as being the inspiration for a complete generation of new shell engineers, it must be the Los Manantiales Restaurant in Xochimilco, Mexico. Felix Candela completed the shell in 1957 and the design was that much of a success that, at the present day, it has been copied several times.

Jorg Schlaich designed a Xochimilco-like shell in 1977 in Stuttgart, Ulrich Muther constructed the Seerose in 1983 in Potsdam and in just recently in 2002 in Valencia another look-a-like has been constructed by Santiago Calatrava: the new l'Oceanografic see figure 1. Furthermore, famous shell builder Heinz Isler was inspired by the slenderness of the Manantiales restaurant. The original Xochimilco shell, seen on figure 2, is an octagonal groined vault composed of four intersecting hypars.

II MATERIALS AND METHODS

Tasks of laboratory experiments: production and achievement of different kind shells, including dome-shaped constructions, clearing up the shell production technological features and technological process advantages, effectiveness, a visual attraction and advantages of products. Laboratory experiment to create on formwork with variable geometry was elaborated Latvian invention patent Nr. LV14308 [4]. Use of a formwork advantages can be mentioned as follows: flexible shapes (being curved created surfaces are of architecturally and technologically complicated shapes), smooth concrete surface quality, formwork weight and volume of tissue is very small comparing to plywood or steel formwork.

Figure 3. Short AR glass fibers homogeneously distributed in the concrete shell

Despite the purpose of variable geometry formwork and their usage conditions, the material of formwork should have a sufficient tensile strength (calculated) and low weight, should be resisting to weather impacts, flexible, fireproof (at least the material should be fire extinguished), heatproof and frost-resisting. The requirements are fulfilled when using composite materials (created on synthetic fibro basis).

Figure 4. Formwork construction

Experiments in order to create concrete shell production technology process were made in 2013 in the Riga Technical University in laboratory in order to create an effective shell production technology. Was produced a formwork with variable geometry by gravity. Formwork construction: veneer 1000×1000×9 mm, rubber sheet 1000×1000 mm, height of frame borders is 9 mm see figure 4. Tasks of laboratory experiments: production and achievement of different kind shells, including dome-shaped constructions, clearing up the shell production technological features and technological process advantages, effectiveness, a visual attraction and advantages of products. In the reported work, on the flat surface mould was imposed and smoothed down (forming a thin layer) glass fiberconcrete mix.
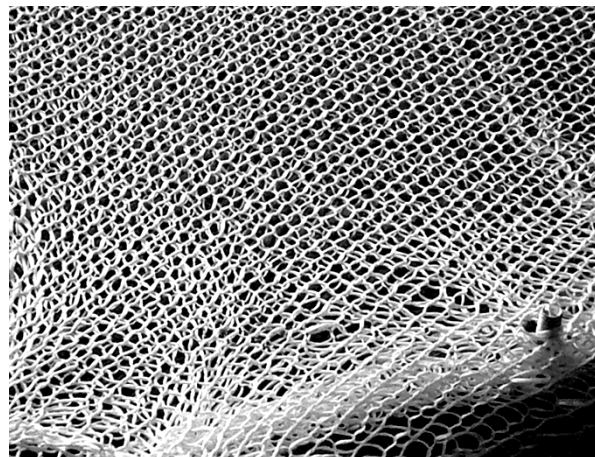

Figure 5. Knitted fabric for concrete shell reinforcement

After concrete mould was by forming a moderate curvature shell. As concrete was hardened mould was kept constant value. Then a mould was out and shell was demolded.

A fresh concrete shell done by such speed, so that there won't appear technological cracks on shell surface. For increasing limits of deformation of a fresh concrete there are used special supplements in its mix, for instance, various desired water-soluble polymers or waterproof polymer emulsions. There are also used different kinds of material fibro reinforcement in concrete mix, which after concrete hardening improves its constructive features.

The shell's should be reinforced:

One solution can be short AR glass fibers homogeneously distributed in the concrete see figure 3. Another option is use of knitted AR glass fibre fabrics (fulfilled by concrete) see figure 4 and placed distance one to another the thickness of the structure.

Knitted fabric reinforced concrete matrix composites have grew rapidly during recent years. Such materials are exhibiting attractive mechanical properties including high energy absorption and impact resistance. Shell production: mould is laid a concrete or fibro concrete mix on prepared formwork flat surface and it is smoothed see figure 5 after molding process should be finished before starting concrete mix hardening. Not allowing the concrete mix hardening start, the formwork surface is curved till defined shell dimensions. A fresh concrete shell is done by such speed, when tension pressure in a fresh concrete mix can be relaxed so that mix tension deformations wouldn't increase its limits of deformations, so that there won't appear technological cracks on shell surface. For increasing limits of deformation of a fresh concrete there are used special supplements in its mix, for instance, various desired water-soluble polymers or waterproof polymer emulsions.

Yarns loops are arranged in structures. In woven fabric, threads traditionally are running horizontally and vertically. Contrary, in the case of knitted fabric, strands are forming loops see figure 6.

Figure 7. Formwork flat surface and it is smoothed

A knitted fabric is highly deformable in all directions. Depending on fibers are used, some of them are more deformable than others. The reason is – yarns are not making any straight line anywhere in the knitted fabric. Is easily to recognize possible motions in the fabric – threads sliding, loops twisting, bending and stretching leading to technological advantage – excellent deformability, shape forming ability and flexibility, which allows it to be used in any complex shape mould without folds.

Before concrete binding, mould with variable geometry (moderate curvature shells were elaborated see figure 7). After the concrete is coming hard out and shell is demolding. Experimentally fabricated and investigated shells were curved round plates with the thickness 9 mm. The horizontal plane created shells dimensions were 900 mm diameter.

Matured short glass fiber concrete shell is shown in figure 8. Then the formwork is taken out see figure 9. Formwork maybe not taken out, it is kept together with the shell and in future it serves like damp course and exterior finishing layer.

Figure 6. Concrete shell fabrication reinforced by three layers of knitted glass fiber fabric

Figure 8. Short glass fiber concrete shell

III RESULTS AND DISCUSSION

Recently, become relevant methods of forming prefabricated thin-shell concrete structures that can are allowed to deflect into naturally occurring funicular geometries, producing molds for lightweight compression vaults and stiff double curvature wall panels. The reduction in material, can be as high as 200-300 percent. Variable geometry formwork that can be formed through the simple act of inverting the tension curves obtained by a loaded material sheet. In this instance the symmetrical inversion of tension and compression geometries is perfectly matched by the symmetrically opposite resistance capacities of the materials involved, i.e. rubber or fabric in tension and the concrete in compression. These simply constructed structural components formed with flat textile sheets are compatible with flat sheet reinforcing such as knitted glass fiber textiles and AR glass fiber cloth.

Figure 9. Concrete shell geometry

Economical and practical effectivity for a wide invention of progressive constructions with a modern design at new construction building principles where as formwork are used variable systems composed of flexible materials. Existing views about techniques and technology of constructions building from monolith concrete mostly is based on plane construction building experience.

Existing views about techniques and technology of constructions building from monolith concrete mostly is based on plane construction building experience. Provide an ideal concrete solution for formwork without any restricting factors connected to complicated geometry. Nowadays systems from flexible materials are developing and improving, new technologies are created. The technology has got a big potential followed by modern events in concrete production and development.

The offered new technology formwork with changeable form allow using them effectively as complete flexible and adjustable formwork systems, in order to create geometrically complicated architecture forms, at the same time not losing the strength indexes of constructed surfaces. New technology is foreseen for plain structures, that allows to create and have different shells, including domelike structures, in one direction curved shell, in two directions curved shell etc., for example, for building roof covering structures. Variable gravity mould use is an approach with a set of advantages among thin wall structural element fabrication technologies.

During the experiments were made shell two variants shells reinforcement: shell is reinforced by uniformly distributed short glass fibers and shell is reinforced by weft knitted glass fiber textiles.

The use of fiber-reinforced concrete in structures with high physical-mechanical characteristics makes it possible to reduce the weight and costs of the structures, to simplify the technology of their production, to reduce or completely eliminate the reinforcement labor, at the same time increasing reliability and durability.

IV CONCLUSION

The results of laboratory experiments show and proved that the technology can be used for fibro concrete shell production and construction. Formworks with variable geometry provide an ideal concrete solution without any restricting factors connected to complicated geometry. Shells reinforced by chopped glass fibre bundles as well as by knitted glass fibre fabric were fabricated.

Formwork with variable geometry give new opportunities in modern architecture, which is impossible using traditional formwork and allows to speak about its advantages, emphasizing the most effective usage sphere, small weight, possibility of multiple usage affects positively its usage in building sphere. It also allows engineers and architects a freedom to explore the shaping of concrete that has been elusive due to the complexities of the formwork.

V ACKNOWLEDGMENTS

VI REFERENCES

[1] Lusis V. Production Technology for Concrete Shells Using Pneumatic Formwork with Variable Elevation// Sc. Proceeding of Riga Technical University, Construction science, 2011, P. 35-39.

[2] Krasnikovs A., Lusis V., Lapsa V., Zaleskis J., Zaharevskis V. and Machanovskis E., Concrete shells reinforced by glass fibers, Sc. Proceedings of Riga Technical University, Transport and engineering, 6, 2012, 6.p. (submitted 2012).

[3] Lusis V., Harjkova G., Machanovskis A., Kononova O., Krasnikovs A., Technology for concrete shells fabrication reinforced by glass fibers. „Civil engineering `13", Jelgava, Conference proceedings. 2013, p. 5.

[4] Lapsa V., Krasnikovs A., Lusis V. Betona plānsieniņu čaulu veidošanas tehnoloģiskais process, Latvian invention patent Nr.14308, (21.01.2011).

Fiberconcrete with Non-Homogeneous Fibers Distribution

Vitalijs Lusis[1], Andrejs Krasnikovs[2]
1 - Riga Technical University, Concrete mechanics laboratory
2 - Riga Technical University, Institute of Mechanics and Concrete mechanics laboratory
Address: 1 Kalku Street, Riga, LV-1658, Latvia

Abstract. **In this research fiber reinforced concrete prisms with layers of non-homogeneous distribution of fibers inside them were elaborated. Fiber reinforced concrete is important material for load bearing structural elements. Traditionally fibers are homogeneously dispersed in a concrete. At the same time in many situations fiber reinforced concrete with homogeneously dispersed fibers is not optimal (majority of added fibers are not participating in load bearing process). It is possible to create constructions with non-homogeneous distribution of fibers in them in different ways. Present research is devoted to one of them. In the present research three different types of layered prisms with the same amount of fibers in them were experimentally produced (of this research prisms of non-homogeneous fiber reinforced concrete with dimensions 100×100×400 mm were designed. and prisms with homogeneously dispersed fibers were produced for reference as well). Prisms were tested under four point bending conditions till crack opening in each prism reached 6 mm. During the testing vertical deflection at the center of a prism and crack opening were fixed by the linear displacements transducers in real time.**

Keywords – **fiberconcrete, non-homogeneous fiber reinforced concrete, layered fibers' distribution, steel fibers.**

I INTRODUCTION

Fiber reinforced concrete is important material for load bearing structural elements. Conventional steel fibre reinforced concrete (SFRC) is fabricated by mixing steel fibres with a concrete mix. The volume fraction of fibres is limited to less than two percent. Although SFRC is a promising material, its flexural strength is yet to be exploited. Since ultimate stress required to fail fibre reinforced concrete (FRC) in flexure and tension is governed by fibre volume fraction, aspect ratio, fibre-matrix / bond strength and fibre distribution, increase in failure stresses can be achieved by increasing these parameters. In the present publication be investigated of fibers distribution and their spatial orientations in structural element volume [2;3;4].

In this research fiber reinforced concrete prisms with layers of non-homogeneous distribution of fibers inside them were elaborated. Present research is devoted to one of them.

II MATERIALS AND METHODS

In the framework of this research prisms of non-homogeneous fiber reinforced concrete with dimensions 100×100×400 mm were designed. The technology of specimen preparation is described in the Latvian invention patent [5]. Three identical prisms of each type of non-homogeneous fiber reinforced concrete were prepared. Prisms were tested under four point bending conditions using Controls Automax 5 loading machine (Figure 1).

Fig.1. Concrete compression machine Controls Automax 5

All specimens with fibers are HPFRC with steel-hooked fibers Dramix RC-80/30-BP with a length of 30 mm and a diameter of 0.38 mm, for a fiber aspect ratio of 80, and tensile strength 1020 MPa. These fibers are commercially available and manufactured by N.V. Bekaert S.A., Belgium (Figure 2).
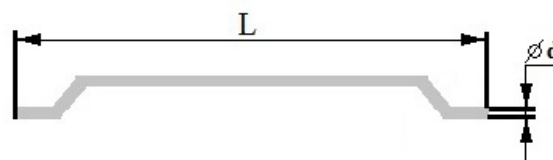

Fig.2. Steel fibers with curved ends E – anchor zone, mm; L – length, 30mm; d – diameter of 0.38 mm

Mechanical properties of fibre concrete

Verification of mechanical properties was performed in Experimental Concrete Mechanical laboratory (CML) according to standard 4-point bending test method. Test samples were tested after 28 days. Resistance strain gauges were placed on test samples. Load was applied in 0,25 kN steps for period of 60s.
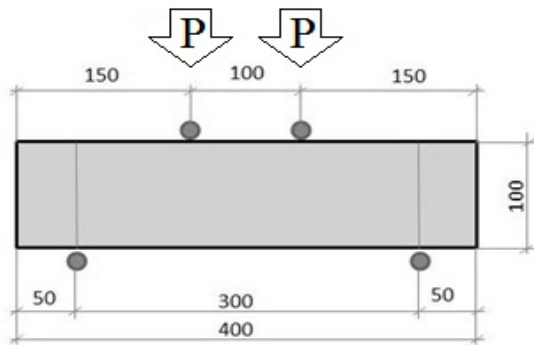

Fig.3. Tested under four point bending conditions

Specimens' preparation

Groups of specimens are presented in the Table 1. Group 1 consists of fiber reinforced concrete with fibers homogeneously dispersed in the sample volume.

TABLE 1.

Group Nr.	Distribution and concentration of fibers in specimens
Group Nr.1.	Fibers mixed in concrete mixer and homogeneously dispersed in the specimen (classical method)
Group Nr.2.	1. 25mm of concrete – 1/2 of the total amount of fibers (60 kg/m^3) were pressed into concrete; 2. 25mm of concrete – 1/2 of the total amount of fibers (60 kg/m^3) were pressed into concrete; 3. 50mm of concrete without fibers
Group Nr.3.	1. 25 mm of concrete – 1/3 of the total amount of fibers (60 kg/m^3) were pressed into concrete; 2. 25 mm of concrete – 1/3 of the total amount of fibers (60 kg/m^3) were pressed into concrete; 3. 25mm of concrete – 1/3 of the total amount of fibers (60 kg/m^3) were pressed into concrete; 4. 25mm of concrete without fibers
Group Nr.4.	1. 55 mm of concrete – fibers (60 kg/m^3) were pressed into concrete; 2. 45 mm of concrete without fibers
Group Nr.5.	1. 25 mm of concrete – 2/3 of the total amount of fibers (60 kg/m^3) were pressed into concrete; 2. 75mm of concrete – 1/3 of the total amount of fibers (60 kg/m^3) were pressed into concrete

These prisms were used as reference. As it is seen in Table 1, while the total amount of fibers is identical for all four groups of specimens, the difference is in their distribution. For specimens of Groups 2, 3 and 4 fibers are distributed in different layers with various concentration and distribution. These specimens can be defined as layered prisms with oriented distribution of fibers.
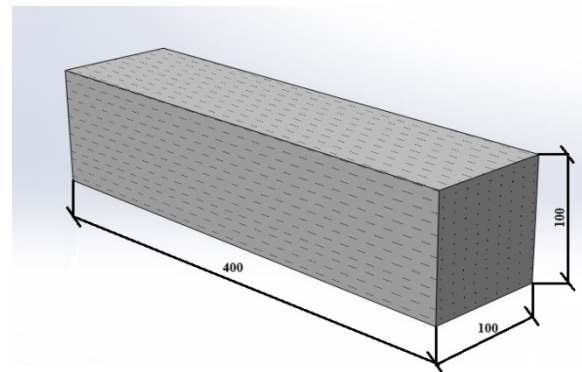
Fig. 4a. Group 1 distribution of fibers in specimens

Fibers were added to the mix during the concrete mixing process and moulds were filled by such fiberconcrete for specimens representing Group 1 (Figure 4a).
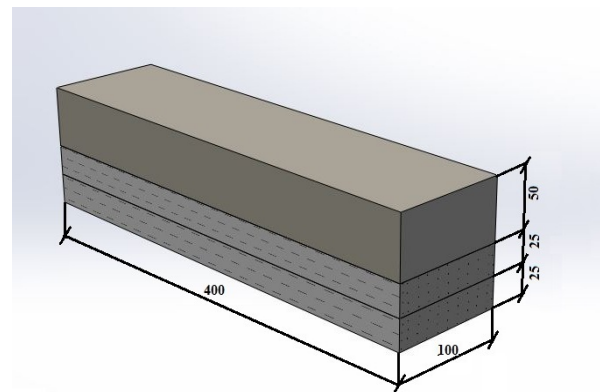
Fig. 4b. Group 2 distribution of fibers in specimens

Then fibers were uniformly scattered on the concrete surface in the mould and were pressed into concrete (Figure 4b, 4c, 4d and 4e). For the specimen from Group 2 mould was filled with 25 mm layer of concrete mix, then fibers (1/2 of the total amount of fibers 60 kg/m^3) were uniformly scattered on the concrete surface in the mould and were pressed into concrete (2 layer) and layer 50 mm of concrete mix, non fibers (Figure 4b).

Fig. 4c. Group 3 distribution of fibers in specimens

For the specimens from Groups 2, 3, 4 and 5 moulds were gradually filled with the concrete mix according to the description of each group.

Fibers were pressed by a steel grid into the concrete in the full length of the prism according to the Latvian invention patent LV14257 technology [5].

For the specimen from Group 3 mould was filled with 25 mm layer of concrete mix, then fibers (1/3 of the total amount of fibers 60 kg/m³) were uniformly scattered on the concrete surface in the mould and were pressed into concrete (3 layer) and layer 25 mm of concrete mix, non fibers (Figure 4c).

Fig. 4d. Group 4 distribution of fibers in specimens

For the specimen from Group 4 mould was filled with concrete mix up to 55 mm and the rest of all fibers (60 kg/m³) were uniformly scattered on the concrete surface in the mould and were pressed into concrete. Fibers were pressed by a steel grid. Finally, mould was filled with concrete mix up to 100 mm (Figure 4d).
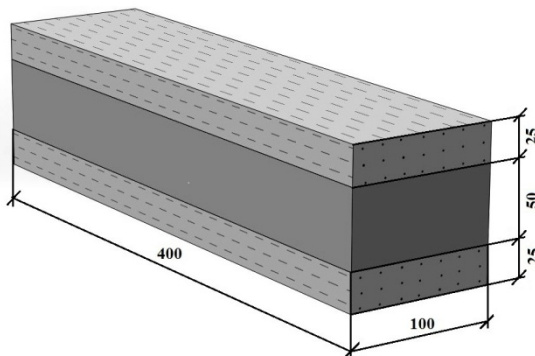
Fig. 4e. Group 5 distribution of fibers in specimens

For the specimen from Group 5 mould was filled with 25 mm layer of concrete mix, then fibers (2/3 of the total amount of fibers 60 kg/m³) were uniformly scattered on the concrete surface in the mould and were pressed into concrete, further layer 75 mm of concrete mix, non fibers and fibers (1/3 of the total am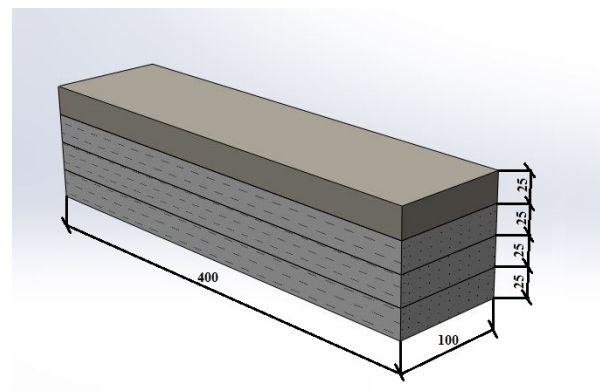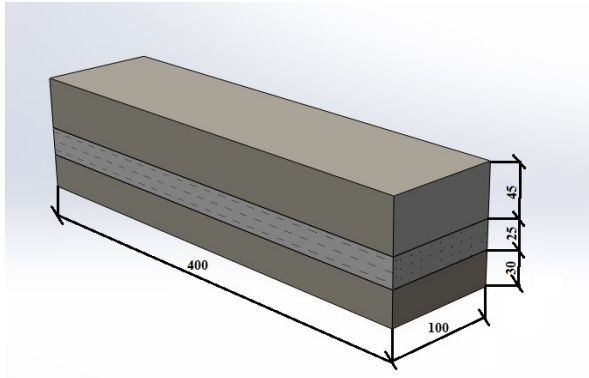ount of fibers 60 kg/m³) were uniformly scattered on the concrete surface in the mould and were pressed into concrete (Figure 4e).

Density of fiber reinforced concrete ranges from 2370 to 2430 kg/m³ (2400 kg/m³ in average) and according to the concrete compressive strength testing results it corresponds to the compressive strength class C70/85. All specimens, namely, fiber reinforced concrete prisms were tested under four point bending conditions using Controls Automax 5 testing machine (Figure 5).
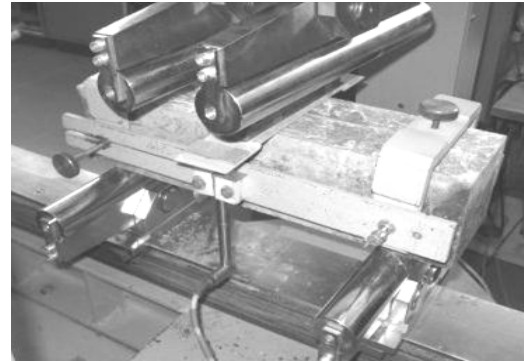
Fig. 5.Testing device with fiber reinforced concrete prism inside it

During the testing vertical deflection at the centre of a prism and crack opening were fixed by the linear displacements transducers in real time. Load bearing chart for the specimen is given in Figure 3. Sensors were connected throw the data acquisition unit to computer where the obtained data were recorded and were available after experiments.

III RESULTS AND DISCUSSION

Specimens were tested under four point bending conditions till the macro crack opening was reached 6 mm.
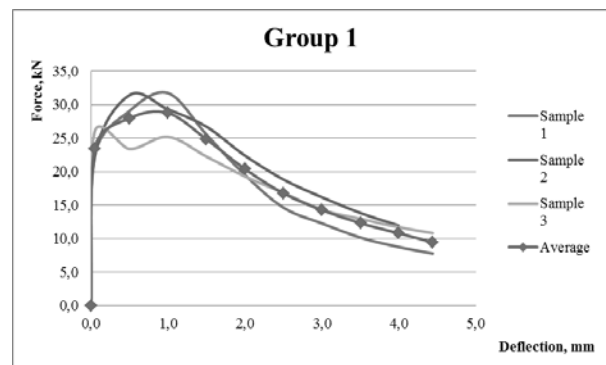
Figure 6a. Load - vertical deflection graphs for specimens in Group Nr.1.

Load bearing - vertical deflection at the centre of each prism graphs for the specimens of Group 1 are given in Figure 6a.

The diagram shows the experimental curve of each specimen as well as the average value curve. Three stages are seen in each curve; first of them is linear elastic deflection (corresponds to deflection under 0,01mm). In this stage fiber reinforced concrete prisms become deformed without visible crack openings.
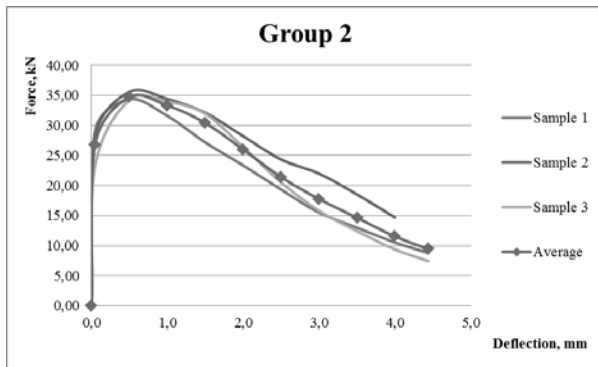
Figure 6b. Load - vertical deflection graphs for specimens in Group Nr.2

Figure 6c. Load - vertical deflection graphs for specimens in Group Nr.3

Fibers in the concrete do not bear significant load. The next stage begins with deviation of curves from the straight line and terminates reaching the maximum value on curve (with deflection of prisms 0,75mm – 1mm).

Figure 6d. Load - vertical deflection graphs for specimens in Group Nr.4

In this stage concrete micro cracks accumulate and grow forming macro crack network. The macro cracks are formed perpendicularly to the longitudinal axis of prism. Density of macro crack network depends on specimen's geometry, size of fibers and their amount. Fibers traversing macro cracks begin to bear load, while cracks are still invisible on the outer surface of specimen.

Figure 6e. Load - vertical deflection graphs for specimens in Group Nr.5

Crack with the lowest load carrying capacity (one with the lower amount of fibers traversing it or fibers located and oriented in a less optimal way) starts to open. It proceeds the following way: fibers bearing load detach from the concrete and start pulling out from one or both ends. Individual load carrying capacity of fiber depends on its distribution towards the crack plane and how far it is extracted.

Experimental observation of fiber pull-out micromechanics [1] showed that the maximum load carrying capacity of fiber depends on the distribution of fiber towards direction of extraction force and how much the fiber has been extracted. The third stage is characterised by the decline of total load carrying capacity of fiber. The capacity decreases proportionally to the size of crack opening. Load bearing - vertical deflection at the center of prism for the specimens of Groups 2, 3 4 and 5 are given in Figures 6b-6e.

Figure 7. Load - vertical deflection graphs for specimens in comparison of average of all sample groups

Diagrams in Figures 6a-6e show the average experimental curves from three specimens. Experimental (average) curves for all five groups are given in Figure 7. As it can be observed, Group 2 reaches the highest load carrying capacity during crack opening stage due to the highest concentration of fibers compared to other groups in the lower part of the prism which bears the maximum tensile load (see Figure 8).
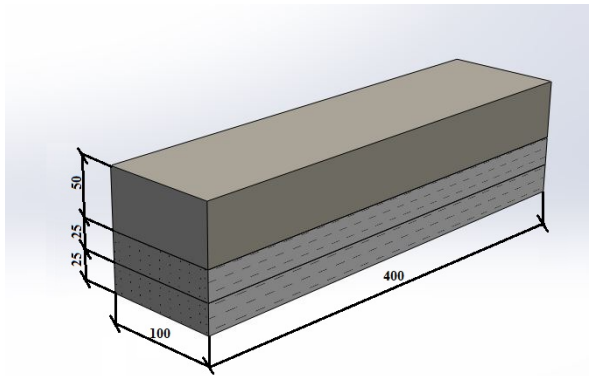
Figure 8.Group 2 distribution of fibers in specimens

As it can be observed, Group 1 (reference specimens) reaches lower average load carrying capacity in the third stage (macro cracks) compared to the specimens with non-homogeneous distribution of fibers. Certain similar tendencies can be observed among the diagrams of average results of specimens – the maximal load carrying capacity is reached with deflection of prisms 0,75 mm – 1 mm, which correlates with the crack opening size.

IV CONCLUSION

The weight reduction of concrete floor structures has recently gained importance in regards to the increased demands on construction materials savings and on further savings related to transportation. The motivation is not only economical but also environmental influenced sustainable development which is becoming more important. In this research fiber reinforced concrete with the concentration of steel fibers 60 kg/m^3 were tested. Fibers were incorporated into concrete specimens in four different ways. Specimens were tested under four point bending conditions observing their load carrying capacity in the macro cracking stage. In specimens of Group 1 fibers were dispersed in all the specimen volume, in specimens of Groups 2, 3, 4 and 5 they were distributed in various layers with specified amount of fibers in each of them. According to the testing results, specimens of Group 2 reached the highest load carrying capacity during crack opening stage as they had the highest concentration of fibers in the part of prisms experiencing maximum tensile load they exhibit improved strength and ductility related properties compared other Group samples. Specimens of Group 1 showed lower average load carrying capacity during crack forming stage compared to the specimens with non-homogeneous distribution of fibers.

VI REFERENCES

[1] Krasnikovs A., Kononova O., Khabaz A., Machanovsky E. and Machanovsky A. (2012) Post-Cracking Behavior of High Strength (Nano Level Designed) Fiber Concrete Prediction and Validation. CD-Proceedings of 4th International Symposium on Nanotechnology in Construction, 20-22 May 2012, Crete, Greece, 6 p.

[2] Krasnikovs A., Kononova O. strength prediction for concrete reinforced by different length and shape short steel fibers// Sc. Proceedings of Riga Technical University. Transport and Engineering, 6, vol.31, p.89-93, 2009.

[3] Lusis V., Galushchaka A., Machanovskis A., Kononova O., Krasnikovs A., Strength of layered fiberconcrete. Civilengineering 13 Conference proceedings. 2013, p. 5.

[4] Li V. C. (2003) On Engineered Cementitious Composites a Revue of the Material an it's Applications. Journal of Advanced Concrete Technology, Vol.1, No3, p. 215-230.

[5] Lapsa V., Krasnikovs A., Strauts K., (2011.20.04) „Fiberconcrete Non-Homogeneous Structure Element Building Technology Process and Equipment", Latvian invention patent LV14257.

Influence of Heat Treatment and the Coefficient of Friction on the Volume of Metal Removed During Grinding Steel 35

Igor Nikiforov, Pavel Maltsev

Pskov state university, Faculty of Mechanical and machine building, Departament of Technology of machinebuilding. Address: Lenin square 2, Pskov, 180000, Russian Federation

Abstract. The role of external friction and chip contraction during microcutting by abrasive grain is showed. The method for determining the relative change in the coefficient of friction during grinding is proposed. The hypothesis about the influence of physical and mechanical properties and microstructure of steel 35 on the volume removes metal through the change in the coefficient of sliding friction of the chip by face of the abrasive grain is experimentally proved.

Keywords – abrasive grain, the front surface, depth of cut, heat treatment, microstructure, hardness, coefficient of friction

I INTRODUCTION

The effect of friction in the cutting process on the formation of shavings is essential, especially when it is a question of separation of thin shavings from the surface of the plastic materials. This is the case in any type of abrading, and particularly, in grinding. The coefficient of friction makes the greatest influence on the formation of shavings on the front surface of the instrument in the vicinity of the cutting edge.

In [1, pp. 218-220] the mechanism of the effect of coefficient of friction on the position of the cutting edge line during a single hyperboloid-shaped abrasive grain microcutting is shown. Spatial configuration of the edges determines the form and the actual area of the front surface of the grain, and, consequently, the geometric parameters of the shavings, which ultimately affects the amount of removed metal and process performance.

The volume of shavings, removed by a single grain, considering the processes of plastic deformation, can be calculated using formulas obtained by the authors in [1, pp. 218-220, 2, pp. 168-172]. Based on regression analysis, presented dependencies can be significantly simplified, if the particular cases are considered, that is if to consider them in the specific conditions of processing and take the most important parameters as variables. For example, the empirical dependence of the effect of the coefficient of friction (μ) and shrinkage coefficient (η) on the volume of shavings (V) can be represented as:

$$V = 0{,}074 + \frac{0{,}033}{\mu} - \frac{0{,}253}{\eta} \qquad (1)$$

The expression (1) was obtained by non-linear regression for the following initial parameters: circle diameter – 250 mm; set depth of cut – 0,010 mm; angle at the top of the abrasive grain – 83…143°; top's radius – 7…50 μ m; grinding wheel peripheral speed – 35,5 m/s; traverse of table – 10 m/min.

Graph of the dependence of amount of shavings, removed by a single abrasive grain, on the coefficient of friction at different chip shrinkage is shown in Figure 1. The graph shows that if the shavings' shrinkage coefficient is small, and the coefficient of friction, on the contrary, takes large values, the shavings will not be removed (V<0 – area of plastic deformation, without separation of metal).

As part of the studies, we hypothesize that the physical and mechanical properties of the processed material and its microstructure effect on the amount of removed shavings, and this influence happens through the corresponding change in the coefficient of friction of shavings on the front surface of the abrasive grain. In other words, the coefficient of friction in the area of frictional contact can be further used to evaluate the performance and workability of grinded plastic material and to predict the output of processing parameters.
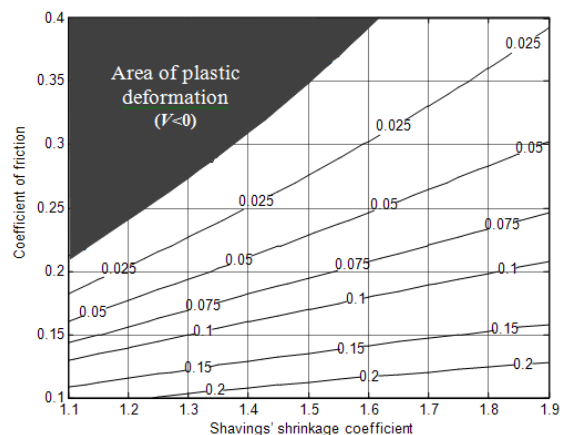

Fig. 1. Level lines of dependence of volume of shavings V (mm³), removed by the single abrasive grain on coefficient of friction μ and shavings' shrinkage coefficient η

II Materials and methods

To confirm or refute this hypothesis, samples (Fig. 2) specially made of structural carbon steel 35 (GOST 1050-88) were treated on surface grinders model 3G71.
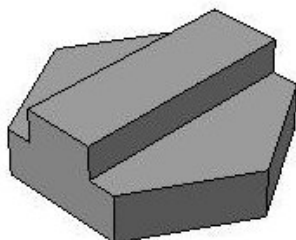

Fig. 2. The appearance of the sample

The chemical composition of the sample material was confirmed by the photoelectric spectral method in accordance with GOST 18895-97 for atomic emission spectrometer DFS-500 (Russia) and is presented in Table 1.

Initial experimental data coincide with the data for which the dependence (1) was obtained; extra information: spindle speed - 2710 r/min, the grinding wheel grade 1 250x20x76 WA F30 L6V 50 2 aluminum oxide white; height of circle - 20 mm.

Prior to testing, samples (5 pcs.) were exposed to various types of heat treatment, except one of them (№ 1), which was a standard - a special heat treatment wasn't applied (normalized rolled metal from the factory). The rectangular surface, being grinded along along the longer side of it, has nominal dimensions of 15×40 mm (600 mm2 area) and its width was less than the width of the circle (15<20). More detailed description of the initial samples is presented in Table 2.

TABLE 1

CHEMICAL COMPOSITION OF THE SAMPLE MATERIAL, %

Carbon, C	Chromium, Cr	Manganese, Mn	Silicon, Si	Sulfur, S	Phosphorus, P
0,35	0,07	0,68	0,28	0,025	0,02

TABLE 2

CHARACTERISTICS OF THE INITIAL SAMPLES

Parameters	Units	Sample number				
		1	2	3	4	5
The surface area	mm^2	592,0	624,1	600,5	594,0	611,5
Type of heat treatment, cooling medium	–	None	850ºC quenching, 600ºC water tempering	850ºC quenching, 400ºC water tempering	850ºC quenching, 200ºC water tempering	1100ºC diffusion annealing, furnace
Hardness	HB	151	226	≈272 (29 HRC$_3$)	≈432 (46 HRC$_3$)	108

Samples were alternately installed and fixed on the magnetic plate. With the limb of the machine cutting depth was set to 10 mm, and then a single power stroke of the table was made (only in one direction). After that the blank was removed from the device, shavings and sludge was carefully swept out, and the mass of removed metal sludge was measured by analytical balance AXIS 200 (Poland) accurate within 0.0001 gram. To reduce the effect of thermal deformations machine was preheated for about an hour and was not shut down during the experiment.

III Results and discussion

The experiments were performed with a 9-fold replicates. Evaluation of homogeneity of dispersion was performed by dint of Cochran's Q test, for which screening of gross values was held and repeated experiments were performed. As a result, the range of values didn't exceed ±17%, and about half of them (≈53%) laid in the ±5% range. Table value of quantile of Cochran's distribution for significance level α =0,05 (with a 9-fold repetition and five experiments) – 0,4387, which exceeds the experimental value – 0,3298; therefore, the dispersions are homogeneous, and the range of these values are within normal limits.

Results of experimental studies are represented in Table 3. The volume of removed metal was calculated by the average weight and the given density of steel sample ($\rho = 7826$ kg/m3), and the actual depth of cut – as the ratio of removed metal to the area of the finished surface. Parameter of roughness Ra was measured by profilograph-profilometer model №250 (Russia).

After performed tests, in order to analyze the microstructure, thin sections of samples were additionally prepared, using polishing and etching (3% solution of nitric acid in alcohol). Metallographic studies were performed on a microscope model Axiovert 40 MAT (Germany). Shavings and sludge, collected after grinding of each sample, were also examined by it.

TABLE 3

Parameters	Units	Sample number				
		1	2	3	4	5
Mass of removed metal	g	0,0407	0,0452	0,0405	0,0389	0,0456
Volume of removed metal	mm^3	5,203	5,776	5,180	4,975	5,822
Actual depth of cut	μ m	8,8	9,3	8,6	8,4	9,5
Roughness	Ra	0,388	0,332	0,306	0,306	0,325

Phase composition, microstructure of thin sections and photos of relevant shavings are represented in Table 4.

Table 3 shows that the highest metal removal occurs when grinding of samples number 5 – after diffusion annealing, number 2 – after quenching and tempering, and number 1 – the standard without heat treatment, i.e. when the hardness and strength of the material is low. At the same time shavings are wide and have strongly marked traces of plastic deformation (Fig. 3a) and small number of nodules is present in the sludge (Fig. 3 a, b) – as a result of melting of the metal due to high local temperatures. Sample number 2 has the largest grains (Table 3) of the samples subjected to quenching (№ № 2, 3, 4). And the samples number 1 and number 5 (without heat treatment and after diffusion annealing) have a coarse-grained structure composed of pearlite (dark grains) and ferrite (white grains). That is, if the grain size is more, processing of material is better. However, the roughness parameter Ra is higher because of the development of plastic deformation and the presence of bulks at the sides of grinding marks.

a)   b)
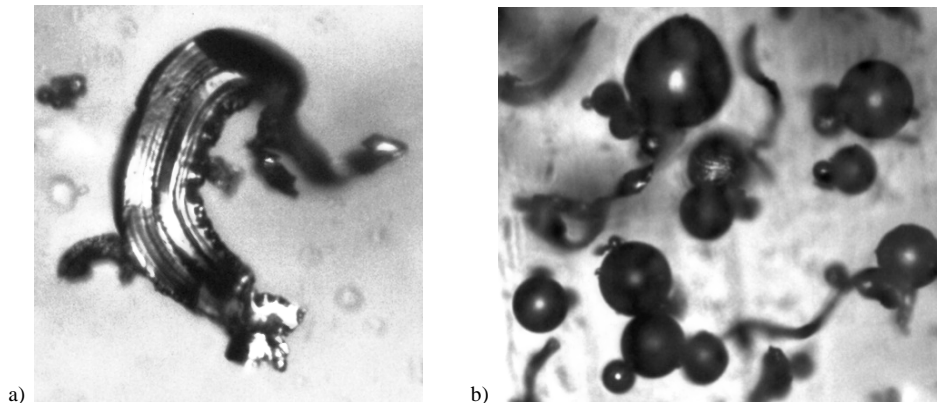
Fig. 3. Plastically deformed shavings, removed by a single abrasive grain (a), nodular melted metal (b)

While grinding the quenched samples № № 2, 3 and 4 the growth of a amount of fused metal with increasing strength is notably traced, i.e. with decreasing annealing temperature. If while the grinding of the sample number 2 nodules are small and its amount is small (see Table 4), then in the sample number 3 its number and size increases. In the most solid and durable test sample number 4, which has martensite in its structure (after a low tempering) nodules are seen in great amount, and they are much larger in diameter. This indicates a high temperature in the cutting zone and intense nature of the grinding process, at the same time the removal of the metal is the smallest, and the elastic deformation is the largest (when the depth of 10 μ m was set 8.4 μ m). But roughness parameter Ra of the samples number 3 and number 4 is smaller, the width of the shavings is small, plastic deformation is less notable.

Figure 4 shows the individual abrasive grains of white fused alumina, and it is even visually seen from it that top's radius varies over a wide range, depending on the orientation of their potential in the volume of circle. Therefore the shape of shavings, the amount of removed metal, the temperature in the cutting zone and other consequences of exposure to a large extent will depend not only on the properties of the material, but also on the geometric parameters of the tops of the abrasive grains.
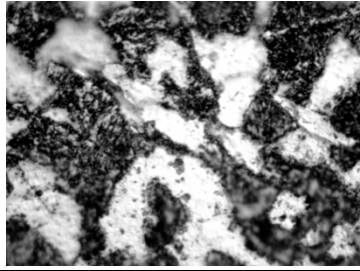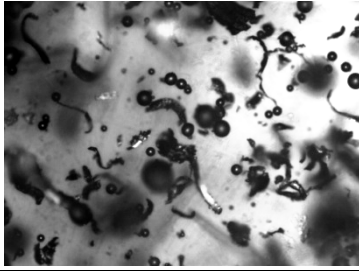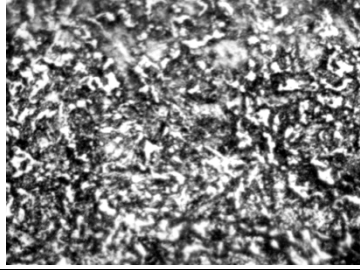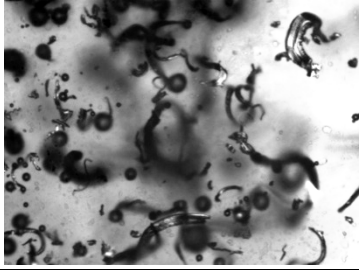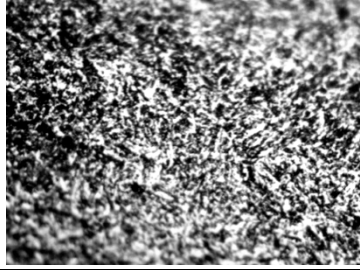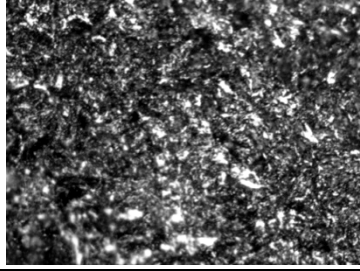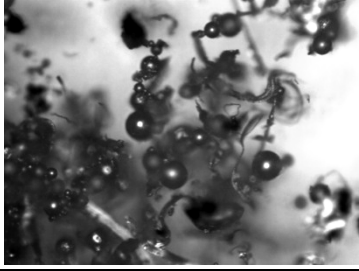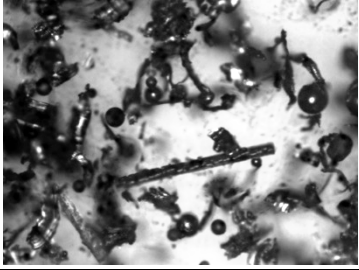
To estimate the workability of steels and alloys with different structure, in our opinion, Hall-Petch law can be used [3, p. 117]: according to it, grain size (we have in mind that it is not abrasive grain, but the grain in the microstructure of the crystalline body – crystallite) and a material yield strength are related by the following relationship:

$$\sigma_T = \sigma_0 + \frac{H}{\sqrt{d}}, \qquad (2)$$

where σ_T – material yield strength; σ_0 – resistance to deformation in single crystals; H – Hall-Petch coefficient, characterizing the contribution of grain boundaries to hardening; d – grain's size (of crystallite). Value of coefficient H for ferrite-perlite steels which steel 35 belongs to is within 0,57…0,73 MPa $\times$m$^{1/2}$, and for steels with austenitic structure – 0,2…0,5 MPa $\times$m$^{1/2}$ [4, p. 112].

TABLE 4
THE MICROSTRUCTURE OF THE SAMPLES AND PHOTOS OF SHAVINGS

Sample number	Basic composition of the phases	Microstructure (1000X)	Shavings (200X)
1	Pearlite + ferrite		
2	Sorbitol of tempering		
3	Troost of tempering		
4	Martensite of tempering		
5	Pearlite + ferrite		
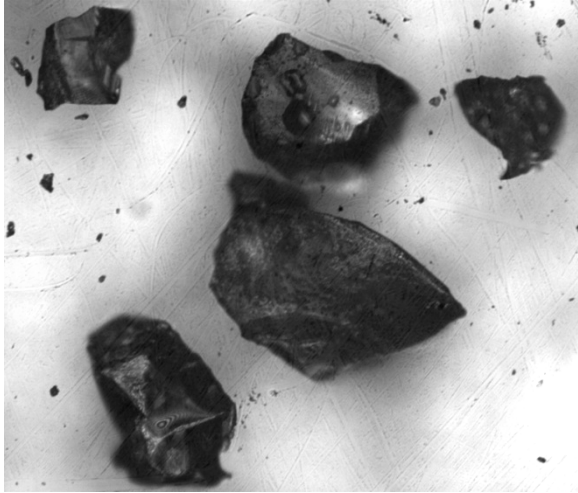
Fig. 4. The individual grains from the surface of the grinding wheel, tool material - white fused alumina

The smaller the grain size, the higher the resistance, and one of its characteristics is yield stress σ_T, and the worse the material processing. But the sample number 1 has larger grains than the material number 2, although it is processing worse. Based on this, we can conclude that the Hall-Petch coefficient takes different values for hardened and unhardened steels.

As stated above, the amount of removed shavings and processes of plastic deformation are significantly affected by the friction in the area of frictional contact of the abrasive grain and shavings. It is known that the magnitude of the friction force is composed of an adhesive (molecular) and mechanical (deformation) components:

$$\mu = \mu_a + \mu_{\text{м}} \qquad (3)$$

The problem of determining the magnitude of the friction force and the coefficient of friction in the zone of frictional interaction in grinding - one of the most complex problems, and today researchers don't finally solve it. Transposing the known methods, techniques and tools to measure the above parameters to grinding process, when there is a short-term high-speed interaction of randomly distributed grains with the processing surface, is impossible in most cases, or is associated with some difficulties. Calculations and measurements errors are too great, and often do not describe the real picture of the processes and phenomena. It is especially difficult to calculate the adhesive component, so it is usually determined experimentally.

But it isn't necessarily to determine the value of the coefficient of friction in absolute terms for a comparative estimate of the impact of friction on the grinding of the samples - in some cases it is enough to know the relative change in the coefficient of friction. We propose a relatively simple method for determining the change in the adhesive component of friction for grinding various samples with respect to the standard sample, and the essence of it is as follows. Initially we believe that time (t_0) to a stop the wheel (when there is no contact with the blank) after

turning off the motor is inversely proportional to the friction torque (T_C) in all inertial rotating interacting parts, including circle, spindle, pulleys, belts, bearings, etc. That is, we can write the following expression:

$$t_0 = \frac{K}{T_C}, \qquad (4)$$

where K – coefficient, which is constant for the given kind of equipment (for this, machine must be preliminary warmed up with a rotating spindle in order to establish the heat balance).

The value of the constant coefficient can be found from (4):

$$K = t_0 T_C. \qquad (5)$$

Stop time of the grinding wheel is determined experimentally by an electronic timer.

If the standard sample number 1 is pressed against the grinding wheel with a force, then stop time will be less, as there will be additional friction torque (T_1), generated by the friction force:

$$t_1 = \frac{K}{T_C + T_1}, \qquad (6)$$

where T_1 – averaged component of the friction torque of the grinding wheel on the surface of the blank during grinding of the sample number 1.

Substituting (5) into (6) we get:

$$t_1 = \frac{t_0 T_C}{T_C + T_1}. \qquad (7)$$

Hence we express the component of friction torque:

$$T_1 = \frac{t_0 - t_1}{t_1} \times T_C. \qquad (8)$$

For sample number 2, similarly, we have:

$$T_2 = \frac{t_0 - t_2}{t_2} \times T_C, \qquad (9)$$

where t_2 – respectively, time to a stop of the wheel, which is in contact with the sample number 2.

The ratio of the moments of the components of friction torque during grinding of the samples number 2 and number 1 can be determined by dividing (9) by (8). After transformations, we obtain:

$$\frac{T_2}{T_1} = \frac{(t_0 - t_2) t_1}{(t_0 - t_1) t_2}. \qquad (10)$$

The same expression can be obtained by applying the formulas of physics for uniformly decelerated rotational motion when the friction torque is proportional to angular acceleration, which is negative in this case.

As we can see, the friction doesn't present in the mechanical parts in (10). To reduce the mechanical components and to establish the equal conditions of frictional interaction, it is necessary to carry out some

of the rules. Firstly, the pressing force to the surface of the blank to the circle should be the same. Secondly, you must turn off the table, and by vertical movement of the grinding wheel (plunge grinding) make equal contact area of the circle and the blank, which should no longer be changed in the subsequent vertical pitch. Thirdly, stop time of spindle should begin immediately after the termination of massive crash sparks from the surface of the sample (for the initial sparks additional vertical pitch of circle performed).

Subject to these conditions expression of ratio of adhesive component of friction with a high degree of accuracy is equal to the ratio of adhesive components of the coefficients of friction (without cutting forces, which should be kept to a minimum):

$$\frac{\mu_{a2}}{\mu_{a1}} = \frac{(t_0 - t_2)\, t_1}{(t_0 - t_1)\, t_2}, \qquad (11)$$

where μ_{a1}, μ_{a2} – adhesive components of coefficients of friction while grinding, respectively, samples №№ 1 and 2.

Experiment to determine the relative change in the adhesive component of the friction force was conducted with 10-fold repetition. Average results of the stop time of the grinding wheel are shown in Table 5. The results of calculations by formula (11) are reflected in the line "Changing the adhesive component of friction". There are also other parameters in the table, including the actual depth of cut, a percentage of the cutting depth of the standard sample number 1, calculated from the data in Table 2. The initial area of the samples were slightly different from each other, that is why it is correct to compare not the mass or volume of removed metal, but the actual value of the depth of cut, which is determined by averaging the height of removed metal in one table stroke.

The relative change in the mechanical component of the friction force ($\mu_{\text{м}}$) was determined analytically, given the fact that its value is proportional to the square of the diameter of the footprint on the test sample [5], which could be adopted on the basis of the known values of Brinell hardness, or using translation tables of hardness. Table 5 presents data on changes in the mechanical component of the coefficient of friction in grinding the sample with respect to the standard sample number 1 (based on calculations by the diameter footprint).

TABLE 5

CHANGE IN THE COEFFICIENT OF FRICTION AND A COMPARISON OF RESULTS

Parameters	Units	Sample number				
		1	2	3	4	5
Spindle stop time while free rotation t_0	s	10,26				
Spindle stop time in contact with the sample t_i	s	2,950	2,969	2,931	2,920	2,985
Changing the adhesive component of the friction force	%	0	–0,90	+0,91	+1,44	–1,65
Diameter of footprint	mm	4,87	4,02	3,68	2,93	5,67
Change of the mechanical component of the friction force	%	0	–31,86	–42,90	–63,80	+35,55
Adhesive component of the coefficient of friction μ_{ai}	–	0,3168	0,3140	0,3197	0,3214	0,3116
Mechanical component of the friction coefficient $\mu_{\text{м}i}$	–	0,0032	0,0022	0,0018	0,0012	0,0043
Coefficient of friction	–	0,320	0,316	0,322	0,323	0,316
Volume of shavings, removed by single grain (calculation)	mm³	0,0190	0,0203	0,0185	0,0182	0,0203
Actual depth of cut (calculation)	%	0	+6,64	–2,55	–4,25	+7,00
Actual depth of cut (experiment)	%	0	+5,68	–2,27	–4,54	+7,95
Relative error	%	0	+16,8	+12,3	–6,3	–11,9

Further it was postulated that while the grinding of steel, the amount of adhesive component is about 99%, whereas the mechanical component - only about 1% [6]. So with a coefficient of friction of 0.32, the adhesive component of the coefficient is approximately equal to 0.3168, and mechanical - 0.0032. Given the known changes in the components of the grinding of different samples as compared to the standard sample, it is possible to determine the value of the coefficient of friction in absolute units.

In order to compare the experimental and analytical results and to show how much the change in the coefficient of friction will affect the change in the volume of removed shavings, we used the empirical expression (1). To do this, we set the following initialization parameters: shrinkage coefficient shavings - 1.6, the coefficient of friction - 0.32 [7, pp. 78-79]. Data on volume of shavings with the variation of the coefficient of friction was included in Table 5.

Table 5 shows that the error between the actual depth of cut obtained empirically, and the depth of cut, obtained by change in the coefficient of friction between the abrasive grains and the surface of blanks, is not more than 20%, which is quite satisfactory.

Thus, the change in the coefficient of friction led to a change of removed shavings and actual depth of cut. This confirms our hypothesis that the physical and mechanical properties and microstructure of the processing material is influenced by the volume of the removed shavings, and this impact is through the corresponding change in the coefficient of sliding friction of shavings on the front surface of the abrasive grain.

IV CONCLUSION

Sliding friction in the vicinity of the edge of the abrasive grain determines the area of the front surface and affects the amount of removed metal in the area of frictional contact.

The intensity of the grinding process can be judged by the shavings form, as well as the number and size of molten globules present in the sludge, which is a consequence of high local temperatures.

The workability of the material by grinding can be determined using the Hall-Petch law, but the constant coefficient that presents in the formula, for hardened and unhardened steels takes different values.

Physical and mechanical properties and microstructure of the processing material influence on the volume of the removed shavings, and this impact happens through the corresponding change in the coefficient of sliding friction of shavings on the front surface of the abrasive grain.

V REFERENCES

[1] Nikiforov I.P. Determination of volume of metal removed by a single abrasive grain for surface grinding. / I.P. Nikiforov, V.K Koshmak, N.F. Kudryavtseva // PPI Proceeding. – Series "Engineering". Electric drive. – 2008. – №11.3. – pp. 218–222.

[2] Maltsev, P.N. Determination of the optimal granularity of the circle, providing maximum cutting power tool / P.N. Maltsev, I.P. Nikiforov // Physical basis of high-speed processing and technological support for computer technology in engineering. Materials of the international young researchers summer School. Ulyanovsk, 12–15 May of 2011th. – Ulyanovsk: Ulyanovsk STU, 2011. – pp. 168–172.

[3] Goldstein, M.I. Metal Physics of high-strength alloys / V.S. Litvinov, B.M. Bronfin. – M. : Metallurgy, 1986. – 312 pp.

[4] Livshits, L.S. Welding metal and heat treatment of welded joints / L.S. Livshits, A. Khakimov. - 2nd ed., Rev. and add. – M. : Engineering, 1989 – 336 pp.

[5] Semenov, V.I. Influence of microstructure of the material in the adhesive component of friction / V.I. Semenov, L.Sh. Shuster, G.I. Raab // Friction, wear, lubrication [Electronic resource]. – 2008. – №28. – Access mode: http://www.tribo.ru/netcat_files/ 313/208/h_994233f617f64e4ea7bbab254fc0714e.

[6] Kuznetsov, A.A. Determination of cutting forces acting on the cutting edge of the unit worn abrasive grain / A.A. Kuznetsov, V.V. Fedotov // Proceeding of IV Russian Conference-seminar «Science and Engineering: Problems and Prospects». Syzran 22 May 2009th – Samara: P.h. "Samara State University", 2009.

[7] Filimonov, L.N. High-speed grinding. – L.: Engineering, Leningrad Department, 1979. – 248 pp.

Case Study on Early Age Shrinkage of Cement-based Composites

Andina Sprince, Leonids Pakrastinsh

Riga Technical University, Department of Structural Engineering. Address: Azenes Street 16, Riga, LV-1048, Latvia.

Abstract. The aim of this paper was to study the behaviour of new high-performance fibre-reinforced cement composite materials (FRCC) that are reinforced with polyvinyl alcohol (PVA) fibres. The shrinkage deformations at early age, the compressive strength and modulus of elasticity of the new compositions had been determined. Test results shows that the addition of PVA fiber 1.10% and 0.55% by weight of the cement has negligible influence on concrete drying shrinkage, however, it is affect the concrete plastic and autogenous shrinkage. The results of the experiments permitted the prediction of long-term deformations of the concrete. Wider use of this material permit the construction of sustainable next generation structures with thin walls and large spans that cannot be built using the traditional concrete.

Keywords – cement-based matrix, fibre reinforced concretes, high performance concretes, PVA fibres, shrinkage

I INTRODUCTION

Concrete shrinkage is a non-elastic deformation in plastic and hardened state that progresses with time and may cause displacement or deflection of a structural element, loss of preliminary tension, re-distribution of stresses, as well as reduction of shear resistance in regions with small moments. Restricted concrete shrinkage can also cause development and growth of cracks, which may lead to operation and serviceability problems. Therefore, when designing structures, the designer must provide for the control of shrinkage stresses and the resulting cracks in a restricted concrete element.

Plastic shrinkage cracks appear after the concrete has been cast but before it has gained strength. Nowadays the most popular method for controlling plastic shrinkage cracks is use of synthetic fibres in the amounts ranging from 0.05% to 0.5%. Synthetic fibres were first used already in the end of the 1960s. Although all synthetic fibres have similar advantages, polyvinyl alcohol (PVA) fibres were used for this study due to their larger tensile strength and modulus of elasticity, as well as good bonding with concrete. The study concentrates on determining the effect of PVA fibres on concrete shrinkage and cracking.

There have been extensive investigations that prove that the use of PVA fibres substantially reduces the plastic shrinkage of concrete (early age shrinkage) and the development of related cracks [1], [2]. In these studies PVA fibres have also been compared to other synthetic fibres.

Plastic shrinkage starts in concrete already within the first few hours after it has been cast into the mould. It is because the concrete mass starts to lose its free moisture, and the rate of evaporation exceeds the rate of bleeding. And if the tensile strength of bonded concrete is insufficient, plastic shrinkage cracks appear. Especially susceptible to plastic shrinkage are structures with a large surface area that is subjected to the environment, e.g. concrete paving, bridge decks, walls, etc.

It was observed that non-reinforced concrete exhibited slow shrinking in the first 30 minutes, but after 1.5 to 4 hours the shrinkage increased rapidly. However, when the amount of free moisture is reduced due to evaporation and the concrete is simultaneously hydrated, it becomes firmer. As a result, when concrete begins to harden, the increase of the plastic shrinkage rate remains minimal. After this period concrete shrinkage stabilizes almost completely. In the first few hours, non-reinforced concrete behaves much in the same way as concrete with PVA fibres, but after that non-reinforced concrete starts to shrink more intensively. In this study, by using PVA fibres, the plastic shrinkage in concrete was reduced by 36.20%. It was also proved that an increase of fibre content from 0.1% to 0.4% has minimum impact on reducing the shrinkage. Therefore, to reduce plastic shrinkage, it is enough to use 0.1% of PVA fibres. In addition, the difference in fibre parameters, moduli of elasticity, lengths, diameters and bonding with concrete do not have significant effect on plastic shrinkage of concrete. Nevertheless, PVA fibres achieve slightly better results than plypropylene and carbon fibres. The drying shrinkage is so large because the experiment provided favourable conditions for plastic shrinkage and the concrete was not cured [1].

One of the reasons why synthetic fibres such as PVA are so effective in reducing the plastic shrinkage in concrete was explained by Mangat and Azari [3]. When the concrete structure is subjected to tensile stresses caused by shrinkage, the fibres reduce the shrinkage because of the shear between the surface of the fibre and the concrete. In addition, the fibres increase the strength and rigidity of the concrete structure. For these reasons, PVA fibres are an effective solution for reducing the plastic shrinkage in

concrete by 40%, as well as limiting the cracking (literature indicates reduction of up to 90%).

Unlike plastic shrinkage, drying shrinkage takes place only after the concrete has hardened. Drying shrinkage develops for a long time and when it is restricted, it can cause significant cracking of the structure both before and after loading. Addition of PVA fibres in the amounts ranging from 0 to 0.2% cannot limit the cracks caused by drying shrinkage, though it can reduce the cracking caused by plastic shrinkage.

Development of drying shrinkage cracks can be effectively limited by increasing the fibre content [4], [5]. In this experiment, the amount of PVA fibres was increased to 0.5%, and established that PVA (F45) micro fibres can reduce the width of the cracks by 90%, while PVA macro fibres can reduce it by 70%. Therefore, smaller fibre dimensions and a larger fibre content help increase the total surface area of fibres that is in contact with the concrete structure. This permits better distribution of stresses in the space between the cracks and more effectively limits the crack width.

Adding 0.5% of PVA fibres (both macro F45, and micro F200) had only a slight impact on reducing the drying shrinkage. Macrofibres F45 show better results in reducing the drying shrinkage, which could be explained with the fact that fibres might change the interior water circulation in the concrete structure. However, this reduction of shrinkage was not sufficient to relieve the stresses [4].

In the last few years infrastructure projects have seen a rise in the application of concrete with improved characteristics. Such high performance fibre-reinforced concrete HPFRCC (high performance fibre reinforced cement compositehidra) has high strength and durability, low permeability and good casting properties. These characteristics permit the construction of larger spans, thinner and more geometrically complicated structures, while simultaneously ensuring better durability and sustainability.

However, concrete shrinkage and permeability are factors that have major influence on the durability of the concrete. Such high-strength concretes (in this case the pressure strength of the samples reached even 200 MPa) have low porosity and high cement content, which causes increased autogenous shrinkage, because the concrete is losing water due to hydration even though it is kept moist from the outside. Although such cement has a low W/C ratio, it usually contains small particles (max 5 mm), therefore drying shrinkage is also important for HPFRCC mixes. The linear deformation data obtained in this study include both autogenous and drying shrinkage.

As described above, fibres in high-performance concretes ensure an increase of tensile strength, the control of crack width, as well as uniform distribution of cracks. In concretes with traditional strength parameters the fibres ensure control of the shrinkage cracks and reduced deformation. However, studies regarding the effect of fibres on high-performance concrete shrinkage are not so straightforward, except as concerns plastic shrinkage (not investigated in this study) where it is effective to use fibres.

This study concentrates on the effect of PVA fibres on the drying and autogenous shrinkage of high-performance fibre-reinforced concrete. it is planned to use such concrete also for the cast in-situ reinforced concrete walls of a wood drying plant, which serves also as an engineer's qualification work. A high-strength fibre-reinforced concrete was selected because the structure will be subjected to aggressive conditions (high humidity, cyclic temperature changes), it has large surface area (7.6 m × 16 m) and unevenly distributed tensile shrinkage stress is expected, because both sides of the walls will be subjected to different environmental conditions. For these reasons, it would be more effective to use fibres, in addition to metal reinforcement, to control the cracks caused by tensile stresses. PVA fibres will be used, because metal fibres might corrode due to the aggressive environment, and PVA fibres also have better tensile strength and modulus of elasticity, as well as an excellent bonding ability with concrete in comparison with other chemical fibres. It is worth noting that PVA (polyvinyl alcohol) fibres are more economical.

In this way, by changing the PVA fibre content from 0% to 0.56% and 1.1%, this study investigates the effect on autogenous and drying shrinkage of high-performance concrete.

II MATERIALS AND METHODS

Three different high-strength concrete mixes were prepared for this study. The compositions differ by their fibre content; see Table 1.

TABLE 1

CONCRETE MIX COMPOSITIONS

Materials		1 mix	2 mix	3 mix
		E (reference mix)	PVA-0.6	PVA-0.8
Cement I 42.5 N	kg/m³	675	675	675
Cement I 52.5 N	kg/m³	225	225	225
Sand 0/1 from Saulkalne	kg/m³	300	300	300
Sand 0/2.5 from Saulkalne	kg/m³	300	300	300
Diabase 0/5	kg/m³	200	200	200
Diabase 2/5	kg/m³	200	200	200
Ground silica 8min.	kg/m³	100	100	100
Microsilica 920 D	kg/m³	100	100	100

80

Water	kg/m³	200	200	200
Superplast. HE-30	kg/m³	24	24	24
PVA fibres	kg/m³	0	5	10
W/C		0.22	0.22	0.22

Since this is a high-strength concrete, it has a small W/C ratio — only 0.22. It is smaller than the theoretical ratio 0.24, which is required for hydration of all cement. In this case the non-hydrated cement particles serve as aggregate [6].

Two different cements were used as a bonding agent — CEM I 42.5 N and CEM I 52.5 N, where CEM I indicates the type of cement, which in this case is Portland cement without additives. It consists and is made of only rock gypsum and common Portland cement clinker, without any special strength-increasing additives. The numbers 42.5 and 52.5 indicate the pressure strength (N/mm^2) of a sample after 28 days of hardening in standard conditions, while letter N means that this is a normal setting cement — after two days of hardening in standard conditions its strength must be at least 10 N/mm^2.

The aggregate was washed quartz sand with fractions of 0/1 mm and 0/2.5 mm, and crushed diabase with fractions of 0/5 mm and 2/5 mm. Aggregate fractions were minimized and did not exceed 5 mm. Smaller aggregate particles increase the surface area between the aggregate and the cement and reduces the development of microcracks [6].

By content the fibres account for 0.56% and 1.1% of cement mass. In this study only PVA fibres were used. The first reason was that metal fibres could start corroding in the high humidity conditions described. The second reason was that although PVA fibres have the same advantages as other synthetic fibres, their tensile strength and modulus of elasticity are much higher, besides PVA fibres have a very good ability to bond with cement paste [7], [8]. The mechanical properties and dimensions of the PVA fibres used in the study are presented in Table 2.

TABLE 2

MECHANICAL PROPERTIES AND DIMENSIONS OF PVA FIBRES

Fibre type	Length, L (mm)	Diametre, D (μm)	Tensile strength (MPa)	Mod. of elasticity (MPa)
MC 40/8	8	40	1600	42000

To improve the casting properties of the mixes, considering the low W/C ratio 0.22, and to ensure uniform distribution of the fibres, superplasticizer HE-30 was added to the mix. To improve the properties of the concrete, Microsilica 920 D (densified silica fume) was added to the mix. This has dual effect — physical and chemical. It fills the voids between larger particles and ensures a denser structure, and a pozzolanic reaction takes place when silicic acid reacts with calcium hydroxide resulting in calcium silicate hydrate, which is stronger.

The mixing of the sample mixes, their moulding, curing and measuring was carried out in accordance with the European standard EN 12617-4 "Determination of shrinkage and expansion".

Non-restricted linear free shrinkage of concrete was measured using the first measurement method. For this purpose, prism samples of 40 mm × 40 mm × 160 mm were required. Their shrinkage was measured in the time period from 24 hours to 56 days after casting into the mould.

The concrete mix was prepared in the laboratory in a vertical mixer. First, the aggregates and water were mixed, then the chemical and artificial mineral additives and fibres were added, and then the mix was mixed once more. After that the concrete was cast into moulds, and all moulds were filled and vibrated in the same manner; the top of the sample was levelled with a trowel if required.

Then the samples were covered with a film for 24 hours and left to harden, after that they were de-moulded. The samples were cured by placing them in water basins.

Once the samples are removed from the basin and the measurement of shrinkage begins, nail-like stainless steel elements with rounded heads are attached (glued) to both ends of the sample. They must be placed directly on the central axis. It is necessary in order to make precise shrinkage measurements.

TABLE 3

SAMPLE TYPES DEPENDING ON THE DURATION OF CURING

Mix	Duration of sample curing			
	1 day	4 days	7 days	14 days
1 mix	PVA-E-4 PVA-E-5	PVA-E-9 PVA-E-10	PVA-E-12 PVA-E-16	PVA-E-18 PVA-E-20
2 mix	PVA-0.6-4 PVA-0.6-5	PVA-0.6-9 PVA-0.6-10	PVA-0.6-11 PVA-0.6-15	PVA-0.6-19 PVA-0.6-20
3 mix	PVA-0.8-3 PVA-0.8-4	PVA-0.8-20 PVA-0.8-24	PVA-0.8-14 PVA-0.8-16	PVA-0.8-6 PVA-0.8-26

The temperature in the laboratory must be 21±2°C, and the humidity must be 60±10%. In this study the samples were cured for different periods: 1 day, 4 days, 7 days and 14 days; see Table 3. After the curing the samples were kept in the laboratory in standard conditions, and their shrinkage was measured.

Before measuring the length of the samples, the ambient humidity and temperature in the laboratory must be noted on the record sheet. The length of the samples is measured with a gauge measurement tool (shrinkage clamp) calibrated to a sufficient length in order to measure the minimum length of the sample ± 5 mm with a precision of ± 0.001 mm. The shrinkage

clamp must have tight contact with the sample and its axis of measurement must directly coincide with the axis of the sample (clamp jaws directly on the rounded steel elements glued to the sample). The shrinkage clamp used in this study is shown in Fig. 1.

Fig. 1.   Shrinkage clamp

The drying shrinkage of a sample is a displacement deformation exhibited as a change of length in relation to the initial length. Each time when the concrete shrinkage is measured, it is recommended to measure also the weight changes, as it signifies changes in the density of the sample.

III RESULTS AND DISCUSSION

Since the properties of freshly cast concrete can be easily influenced by different factors, such as the mixing procedure and environmental conditions, small variations may cause differences in the experimental results. The values shown in the graphs below are the average values of two simultaneously cast samples. The differences between the same mixing and curing procedure samples at each test were within a 5-13% limit.

As mentioned before, the samples were left to harden for 24 hours and then subjected to curing for different periods of time. The measurement of the shrinkage deformations of samples subjected to only 1 or 4 days of curing include both drying and autogenous shrinkage deformations. Since autogenous shrinkage occurs only in the first few days, in samples that were cured for 7 and 14 days hydration had already completed and autogenous shrinkage constitutes only an minor portion of the linear shrinkage deformation.

The results illustrating the effect of PVA fibres on the unrestrained shrinkage of high-strength concrete are shown in Fig. 2 to 5. As seen in the graphs, PVA fibres have minimum impact on shrinkage of the concrete. All graphs show a common tendency, except for the mix that was cured for 4 days, namely, mix compositions with a PVA fibre content of 0.56% shrink as much or slightly less that the reference mix without any PVA fibres, while the mix containing 1.1% of PVA fibres is shrinking more than the reference mix. The shrinkage deformation shown in Fig. 3 is different from the other measurements in that the reference mix exhibits more shrinkage than both

mixes with PVA fibres, and the difference reaches even 15.5%. However, these results may reflect the influence of PVA fibres imprecisely, as the average value of the reference mix might be imprecise — the difference between the first and second reference sample was 13%, and the second sample exhibited te same shrinkage as the mix with PVA fibre content of 0.56%.

TABLE 4

FREE DRYING SHRINKAGE FOR CONCRETES WITH DIFFERENT PVA FIBRE CONTENT IN COMPARISON WITH REFERENCE CONCRETE WITHOUT FIBRES AT 35 DAYS

Curing period	V_f(%)	Shrinkage deformation ε (x10^{-6})	+/- (increase/ reduction)%
	0.00	982.1	
1 day	0.56	1000.0	+1.79
	1.11	1089.3	+9.84
	0.00	803.6	
4 days	0.56	678.6	-15.5
	1.11	767.9	-4.4
	0.00	675.0	
7 days	0.56	628.6	-6.87
	1.11	785.7	+14.1
	0.00	482.1	
14 days	0.56	517.9	+6.9
	1.11	500.0	+3.6

Fig. 2. Unrestrained shrinkage in concrete with different PVA fibre content after 1 day of curing

Fig. 3.   Unrestrained shrinkage in concrete with different PVA fibre content after 4 days of curing
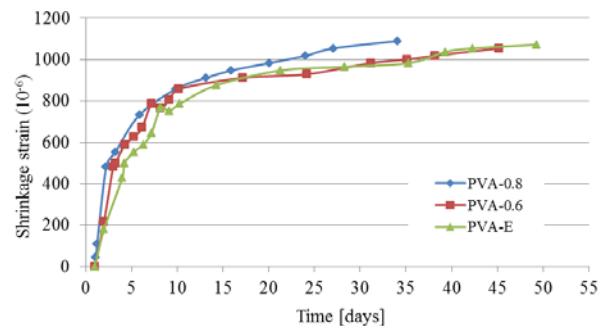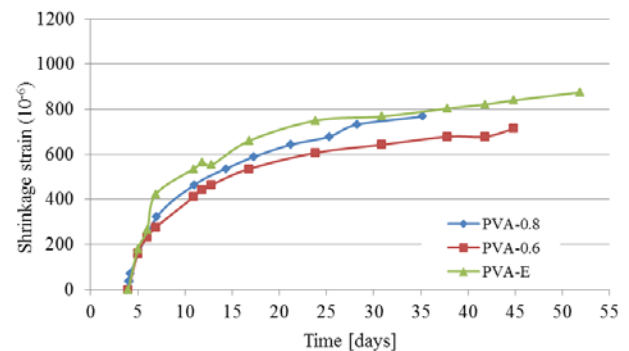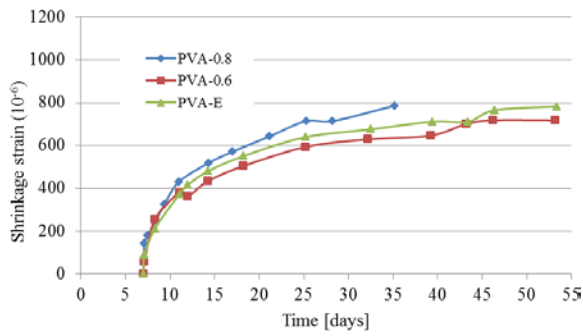
Fig. 4.   Unrestrained shrinkage in concrete with different PVA fibre content after 7 days of curing
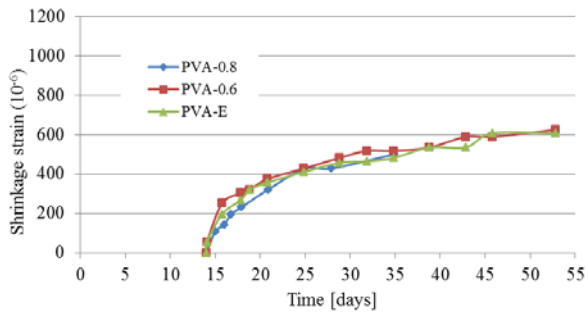
Fig. 5.   Unrestraibed shrinkage in concrete with different PVA fibre content after 14 days of curing

The obtained data vary, therefore, in order to draw conclusions regarding the effect of fibres on concrete shrinkage, the moisture loss (weight reduction) of the concrete samples was measured and compared taking into consideration the different mix compositions, because both autogenous and drying shrinkage occurs by loss of water.
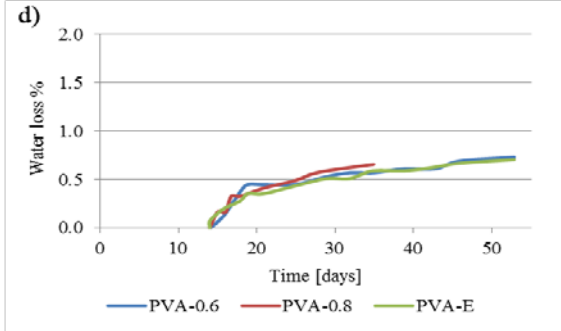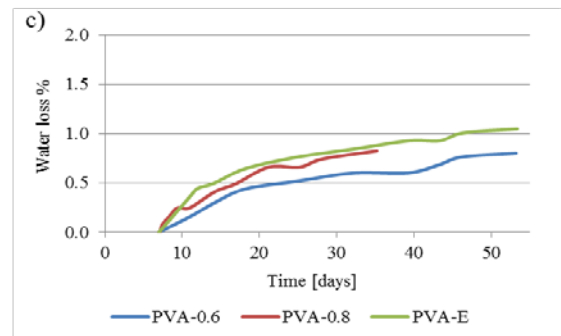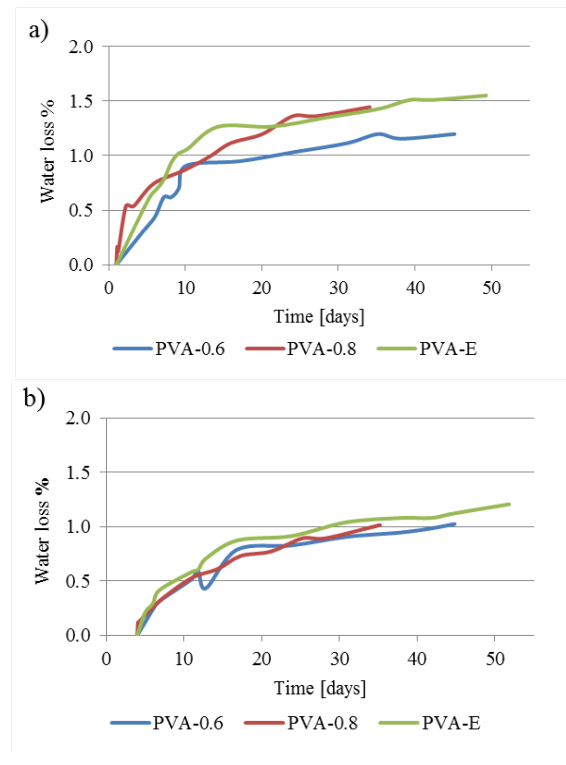
Fig. 6.   Relative water loss vs time in concrete with different PVA fibre content and different curing periods: a) at 1 day; b) at 4 days; c) at 7 days; d) at 14 days

The moisture loss curves reflect the shrinkage deformations of the concrete samples, and it can be concluded that PVA fibres (0.56%) help reduce shrinking in concrete if the concrete is cured for 1 to 7 days. This in turn may prove that with the help of PVA fibres it is possible to reduce the autogenous shrinkage in concrete (2–10%), but, as shown in Fig. 4 and 5, PVA fibres have virtually no effect on drying shrinkage.

Unlike in other studies, the increase of fibre content from 0.56% to 1.1% did not reduce the shrinkage; quite the contrary — it increased in comparison with the reference sample, even though a fibre content of 1.1% (PVA-0.8) slightly reduces the moisture loss in comparison with that of the reference sample; see Fig. 6. Considering that in high-performance concretes the fibre content is 1.5% to 5%, and the obtained results are in contradiction with similar studies [1] and [8], the fibre content of the composition should be changed (to, e.g. 2%) to achieve clear results.
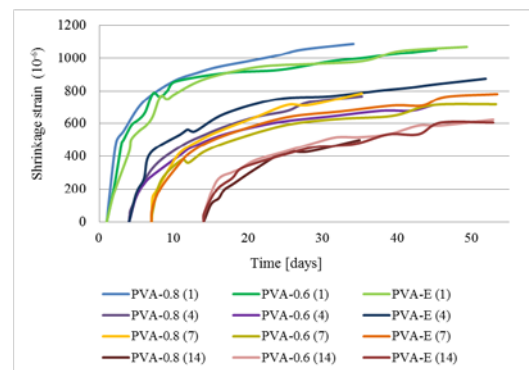
Fig. 7.   Unrestrained shrinkage of concrete depending on the duration of curing

83

In Fig. 6 it is evident that the shorter is the curing period, the larger is the moisture loss. If concrete is cured for 4 days, the moisture loss may be reduced by 23%; for 7 days — by 33% and for 14 days — by 46%. As a result the concrete loses less water and the concrete shrinkage is consequently smaller; see Fig. 7, which shows that the shrinkage at 50 days with 1 day of curing is -1100; with 4 days of curing it is -800; with 7 days of curing -700, and with 14 days of curing -600 (all values $\times 10^{-6}$). However, samples that have been cured for more than one day, already have undergone some autogenous shrinkage, which is not reflected in these graphs. Since this is high-performance concrete, its autogenous shrinkage constitutes a substantial part of the linear deformation. For this reason, the obtained results cannot be attributed solely to the drying shrinkage, and in reality the samples may exhibit larger deformations. Therefore, it would be useful to perform a separate autogenous shrinkage test to determine just how effectively PVA fibres can influence the chemical shrinkage of concrete (moisture loss due to cement hydration), which for high-performance concretes is quite substantial. To obtain clearer results it would also be necessary to increase the number of samples.

IV CONCLUSIONS

Experimental shrinkage tests of high-performance fibre-reinforced concretes with different content of polyvinyl alcohol (PVA) fibres — 0.56% and 1.1% of cement mass — were carried out in the RTU laboratory and compared with the data from reference mix. The obtained shrinkage test results indicate that addition of PVA fibres to high-performance concrete does not have substantial effect on its shrinkage.

Since this was a high-strength concrete, the autogenous shrinkage in the first few days constitutes a major part of the linear deformation. Therefore the obtained results cannot be attributed solely to the drying shrinkage.

Samples that have been cured for more than four days, already have undergone some autogenous shrinkage which is not reflected in these shrinkage results. Therefore, in samples that have been cured for more than one day, the resulting deformation does not reflect the true shrinkage deformation of these samples. To find the final shrinkage deformation of PVA fibre-reinforced concrete, as well as the effect of PVA fibres on the autogenous shrinkage, it would be necessary to continue the experiment by performing a separate autogenous shrinkage test.

The moisture loss results reflect the shrinkage deformations of the concrete, and it can be concluded that PVA fibres (0.56%) help reduce shrinking in concrete if the concrete is cured for 1 to 7 days, which in turn may prove that with the help of PVA fibres it is possible to reduce the autogenous shrinkage in concrete (2–10%), since in samples cured for 14 days the fibres have no effect on the moisture loss. Thus it can be concluded that PVA fibres are not an effective solution for reducing the shrinkage in concrete.

The results of the moisture loss measurements reflect the evident connection that the shorter is the curing period, the larger is the moisture loss. If concrete is cured for 4 days, the moisture loss may be reduced by 23%; for 7 days — by 33% and for 14 days — by 46%. By reducing the moisture loss, shrinkage is also reduced.

It can be presumed that the use of PVA fibres might be justified in cases where shrinkage deformation is exhibited by a restricted concrete element and where PVA fivres could help control the crack propagation and quantity, their width and distribution. This could be a direction of further research.

In future experiments the researchers could also change the PVA fibre content (2%), combine PVA macro and micro fibres or different fibre materials, e.g. cellulose.

V REFERENCES

[1] Wongtanakitcharoen T., Naaman A. E. Unrestrained early age shrinkage of concrete with polypropylene, PVA, and carbon fibers. Materials and structures Vol. 40, No 3, 2007, pp. 289-30. doi:10.1617/s11527-006-9106-z.

[2] Fischer G., Li V. 2007. Effect of fiber reinforcement on the response of structural members. Engineering Fracture Mechanics, Vol. 74, 2007. pp. 258-272. doi:10.1016/j.engfracmech.2006.01.027.

[3] Mangat P. S., and Azari M. M. A theory for the free shrinkage of steel fiber reinforced cement matrices. *J. Mat. Sci.*, 19, 1984, pp. 2183–3194.

[4] Passuello A., Moriconi G., .Shah S. P. Cracking behavior of concrete with shrinkage reducing admixtures and PVA fibers. Cement and Concrete Composites, Volume 31, Issue 10, November 2009, pp. 699-704. doi:10.1016/j.cemconcomp.2009.08.004.

[5] Pease, B. J, Shah, H, Hossain, A. & Weiss, J. Restrained Shrinkage Behavior of Mixtures Containing Shrinkage Reducing Admixtures and Fibers, in: ICACS 2005 International Conference on Advances in Concrete Composites and Structures, Chennnai, India, January 6th-8th 2005, 265-274.

[6] Justs J., Shahmenko G. Effect of Mix Proportions and Curing Regimes on Ultra High Performance Concrete. Proceedings of 8th FIB International Symposium in Civil Engineering, Denmark, Lyngby, 20.-23. June, 2010, pp 425-430.

[7] Toutanji H., Xu B., Gilbert H., Lavin T. Properties of polyvinyl alcohol fiber reinforced high-performance organic aggregate cementitious material: Converting brittle to plastic. Construction and Building Materials, Volume 24, Issue 1, January 2010, pp. 1-10. doi:10.1016/j.conbuildmat.2009.08.023.

[8] Sun W., Chen H., Luo X., Qian H. The effect of hybrid fibers and expansive agent on the shrinkage and permeability of high-performance concrete. The Department of Materials Science and Engineering, Southeast University, China, 2000.

Solution of Linearized Flat Problem of Hydrodynamics (IVF)

Strochkov I.A., Khvattcev A.A.

Pskov State University, department of high mathematics, faculty of informatics
Address: 180680 Pskov, Leo Tolstoy Street 4, Russia

Abstract. In the present paper a method of the generalized potential to planes is applied for the solution of the linearized according to Oseen of flat problem of hydrodynamics incompressible viscous fluid (IVF). Generalized potential simple layer containing McDonald function serves kernel for generalized potential to planes.

For finding of an unknown density of the potential simple layer is received linear integral equation, containing double integral from curvilinear integral along border of the streamlined area.

Sharing the pressure is in turn defined by potential simple layer with density of the potential, determined by linear integral equation, hanging from solution specified above integral equation. The offered method of the successive iterations, allowing elaborate the solution of the problem before achievement given to accuracy.

As example of exhibit to theories is considered solution of the problem theory of hydrodynamic greasing

Keywords - incompressible viscous fluid, flat problem of hydrodynamics, problem theory of hydrodynamic greasing, linear integral equations, stream function.

I

Consider problem of a flow of a contour l uniform flow (IVF) $\vec{u}(u_x; u_y)$. Choose the Cartesian system coordinates (XOY) with the centre O into domain D, bounded by contour l (Fig. 1.).
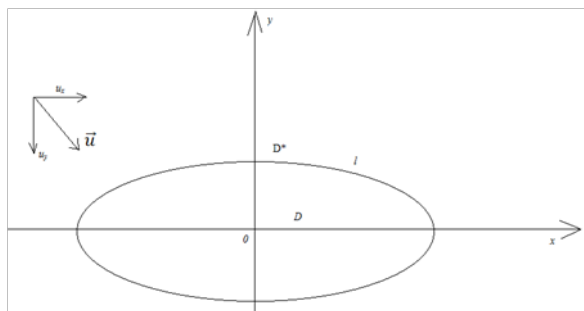
Fig. 1.

Navier – Stokes equations (NS) of flat problem (IVF)

$$(\vec{v}\vec{\nabla})\vec{v} = -1/\rho \cdot \vec{\nabla}p + \nu\Delta\vec{v}$$

$$div\ \vec{v} = 0. \tag{1}$$

Boundary conditions

$$\vec{v}\big|_l = 0, \vec{v} \to \vec{u}, \quad p \to p_0, \quad r \to \infty; r = \sqrt{x^2 + y^2} \tag{2}$$

Introduce non-dimensional variables

$$\vec{v} = u\vec{v^*}; \quad u = \sqrt{u_x{}^2 + u_y{}^2};$$

$$\vec{u} = \vec{u}\ (\alpha,\beta); \ \alpha = \frac{u_x}{u}; \ \beta = \frac{u_y}{u} \tag{3}$$

$$p = \rho u^2 p^*, \vec{r} = d\vec{r^*}(x^*, y^*), \ d = diam(D)$$

Equation (1) and conditions (2) are written in non-dimensional variables (3)

$$Re(\vec{v}\vec{\nabla})\vec{v} = -\vec{\nabla}p + \Delta\vec{v}, \ div\ \vec{v} = 0 \tag{4}$$

$$\vec{v}\big|_l = 0, \vec{v} \to \vec{u}(\alpha,\beta), \quad p \to p_1, \quad r \to \infty; p_1 = \frac{p_0}{\rho u^2}\cdot \tag{5}$$

According to Oseen [1-3, 6-9, 12] execute linearization of the relation (4)

$$Re(\vec{u}\vec{\nabla})\vec{v} = -\vec{\nabla}p + \Delta\vec{v}. \tag{6}$$

Introduce stream function

$$v_x = \frac{\partial\Psi}{\partial y}, v_y = -\frac{\partial\Psi}{\partial x}. \tag{7}$$

And rewrite (6), (7) in form of the generalized Helmholtz equation [4]

$$Re\left(\alpha\frac{\partial\Omega}{\partial y} + \beta\frac{\partial\Omega}{\partial x}\right) = \Delta\ \Omega; \tag{8}$$

$$\Omega = -\Delta\psi; \vec{\Omega} = (0,0,\Omega); \vec{\Omega} = \overrightarrow{rot}\ \vec{v}. \tag{9}$$

By supposing, that $\gamma = \frac{Re}{2}$

and $\Omega = e^{\gamma(\alpha x + \beta y)}\omega(x, y)$ (10)

obtain canonical form for (8)

$$\Delta\vec{\omega} = \gamma\vec{\omega} \tag{11}$$

McDonald function is a solution of the equation (11). This solution must depend that r only and $\lim \bar{\omega} = 0$, if $r \to 0$. Therefore,

$$\omega = K_0(\gamma \cdot r); \quad K_0(r) = \int_1^\infty (e^{-\rho\xi} \cdot d\xi)/\sqrt{\xi^2 - 1} \quad (12)$$

Integral presentation of the solution of the linear equation (8) has form

$$\Omega(m) = \frac{1}{\pi} \int_l e^{\gamma q_{mp}} K_0(\gamma r_{mp}) \cdot \mu(p) \cdot dlp; \quad (13)$$

$$q_{mp} = \alpha(x_m - x_p) + \beta(y_m - y_p);$$
$$r_{mp} = \sqrt{(x_m - x_p)^2 + (y_m - y_p)^2}$$

$\mu(p)$ - unknown density of the potential (13).
If $r \to 0$, McDonald function has log feature

$$K_0(r) = \ln\left(\frac{1}{r}\right) + \varepsilon(r); (14)$$

but if $r \to \infty$,

$$K_0(r) = \sqrt{\frac{\pi}{2r}} e^{-r} + \varepsilon\left(\frac{1}{r}\right). \quad (15)$$

Therefore, expression (13) is generalized potential of the type of the potential simple layer. [10]
Now write formal solution of the Poisson equation (9)

$$\psi(m) = \frac{1}{\pi} \iint_{D^*} \Omega(p) \cdot \ln(1/rmq) \cdot dS_p + \psi_0; \quad (16)$$

$$\Delta\psi_0 = 0. \quad (17)$$

By applying (15), (13) obtain $\Omega \to 0, r \to \infty$
Boundary conditions (5) for velocity will be rest satisfied if

$$\psi_0 = \alpha y - \beta x. \quad (18)$$

$$\frac{1}{\pi} \iint_{D^*} \Omega(p) \cdot \ln(1/rmq) \cdot dS_p \bigg|_l = (\beta x - \alpha y)\big|_l. \quad (19)$$

Now assume that $\mu(m)$ (a solution of the linear integral equation (19), (13) relatively density) can be expanded in Fourier polynomial

$$\mu(\theta) = \sum_{k=0}^n (a_k \cos k\theta + b_k \sin k\theta). \quad (20)$$

θ – polar angle,

x=x(θ), y=y(θ) – equations for contour l, $\theta \epsilon [0, 2\pi]$.

Substituting (20) into (13), (16), (19), obtain

$$\mu(x) = \sum_{k=0}^n (a_k A_k(m) + b_k B_k(m)), \quad (21)$$

Where

$$A_k(m) = \frac{1}{\pi^2} \iint_{D^*} \ln\left(\frac{1}{r_{mp}}\right) dS_p \int_0^{2\pi} e^{\gamma q_{pQ}} K_0(\gamma r_{PQ}) \times$$

$$\times \sqrt{\dot{x}^2(\theta_Q) + \dot{y}^2(\theta_Q)} \cos(\theta_Q) d\theta_Q;$$

$$B_k(m) = \frac{1}{\pi^2} \iint_{D^*} \ln\left(\frac{1}{r_{mp}}\right) dS_p \int_0^{2\pi} e^{\gamma q_{pQ}} K_0(\gamma r_{PQ}) \times$$

$$\times \sqrt{\dot{x}^2(\theta_Q) + \dot{y}^2(\theta_Q)} \sin(\theta_Q) d\theta_Q. \quad (22)$$

In order to find $A_k(m)$ and $B_k(m)$ break $[0, 2\pi]$ on (2n+1) parts (on number of required coefficients) arbitrarily, for example, points

$$\theta_i = \frac{2\pi}{2n+1} i, i = 0,1, \dots, 2n. \quad (23)$$

Calculating $A_k(\theta_i)$ and $B_k(\theta_i)$, then setting up them into (21) and (19), get system of the linear algebraic equations relative $A_k(\theta_i)$ and $B_k(\theta_i)$ solving which find stream function (21), density of the potential (20), a rotor of velocity (13) and a field of velocities (7).
Calculating div from both parts (6) of that α = const, β = const, and div$\vec{v}$=0, obtain

$$\Delta p = 0 \quad (24)$$

Multiplying (6) scalar by a vector $\vec{n}(n_x; n_y,)$ which is normal to l, write down

$$\frac{\partial p}{\partial n}\bigg|_l = \Phi(x, y), \quad (25)$$

$$\Phi(x, y)|_l = [\Delta\vec{v} - Re(\vec{u}\vec{\nabla})\vec{v}]|_l \vec{u}, \quad (26)$$

The solution of an external regional task of Neumann (24), (26) looks

$$P(m)=P_0+\frac{1}{\pi} \oint_l \ln\left(\frac{1}{r_{mp}}\right) \chi(p) dl_p, \quad (27)$$

Where density of potential (27) satisfies to Fredholm`s linear integrated equation of the second kind.

$$\pi\chi(m) + \int_0^m \frac{\cos\varphi_{mp}}{r_{mp}} \chi(p) dl_p = \Phi(m). \quad (28)$$

φ_{mp}- angle between the normal to l at P and r$_{mp}$.
Solving (28), (29), find the pressure distribution (27).

II

The resulting solution gives zero approximation of the considered problem in the Oseen approximation.

For his "improvement" write the resulting field of velocities in the form [5]

$$v_x = \alpha + \sum_{k=1}^{m} \frac{\varphi_k(x,y)}{r^k}, \quad v_y = \beta + \sum_{k=1}^{m} \frac{\delta_k(x,y)}{r^k},$$

$$r = \sqrt{x^2 + y^2} \tag{1}$$

φ_k, δ_k – known functions.

Linearize the equation (1.4) by (1) and then look for its solution in the form of

$$\Omega = \Omega_0 + \sum_{k=1}^{m} \frac{\Omega_k}{r^k} \tag{2}$$

$$Re\left(\alpha + \sum_{k=1}^{m} \frac{\varphi_k}{r^k}\right) \frac{\partial}{\partial x} \left(\Omega_0 + \sum_{k=1}^{m} \frac{\Omega_k}{r^k}\right) + \left(\beta + \sum_{k=1}^{m} \frac{\delta_k}{r^k}\right) \frac{\partial}{\partial y} \left(\Omega_0 + \sum_{k=1}^{m} \frac{\Omega_k}{r^k}\right) = \Delta\left(\Omega_0 + \sum_{k=1}^{m} \frac{\Omega_k}{r^k}\right) \tag{3}$$

Collecting in (3) the terms of the same powers r, obtain the equation for the decomposition (2). It should be noted that Ω_0 already known (1.13). The equation for Ω_1 is

$$\Delta\Omega_1 - Re\left(\alpha \frac{\partial}{\partial x}\Omega_1 + \beta \frac{\partial}{\partial y}\Omega_1\right) = f_1(x,y); \tag{4}$$

$$f_1(x,y) = Re\left(\varphi_1 \frac{\partial}{\partial x}\Omega_0 + \delta_1 \frac{\partial}{\partial y}\Omega_0\right). \tag{5}$$

Consequently,

$$\Omega_1 = \frac{1}{\pi}\oint_l e^{\gamma qmp} K_0(\gamma rmp)\mu_1(p)\, dl_p - \frac{1}{\pi}\iint_{D^*} ln\left(\frac{1}{rmp}\right) f_1(p)dS_p. \tag{6}$$

Solving the Poisson

$$\Delta\psi_1 = -\Omega_1, \tag{7}$$

finding

$$\psi_1 = \frac{1}{\pi}\iint_{D^*} ln\left(\frac{1}{rmp}\right)\Omega_1(p)dS_p, \tag{8}$$

and boundary condition

$$\psi_1|_l = 0. \tag{9}$$

Since D^* is arbitrary domain (l – anyone sufficiently smooth contour), then from (8) and (9) that $\Omega_1|_l = \theta_{\tau l}$

$$\oint_l e^{\gamma qmp} K_0(\gamma r_{mp})\mu_1(p)dl_p\Big|_{m\in l} = \iint_{D^*} ln\left(\frac{1}{rmp}\right) f_1(p)dS_p\Big|_{m\in l} \tag{10}$$

Thus, obtain a linear integral equation of the first kind of Fredholm type

Solving equation (10), obtain (6), (8) and

$$v_x^{(1)} = \frac{\partial\psi_1}{\partial y}, v_y^{(1)} = -\frac{\partial\psi_1}{\partial x}. \tag{11}$$

Furthermore, assuming

$$P = P^0 + \sum_{k=1}^{m} \frac{P_k(x,y)}{r^k}, \tag{12}$$

where $P^0(x,y)$ is known from (1.27), finding $P_1(x,y)$ in the form of

$$P_1 = \frac{1}{\pi}\oint_l e^{\gamma qmp} \chi_1(p)dl_p;$$

$$\pi\chi_1(m) + \int_0^m \frac{cos\varphi_{mp}}{r_{mp}}\chi_1(p)dl_p = \Phi_1(m). \tag{13}$$

Expression $\Phi_1(m)$ contains already known functions Ω_0, φ_1, ψ_1 and their multiplies.

III

In a case when the field of velocities and pressures (IVF) is considered in bounded domain (for example, in a problem of movement (IVF) in the area due to the motion of part of the boundary of this domain (cavity)) solution procedure considered in sections (1, 2) can be inapplicable.

For example, consider solution of the well-known problem of theory of hydrodynamic greasing [4], when the motion (IVF) is investigated in the area between the two circles of radius R_1 and R_2 off-center due to the rotation of the smaller circle with a given angular velocity ω. (Fig.2.)

Introduce polar coordinates (r, θ) with the center O_1. The equation of the rotating circle is r=R_1, the equation of the fixed circle r=R(θ) is defined by Theorem cosines.

$$R(\theta) = \varepsilon \cos(\theta - \varphi) + \sqrt{R_2^2 - \varepsilon^2 sin^2(\theta - \varphi)} \tag{1}$$

$$\varepsilon = O_1O_2;$$

φ – angle between the O_1O_2 and the axis Ox (if $\theta = \varphi$, then $r = R_2 + \varepsilon$, if $\theta = \pi + \varphi$ then $r = R_2 - \varepsilon$). Thus $M(r,\theta) \in D, r \in [R_2 - \varepsilon, R_2 + \varepsilon], \theta\epsilon[0, 2\pi]$
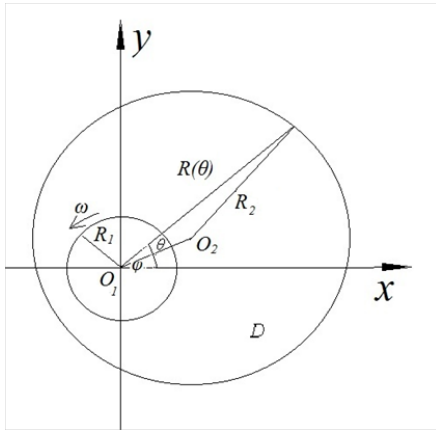
$$\tag{2}$$

Fig. 2.

In cylindrical coordinates generalized Helmholtz equation is

$$v_r \frac{\partial \Omega}{\partial r} + \frac{v_\theta}{r}\frac{\partial \Omega}{\partial \theta} = v\Delta\Omega; \qquad (3)$$

$$\frac{1}{r}\frac{\partial}{\partial r}(r\theta_r) + \frac{\partial v_\theta}{\partial \theta} = 0. \qquad (4)$$

$$\Delta\psi = -\Omega. \qquad (5)$$

Now introduce the dimensionless variables: $r^* = \frac{r}{R_2}$, $\Omega^* = \frac{\Omega}{\omega R_2{}^2}$, $v^* = \frac{v}{\omega R_2}$, $p = \rho\omega^2 R_2^2 p^*$ and write

$$Re\left[v_2 \frac{\partial \Omega}{\partial r} + \frac{v_Q}{r}\frac{\partial \Omega}{\partial \theta}\right] = \Delta\Omega. \qquad (6)$$

$$Re = \omega\frac{R_2^2}{v}, \delta = \frac{R_1}{R_2}. $$

Substituting $v_\theta = \frac{1}{r}, v_r = 0$ (7), linearize (6), that satisfy the continuity equation, and obtain

$$\frac{Re}{r^2}\frac{\partial \Omega}{\partial \theta} = \Delta\Omega \qquad (8)$$

With the substitution

$$\Omega = e^{\gamma\theta}\lambda(r,\theta) \qquad (9)$$

reduce (3.8) to the canonical form

$$\frac{\partial^2\lambda}{\partial r^2} + \frac{1}{r}\frac{\partial\lambda}{\partial r} + \frac{1}{r^2}\frac{\partial\lambda^2}{\partial\theta^2} - \frac{\gamma^2}{r^2}\lambda = 0, \gamma = \frac{Re}{2} \qquad (10)$$

Solution of equation (10), depending only on r is

$$\lambda = C_1 r^\gamma + C_2 r^{-\gamma} \qquad (11)$$

By (7) choose

$$\lambda = C r^{-\gamma} \qquad (12)$$

that allows us to write the integral representation of the solution (8):

$$\Omega(m) = \frac{1}{\pi}\oint_{l_1} e^{\gamma(\theta_m - \theta_p)} r_{mp}^{-\gamma}\mu_1(p)dl_p -$$

$$-\frac{1}{\pi}\oint_{l_2} e^{\gamma(\theta_m - \theta_p)} r_{mp}^{-\gamma}\mu_2(p)dl_p. \qquad (13)$$

$$r_{mp} = \sqrt{r_m{}^2 + r_p{}^2 - 2r_m r_p \cos(\theta_m - \theta_p)}$$

l_1 – circle radius δ, l_2 – circle radius R_2.

Usually, the section connecting contours of l_1 and l_2 when area D round along its border is made becomes. If the contour of l_1 manages counterclockwise, l_2 – on hour. For this reason there is a minus sign in (13) before integral along l_2.

Let's write down the solution Poisson's equation (5) in a form

$$\psi(m) = \frac{1}{\pi^2}\left[\iint_D \ln\left(\frac{1}{r_{mp}}\right)\left[\oint_{l_1} e^{\gamma(\theta_m - \theta_p)} r_{mp}^{-\gamma}\mu_1(p)dl_p\right.\right.$$
$$\left.\left. -\frac{1}{\pi}\oint_{l_2} e^{\gamma(\theta_m - \theta_p)} r_{mp}^{-\gamma}\mu_2(p)dl_p\right]\chi_1(p)dS_p\right]$$
$$+ +\frac{1}{\pi}\left[\oint_{l_1} \ln\left(\frac{1}{r_{mp}}\right)\chi_1(p)dl_p\right.$$
$$\left. -\oint_{l_2} \ln\left(\frac{1}{r_{mp}}\right)\chi_2(p)dl_p\right]$$

(14)

Boundary conditions

$$v_r|_{m\in l_1} = 0; \quad v_r|_{m\in l_2} = 0;$$

$$v_\theta|_{m\in l_1} = \frac{1}{\delta}; \quad v_\theta|_{m\in l_2} = 0. \qquad (15)$$

$$v_r = -\frac{1}{r}\frac{\partial\psi}{\partial\theta}, \quad v_\theta = -\frac{\partial\psi}{\partial r}. \qquad (16)$$

give system of four linear integrated equations concerning density of potentials $\mu_1(m)$, $\mu_2(m)$, $\chi_1(m)$, $\chi_2(m)$.

Rewrite conditions (15) and (16) in a standard form

$$\left.\frac{\partial\Psi}{\partial n}\right|_{r=\delta} = \frac{1}{\delta}; \left.\frac{\partial\Psi}{\partial n}\right|_{r=R(\theta)} = 0; \qquad (17)$$

$$\left.\frac{\partial\Psi}{\partial \tau}\right|_{r=\delta} = 0; \left.\frac{\partial\Psi}{\partial \tau}\right|_{r=R(\theta)} = 0. \qquad (18)$$

Where

$$\left.\frac{\partial\Psi}{\partial n}\right|_{r=\delta} = \left.\frac{\partial\Psi}{\partial r}\right|_{r=\delta}; \qquad \left.\frac{\partial\Psi}{\partial n}\right|_{r=R(\theta)} = \left[\frac{\partial\Psi}{\partial r}\cos\zeta + \frac{1}{r}\frac{\partial\Psi}{\partial\theta}\sin\zeta\right]_{r=R(\theta)} \qquad (19)$$

88

$$\left.\frac{\partial \Psi}{\partial \tau}\right|_{r=\delta} = \frac{1}{r}\left.\frac{\partial \Psi}{\partial \theta}\right|_{r=\delta} ; \left.\frac{\partial \Psi}{\partial \tau}\right|_{r=R(\theta)} = \left[\frac{1}{r}\frac{\partial \Psi}{\partial \theta}cos\zeta - \right.$$
$$\left.\frac{\partial \Psi}{\partial r}sin\zeta\right]_{r=R(\theta)}$$

According to the theorem of sine, find

$$sin\zeta = \varepsilon sin(\theta - \varphi) ,$$

$$cos\zeta = \pm\sqrt{1 - \varepsilon^2 sin^2(\theta - \varphi)} \tag{20}$$

From (18) follows that stream function accepts constant values on circles $r = \delta$ и r=R(θ). As Ψ is defined to within constant composed, can put

$$\left.\psi\right|_{r=R(\theta)} = 0 \tag{21}$$

From (17) and (19) find

$$\left.\psi\right|_{r=\delta} = -ln\delta. \tag{22}$$

In other words, stream function is the solution of the equation of Poisson (5) with boundary conditions

$$\left.\frac{\partial \Psi}{\partial n}\right|_{r=\delta} = \frac{1}{\delta}, \text{ (Neumann's external task)} \tag{23}$$

$$\left.\frac{\partial \Psi}{\partial n}\right|_{r=R(\theta)} = 0, \text{ (Neumann's internal task)} \tag{24}$$

and conditions (21), (22).

Solving these problems, get system of four linear integrated equations

$$\iint_D \frac{\partial}{\partial n}\left(ln\frac{1}{r_{mp}}\right)\Omega(p)dS_p + \oint_{l_1} \frac{\partial}{\partial r}\left(ln\frac{1}{r_{mp}}\right)\chi_1(p)dl_p -$$
$$\oint_{l_2} \frac{\partial}{\partial r}\left(ln\frac{1}{r_{mp}}\right)\chi_2(p)dl_p + \pi\chi_1(m) = \frac{\pi}{\delta}; m \in l_1; \tag{25}$$

$$\iint_D \frac{\partial}{\partial n}\left(ln\frac{1}{r_{mp}}\right)\Omega(p)dS_p + \oint_{l_1} \frac{\partial}{\partial r}\left(ln\frac{1}{r_{mp}}\right)\chi_1(p)dl_p -$$
$$\oint_{l_2} \frac{\partial}{\partial r}\left(ln\frac{1}{r_{mp}}\right)\chi_2(p)dl_p + \pi\chi_2(m) = 0; m \in l_2; \tag{26}$$

$$\left.\psi\right|_{r=\delta} = -ln\delta; \tag{27}$$

$$\left.\psi\right|_{r=R(\theta)} = 0. \tag{28}$$

In (25) and (26) ψ is defined according to (14).

The solution of this system can be transformed to solution of the system $8n+4$ the linear algebraic equations if to look for density of potentials in the form of Fourier's polynomials as it was made in section 1.

Rewrite the linearized Navier – Stokes equations (NS)

$$\frac{\partial p}{\partial r} = -Re\left(\frac{1}{r^2}\frac{\partial v_2}{\partial \theta} - \frac{1}{r^2}\right) + \frac{\partial^2 v_r}{\partial r^2} + \frac{1}{r^2}\frac{\partial^2 v_r}{\partial \theta^2} +$$

$$+\frac{1}{r}\frac{\partial v_r}{\partial r} - \frac{1}{r^2}\frac{\partial^2 v_\theta}{\partial \theta} - \frac{v_r}{r^2};$$

$$\frac{1}{r}\frac{\partial p}{\partial \theta} = -\frac{1}{r}\frac{\partial v_\theta}{\partial \theta} + \frac{\partial^2 v_\theta}{\partial r^2} + \frac{1}{r^2}\frac{\partial^2 v_\theta}{\partial \theta^2} + \frac{1}{r}\frac{\partial v_\theta}{\partial r} - \frac{1}{r^2}\frac{\partial^2 v_\theta}{\partial \theta} - \frac{v_\theta}{r^2}. \tag{29}$$

Calculating div grad(p), obtain the equation of Poisson in which the right part depends on the solution of the task gotten above

$$\Delta P = f; f = \vec{v}\overrightarrow{\Delta v} - Re\left(\frac{\Delta v^2}{2} - \vec{\Omega}\overrightarrow{rot}\ \vec{v_0}\right) \tag{30}$$

$$\vec{V_0} = \left(0, \frac{1}{r}\right), \vec{v}(v_r, v_\theta), \vec{\Omega} = (0,0,\Omega)$$

$$\left.\frac{\partial p}{\partial n}\right|_{l_1} = \left.\frac{\partial p}{\partial r}\right|_{l_1},$$

$$\left.\frac{\partial p}{\partial n}\right|_{l_2} = \Phi,$$

$$\Phi = \left.\frac{\partial p}{\partial r}\right|_{l_2}cos\zeta + \frac{1}{r}\left.\frac{\partial p}{\partial \theta}\right|_{l_2}sin\zeta\Big|_l \tag{31}$$

For (27), write down

$$\iint_D \left(ln\frac{1}{r_{mp}}\right)f(p)dS_p + \oint_{l_1} \left(ln\frac{1}{r_{mp}}\right)\varphi_1(p)dl_p -$$
$$\oint_{l_2} \left(ln\frac{1}{r_{mp}}\right)\varphi_2(p)dl_p; \tag{32}$$

Functions $\varphi_1(m)$, $\varphi_2(m)$ are defined from the solution of the linear integrated equations similar (23), (24).

The subsequent approximations can be found similar to the procedure described in section 2 if to put

$$v_r = \sum_{k=1}^m w_k\varepsilon^k ; v_\theta = \sum_{k=0}^m z_k\varepsilon^k ; \Omega = \sum_{k=0}^m \Omega_k\varepsilon^k;$$

$$\psi = \sum_{k=0}^m \psi_k\varepsilon^k; p = \sum_{k=0}^m p_k\varepsilon^k; \text{ as } \varepsilon<<1, \text{ it is}$$
possible to assume that these decomposition have to tend quickly to achievement given to accuracy.

IV References

[1] C.W.Oseen. Über die Stockssehe Formelund eine verwandze Aufgabe in der hydrodynamik. Arkiv f math., Astr, och Fysik, 6(1910), №29.

[2] C.W.Oseen. Über die Stockssehe Formelund eine verwandze Aufgabe in der hydrodynamik. Arkiv f math., ast, och fysik, G.B. , №29, 1910, 7b, №1, 1933.

[3] C.W.Oseen. Neuere Methoden und Ergebuisser Hydrodynamik. Leipzig, 1927.

[4] Кочин Н.Е., Кибель И.А., Розе Н.В. Теоретическая гидромеханика. М., 1963.

[5] Л.Д. Ландау, В.М. Лифшиц. Гидродинамика. Москва «Наука» 1988г.

[6] F.K.G. Odquist. Über die Randwertaufgaben der Hydrodynamik zäher Flüssigkeiteu. Math.z., 32 b., s. 329, 1910.

[7] Lamb H., On the Uniform Motion of a Sphere through a Viscous Fluid, Phil. Mag., 21 (1911), стр. 120.

[8] Hilding Faxen. Exacte Lösung der Oseen cheu Differential – qleichungen einer zähen Flussigkeit für der Fall Traus latiousbewegung eines zylinders. Nova acta Regial Soc. scient. Upsaliensis, vol. Extra Ordinareu Editum, 1927.

[9] S. Tomotica, T. Aoi. The steady flow of visous fluid a sphere and circular cylinder at small Reynolds number. Quart. Y. Mech. and Appl. Math., v. III, p. 140, 1950, там же V.IV, p. 401, 1951.

[10] О.И. Панич. Решение системы уравнений Озейна для установившегося обтекания плоского контура потоком несжимаемой вязкой жидкости методом потенциалов. Известия высших учебных заведений. Математика. 1962 №3(28), там же, №41962, №6(31), 1962.

[11] О.А. Ладыженская. Математические вопросы динамики несжимаемой вязкой жидкости. «Наука» Москва 1970.

[12] Строчков И.А., Хватцев А.А. Решение задачи поперечного обтекания цилиндра однородным потоком несжимаемой вязкой жидкости (НВЖ) в приближении Озеена. Математические методы в технике и технологиях ММТТ-25: Сборник трудов XXV международной научной конференции. Саратов: Изд-во СГТУ, 2012. – том 1–С. 33 -38.

VI

ELECTRICAL DRIVE, ELECTROTECHNICS, ELECTRONICS AND MECHATRONICS

Model of Radio Managing System for Electro Vehicles' Accumulators Wireless Feeding

Hrayr Abrahamyan[1,2], Arevik Sargsyan[1,2], David Davtyan[1], Harutyun Minasyan[1]

1 - State Engineering University of Armenia, Teryan str. 105, 0009 Yerevan, Armenia
2 - National Institute of Metrology, Komitas Ave. 43/2, Yerevan, Armenia
h.abrahamyan@seua.am, (+37498)109810

Abstract. **This article refers to studying of the system for wireless feeding of electro vehicles' accumulators, and the description of it's applicable efficiency. Preliminary design of the radio managing system is done. The electro vehicle feeding system is calculated for the freeway. By using LabVIEW program package model of radio managing system was designed.**

Keywords: **electro vehicle, wireless feeding, resonant induction, rectenna, radio managing system, LabVIEW program package.**

I INTRODUCTION

According to projections oil, natural gas and other mineral fuel reserves will run out within the next 50 years. Developing tendencies of vehicles are adequately connected with alternative power. Electro vehicles, as means of alternative fuel fed transportation, are widely developing nowadays [1]. Certainly, electro vehicles, are considered to be transportation of future, but it is important to mention, that for nowadays' development there are many obstacles. Supply of electrical batteries can be implemented in special-home charging stations, but they are time consuming.

There are many Companies, who's technological approach and principles are based on Inductive Power Transfer (IPT) idea. IPT wireless charging is widely used by magnetic resonance to transfer power from a transmitting pad on the ground to a receiving pad on electric vehicle. That's why an IPT wireless charging system comprises two separate elements: a primary-side power supply with track; and a secondary-side pick-up pad with controller. In order to charge the electric vehicle, it is simply required to park the car over a pad [2,3].

Recently, extensive work has been done for wireless and dynamic power of accumulators of electro vehicles. In some works electric vehicles charge wirelessly via underground electricity induction for dynamic charging of accumulators has been used. It gives opportunity for the electro vehicle to have powered accumulators along the whole road, but that technologies come to be difficult and expensive. The problems of charging the accumulators of electro vehicles, will find their solution by using wireless power transmission technology [4-7].

Wireless power transmission technology via microwave was advanced from 1960's [8]. The rectenna, rectifying antenna, is one of the primary components in the application of wireless power transmission system. The rectenna has receives much attention in the development process of transmission for receiving and converting the microwave power to direct current power. The application of this technology can be used in radio-frequency identification and electric vehicles [6,9].

II MATERIALS AND METHODS

In our previous work we have suggested sketch project of wireless system electro vehicle accumulator power by using the radio management system. It enabled the accumulator charging of electro vehicle during it's movement. The system is based on wireless transmission of electrical energy. Appropriate calculations, based on characteristics of technical description of electro vehicles were done in the work. Cases of both sided traffic as well as opportunity to provide electrical supply of several electro vehicles were examined [4].

The transmitter parts of the components of radio managing system are: power source (PS), modulator (M), transmitter (T), Radio managing system (RMA) which, after receiving the relevant information from the electro mobile, determine the coordinates and movement speed, and with the help of automation device (AD) realizes beam-controlling (BC). Radio RMA verifies the customer with all the necessary information and coordinates the entire feeding process. The receiver system's component parts are: rectena (R), receiver (Rec), demodulator (DM), car accumulator (Ac). The accumulator provides the necessary information about the need of accumulator charge or the end of feeding process, then the information is processed by the information processing device (IPD) and is reported to RMS. The latter checks the necessary information connected with the customer and conducts the feeding process.
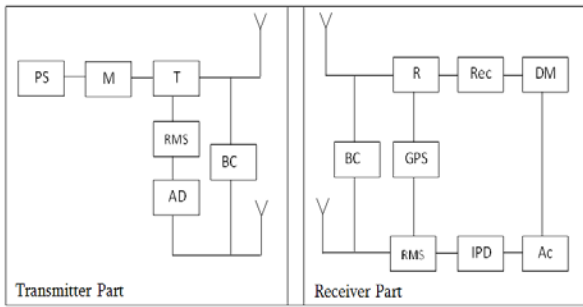
Fig.1. The sketch scheme of radio managing system

Fig.3. The coverege of feeding station

According to accumulator charging data, in order to provide the average speed of 80 km/h it will take 110 W * h / km * 80 km / h = 8.8 kW capacity [1] .Fully charged electro vehicle, which is 4.4 kWt /h passes 40 km. It means, that within an hour it needs two refills, but if charging is constant. It means, that no less than 2.5 W of energy supply is needed to provide. We accept reported antenna gain no less than 30 dB, the signal wave length being reported $\lambda = 3$ m Based on strength construction, plant height was calculated up to $h_1 = 30$ m, height of electro vehicle $h_2 = 2$ m.

Based on these data, by using well-known radiolocation formula, the maximum radiation power was calculated, and was built a graph describing the distance dependence from the transmission power [4].
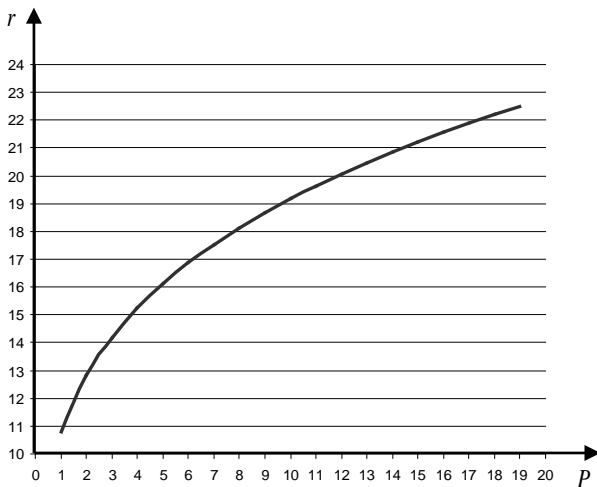

Fig. 2. Dependence of radiation distance from power transmission

From the graphic (figure.2) it is easy to see that in case of P = 5 W value for r we shall get $r = 16$ km. As service road segment was taken Ararat region M-2 motorway in Armenia, and specifically Ararat-Artashat 20 km long section (figure 3).

In order to get power system with great efficiency the spherical mirror antenna and Phase Array Antenna complex were chosen. [10,11]. As the spherical mirror antenna complex can provide a maximum 120 ° angle visibility, the distance from the road outside the station is approximately 6 km. So, in case of having one station, it is possible to supply 20 km of the road segment.
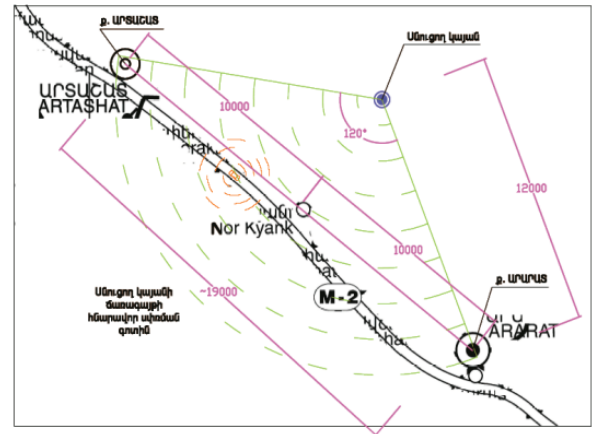
III RESULTS AND DISCUSSION

By using spherical mirror antenna and Phase Array Antenna it becomes possible to provide independent and separately managed beams in space. By using LabVIEW programming package was developed the digital beam-forming scheme of   antenna array, which allows to managing antenna radiation pattern (RP). This model is based on antenna array mathematical model. The signal, which is radiating by the Phase Array Antenna each element, can be represented by the following formula.

$$\dot{X}_n = \frac{I_n}{I_0} e^{jknd \cdot \sin(\theta)} ,$$

Here Xn is complex description, which is obtained from array of n-th element under θ, angle: I_n/I_0 the power distribution between the elements, K-number of waves, D-distance between feeding elements.

Output signal is formed by all incoming signals and weight coefficient of feeding elements multiplicative complexive amount.

$$\dot{U}_n(\theta) = \sum_{n=0}^{N-1} \dot{W}_n^H \cdot \dot{X}_n,$$

Where $\dot{W}_n^H$ the conjugate matrix weight coefficient for the n-th path, N- is number of feeding elements in antenna array. Antenna RP can be changed from -180^0 to $+180^0$.

The front panel appearance designed by LabVIEW program package is shown in figure 4, and the functional part of the block diagram is shown in figure 5.

Fig.4. Front panel of mathematical modeling of radiation pattern

Fig.5 Block diagram of mathematical modeling of radiation pattern
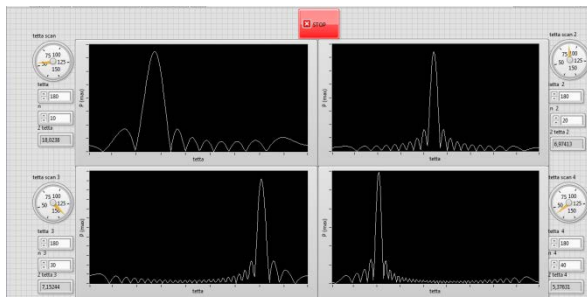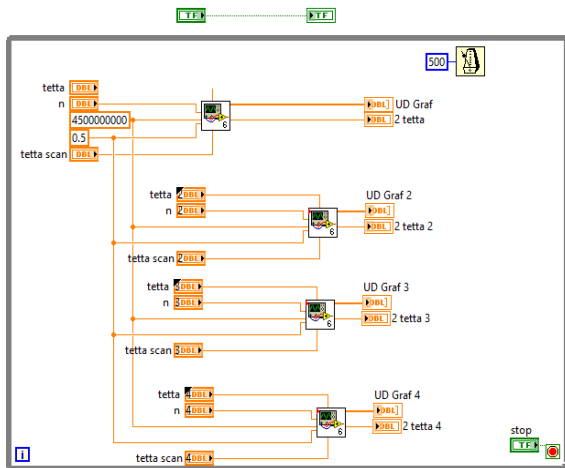
This model allows to configure one and multi beam system antenna array. The Front panel presents antenna RP based on Cartesian coordinate system. This work simulates antenna array with 4 beams. Each beam can be scanned (Beam scanning) through the program. This model makes possible to control all 4 radiation patterns simultaneously.

The model of wireless accumulator charging system of electro vehicles was developed using LabVIEW program package. Receiver and transmitter antennas' RP automatic alignment is working continuously. With the help of narrow beam it enables to charge not only real but also mobile units, providing continuous charging, with the help of GPS system. The calculation of antennas RP alignment are being determined by coordinates of GPS system: At first, the distance between transmitter and receiver stations is being calculated by Haversine formula. Then the angular coordinates between stages are calculated.

$$d = 2r \arcsin\left(sin^2\left(\frac{\phi_2 - \phi_1}{2}\right) + \cos\phi_1 \cos\phi_2 sin^2\left(\frac{\lambda_2 - \lambda_1}{2}\right) \right)$$

d - distance between two points.
r - the average radius of the Earth
$\phi_1\lambda_1$ and $\phi_2\lambda_2$ the stations coordinates.

The front panel receiver part and antennas RP alignment with the help of GPS system designed by LabVIEW program package is shown in figure 6, and the functional part of the block diagram is shown in figure 7.

Fig.6. Front panel of receiver part and antennas RP alignment
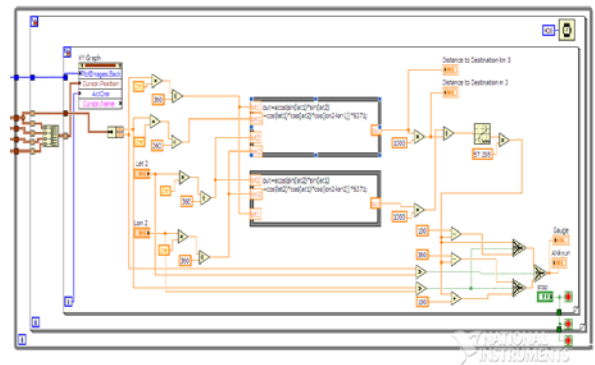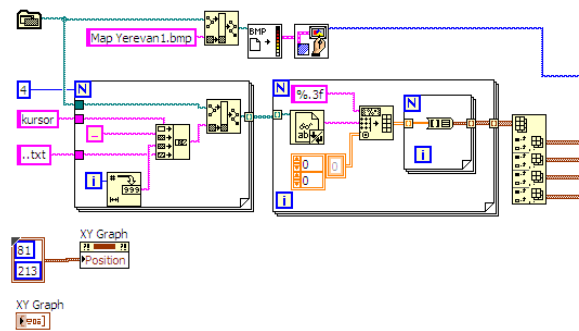
Fig.7. Block diagram of receiver part and antennas radiation pattern alignment

IV CONCLUSION

The radio managing system of feeding process of accumulators of electro mobiles provides both moving and stationary objects accumulator feeding efficiency. The model of wireless feeding process by using LabVIEW program package will give opportunity to provide high efficiency and dynamic regime of feeding process. The model will also give the opportunity to control one and multi beam antenna array, enabling the tracing ability. Also, the model which has an opportunity of alignment antennas RP will allow minimization of feeding losses.

95

V REFERENCES

[1] www.commutercars.com

[2] http://www.qualcomm.com/solutions/wireless-charging/qualcomm-halo#n_home-intro

[3] http://www.treehugger.com/cars/e-cars-and-buses-charge-magically-with-underground-induction.html

[4] Sargsyan A., Abrahamyan H., Khocharyan H. Study of the Radio Managing System for Wireless Feeding of Electro Vehicle's Accumulators. Lraber-76, SEUA (Polytechnic), Collection of scientific and methodical papers. - Part1 №2. - Yerevan 2008. -Pp. 343-345.

[5] Landis G. A, "Charging of Devices by Microwave Power Beaming," U.S. Patent 6,967,46, November 22 2005)

[6] Chang-Jun Ahn, Takeshi Kamio, Hisato Fujisaka, Kazuhisa Haeiwa. Prototype of 5.8 GHz Wireless Power Transmission System for Electric Vehicle System. 2nd International Conference on Environmental Science and Technology. IPCBEE vol.6 (2011) © (2011) IACSIT Press, Singapore. pp. 126-131. 2011.

[7] Vijay Kumar A., Niklesh P., Naveen T., Wireless Power Transmission. International Journal of Engineering Research and Applications (IJERA), Vol. 1, Issue 4, pp. 1306-1310.

[8] W.C. Brown, "The history of power transmission by radio waves," IEEE Transactions on Microwave Theory and Techniques, vol. 32, no. 9, pp.1230–1242, Sept. 1984.

[9] Christi Walsh, Sebastien Rondineau, Milos Jankovic, George Zhao, Zoya Popovic, "A Conformal 10 GHz Rectenna for Wireless Powering of Piezoelectric Sensor Electronics," to be presented at the 2005 IEEE International Microwave Symposium, Long Beach, June2005.

[10] Sargsyan A., Architectural Design of the Multiple Feed Spherical Reflector Terminal, 29th ESA Antenna Workshop on Multiple Beams and Reconfigurable Antennas, ESTEC, 18-20 April, 2007.

[11] Abrahamyan H. Synthesis of Reconfigurable Slotted Waveguide Array Antenna. Environment. Technology. Resources // Proceedings of the 8th International Scientific and Practical Conference, Latvia /Rezekne/. Volume II.,- Rezekne 2011, June 20-22, 2011.- P. 211-216.

Autonomous Power Station Based on Rotary-Vane Engine with an External Supply of Heat

Mikhail Andreev, Yuriy Zhuravlev, Yuriy Lukyanov, Leonid Perminov
Pskov State University, Faculty of Electrical Engineering, Department of Drive and automation systems. Address: 180760, Russia, Pskov, Lenin Square 2

Abstract. Rotary-vane engine (RVE) with an external supply of heat is an aggregate consisting of two modules with a common output shaft, the heating device (heater) of working medium and the cooling device (cooler) of working medium, which connected with inlet and outlet ports of modules by system of pipeworks. Each module has two rotors with two vanes on each. Between the corresponding plane surfaces of the four vanes four working volumes are formed wherein thermodynamic cycle steps: ingress, compressing, heat intake, expansion stroke, discharge, outward heat transmission are going simultaneously. The angular displacement of modules relative to one another occurs pumping the working medium through the heater and cooler, which allows the conversion of thermal energy into mechanical work. Design features of the RVE with an external supply of heat allows create a closed gas-vapor cycle.

The main specified advantages of the RVE with an external supply of heat are: fewer noxious emissions, multifuel capability, high motor potential (service life). Different problems of creation external combustion engines such as structural complexity of construction units, absence of adequate mathematical model of designed RVE with an external supply of heat are also pointed. The construction of the RVE with an external supply of heat developed in Pskov Polytechnic Institute (now the Pskov State University), the operation concept of the engine, the physical processes in the chamber modules RVE with an external supply of heat during each step and the mathematical model describing the physical processes proceeding in chamber RVE with an external supply of heat modules are considered.

Keywords – internal combustion engine, rotary-vane engine, autonomous power station based on RVE.

I INTRODUCTION

The development and application of internal combustion engines (ICE) are now acquired comprehensive. Numerous research and development engine have made into a very complex and at the same time, reliable and universal system. However, experience in long-term operation in the vehicle identified weaknesses that are nearly impossible to exclude by upgrading the design of the engine without affecting the basic principles of its construction, such as mechanical friction and the process of internal combustion.

The main drawback of the ICE, which is a result of the mass distribution of automobile transport has taken the lead, became a factor in environmental pollution by exhaust gases. The share of pollutants released into the air from the exhaust gases of automobile engines, up to 63% of the total pollution. Therefore, in recent decades, the world's stricter requirements for environmental standards for vehicles, and in particular this applies to internal combustion engines. [1] ICE, consuming a fifth of primary energy [2], are a major source of pollution in the immediate area of human breathing. [3] However, the planned measures, even if their full implementation, can only reduce the rate of increase of the polluting engines, especially vehicles, by the rapid growth of the number and capacity.

Thus, there is a need of a fundamentally different production engine capable to change the situation, working on different types of fuel and with no hazardous emissions. In this regard, one can submit the following requirements for modern engines:

- Reduce the amount of toxic emissions
- Reduce the release of heat into the atmosphere
- Reduce metal consumption engine
- Reduce Noise and Vibration
- Use for any type of motor fuels, including hydrogen
- Use renewable energy sources.

II ENGINES WITH AN EXTERNAL SUPPLY OF HEAT

By ecological use of any type of fuel, the engine has the best characteristics with an external supply of heat realizing the Stirling cycle. External supply of heat allows to apply different heat sources, without any substantive changes engine design. Practically all fossil fuels from solid to gaseous can be used in such engines.

Consider the main advantages of engines with an external supply of heat (external combustion engine).

Thermal coefficient of efficiency is the efficiency of the Carnot cycle and considering temperature achieved at now is about 60%. In external combustion engine power is controlled by changing the pressure of working medium in the inner cavities of the engine. At the same time, the temperature of the heater and cooler automatically maintained constant. Therefore, when the power and speed of the shaft boundary temperatures and their quotient remain constant. Through this engine efficiency when operating at Unrated mode varies only slightly. External combustion engine, having high-pressure working substance in internal cavities and sufficiently high temperature heater tubes, easy starts at any ambient

temperature. It depends solely on the starting reliability, which can be ignited fuel in the combustion chamber.

Since the external combustion engine is fully sealed, dust, falling into the air charge the combustion chamber from the environment, does not fall into the cylinders and crankcase. As a consequence, there is no additional abrasive wear of moving parts drive mechanism.

Speed limit offensive creep of a material heater parts operating at high temperature determines external combustion engine motor resource. In general, any external combustion engine can be guaranteed to withstand brief 50-80%-ing the overload without significant reduction in longevity, as the temperature of parts remains unchanged.

External combustion is continuous and does not have an explosive character, so the combustion and exhaust noise is almost no generated. In addition, the pressure in the cylinder external combustion engine changes smoothly, almost sinusoidally. Inlet and outlet valves, and valve gear is missing. The noise level of the engine by an average of 20-30 dB lower than that of diesel the same power.

Based on the above can say that in the field of engines had technical contradiction: on the one hand we have a compact and low-cost internal combustion engines, on the other hand, massive and expensive to manufacture engines with an external supply of heat.

III PROBLEMS IN CREATING ENGINES WITH AN EXTERNAL SUPPLY OF HEAT

The shortcomings plunger Stirling engine. The first is the complexity of the case design of individual units, problems with the seals, power control, etc. Features of embodiment conditioned by employed working medium. So, for example, helium has superfluidity, which places greater demands on the sealing elements of the working plunger, etc. Second formation of promising image, intended for production Stirling machines is impossible without the development of new technical solutions to the major units. The third problem – is a high level of production technology.

This problem needs to be used in machines Stirling heat resistant alloys and nonferrous metals, their welding and soldering. A separate question – making the regenerator and attachments for it to provide on the one hand a high heat capacity, and on the other hand – a low hydraulic resistance. All this requires highly skilled manpower and modern technological equipment.

The main problems associated with the creation of highly effective plunger Stirling machines and constraints still be widely used in various fields of technology are, above all, the creation of adequate mathematical models of a machine Stirling and the appropriate method of calculation. The complexity of calculating the projected machine is determined by the complexity of the implementation of the Stirling

thermodynamic cycle in real machines, due to nonstationarity heat-mass exchange in the inner loop, by the continuity of movement of the plunger. The lack of adequate mathematical models and calculation methods are the main causes of failure of some known foreign companies and domestic companies trying without serious scientific study, only through a rough calculation and experimental data to solve the problem of creating Stirling engines and refrigerators. Currently, how many firms and many methods of calculating Stirling machines, with the calculation methods are trade secrets.

Foreign experience of a modern high-efficiency Stirling machines shows that without accurate mathematical modeling of workflows and the optimal design the basic units finishing machines designed becomes a long-term debilitating experimental studies.

IV ROTARY-VANE MACHINE

In 2007, the Pskov Polytechnical Institute (now Pskov State University) won the tender under the federal program and signed a state contract № 02.516.11.6031 with the Federal Agency for Science and Innovation to prosecution of research on "Development of a mathematical model the flow thermodynamic cycle with an external supply of heat, allowing to create an environmentally clean engine rotary-vane type".

The result was the creation of methods analysis and design RVE with an external supply of heat, in particular to create a mathematical model of single engine components: the motion conversion mechanism, rotary-vane groups, and a mathematical model, which confirms possibility of implementing the thermodynamic cycle with an external supply of heat in RVE. For experimental studies have been created and studied the breadboard construction of mechanism transducer motion and breadboard construction of the combustion chamber. Obtained results were evidence base correctness of theoretical calculations. As an example, figure 1 shows the general construction of the two-module RVE with an external supply of heat.
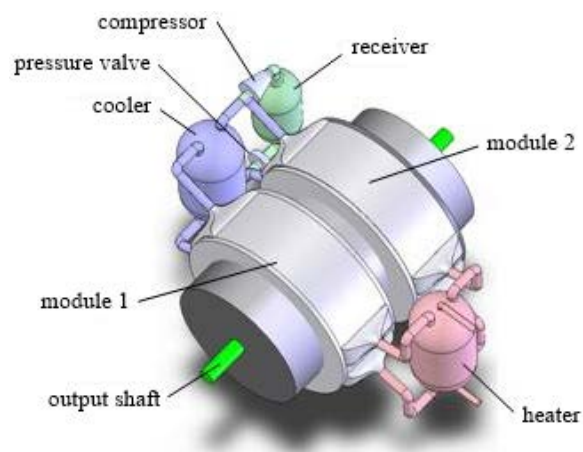

Fig. 1.   RVE with an external supply of heat

V THE DESIGN

RVE with an external supply of heat consists of two working modules 1 and 2. The modules have a common output shaft. The engine contains working medium heating device (heater) and cooling the working medium (cooler), which are related to the conduit system inlet and outlet windows modules. To control the output torque provides controlled pressure valve, receiver and compressor, which are connected to the cold pipes. Torque control on the output shaft with the temperature by changing fuel supply to the heater.

Each module includes a main cylinder the working volume (figure 2) and the motion conversion mechanism (figure 3). In the main cylinder, the working volume has two windows connected with the heater pipes, and two windows connected with cooling pipes.
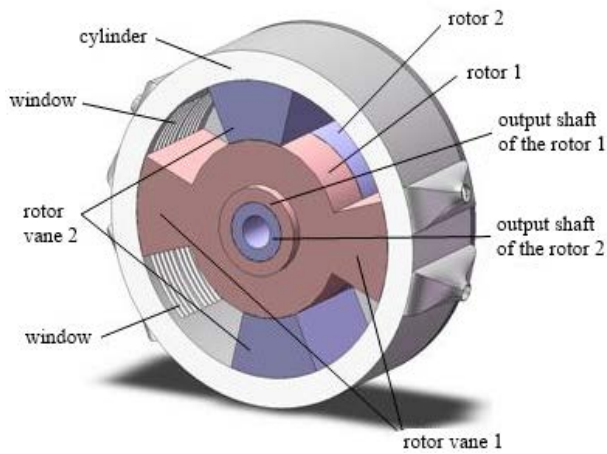

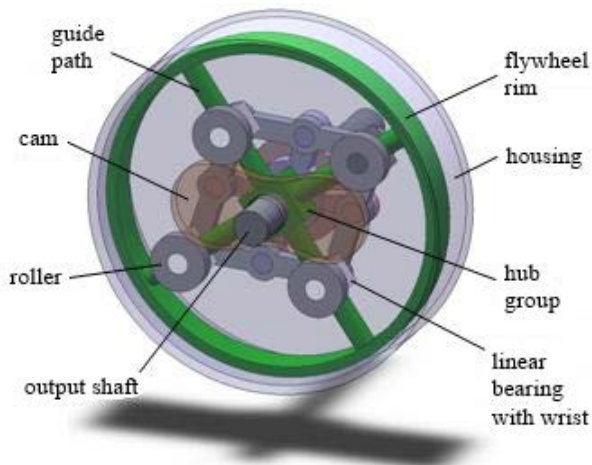Fig. 2.   Module of the RVE with an external supply of heat

Fig. 3.   Motion conversion mechanism

In the main cylinder of the working volume, energy is converted into the working medium motion of the rotor.

RVE with an external supply of heat has a cylindrical body, which are two rotor 1 and 2 with two vanes. Between the respective planes of the four vanes are formed four working volume. The output shafts of the rotor 1 and rotor 2 are hollow and mounted coaxially to each other. Inside the output shaft of the rotor 2 is the engine output shaft.

The output shafts are connected with the mechanism of the transformation movement. Engine capacity formed between the vanes rotor 1 and 2.

Possible implementation the working volume of the cylinder in the form of spherical segments. The internal surface of each cylinder forms a hollow torus.

Motion conversion mechanism converts the vibrational-rotational rotor motion in the uniform rotation the output shaft.

Motion conversion mechanism has a housing in which the anti-friction bearings mounted engine output shaft. To the housing transmission mechanism is rigidly fixed profiled cam. On the output shaft of the motor is rigidly fixed hub group with four guide paths. On the guide paths are linear bearings with wrists that have the ability to move along the guide paths. At one end of the wrist linear bearing mounted roller which driven around on the surface of the cam.

The basis of the motion conversion mechanism is articulated four-link chain (rhomboid), consisting of four units the same length and two shafts with forks.

The ends of the rhomboid links pivotally connected to each other and are located on the wrist of a linear bearing. Shafts with forks conversion mechanism rigidly connected to the output shaft rotor. Shafts with forks have two wrists, which are inserted in the middle of the relevant parts of the rhomboid.

It should be noted that the hub with guide paths one module and the second module are rotated relative to each other at an angle of 45 degrees.

In four working volume of each module to perform simultaneous steps of the thermodynamic cycle: intake, compression, heat input, working stroke, release, heat dissipation. Due to the angular displacement modules relative to each other occurs transfer of the working fluid through the heater and cooler, which allows the conversion of thermal energy into mechanical work. Design features of the rotary-vane engine can organize a closed steam-gas cycle.

VI POWER STATION BASED ON RVE

Power station based on RVE can work in the long offline mode, in single mode by double overloads. If required the power station can work in parallel with the external mains.
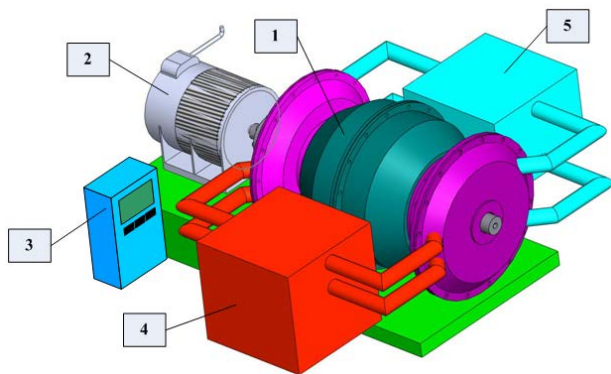
Fig. 4. Autonomous power station based on RVE with an external supply of heat

Autonomous power station based on the RVE with an external supply of heat (figure 4) consists of: two-module rotary vane engine with an external supply of heat 1, coaxially connected to the electric generator 2, the control system 3, a heater with a heat exchanger 4 and cooling with heat exchanger 5. By using different types of fuel in the design may include a device for the production of synthesis gas, batteries or capacitors, reactors for biogas, pyrolysis plant, etc.

Block diagram of the new generation power station consists of blocks of fuel preparation, storage and use of energy, including the control modes.

In accordance with the basic variants of for use different types of fuel is necessary to develop the following types of gas-generating device:

- multi-fuel gas generator, using local and renewable fuel (wood, etc.);
- multi-gas generator that uses a liquid fuel (diesel, gasoline, etc.) are available by using the existing infrastructure of filling stations.

To improve the efficiency of power stations will be used in gas generators multistage combustion, hydrogen generation initiating additives, thermochemical recuperation of exhaust gases.

VII REFERENCES

[1] Lukyanov Y.N., Plohov I.V., Zhuravlev Y.N. The mechanism for converting motion. Patent RF № 2374526 from 27.11.2009.
[2] Lukyanov Y.N., Plohov I.V., Zhuravlev Y.N. Rotary-vane engine with an external supply of heat. Patent RF № 2387844 from 27.04.2010.
[3] Minihanov R.N., Kogotin S.A., Degtyarev G.L., Gafurov R.A. Scientific, technical and production to ensure the development of automotive industry. Proceedings of the Second International Scientific Conference «Automobile & technosphere». Kazan. 2001, pp. 13-19.
[4] Yuldashev A.A., Yunusov K.A., Fomin V.P. Status and prospects of the use of natural gas as a motor fuel. Proceedings of the Second International Scientific Conference «Automobile & technosphere». Kazan. 2001, pp. 181-186.
[5] Samoilov N.P. The problem of reducing air pollution by automobile transport. Proceedings of the Second International Scientific Conference «Automobile & technosphere». Kazan. 2001, pp. 333-334.
[6] Stirling engines. Edited by Kruglov M.G. 1977.
[7] Kirillov N.G. Stirling machines for high-performance and environmentally clean autonomous power supply systems. Chemical and Petroleum Engineering. Vol. 12. 2000, pp. 21-24.

Simulation Technique of Synchronous Reluctance Bearingless Machine

Yulia Domracheva, Sergey Loginov

Pskov State University, Electrical Engineering Faculty, Department of Drive and automation systems.
Address: Lenin Square 2, Pskov, 180000, Russian Federation

Abstract. **Magnetically levitated rotor electric machines can be used under such conditions wherein application of conventional bearings is impossible because of presence of lubrication. Active magnetic bearings application requires rotor length increase and stalling speed is decreased. Bearingless electric machines are the next step up of the magnetically levitated rotor machines. A bearingless electric machine module generates electromagnetic torque and radial forces. This feature makes possible to decrease the rotor length on retention of capacity of torque and forces. It is necessary to verify a control system operation algorithm via simulation model owing to complexity of machine electromagnetic interaction. It is practical to use a variable attribute set model for this purpose. The following article considers one of these models for researching the system via MATLAB Simulink. Basic relations for programmatic model creation are presented. Comparative assessment of various machine model types is made.**

Keywords **- computer simulation, bearingless electric machine, simulation technique, programmatic model.**

I INTRODUCTION

Magnetically levitated rotor electric machines (EM) can be used under such conditions wherein application of conventional bearings is impossible because of lubrication presence. On these machines active magnetic bearings (AMB) are currently used. Application AMB requires increase of the rotor length, thus reducing stalling speed [1].
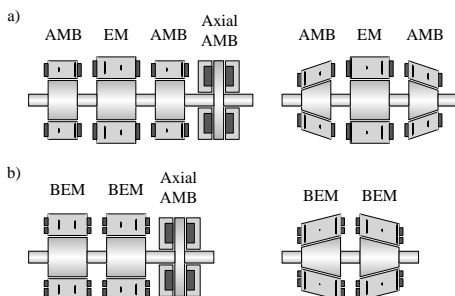

Fig. 1. Magnetically levitated rotor electric machine modifications: a) active magnetic bearing construction variants, b) bearingless electric machines.

Bearingless electric machines (BEM) are the next step up of development the magnetically levitated rotor machines. Into the stator slots of the bearingless module two sets of windings are placed: motor and suspension windings. It enables to generate electromagnetic torque and radial forces, which suspend the rotor at center of the stator. This feature makes it possible to decrease the rotor length on retention of capacity of torque and forces [2]. Overall dimensions decrease is associated with application the field of the motor winding as an integral part of the field of the suspension winding. It also allows to reduce power consumption.

Interference of the radial forces and the torque is an essential disadvantage of BEM. A special construction of the BEM modules makes it possible to control them separately. BEM construction principle was proposed in 1974 [3]. By this definition, one of the stator windings must have *p* pair of poles, and the other *p+1*. The number of the rotor poles must be equal to the number of the motor winding poles. In this case total electromotive force (EMF), induced by one of the windings in the other winding, is zero. The magnetomotive force (MMF) of the suspension winding doesn't produce a torque. But this mechanism works in case of the central position of the rotor. The MMF distribution becomes unsymmetrical because of displacement of the rotor. As a consequence, the suspension winding field generates a torque and the motor winding field generates a radial force.
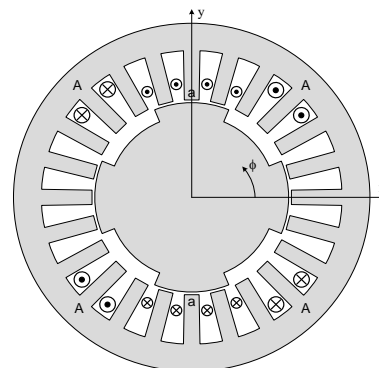

Fig. 2. Cross sectional drawing of synchronous reluctance bearingless machine. The example of winding sets phase placement: a – suspend winding phase, A – motor winding phase.

Interference of the radial forces and the torque can be reduced by employing a special control algorithm of the winding current. Some versions of

building such algorithm for a synchronous reluctance bearingless machine (SRBM) were proposed. One of them uses a special compensator, calculating the motor current control signal subject to the suspension current magnitude, and conversely [4]. In 2010 a control system structure had constructed on the basis of an inverse system [5].

SRBM design parameters in all of the proposed control systems has presented with inductances L_d and L_q. Authors of [6] suggest to define relationship between these inductances and displacements x and y by experiment. It allows to obtain sufficiently accurate model to create the control system. There is no feasibility to create design procedure because of lack the analytic formula of inductance in relation to the BEM design parameters.

For creation of the SRBM mathematical model commonly used next conventions: a) reciprocal value of the air gap defined by approximate expression, b) the air gap permeance between rotor poles is zero, c) the MMF upper harmonics and tooth kinks are disregarded, d) the core steel saturation is neglected. Desired precision of the mathematical model creation defined by functionality of the control system, developed on its basis.

Testing control system functionality shouldn't be carried out with model which contains same assumptions. It is easy to use a model with variable array of the attributes for this purpose. At this article one modification of such models for researching the system via MATLAB Simulink is presented. All computations are executed via C++ programming language. Thereby hereinafter it is named *programmatic model*.
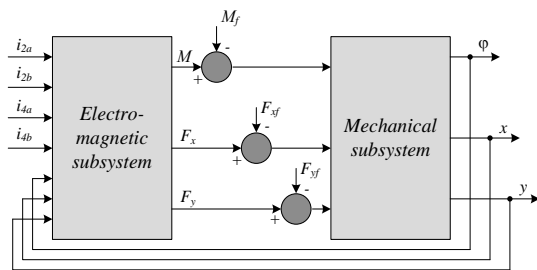
II MAIN MODEL EXPRESSIONS

Fig. 3. Variable attribute set model block diagram.

The SRBM model can be divided into two subsystems: electromagnetic and mechanical (fig. 3). The electromagnetic subsystem computes a torque M and radial forces F_x and F_y in terms of the rotor position and currents of the stator windings. The torque and the forces are added to disturbances, and then arrived at the mechanical subsystem. Output coordinates of the model are a turning angle φ and radial rotor displacements x and y.

The torque and the radial forces must be computed considering geometry of the windings and the cores. These variables are the partial derivatives of magnetic energy. Magnetic energy equation must consider its dependence on the turning angle and the radial rotor displacements. For the analytical derivation of this expression are used the simplified expression for the air gap reciprocal value. However, in the model must be capability of computation of the air gap value by all means. Therefore the electromagnetic torque and the radial forces are defined as a resultant of torques and forces, applied to some elementary parts of the rotor surface.
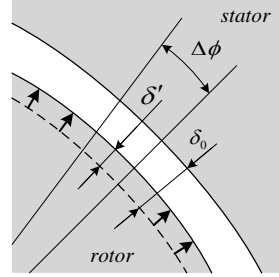
Fig. 4. The SRBM air gap piece. The rotor was displaced on δ'. Until this moment the air gap value was equal to δ_0.

Let's divide on elements the surface of the rotor. The length of each element is equal to the core reactive part length, and width is equal to the arc length $\Delta\phi$ (fig. 4). The angle must be so small that the air gap value inside of any of the elements may be considered constant. The air gap value depending on the angular coordinate ϕ and the radial rotor displacements x and y is defined by next expression.

$$\delta = \delta_0 - x \cdot \cos\phi - y \cdot \sin\phi = \delta_0 - \delta' \qquad (1)$$

Where δ_0 is the air gap value, when displacements of the rotor are zero. Value of δ' is constant inside of the element $\Delta\phi$. The electromagnetic torque and the radial forces are computed numerically by next expressions.

$$M_i = \frac{\Delta W_i}{\Delta\phi} \qquad (2)$$

$$F_{xi} = \frac{\Delta W_i}{\Delta x} \quad F_{yi} = \frac{\Delta W_i}{\Delta y} \qquad (3)$$

Where M_i is electromagnetic torque, affecting on the element $\Delta\phi_i$; F_{xi} and F_{yi} are radial forces, affecting on the element $\Delta\phi_i$; ΔW_i is magnetic energy, stored in the air gap, close to the element $\Delta\phi_i$.

$$\Delta W_i = \frac{1}{2} \sum_{j=1}^{N} \sum_{k=1}^{N} \Delta L_{ijk} \cdot i_j \cdot i_k \qquad (4)$$

Where N is the number of the stator windings; i is a winding current; ΔL_i is a self inductance or mutual inductance of a winding, being defined by the air gap element $\Delta\phi_i$.

$$\Delta L_{ijk} = \frac{\mu_0 \cdot \Delta\phi_i \cdot r \cdot l}{\delta_0 - \delta'} \cdot w_j \cdot w_k$$

Where $\mu_0 = 4\pi \cdot 10^{-7}$ is vacuum permeance; $S = r \cdot \Delta\phi \cdot l$ is an element area; r is the rotor radius; l is the core reactive part length; w is an appropriate winding turns number.

The total electromagnetic torque and radial forces are defined by next equations.

$$M = \sum_{i=1}^{n} M_i$$

$$F_x = \sum_{i=1}^{n} F_{xi} \qquad F_y = \sum_{i=1}^{n} F_{yi}$$

Where n is the count of the elements.

Computations of the output variables of the electromagnetic subsystem by (1) – (7) are executed every modeling iteration.

The turning angle φ and the radial displacements x and y of the rotor at the mechanical subsystem block can be defined by motion equations.

$$m \cdot \ddot{x} = F_x - F_{xf}$$
$$m \cdot \ddot{y} = F_y - F_{yf}$$
$$J \cdot \ddot{\varphi} = M - M_f$$

Where m is the rotor mass; J is the rotor moment of inertia; F_{xf}, F_{yf} and M_f are disturbances. Let's obtain equations for computation of the displacements and the turning angle in the step j from (8).

$$x_j = \frac{T_k}{m}\left(F_x - F_{xf}\right) + 2x_{j-1} - x_{j-2}$$

$$y_j = \frac{T_k}{m}\left(F_y - F_{yf}\right) + 2y_{j-1} - y_{j-2}$$

$$\varphi_j = \frac{T_k}{J}\left(M - M_f\right) + 2\varphi_{j-1} - \varphi_{j-2}$$

Where T_k is the computation step size.

To improve accuracy of the output model variables computation it is necessary to minimize the step size and the angle $\Delta\phi$.

Via programmatic model it is possible to regard or disregard any attribute of the machine. It enables to investigate its influence on the system performance. Let's consider some ways of research of influence assumptions.

Approximate expression for the air gap reciprocal value

It has to use an approximate expression for reciprocal value of the air gap to obtain analytic dependences of the inductances from the radial displacements of the rotor. It is because of inconvenience of using the exact equation for the control system creation.

Exact expression for the air gap reciprocal value is presented here.

$$\frac{1}{\delta} = \frac{1}{\delta_0 - x \cdot \cos\phi - y \cdot \sin\phi} = \frac{1}{\delta_0 - \delta'} \tag{10}$$

The approximate expression is obtained by its decomposition for geometric sequence.

$$\frac{1}{\delta} = \frac{1}{(\delta_0 - \delta')} = \frac{1}{\delta_0} \cdot \frac{1}{1 - \overline{\delta}} = \frac{1}{\delta_0} \cdot \left(1 + \overline{\delta} + \overline{\delta}^2 + ...\right) \tag{11}$$

Where $\overline{\delta} = \delta'/\delta_0 < 1$.

Generally in (11) only the first-order summand are used [6]. In this case the air gap value is computed correct only when the rotor displacements are small ($\approx 20\%$ from δ_0). There are essential inaccuracy in other cases. By using the second-order summand in (11) the air gap value can be exactly computed when the displacements are equal to 30% from δ_0. The using of approximate expression for the air gap value in the model should to exclude influence of computation accuracy on work of the control system, created according to this expression. It may be carried out by recounting δ'. Having assimilated the exact and approximate expressions for the air gap value, we obtain next relation.

$$\delta' = \delta_0 \cdot \frac{\overline{\delta}}{1 + \overline{\delta}} \tag{12}$$

By doing likewise, we obtain relation, when using the second-order summand in (11).

$$\delta' = \delta_0 \cdot \frac{\overline{\delta} + \overline{\delta}^2}{1 + \overline{\delta} + \overline{\delta}^2} \tag{13}$$

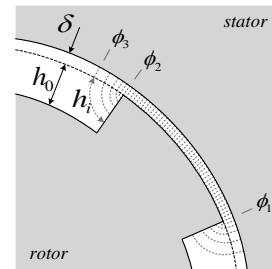*D.   The air gap permeance between the rotor poles*

Fig. 5. The air gap piece of SRBM. Main magnetic flux comes through the poles surface, because of smallness of the air gap.

In the SBRM mathematical model, used for the control system creation, the air gap permeance between the rotor poles is neglected. In this case, equations (6) and (7) include summands which describe exposure to the elements, located on the pole surface: from ϕ_1 to ϕ_2 (fig. 5).

It has to include corresponding summands in equations (6) and (7) to considered the air gap permeance between the poles. For example, the elements from ϕ_2 to ϕ_3 must be included in these equations to consider the permeance of the lateral pole surface. In this case, the air gap value is increased by the value h_i, which can be defined according to a path shape of the flux [7]. In the range of the element $\Delta\phi_i$ the value h_i is constant. Therefore the equations model are not changed. But, should be taken into account next modification.

$$\delta = \delta_0' - \delta' = \delta_0 + h_i - \delta'$$

MMF upper harmonics and tooth kinks

The output parameters of the electromagnetic subsystem are computed numerically; therefore the MMF shape changes don't require modification of the computing algorithm. Upper harmonics are added to the first harmonic in the equation magnetic energy as optional summands.

Tooth kinks can be considered by adding the MMF harmonic, which have order equal to the stator slots number. If the stator slots are allocated uneven or there is an essential difference between tooth and slot width, tooth kinks should be modeled by changing the air gap permeance.

Core steel saturation

The iron core reluctance must be considered by adding it consecutively to the air gap reluctance. In the proposed model conveniently bring it to the air gap value.

$$R_\delta + R_c = \frac{\delta_0 - \delta'}{\mu_0 \cdot S} + R_c = \frac{\delta_0 - \delta' + \mu_0 \cdot S \cdot R_c}{\mu_0 \cdot S} \quad (15)$$

Where R_δ is the air gap reluctance; R_c is the iron cores reluctance. Therefore the air gap value is described by next expression.

$$\delta = \delta_0 - \delta' + \mu_0 \cdot S \cdot R_c \quad (16)$$

The core steel saturation can be considered by changing the iron core reluctance depending on an applied MMF.

$$F_{cj} = F_\Sigma \cdot \frac{\mu_0 \cdot S \cdot R_{cj-1}}{\delta_0 - \delta' + \mu_0 \cdot S \cdot R_{cj-1}} \quad (17)$$

Where F_{cj} is the drop in MMF in the cores of the stator and rotor on j iteration; F_Σ is total MMF of the windings; R_{cj-1} is iron core reluctance on $j-1$ iteration.

A relation $R_c = f(F_c)$ is created according to the characteristic of the magnetization iron. When computation the model via program, it's easy to prescribe this relation both numerically and by an approximate expression. After computation F_{cj} is defined new value of R_{cj}.

$$R_{cj} = f(F_{cj}) \quad (18)$$

Computation F_{cj} with (17) by (17) introduces an error in the steel reluctance compute owing to use R_c value, obtained on previous iteration. Therefore, if the MMF changes drastically, it has to reiterate the computations with (17) and (18) several times for accuracy increase.

II CONCLUSION

The research of electromechanical system can be carried out via models various types: an analytical model, a finite element method (FEM) model, a programmatic model. Every one of them has benefits and drawbacks. Let's compare them in terms of research of the effect assumptions onto the system performance.

TABLE I

COMPARISON OF VARIOUS MACHINE MODEL TYPES

Assumption	Model — Analytical model	Finite element method model	Programmatic model
Defining reciprocal value of the air gap by approximate expression	difficult	impossible	easily
Neglect of the air gap permeance between the rotor poles	difficult	possible	possible
Disregard MMF upper harmonics and tooth kinks	difficult	difficult	easily
Neglect of the core steel reluctance and saturation	difficult	easily	possible

In the table I is presented assessment possibility of allowing for and exclusion from models machine various type the assumptions.

Creation of an analytical model presupposes the obtaining of equations set describing all necessary characteristics of the machine. If one of them is added

or is excluded, then is necessary to obtain new equations set. For the SRBM it is difficult, even if all assumptions are made.

FEM is a most wide-spread and simple method of the modeling of electromagnetic fields. FEM model permits to exactly compute forces of electromagnetic

interaction. Herewith any characteristic, property of material and MMF shape isn't simplified. But exclusion from the model any attribute isn't always possible and easy.

Via programmatic model it can be enough easily done it, by changing attribute set of the model. Herewith other types of modeling are used. For example, to create the relation $R_c = f(F_c)$ it is need to use FEM, which allows to consider local saturation of iron core.

III REFERENCES

[1] Y. N. Zhuravlyov, Active magnetic bearings: theory, design, applications. St. Petersburg: Polytechnica, 2003.

[2] S. Y. Loginov and Y. V. Domracheva, "Overall dimensions comparison of bearingless reluctance machine and machine with active magnetic bearings," Electrotechnical complexes and control systems, vol. 2, pp. 20-24, Feb. 2012.

[3] P. K. Hermann, "A Radial Active Magnetic Bearing Having a Rotating Drive," London Patent 1 500 809, February 9, 1974.

[4] Hannian Zhang, Huangqiu Zhu, Zhibao Zhang and Zhiyi Xie, Design and Simulation of Control System for Bearingless Synchronous Reluctance Motor: Electrical Machines and Systems, 2005. ICEMS 2005. Proceedings of the Eighth International Conference, vol. 1, pp. 554-558, 2005.

[5] Zou Hualei, Diao Xiaoyan, Zhu Huangqiu, Li Tianbo and Zhu Dehong, Decoupling control of bearingless synchronous reluctance motor based on inverse system method: Robotics & Control Systems: Control and Decision Conference (CCDC), pp. 2120-2125, 2010.

[6] A. Chiba, T. Fykao, O. Ichikawa, M. Oshima, M. Takemoto and D.G. Dorrell, Magnetic Bearings and Bearingsless Drives. ELSEVIER, 2005.

[7] A. G. Slivinskaya, Electromagnets and permanent magnets. Moscow: Energy, 1972.

Simulation of Traction Electric Drive with Vector Systems of Direct Torque Control

Ilya Fedotov, Vyacheslav Tikhonov

Pskov State Univeristy, Faculty of Electrical Engineering, Department of drive and automation systems. Address: Russian Federation, 180760, Pskov, Lenin Square, 2

Abstract. The article deals with investigation of electromechanical and energetic characteristics of traction electric drive with vector systems of direct torque control.

As a controlled object the traction asynchronous motor ДТА-1У1, which is used to drive the trolley-bus is considered. At the present time the usage of traction asynchronous electric drives for town transport is relevant. Due to development of power electronic devices and microprocessor-based control systems it became possible to replace DC electric drives with electric drives with asynchronous motors.

The article contains brief description of two different types of control systems: field-oriented control (FOC) and direct torque control (DTC). Principles of work for both systems are considered and the main advantages and disadvantages associated with the use of these systems are pointed out. The models of both systems for traction asynchronous electric drive, built in modeling environment MATLAB/Simulink, are given in this article for further comparative analysis. As the main quality factor of control total harmonic distortion (THD) is used.

Keywords – DTC, FOC, simulation models, THD, traction electric drive.

I INTRODUCTION

The mass usage of traction asynchronous motors for town transport is very promising direction. The implementation of electric drives with traction asynchronous motors has some executive and technical difficulties, described at [1]. Among them is the requirement to use complicated systems of electrical transformations based at the usage of power and information electronic devices. The efficient solution that can be used at this situation is the usage for power IGBTs combined with microprocessor-based control systems.

Department of Drive and automation systems of Pskov State University in tandem with The Pskov Factory of Electric Machines do mutual research works for development of traction electric drive, based on the usage of traction asynchronous motor, and for the simulation of its operating modes.

II VECTOR SYSTEMS OF DIRECT TORQUE CONTROL

The most preferable control systems used for traction electric drives are vector systems of direct torque control. These ones are: FOC, which is used pulse-width modulation (PWM) of base vectors to control the torque while maintaining the rotor flux linkage, and DTC wherein torque control is performed by stator flux linkage adjustment without using PWM.

FOC Principles

At 1971 F. Blaschke [2] formulated the control method, which was patented by Siemens and called «transvector control». Mathematically it is based at the equations of electromagnetic processes at an asynchronous motor written at the vector form in the reference frame oriented by the direction of magnetic field [3].

For the implementation of systems with vector control of asynchronous motor the every couple of vectors, which can be used at the equation for electromagnetic torque of unified electric machine, can be taken, but the level of system complication depends on this selection.

The equations of electromagnetic processes at an asynchronous motor have the simplest form when it written in the rotor flux linkage terms. If the vectors of rotor flux linkage and stator current are chosen combined with synchronous $(d-q)$ reference frame, and the d-axis aligned with the vector of rotor flux linkage, then the equation of electromagnetic torque of can be written as:

$$M = \frac{3 \cdot p \cdot L_m}{2 \cdot L_2} \psi_{2d} i_{1q} \qquad (1)$$

where L_μ - magnetizing inductance, L_2 - rotor inductance.

The form is similar for the one that used for DC motors, so the main problem will be the identification of ψ_{2d} and i_{1q}.

Hence, the main principle of vector control can be formulated as: in the rotor flux reference frame, the decoupled control of torque and rotor flux magnitude of asynchronous motor can be achieved acting on the q and d axis stator current components, respectively [4].

DTC Principles

The disadvantages of the vector control method are the high complexity of computational algorithm and that the control performance directly depends on the accuracy of measuring and computational operations. The algorithm based on discontinuous control and sliding modes is free of these lacks. It provides the invariability to the external disturbances and therefore, is preferred for the electric drives with severe

operating conditions. For the first time the control system for variable frequency electric drives based on the discontinuous control was introduced at 1985. Later this type of control methods was called «direct torque control (DTC)».
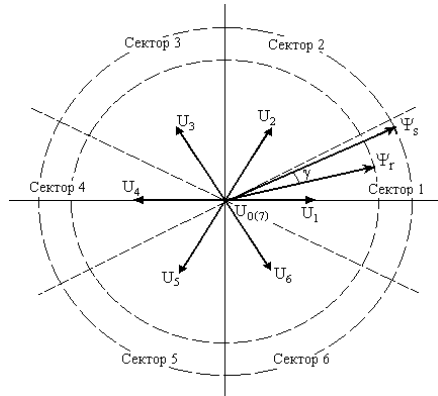

Fig. 1. Positioning the flux and voltage vectors at the $(\alpha - \beta)$ plane

The name direct torque control is derived by the fact that, on the basis of the errors between the reference and the estimated values of torque and flux, it is possible to directly control the inverter states in order to reduce the torque and flux errors within the prefixed band limits [4].

The main features of the system with DTC are [5]:

- hysteresis-band controllers of the stator flux linkage and electromagnetic torque;
- the presence of model of the motor for the estimation of non-observable parameters (stator flux linkage, electromagnetic torque of the motor and the rotor speed for the sensorless systems) at the control system;
- switching table for the optimal inverter voltage vector selection;
- the identificator of phase sector which the stator flux linkage vector lies in at the current moment;
- the absence of linear coordinate transformations;
- current controllers are expressly absent;
- the absence of PWM signals generator.

The electromagnetic torque of traction asynchronous motor in a DTC scheme is calculated by the expression (2):

$$m = \frac{3}{2} p \frac{k_1 k_2}{\sigma L_m} |\Psi_s \times \Psi_r| =$$
$$= \frac{3}{2} p \frac{k_1 k_2}{\sigma L_m} \Psi_{sm} \cdot \Psi_{rm} \cdot \sin \gamma, \quad (2)$$

where p is the pole pair number; k_1, k_2 - the coefficients, which are calculated as, $k_1 = L_m/L_1$, $k_2 = L_m/L_2$; L_1 - stator inductance; $\sigma = 1 - k_1 k_2$ - leakage factor of the motor; γ - space angle between stator and rotor flux vectors.

The main principle of DTC is: the electromagnetic torque of the motor can be regulated by regulation of γ angle while maintaining the rotor and stator flux magnitudes constant $|\Psi_s| = \Psi_{sm}$ and $|\Psi_r| = \Psi_{rm}$ (Fig. 1).

III SIMULATION MODELS

To analyze the performance of traction electric drive with using vector systems of direct torque control in the various operating modes the simulation models for both systems were built in modeling environment MATLAB/Simulink.

FOC Model

At the model of system with vector control, shown at Fig. 2, the motor is fed by 3-phase inverter (block «DC/AC Convertor»), which works as the voltage source. For measuring phase stator currents and voltages «Three-Phase V-I Measurement» block is used. The output values of this block go to the «Currents measurement» and «Voltages measurement» blocks, respectively, which are used for transition from 3-phase reference frame to stationary $(\alpha - \beta)$ reference frame and described by the equations (3), shown below:

$$\begin{cases} i_\alpha = i_a \\ i_\beta = \frac{i_a + 2i_b}{\sqrt{3}} = -\frac{i_a + 2i_c}{\sqrt{3}}, \end{cases}$$
$$\begin{cases} u_\alpha = u_a \\ u_\beta = \frac{u_a + 2u_b}{\sqrt{3}} = -\frac{u_a + 2u_c}{\sqrt{3}} \end{cases} \quad (3)$$

The calculated stator currents $i_1^{(\alpha,\beta)}$ and voltages $u_1^{(\alpha,\beta)}$ are used as input signals at the «Flux identification system» block, which is used for rotor flux calculation at stationary $(\alpha - \beta)$ reference frame, basing on the stator equations and equation for the rotor flux at stationary $(\alpha - \beta)$ reference frame:

$$\frac{d\psi_1}{dt} = u_1 - i_1 r_1; \quad \psi_2 = (\psi_1 - i_1 \sigma L_m / k_1)/k_2 \ . (4)$$

where r_1 is stator resistance.

The «Vector-filter» block is used for the calculation of rotor flux magnitude and trigonometric functions defining current space positionace of synchronous reference frame - $\cos \vartheta_1 = \psi_{2\alpha}/|\psi_2|; \sin \vartheta_1 = \psi_{2\beta}/|\psi_2|$. «Rotator1» and «Rotator» blocks are used for direct and inverse Park transformation, respectively. Therefore, above-described blocks provide the transition from 3-phase reference frame to synchronous $(d - q)$ one and vice versa.

Control system has two independent feedback loops: rotor speed and rotor flux ones, and two stator current components subordinate loops, which form the stator current feedback. The information about rotor speed is received from the speed sensor. This signal is subtracted from the reference speed («Speed reference» block), and the calculated error signal is transferred to the speed controller, which forms the torque reference signal.
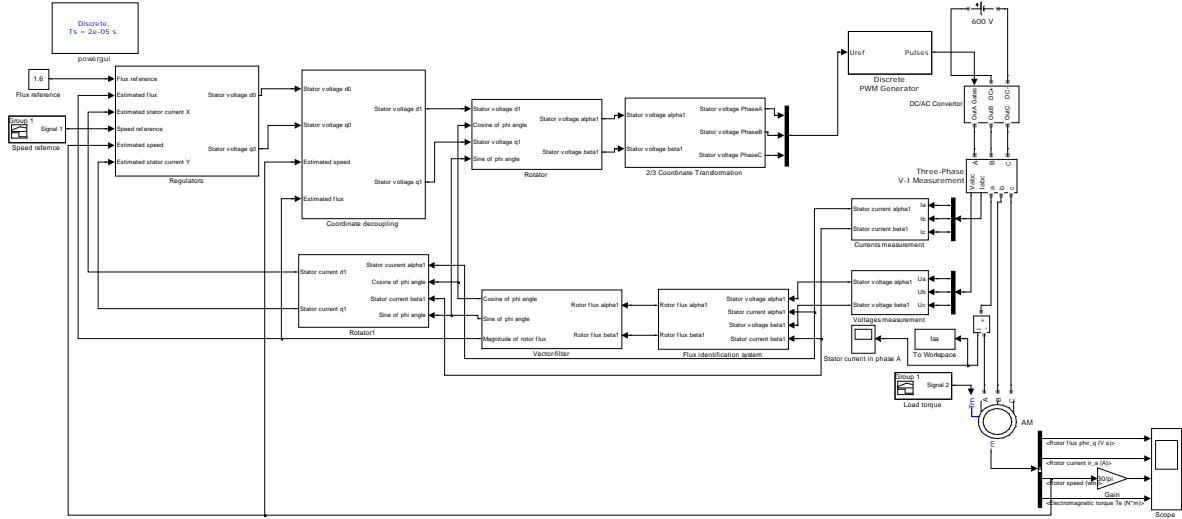

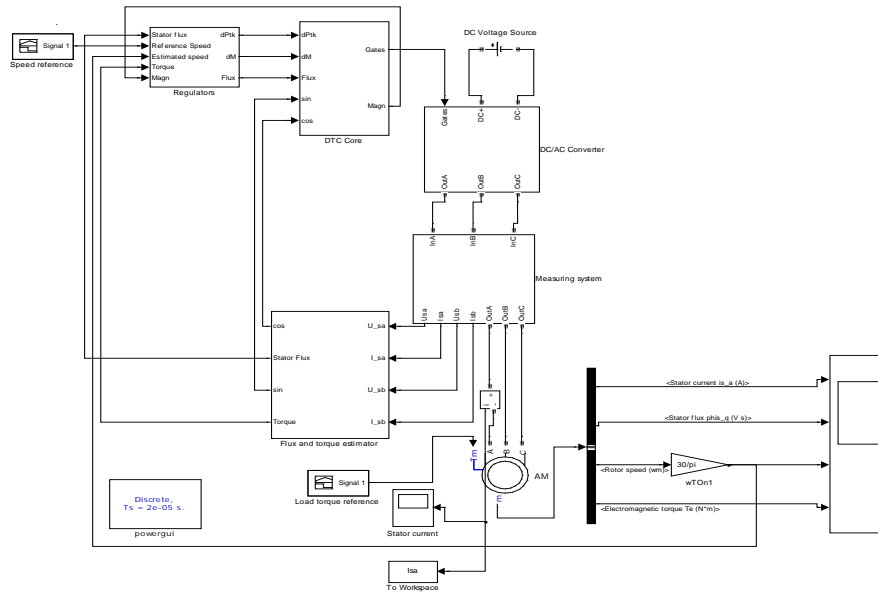Fig. 2. Simulation model of FOC system with PWM

Fig. 3. Simulation model of DTC system

The q-axis stator current reference signal i_{1q}^{*} is formed by the division of torque reference signal by $|\psi_2|$. Stabilization of rotor flux is provided by rotor flux controller, which forms the d-axis stator current reference signal i_{1d}^{*}.

«Coordinate decoupling» block is used for the compensation of cross coupling between control loops and described by the expressions (5):

$$\begin{cases} u_{1d} = u_{d0}^{*} r_1 \left(1 + T_1' p\right) - u_{q0}^{*} \omega L_1' \\ u_{1q} = u_{q0}^{*} r_1 \left(1 + T_1' p\right) + u_{d0}^{*} \omega L_1' + \omega |\psi_2| k_2 \end{cases}, (5)$$

where L_1' - transient stator inductance, which is calculated as $L_1' = L_1(1 - k_1 k_2)$; T_1' is calculated as $T_1' = L_1'/r_1$.

The output vector of signals $u_1^{(dq)'}$ of this block is transformed by «Rotator» block to stationary $(\alpha - \beta)$ reference frame, and then to the 3-phase reference frame by the «2/3 Coordinate Transformation» block. The output signals $u_1^{(abc)}$ go to the «Discrete PWM Generator» block. The inverter is controlled by signals received from the «Discrete PWM Generator» block.

DTC Model
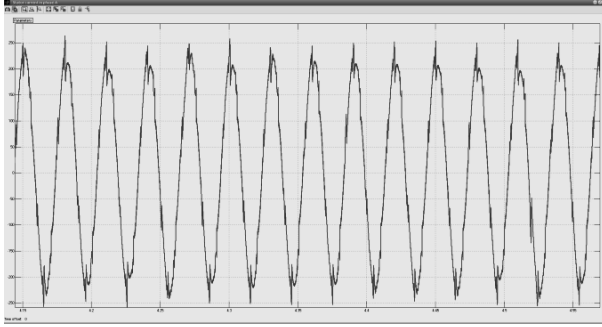
<div style="text-align:center">(a) – FOC system</div>
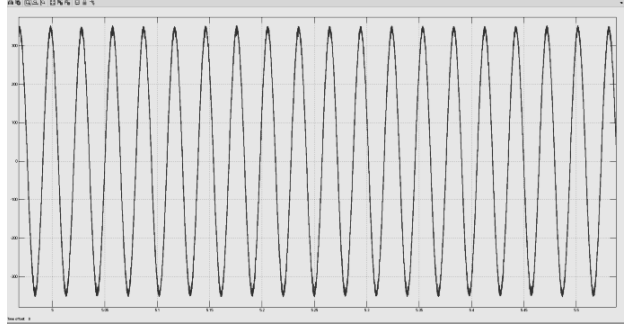
<div style="text-align:center">(b) – DTC system</div>

Fig. 4. Stator current waveforms for simulated systems.

Model of system with DTC, shown at Fig. 3, consists of:
- «Speed reference» block, which allows to provide the desirable form of reference signal to the system input;
- «Regulators» subsystem, which have «Reference speed», «Estimated speed», «Torque», «Stator flux» signals as input ones and the commutation functions of stator flux and electromagnetic torque hysteresis-band controllers *dPtk* and *dM*, respectively, as output signals;
- «DTC Core» subsystem;

subsystems. The input signals of «Row Number» subsystem are the commutation functions of stator flux and electromagnetic torque hysteresis-band controllers *dPtk* and *dM*, respectively. Based on these signals the row number of switching table is calculated. To calculate the targeted column number of switching table, the «Column number» subsystem is used. This subsystem has trigonometric functions *sin* and *cos*, defining position of stator flux vector at base vectors plane, as input signals. The output signal of switching table *Gates*, constituting an eight possible states of inverter output voltage vector U_0-U_7, wherein U_0 and U_7 are zero vectors, is calculated based on the signals entering from the outputs of «Row Number» and «Column number» subsystems.

Measuring system consists of stator current and voltage sensors and coordinate transformers, which are used for transition from 3-phase reference frame to the stationary one based on the equations (6):
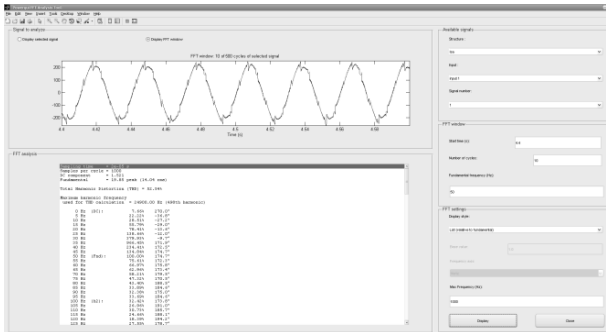
<div style="text-align:center">(a) – FOC system</div>
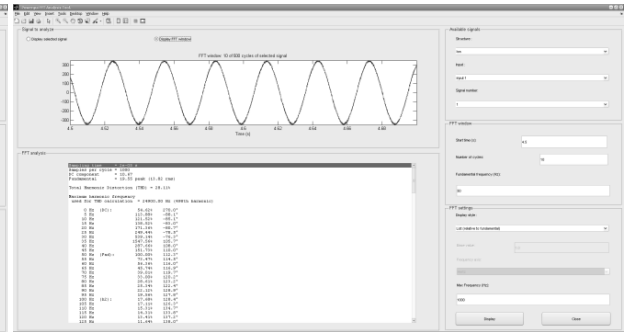
<div style="text-align:center">(b) – DTC system</div>

Fig. 5. Spectral composition of stator current for simulated systems calculated at «FFT Analysis» window

- DC voltage source, simulating the voltage of trolley-bus overhead contact system;
- DC/AC Converter, which transforms DC voltage of trolley-bus overhead contact system into AC voltage to feed the traction asynchronous motor;
- measuring system;
- flux and torque estimator.

«DTC Core» subsystem consists of «Row Number», «Column number» and «Switching table»

$$i_{s\alpha} = \frac{2}{3}\left(i_a - \frac{i_b - i_c}{2}\right); \quad i_{s\beta} = \frac{i_b - i_c}{\sqrt{3}};$$

$$u_{s\alpha} = \frac{2}{3}\left(u_a - \frac{u_b - u_c}{2}\right); \quad u_{s\beta} = \frac{u_b - u_c}{\sqrt{3}} \quad (6)$$

Vectors $i_s^{(\alpha\beta)}$ and $u_s^{(\alpha\beta)}$ serve as the basis of stator flux and torque calculation in «Flux and Torque

Estimator» block by the means of expressions (7) shown below:

$$\Psi_s^{(\alpha\beta)} = \int \left(u_s^{(\alpha\beta)} - i_s^{(\alpha\beta)} R_s \right) dt,$$

$$M = \frac{3}{2} p \left(\Psi_{s\alpha} i_{s\beta} - \Psi_{s\beta} i_{s\alpha} \right). \qquad (7)$$

It is useful to calculate trigonometric functions of turning angle of stator flux vector with the reference to the α-axis at this block, because they are required for further calculations. The functions can be found by the means of equations (8):

$$\cos \Psi_s = \frac{\Psi_{s\alpha}}{\Psi_{sm}}; \sin \Psi_s = \frac{\Psi_{s\beta}}{\Psi_{sm}}, \qquad (8)$$

where $\Psi_{sm} = \sqrt{\Psi_{s\alpha}^2 + \Psi_{s\beta}^2}$ is the stator flux magnitude.

IV RESULTS OF SIMULATION

The following operating modes of the traction electric drive were investigated during the simulation:
- acceleration from the zero to the rated speed;
- rated speed motion;
- deceleration from the rated speed to the zero.

The characteristics shown the stator current waveforms in the different operating modes were obtained by the simulation of both control systems. The parts of these waveforms corresponding to the rated speed motion with the constant load torque M=1000 N*m are shown at Fig. 4 (a), (b) .

Total harmonic distortion (THD) was chosen as one of the features to investigate. THD is calculated as ratio between mean-square sum of spectral components of output signal, which are absent at the spectrum of input signal, and mean-square sum of spectral components of input signal.

For measuring THD in both systems «FFT Analysis» built-in Simulink tool was used, which calculate the spectral composition and meanings of harmonics at the numerical form or as histogram for the specified signal. The results of using this tool on the investigated models are shown at Fig. 5 (a), (b).

As it is possible to see from the plots above, the meanings of THD for the modeled systems are: THD=52,54% for the system with FOC, THD=28,11% for the system with DTC.

V CONCLUSION

Based on the obtained results it can be noted that DTC algorithm might be preferred for traction electric drives from the energetical standpoint. During the following investigations is in contemplation to receive the meanings of other energetical features to compare: power factor, efficiency, energy efficiency factor, which is calculated as $\eta_{ef} = \eta \cdot \cos \varphi$.

VI APPENDIX

The test machine is a three phases and 50 Hz induction machine having the following parameters as shown in Table I.

TABLE I
PARAMETERS OF THE TESTED INDUCTION MACHINE

Parameter	Parameter value
Power rating, P_{rated}	180 kW
Rated voltage, V_{rated}	450 V
Rated current, I_{rated}	276 A
Pole pair, p	2
Torque rating, M_{rated}	1150 N·m
Stator resistance, R_s	0,02 Ω
Leakage stator inductive reactance, x_s	0,00967 Ω
Rotor resistance, R_r	0,00859 Ω
Leakage rotor inductive reactance, x_r	0,0962 Ω
Magnetizing inductive reactance, x_m	2,6 Ω
Inertia, J	3,2 kg·m²

VII REFERENCES

[1] Иньков Ю.М., Федяева Г.А., Феоктистов В.П., «Системы управления для электроприводов с асинхронными тяговыми двигателями», Электротехника, №4, с. 8 – 12, 2009.

[2] F. Blaschke, «A new method for the structural decoupling of A.C. induction machines», in *Conf. Rec. IFAC,* Dusseldorf, Germany, Oct. 1971, pp. 1 – 15.

[3] Усольцев А.А. Частотное управление асинхронными двигателями/ Учебное пособие. СПб: СПбГУ ИТМО, 2006. – 94 с.

[4] D. Casadei, F. Profumo, G. Serra, A. Tani, «FOC and DTC: Two Viable Schemes for Induction Motors Torque Control», IEEE Transactions on Power Electronics, vol. 17, no. 5, pp. 779 – 787, Sep. 2002.

[5] Козярук А.Е., Рудаков В.В. Прямое управление моментом в электроприводе переменного тока машин и механизмов горного производства: Учебное пособие/ Санкт-Петербургский государственный горный институт (технический университет). СПб, 2008. – 99 с.

The Simulation Model of a Sliding Contact

Alexander Ilyin, Igor Plokhov, Andrey Isakov

Pskov State University, Faculty of Electrical Engineering, Department of Drive and Automation Systems. Address: Lenina 8, Pskov, 180000, Russia.

Abstract. **This paper deals with the brush slip ring contact modeling. Approaches the sliding contact problem with the synergy theory. The contact layer is considered using mechanical, electrical and thermal properties.**
The simulation model includes algorithms of:
- **generation of microscale contact surface,**
- **approachment of two surfaces,**
- **fritting and breakdown effects of oxide layer,**
- **extracting clusters of conducting area,**
- **calculating constriction resistance using fractal dimensionality,**
- **generation of heat caused by electrical current and mechanical friction,**
- **calculation of integral characteristics.**

The program implementing the model may be used to optimize the contact materials before time-consuming and expensive tests.

Finally discusses the implemented model and its results, problems of verification and validation.

Keywords – **brush, slip ring, sliding contact, modeling.**

I Introduction

Improvement of reliability of electrical machines is related to progress of fundamental and applied study in diagnostics and prediction of its technical condition. Methods of mathematical computational simulation of dynamic processes are developing nowadays.

Sliding contacts are widely used in engineering despite the trend towards non-contact methods of transmission of electrical current. In some cases, the use of brush-contact devices is appropriate due to their low cost and continuity of operations.

Up to now there is no consensus on the adequate modeling of the main properties and characteristics of sliding electrical contact, due to a wide variety and complexity of electric friction interaction processes.

Therefore, theoretical and experimental research in this area increasing range of scientific ideas about electrical contacts which provides new ways of modeling is topical problem.

Particular attention should be given to computational simulation modeling, intend to obtain the integral characteristics of the site to the parameters of current collection sliding contact pairs and external influences.

This approach can significantly reduce the amount of expensive practical experiments in the study of the characteristics of different contact pairs.

Dynamic processes occurring in sliding electrical contact can be divided into the following categories:
1. mechanical,
2. electromagnetic,
3. thermal,
4. chemical .

These processes are bonded directly or through intermediate functional blocks.

The processes occurring directly in the contact layer include:
- frictional interaction processes of microscale contact surfaces;
- the evolution of the contact conductance in the contact layer;
- the evolution of nonsteady temperature field in the contact layer;
- oxidation-reduction and electrolytic reactions.

In addition there are external effects:
- brush fluctuations caused by kinematic and dynamic disturbances;
- oscillating processes of dynamic electrical current distribution among the parallel contacts;
- overall heating of contact pairs.

The objective of the developing model is calculation of dynamic electrical current transmission processes in the intermediate layer of sliding contact [1].

II System approach to the sliding contact modelling

When two bodies are pressed together, the contact of its surfaces can be described as a system of discrete elements. The intermediate layer can be considered as a "third body" consisting of a number of interrelated areas, located in the plane equidistant from the two contacting surfaces. Thus the intermediate layer is replaced by an abstract object that allows using a purely mathematical definitions and operations.

Divide the intermediate layer on the set of elementary parts of the same area ΔS, which can be called the contact elements. They are located in grid with increments Δx by the axis X and with

increments Δy by the axis Y. In the practice of computational modeling it takes $\Delta x = \Delta y$.

The contact elements of the system have different properties depending on the way of current transmission through them and are united in the subsystems. The subsystems present a flock of fractal clusters of different nature. The cluster system is a projection plane of contact conductivity of various types phenomena in the intermediate layer, as conductive objects between two microscale surfaces formed by various types of connection (direct contact, contact through the oxide film, contact through wear products and contact through a low-temperature plasma). The conducting clusters specify these properties in the form of appropriate mathematical models to the contact elements.

Introducing the intermediate layer, the binary relations of two sets (microscale surfaces) are replaced by unary relations in the conductive properties of the contact layer clusters. This approach opens the possibility of system simulation of the electrofrictional interaction and study its integral characteristics within the synergetic open system.

Thus a generalized model of a sliding electrical contact appears as a regular set of finite elements in the intermediate layer combined with the properties and relationship bonds. The contact elements of the same type form the clusters. The contact element properties appear when external influences are applied to the contact pair.

This system is an evolutionary, because for the first time application of the external influences the conductive structure of clusters is minimal. The evolution of the conducting clusters is a result of changes in the type and magnitude of conduction in the associated contact elements. Changing of the cluster parameters are determined by the values of external influences, the evolutionary properties of the contact elements and their evolutionary relationships [2].

The main external factors at the input of the "sliding electrical contact" can be divided into the following categories:
1) controlled and regulated; these include steady components of electric voltage on the contact pair and applied pressure, the velocity of contact pairs relative movement;
2) controlled but nonregulated; these include variable components of the voltage and applied pressure, temperature and chemical composition of the environment, the microscale of contact surfaces;
3) uncontrolled (disturbances).

III THE SYNERGETIC MODEL OF ELECTROFRICTIONAL INTERACTION

The intermediate layer can be represented as a set of contact elements placed in the regular grid. Each contact element can be described with a state vector V.

The basic components of the state vector of the contact element is divided into the following classes.
1. Mechanical V_M:
   - contact stiffness C_C;
   - contact damping K_C;
   - contact convergence Y_C;
   - contact force F_C;
   - microhardness q;
   - density ρ_M;
   - coefficient of boundary friction k_{FR}.
2. Electrical V_E:
   - voltage U (the same for all contact elements);
   - fritting voltage U_F;
   - electrical conductivity ρ_E or R;
   - contact capacity C_E;
   - the current I through the contact element.
3. Thermal V_T:
   - heat capacity C_θ;
   - thermal conductivity k;
   - melting temperature θ_M;
   - evaporation temperature θ_{EV};
   - instant temperature θ;
4. Chemical V_H:
   - vector of chemical composition $\hbar$;
   - intensity of the basic chemical reactions $V_\hbar$.

The contact stiffness of the element is nonlinear function of temperature. The exact definition of this dependence is associated with considerable difficulties. Therefore, it can be defined by the following considerations.

The contact stiffness has a weak temperature dependence in the range from room temperature to the temperature of recrystallization (θ_R). In the range from θ_R to the melting temperature θ_M softening of the material starts and the gradual loss of hardness occurs (up to $C_M = 0$). After that, there is only a viscous drag force proportional to the velocity of convergence Y_C changing and determined by damping factor K_C. Changing the stiffness to zero is in the range $]\theta_R, \theta_M[$ so:

$$C_C = \begin{cases} C_{CN} \forall \theta \le \theta_R, \\ C_{CN} \cdot \dfrac{\theta_M - \theta}{\theta_M - \theta_R} \forall \theta \in]\theta_R, \theta_M[, \\ 0 \forall \theta \ge \theta_M, \end{cases} \qquad (1)$$

where C_{CN} – the nominal stiffness of the element. [3]

Recrystallization temperature of copper is about 190°C, of iron 500°C. The strength characteristics of graphite increase with temperature. Decreasing of the mechanical strength of the contact material (softening) starts at the contact surface at about 0.3 of the melting temperature [4].

The contact force F_C can be presented as two components $F_C = F_1+F_2$. The first is the reaction of the contact stiffness to convergence and viscous drag force

$$F_1 = C_C Y_C + K_C \frac{dY_C}{dt} \qquad (2)$$

and the second is the total electrodynamic force

$$F_2 = \frac{\mu_0 I^2}{4\pi} \ln \frac{R_0}{r} + \frac{\mu_0 I^2}{6\pi}, \qquad (3)$$

where R_0, r – the equivalent radius of the direct current transmission area and the radius of the contact; μ_0 – the magnetic conductivity.

The density ρ is defined in terms of mass m_i of contact materials in the fixed volume of the contact element

$$\rho = \frac{1}{V_{CE}} \sum_{i=1}^{n} m_i. \qquad (4)$$

Electrical resistance or conductivity of the contact element is described with complex model. The model is a system of submodels which work alone or in groups depending on the conditions. The submodels describe the different types of conduction through contact element: conduction through the oxide films, conduction through the gas gaps, direct conduction, conduction through the wear particles.

a) Conduction through the oxide films.

The films are formed by the interaction of a contact material with oxygen, sulfur, nitrogen and other substances and conditionally subdivided into thin and thick.

Adhesive films have a thickness of 9–30 Å and are the result of adsorption of oxygen molecules on the contact surface. Dependence of the tunneling resistance on the film thickness d is practically linear

$$\sigma_f = \rho_f d, \qquad (5)$$

where ρ_f – linear resistivity of the film material.

Thick films (tarnishing films) divided into oxide and sulphide. Maximum thickness of the oxide film is a function of time and temperature. For example, for copper this value is given by the empirical relation

$$\Delta h = \sqrt{100 + t 10^{8,2-\frac{1310}{\theta}}}. \qquad (6)$$

Fritting of the thick films takes place when the electric field $E\approx10^6$ V/m. Fritting voltage $U_F = E\Delta h$

determine for each contact element. In the breakdown of the film forms a conductive metal bridge, which changes the conduction submodel of the direct conduction for the contact element.

b) Conduction through the gas gaps.

For plasma conductivity is a function of temperature. Calculations show that the value of the gas component in the total contact conductance becomes significant only at temperatures above 4000 K. Only contact elements located in the place of the intense "heat flashes" have this type of conductivity. For the contact elements that have a lower temperature it is possible to neglect the gas conductivity without loss of accuracy.

c) Direct conduction

Direct conduction occurs by direct contact of the roughness of contacted bodies surfaces. In addition the contact elements affected by fritting have similar conductivity.

The value of the electric current flowing through direct contact is determined by constriction resistance. For n spots of radius a the contact resistance is given by Holm equation

$$R_C = \rho \left(\frac{1}{2 \cdot n \cdot a} + \frac{1}{2 \cdot a_k} \right), \qquad (7)$$

where a_k is the equivalent radius of all spots area [5]. Greenwood improved the second part [6]

$$R_C = \rho \left(\frac{1}{2 \cdot n \cdot a} + \frac{16}{3 \cdot \pi^2 \cdot a_k} \right). \qquad (8)$$

Plokhov suggested to define the constriction resistance of the conducting cluster as

$$R_{CL} = \frac{\rho}{2 \cdot a_{CL} \cdot D_F}, \qquad (9)$$

where a_{CL} is the equivalent radius of the cluster; D_F is the fractional dimensionality of cluster. The fractional dimensionality is described in the fractal theory. The proof of the equation in general is considerably complexity. Therefore, a series of experimental studies were made to verify the above formula [1].

d) Conduction through the wear particles

With data on the size of the particles and the conductivity of its material an additional electrical resistance in the contact element can be defined. If the particle covers several contact elements then it is presented as the conglomerate of several separate particles.

Each contact element has a heat capacity C which is determined by its mass m and specific heat of the material c

$$C = c \cdot m, \ m = \Delta x^2 \cdot \Delta h \cdot \rho, \qquad (10)$$

where Δh is the height of the element; Δx is the value of the grid size; ρ is density of the contact element material.

The specific heat depends on the temperature of the material. This dependence of each material can be presented in the model corresponding to the approximating function. According to studies using a linear approximation is sufficient.

Redistribution of heat in the contact area due to the thermal conductivity k, which also depends on the temperature. For most materials this dependence with sufficient accuracy can be considered as linear

$$k = k_0 \cdot \left[1 + b \cdot (\theta - \theta_0)\right], \qquad (11)$$

where k_0 is the value of thermal conductivity at θ_0; b is the constant determined empirically.

IV The simulation model structure

Basic algorithmic actions performed during simulation can be divided into the following units: a) setting the initial values of the contact elements state vector, b) generating the vector of controls and disturbances, c) modification of the contact elements state vector, d) the calculation and presentation of integral characteristics.

Together these actions can be described as a list of operations.

For block (a).

1. Generation of two-dimensional arrays of cells that define microscale of two contacting surfaces with the oxide films.
2. Setting the parameters of materials and surface films.
3. Convergence of surfaces is determined by the value of the force pushing to the contact and the contact stiffness.
4. Filling the two-dimensional array of intermediate layer, which determines the distribution of clusters of direct conduction and conduction through films.

For block (b).

1. Setting the speed of sliding and sampling time.
2. Setting step movement of microscales by reassignment of surfaces arrays.
3. Setting force and the initial convergence of microscales.
4. Specifying the electric voltage.
5. Setting the initial temperature.

For block (c).

1. Calculation of the constriction resistances of allocated clusters.

2. Calculation of conducting clusters currents.
3. Calculation of the heat generated in clusters.
4. Calculation of nonsteady temperature field.
5. Modification of the contact stiffness as a function of temperature.
6. Modification of convergence depending on the contact stiffness and contact pressure.
7. Modification of the values and types of conductivity as a function of temperature.
8. Modification of conductivity type as result of fritting.
9. Modification of the thickness of surface films by chemical, thermal, and mechanical processes.

For block (d).

1. Calculation of the total current and voltage drop on intermediate layer.
2. Determination of the average cluster temperature and of the overall contact.
3. Calculation of physical (actual) contact area.
4. Forming a dynamic voltage-current characteristics, charts of current, temperature, etc.
5. Visualization of microscales, of the temperature field and the contact conductance.

V Conclusion

The proposed model is implemented as a computer program. The figures show examples of two-dimensional arrays visualization (Fig. 1 – Fig. 3).
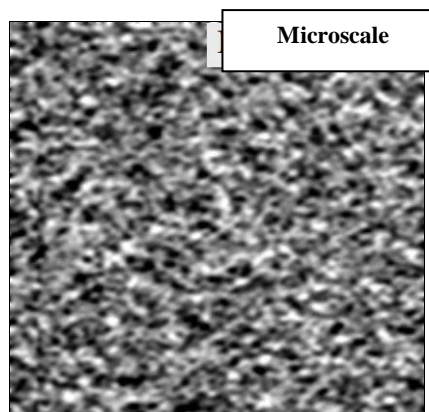
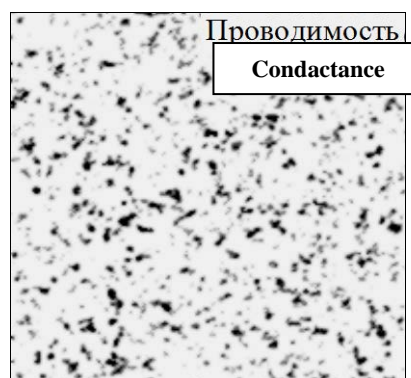

Fig. 1. Visualization of microscale contact surface

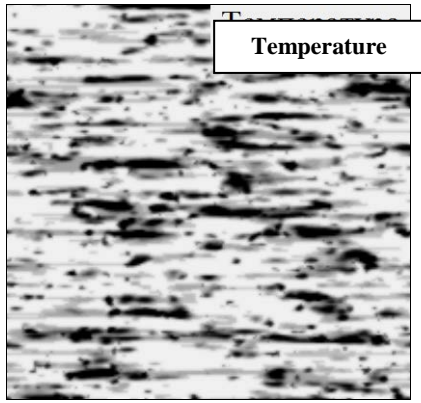Fig. 2. Visualization of conductance in intermediate layer

Fig. 3. Visualization of nonsteady temperature field

Currently research on the verification and validation of the simulation model is performed. An experimental stand of brush and slip ring assembly is developed. The stand allows taking the current-voltage characteristics of the brushes in various operation modes.

VI REFERENCES

[1] Plokhov I. V. Comprehensive diagnosis and prediction of technical state of nodes moving current collection turbogenerators. // Dissertation for doctor degree — Saint Petersburg, 2001

[2] Plokhov I. V. Cluster model of electrofriction interaction (EFI) // Proceedings of the Pskov Polytechnic Institute. – Saint Petersburg /Pskov: SPbSTU, 1997. #1. P.55-57.

[3] 9. Mechanics of sliding contact / V. I. Nellin, N. Ya. Bogatyrev, L. V. Lozhkin and others – Moscow, 1966.

[4] 160. Guide to the calculation and design of high-contact parts of electrical apparatus / N. M. Adonyev, V. V. Afanasyev, V. V. Borisov and ohers – Leningrad, 1988.

[5] Holm R. Electric contacts. – Moscow, 1961.

[6] Greenwood J. A. Constriction resistance and the real area of contact. – British Journal of appl. Physics. 1966. V.17.P.1621-163.

Device for Reduction Sparking of Slip Ring of Turbo Generator

Andrei N. Isakov, Andrei V. Andrusich, Igor E. Savraev

Pskov State University, Faculty of Electrical Engineering, Department of Drive and automation systems. Address: 180760, Russia, Pskov, Lenin Square 2.

Abstract. **Most modern power plants generating electric power equipped with synchronous generators. The correct operation of energy economy depends on reliability of such electrical machines.**

In this article issue of increasing reliability of turbo generator by increasing reliability of its brush contact unit is considered. Description of brush contact unit and its possible damages is given. Equivalent electrical circuit of contact layer of brush contact unit is performed. The equations are formed and the dynamical simulation model consisting of electric source and two brush contact units is created. With help of this model alternative method of improving parameters of brush contact unit and increasing reliability of turbo generator at once is calculated and shown.

The implementation of the proposed method of increasing the turbo generator brush contact units reliability can have different technical performance, but the principle laid down in the method remains the same.

Keywords – **contacts, brushes, turbogenerators, sparks, modeling.**

I INTRODUCTION

Reliable and uninterrupted power supply is placed at the center of the most important sites of the country, including the military and the civilian sector. Most modern power plants that provide electricity generation, equipped with synchronous machines [1]. The reliability of these machines depends on the work of almost all the energy complex.

According to the RAO UES of Russia, most failures, or 25.2% of all faults, turbo generators account for failure of brush-contact device (BCD) [2]. Stopping of turbo generator connected to its repair, can result in serious financial losses to the generating company. Therefore there is a need to improve the reliability of the unit BCD and turbo generators overall.

Brush-contact device of synchronous machine consists of a contact ring, located on the rotor, and several groups of brushes, brush holders located in the stator machine. Due to the pressure forces acting on the brush, the brush provided a mechanical contact with the ring, including at their relative movement.

The main part of the site BCD breakdowns associated with the failure of the brushes in connection with the processes occurring in the contact layer between the brush and the surface of the ring. Sliding between the brush and the surface of the ring arcing occurs, causing burn brush contact surface [3]. In addition to the contact layer derating brush sparking can cause a circular fire – emergency operation of BCD, damaging turbo generator. Therefore, the main objective of increasing the service life of the unit will be reduced BCD sparking and reduce the possibility of a circular fire.

II MATERIALS AND METHODS

From the point of view of an electrical circuit contact layer "brush-ring" is replaced by parallel connection of the resistance and capacitance [4], Fig. 1.
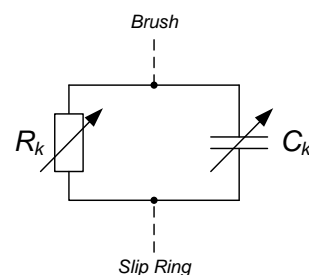

Fig. 1.   The electrical equivalent circuit of the contact layer node moving current collection

Where R_k, C_k – the resistance and capacitance of the contact layer "brush-ring."

It should be noted that the items included in the electrical equivalent circuit of the contact layer are variable parameters. This is due to the fact that the relative movement of the brushes and rings due to irregularities on the surface of the ring, the heterogeneity of the material brushes, micro vibrations brushes, brush holders and other factors change the parameters of the contact layer, which is reflected in its characteristics.

When feeding a closed loop consisting of a generator (electrical power source), two connecting conductors and the two nodes of brush-contact device electrical equivalent circuit of a closed circuit shown in Fig. 2.
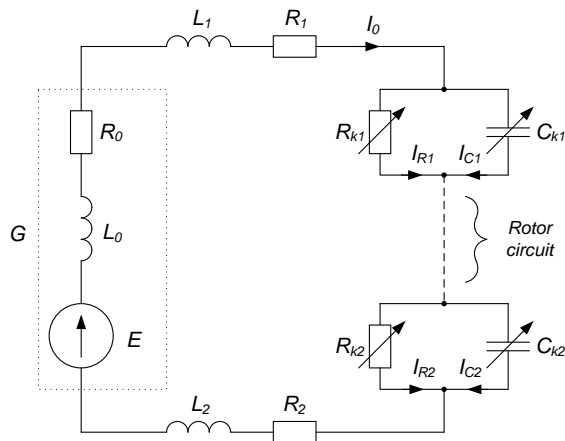
Fig. 2. The equivalent circuit of an electrical circuit with two nodes moving current collection

In Fig. 2 indicated:

G – Generator circuit loop, which includes: E - electromotive force (EMF) generator, L_0 - self-inductance of the generator, R_0 - own resistance of the generator;

L_1, R_1, L_2, R_2 — the inductance and resistance of lead wires;

R_{k1}, C_{k1}, R_{k2}, C_{k2} — the resistance and capacitance of the contact layer "brush-ring" for the respective groups of parallel sliding contacts.

Assuming that the rotor circuit is a bridge between the rings BCD and its resistance is zero, compiled by the laws of Kirchhoff's mathematical models for the equivalent circuit is as follows:

$$\begin{cases} I_0 R_0 + L_0 \dfrac{dI_0}{dt} + L_1 \dfrac{dI_0}{dt} + I_0 R_1 + I_0 R_{k1} + I_0 R_{k2} + I_0 R_2 + L_2 \dfrac{dI_0}{dt} = E, \\ I_{R1} R_{k1} - \dfrac{1}{C_{k1}} \int I_{C1} dt = 0, \\ I_{R2} R_{k2} - \dfrac{1}{C_{k2}} \int I_{C2} dt = 0, \\ I_{R1} + I_{C1} = I_0, \\ I_{R2} + I_{C2} = I_0. \end{cases}$$

With the help of the Laplace transform express currents of the above equations:

$$\begin{cases} I_0 = \dfrac{1}{p} \dfrac{1}{L_0 + L_1 + L_2} \left[E - (R_0 + R_1 + R_2) I_0 - R_{k1} I_{R1} - R_{k2} I_{R2} \right], \\ I_{R1} = \dfrac{1}{p} \dfrac{I_{C1}}{C_{k1} R_{k1}}, \\ I_{R2} = \dfrac{1}{p} \dfrac{I_{C2}}{C_{k2} R_{k2}}, \\ I_{C1} = I_0 - I_{R1}, \\ I_{C2} = I_0 - I_{R2}. \end{cases}$$

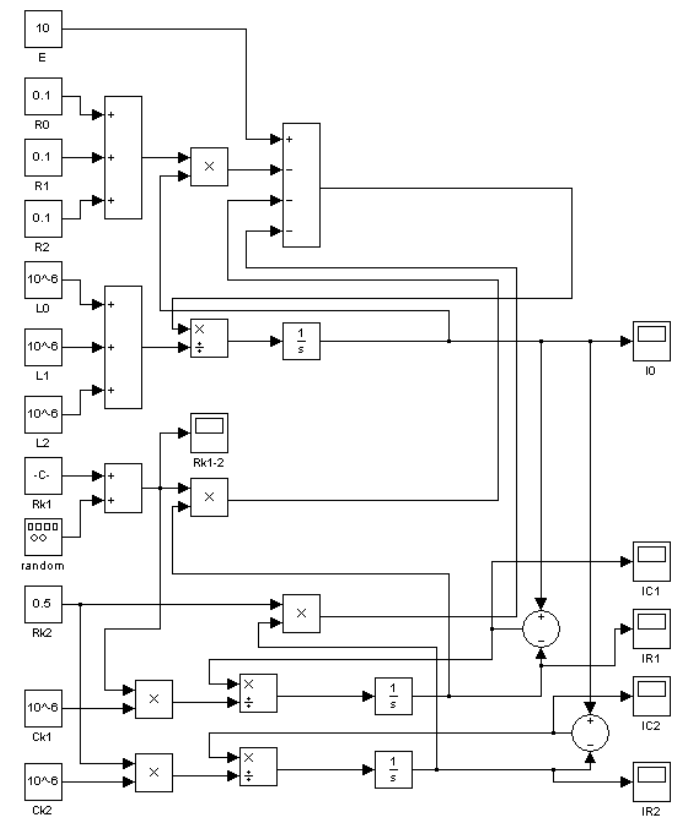According to the obtained equations builds a dynamic simulation model in specific computer environment

Fig. 3. Dynamic simulation model of current collection system moving in an specific computer environment

Built model system allows us to study the dependence of currents flowing through individual circuit elements, from changing their parameters. Model the change in the current scheme for dynamically changing the resistance of the contact layer of the first node BCD.

Initial data for the simulation:

$E = 10\ V$ - EMF generator;

$R_0 = R_1 = R_2 = 0,1\ Ohm$ - resistance oscillator circuit and connecting conductors;

$L_0 = L_1 = L_2 = 1\ \mu H$ - inductance of the generator and connecting conductors;

$\tilde{N}_{k1} = C_{k2} = 1\ \mu F$ - capacity contact layers of two transitions "brush-ring";

$R_{k2} = 0,5\ Ohm$ - resistance contact layer BCD second node.

$R_{k1} = 0,01...500,01\ Ohm$ - resistance of the contact assembly BCD.

117

It should be noted that the data presented resistance contact layer of the first node BCD varies within these ranges at random. [5]

The result of the model are the following timing diagrams of the currents in the main chain (Fig. 4) and the current (Fig. 5):
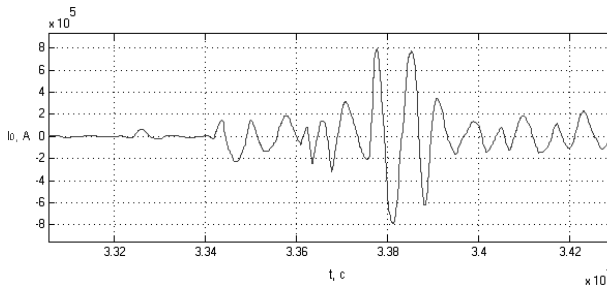

Fig. 4.   The timing diagram of the main current in a circuit with two nodes moving current collection
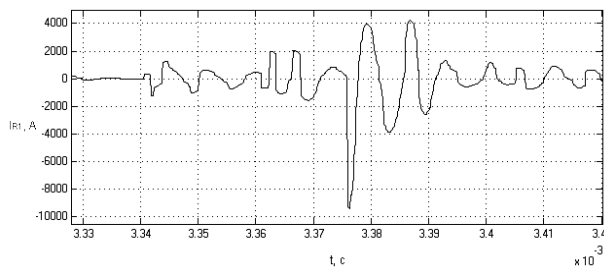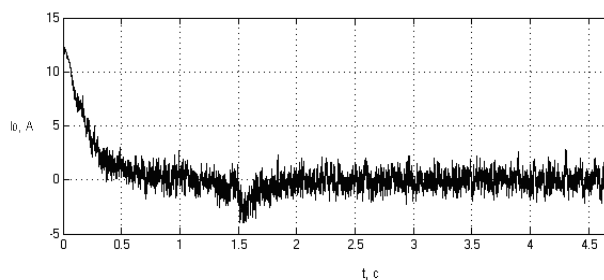

Fig. 5.   The timing diagram of current through the resistance of the contact layer of the first node BCD

Seen from the figures that the dynamic change of the resistance of the contact layer having short but very significant emissions of the electric current flowing in the circuit, which can reach values of several thousand amperes, with an average current in amperes. This is explained by the fact that dynamically changes the resistance of the contact layer of the first node BCD provokes parametric resonance in the system, causing a sharp increase in the amplitude of the currents in the circuit.

To combat the parametric resonance arising in the circuit with two nodes BCD, increase the capacity of the contact layer of the first node to the value $\tilde{N}_{k1} = 1 \ mF$ BCD. The result of the model in this case (Fig. 6 and Fig. 7):

Fig. 6.   The timing diagram of the main current in a circuit with two nodes moving current collection
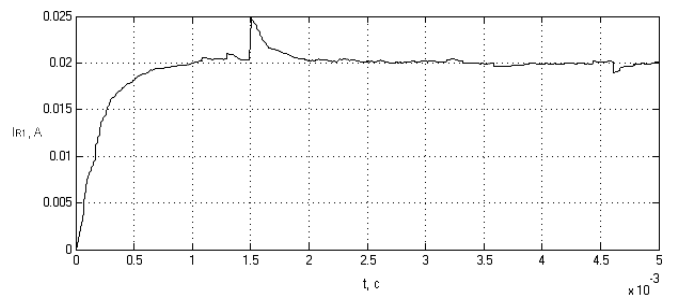

Fig. 7.   The timing diagram of current through the resistance of the contact layer of the first node BCD

III RESULTS AND DISCUSSION

Seen from the figures that when the capacity of the contact layer dynamic currents in the circuit have decreased significantly, from a few thousand to a few Amperes with RMS value about few Amperes. This result shows that an artificial increase in the capacity of transition "brush-ring" leads to a reduction of emissions of current flowing through the junction, causing a reduction in sparking host BCD and decrease the possibility of a circular fire.

Thus, increasing the capacity of transition "brush-ring" leads to a drastic reduction in dynamic currents affecting the work BCD. Decrease in the amplitude of dynamic currents will reduce sparking BCD in the contact layer, which would prolong the operational life of the brushes, and reduce the risk of circular fire. This in turn increases the overall reliability of the turbo generators.

The implementation of this approach to increase the reliability of nodes BCD can have different technical performance, but the principle laid down in the approach remains the same.

IV ACKNOWLEDGMENTS

V REFERENCES

[1]   I.P. Kopylov. *Electrical Machines*. - Moscow: Logos, 2000. - 607 p.

[2]   ELISA, "*Problems of BCD*". [Online]. Available: http://npf-elisa.ru/problemy-shka

[3]   S.I. Kachin, O.S. Kachin. "*Modeling of processes of wear electric brushes universal motors considering mechanical factors*" / / Electricity. - 2009. - № 12. - pp. 68-70.

[4]   I.V. Plokhov. "*Comprehensive diagnosis and prediction of technical state of nodes moving current collection turbo generators*" / Author. Dissertation. on competition. step. Doctor. tech. Science. – Saint-Petersburg: SPbGTU, 2001. – 36 p.

[5]   Probability and Statistics: Encyclopedia / Ch. Ed. Prokhorov Y.V. - Moscow.: the Great Russian Encyclopedia, 1999. - 910 p.

Electrical subsystem of the low-power cogeneration plant with low-speed vehicle

Andrei Khitrov, Alexander Khitrov

Pskov State University, Electro mechanic Faculty. Address: Russian Federation, Pskov, Lenin square, 2

Abstract. **Nowadays diesel power plants form the basis of distributed power generation in Russia, but they have disadvantages. The alternative variant is cogeneration plant based on the rotary-vane machine. One of the types of such machines is the rotary-vane external combustion vehicle (engine) developed in Pskov State University.**

Electrical subsystem of the plant requires its effective work to provide both start and generation modes. Development of such subsystem structure, employment of elements for links with other subsystems in the hierarchic control system is an actual task.

The paper considers structures of the electrical part of the plant, simulation and experiment results.

Keywords – **rotary-vane external combustion engine, co-generation plant, autonomous electrical supply system, permanent magnet synchronous machine, power factor corrector.**

I INTRODUCION

Decision of problems related to electric supply reliability improvement is one of the strategic aims of Russian electrical energy industry [1]. For this purpose it is necessary to build different types of electrical low-power generating plants (distributed power generation) which includes renewable energy sources. According to energy strategic program of Russia (until 2030 year) small and renewable energy generation have to increase 4 times as a whole.

In many distributed electrical grids there are no power reserves, low-voltage networks are overloaded; thus it requires electric energy generation to be close to user. Mobile autonomous energy plants and electrical power generating sets are designed to solve this problem. Such plants will be in demand – in energy providing systems in remote regions, elimination of emergency situations causing loss of normal electric power – as a backup power supply systems in mobile energy plants, for use in housing and communal services, agriculture.

At the present time the most effective decentralized autonomous power supply system (APSS) is a diesel power station (DPS). Energy of the gases expansion is generated during combustion of ignited from compression diesel fuel in diesel internal combustion engine (DICE) and is converted by crank-and-rod mechanism into mechanical energy of crankshaft rotation. Output shaft of an engine is connected to the rotor of a synchronous generator. Together they make mechatronic motion module.

When DPS works at low loads, specific fuel consumption of expensive diesel fuel per 1 kW of electric power increases significantly. In addition longtime power station work on the loads below 25% of the rated load leads to emergency modes (coking cylinder and reduced engine service life) [2]. Well-known disadvantages of piston engines: vibrations, significant friction losses in piston and cylinder unit. Another known disadvantage is that valve drive requires energy expenditure and reduces energy conversion efficiency. This negative attributes require a search of alternative variations. One of the alternative constructions is a rotary-vane engine (RVE) – low-speed vehicle [3].
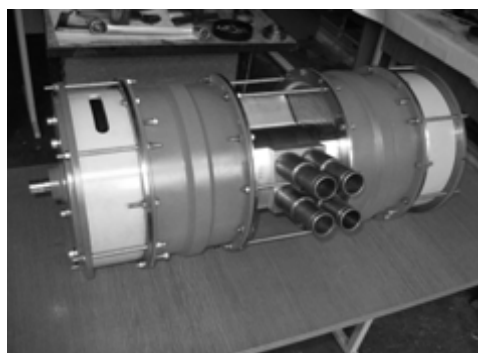

Fig. 1. Rotary-vane external combustion engine.

Developed (in Pskov State University) and patented design concepts for the rotary-vane external combustion engine (RVECE) of different electric power allowed at the present day to produce the development prototype which has a power of 1.5 kW [4] (Fig. 1).

RVECE falls into thermal energy converters; as distinct from DICE it can use more cheap resources as a source of thermal energy: natural gas and other types of fossil fuels as well as low-grade heat. Thermal energy conversion to the mechanical rotation of the RVECE shaft is performed by a specialized thermal cycle without a contact of cycle fluid and outside environment (ecological compatibility).

Currently developed in Pskov State University power plant is designed for autonomous use as a source of thermal and electric energy (cogeneration plant). In this paper details of the electrical part of a multi-level system are considered.

II STARTER AND GENERATOR FOR ROTARY-VANE ENGINE WITH PERMANENT-MAGNET SYNCHRONOUS MOTOR

Cogeneration plant control system (Fig. 2) based on the RVECE consists of top hierarchy level control module and three local subsystems: thermal energy control, control of torque and speed of the engine and electric energy control.
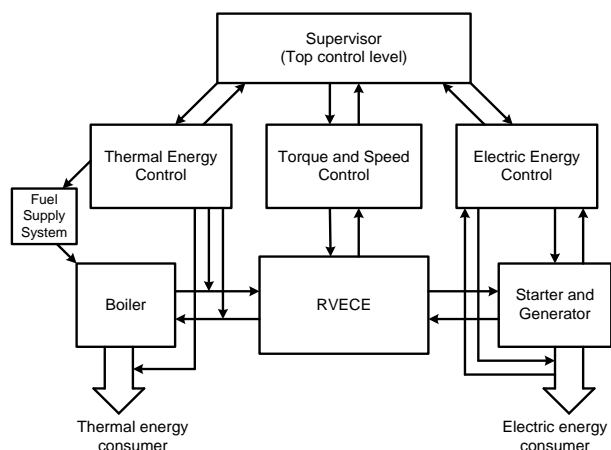

Fig. 2. Cogeneration plant control system.

Consider electric energy control subsystem of the power plant with RVECE.

It is known that most of the APSS are realized by structures that provide either constant shaft rotation speed of the vehicle or variable speed with regulation of power through the electric parameters [2, 5].

The presence of external electric source (direct voltage or alternating voltage) is also possible in cogeneration plants. It allows ensuring the effective start modes of the RVECE. Economical run-up RVECE in it's start mode is allowed by use of brushless DC (direct current) motor (BLDC) – permanent magnet synchronous motor (SMPM). In this case the unit must include recuperation module (active commutator – AFE (active front end converter)) and voltage inverter with the possibility to connect through the DC link.

Stabilization of the electrical part output parameters in system with the BLDC is usually provided by inverter of required power (voltage of the DC link in the range 450-600 V).

Shaft position sensor, indispensable component of the BLDC, in generator mode can provide organization of the shaft position and rotation speed signal in order to use in closed-loop control of thermo-mechanical subsystem in hierarchic control system of RVECE.

For running of the experiments to examine operating modes of BLDC (SMPM) as a starter and generator the test stand was created [6]. Stand uses the motor DVU2M165S (Fig. 3).

Tests have shown that in use of SMPM of DVU2M type (permanent magnets – strontium ferrites) working as a generator emf ratio is in the range $K_E = (0,6\text{-}3,0)$ V·s/rad.

The analysis and tests suggest it possible to use general-purpose SMPM as a starter-generator for RVECE in power plants with an output power from 1 kW to 20 kW [7].

Fig.3. The test stand.

The most promising domestic (Russian industrial general-purpose motors) SMPM for APSS with RVECE starter-generator using are motors of 6DVM series with Ne-Fe-B permanent magnets.

In addition SMPM weight is in the range from 30 to 80 kg: that is considerably lower than mass and dimension parameters of traditional asynchronous and synchronous generators.

III ELECTRICAL SUBSYSTEM OF THE LOW-POWER PLANT WITH LOW-SPEED VEHICLE

Fig. 4 shows the structure of the electrical subsystem of the plant for all necessary modes of operation:

- accumulator battery start (AB);
- generator mode: one of the converters is active (AFE (G)), the second one – inverter (INV (G));
- network start: commutators are swapped functionally (AFE(netwok) – INV(S));
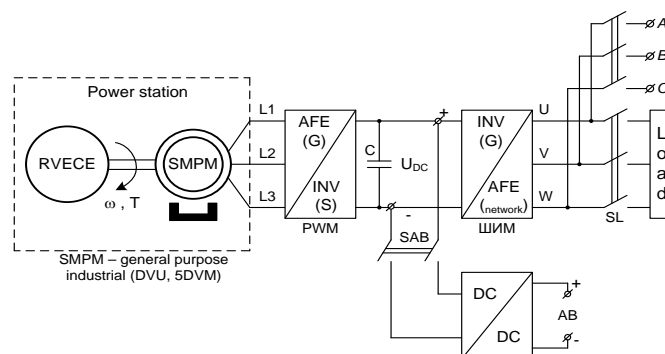- parallel operation with network.

Fig. 4. The structure of the electrical subsystem of the autonomous power supply system based on rotary-vane external combustion engine.

However, in creating APSS with SMPM for low-speed RVECE (<500 rpm) there is a need in multiplier of shaft speed or generator output voltage. Such device can be mechanical (reduction gear, Fig. 5a), electrical (step-up transformer, Fig. 5b) or electronic (DC/DC converter – power factor corrector (PFC), Fig. 5c).
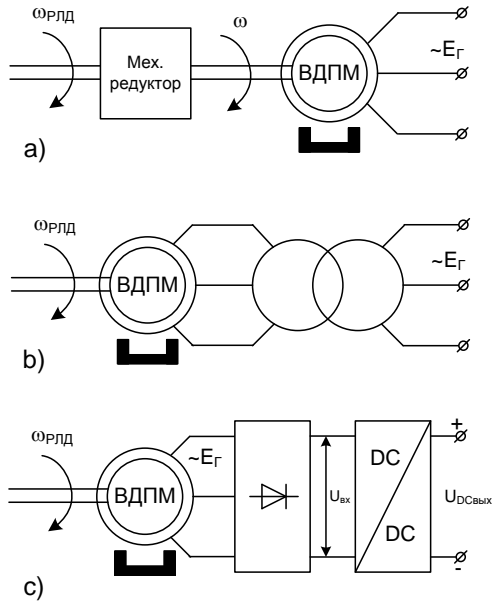

Fig. 5. Different options of speed or output generator voltage multipliers.

Researches of the DVU working in generator mode based on the well-known structure with transformer-multiplier were made – the results of the computer simulation and experiments of DVU2M165S in accordance with the functional diagram Fig. 6 are shown in the Fig. 7 (modeling was made using the program MATLAB Simulink). There are output voltage of the general-purpose SMPM confirming its ability to work as a generator (plus rectified voltage) and output voltage of the PWM-inverter. But the greater interest is in researches of structures with scheme 5c because of its controllability and thus the ability to influence the system parameters and embeddability in a general hierarchy of the plant control.
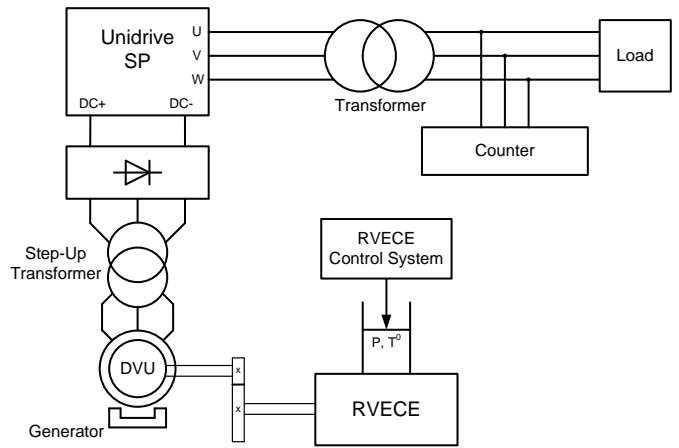

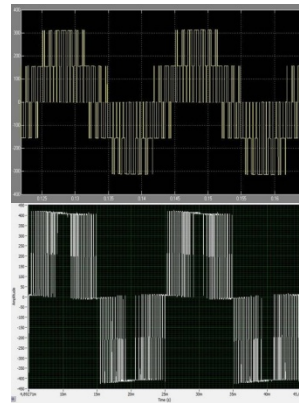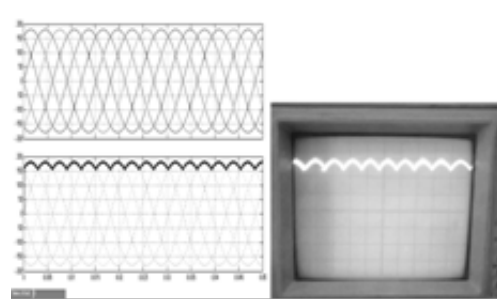Fig. 6. The functional diagram of the experiments with electrical multiplier.

Fig. 7. Results of the simulation and experiments of DVU motor.

PFC is set between the output of a straight rectifier, and various non-linear loads, including power semiconductor converter. Single-and multi-phase PFC can be constructed on the basis of step-up pulse converter (Fig. 8).
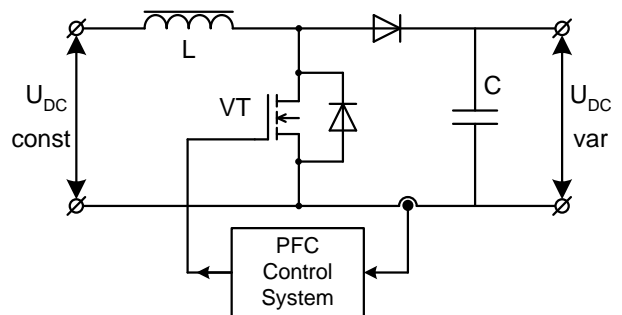

Fig. 8. PFC (DC/DC) module.

In this case, the system takes the form similar structures applied in wind-driven plants for returning maximum electric power at any rotation speed, as shown in Fig. 9. This is so-called variable speed system, in which rectified voltage can be obtained either by AFE or conventional rectifier. The value of the output PFC voltage be a function of DC voltage or current, or load parameters (regulator R).
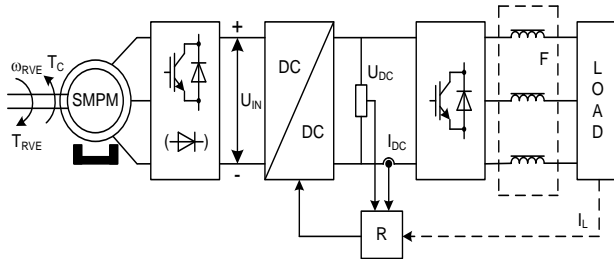

Fig. 9. The structure of the electric part with PFC-module.

Controlled DC-DC module allows providing amplitude regulation with constant output variable load voltage and current frequency; it increases the range of applied industrial inverters.

It was accepted that the DC-DC module provides the following law regulating the output voltage:

$$U_{dc}^{var} = U_{dc}^{const} \times \frac{1}{1 - \gamma} \qquad (1)$$

$$U_{dc}^{const} = \omega_{rve}^{const} \times k_e \times k_{sch}, \qquad (2)$$

where U_{dc}^{const} – output voltage of the three-phase straight rectifier, U_{dc}^{var} – output voltage of the PFC module, $\gamma = \frac{t_1}{T}$ – on-state power transistor VT pulse duration to the full period (also including active power diode state), ω_{rve}^{const} – RVECE shaft speed, k_e – emf transfer ratio, k_{sch} – coefficient of mechanical and electrical multiplexing scheme.

For accepted structure based on the DVU2M165S motor $\omega_{rve}^{const} = 104$ rad/s, $k_e = 0.6$, $k_{sch} = 4.9$.

Construction of PFC control system can be performed in hardware or software. For a software implementation, there are two approaches – classic digital PID (PI) – controller, or the fuzzy logic regulation – fuzzy-controller. Fuzzy control does not require knowledge of the exact model of the object (which is currently under development), but it can organize an approximate control strategy.

Fig. 10 shows the simulation results when the load switching on in APSS with PFC; the diagrams of inverter output voltage, load current, output and input voltages of PFC and DC-current (obtained on the model of the structure Fig. 9) are sequentially presented.
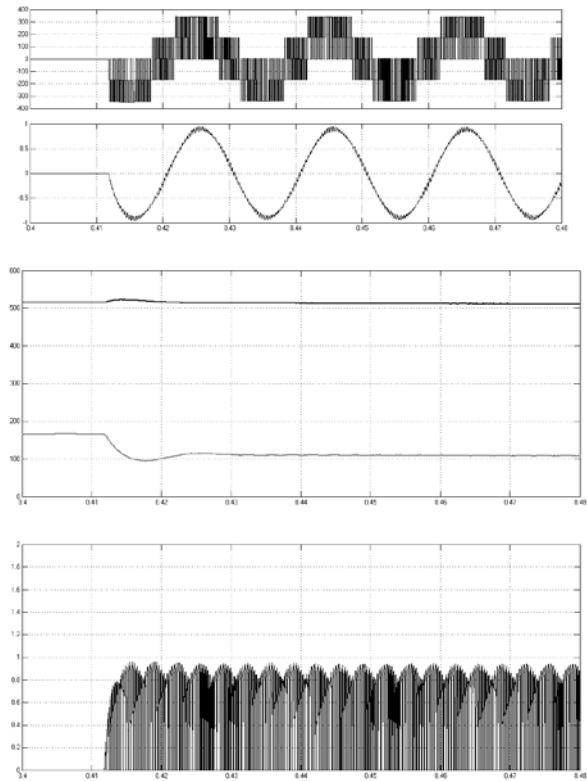

Fig. 10. The simulation results of the system with PFC.

IV CONCLUSION

The electrical part of the low-power (< 20 kW) power plant with low-speed rotary-vane engine (which is the setting for providing various modes of start and generation) can be implemented on typical industrial general-purpose BLDC (SMPM).

The structure of the electric subsystem for the APSS based on the RVECE providing efficient work in various modes is designed – structure with PFC module, considering features of rotary-vane engine shaft rotation. PFC control system, including the use of fuzzy-logic, can be embedded in the hierarchical control system of the entire plant. Also perspective is the potential integration of the motor in the mechanical part of the system (single capsule).

V REFERENCES

[1]. Бурман А.П. Управление потоками электроэнергии и повышение эффективности электроэнергетических систем:/ учебное пособие/ А.П.Бурман, Ю.К.Розанов, Ю.Г.Шакарян.- М.: Издательский дом МЭИ, 2012.-336 с.

[2]. Обухов С.Г. Системы генерирования электрической энергии с использованием возобновляемых энергоресурсов: учебное пособие: Изд-во Томского политехнического университета, 2008.- 140с.

[3]. Коломин И.В., Довгялло А.И., Русанов Ю.М., Лысенков В.В., Трубников Ю.М. Предварительные испытания роторно-лопастной машины. Вестник Самарского государственного аэрокосмического университета. №2. 2006., стр.302-305.

[4]. Плохов И.В., Донченко М.А., Лукьянов Ю.Н. Энергоэффективная автономная энергоустановка нового поколения. Доклад на международной конференции «Инновационные технологии 2009». М.:Иннотехэкспо, 2009.

[5]. Харитонов С. А. Электромагнитные процессы в системах генерирования электрической энергии для автономных объектов. – Новосибирск: Изд-во НГТУ, 2011. – 536с.

[6]. Федотов И.М., Хитров А.А. Structure designing of test stand for investigation of variable frequency electric drives. Cilvēks. Vide. Tehnoloģijas: 16 starptautiskās studentu zinātniski praktiskās konferences rakstu krājums 2012. gada 25. aprīlis. Rēzekne: 2012. – 464 lpp. p. 448-452.

[7]. Перминов А. Л., Хитров А. А., Хитров А. И. Мехатронная система «магнитоэлектрический синхронный двигатель - активный выпрямитель» для автономной системы электроснабжения на базе роторно-лопастной машины с внешним подводом тепла. Труды VII Международной (VIII Всероссийской) конференции по автоматизированному электроприводу АЭП-2012: ФГБОУВПО "Ивановский государственный энергетический университет им. Ленина". - Иваново, 2012. - 708 с. с. 330-335

[8]. Мелешин В.И., Овчинников Д.А. Управление транзисторными преобразователями электроэнергии. М. Техносфера, 2011. - 576 с.

123

Digital Control of Variable Frequency Interleaved DC-DC Converter

Kaspars Kroics

Institute of Physical Energetic. Aizkraukles 21, Riga. LV-1006, Latvia

Abstract – **This paper represents a design and implementation of a digital control of variable frequency interleaved DC-DC converter using a digital signal processor (DSP). The digital PWM generation, current and voltage sensing, user interface and the new period and pulse width value calculation with DSP STM32F407VGT6 are considered.**

Typically, the multiphase interleaved DC - DC converters require a current control loop in each phase to avoid imbalanced current between phases. This increases system costs and control complexity. In this paper the converter which operates in discontinuous conduction mode is designed in order to reduce costs and remove the current control loop in each phase. High current ripples associated with this mode operation are then alleviated by interleaving.

Pulse width modulation (PWM) is one of the most conventional modulation techniques for switching DC - DC converters. It compares the error signal with the sawtooth wave to generate the control pulse. This paper shows how six PWM signals phase-shifted by 60 degrees can be generated from calculated values.

To ensure that the measured values do not contain disturbances and in order to improve the system stability the digital signal is filtered. The analog to digital converter's (ADC) sampling time must not coincide with the power transistor's switching time, therefore the sampling time must be calculated correctly as well.

Digital control of the DC-DC converter makes it easy and quickly to configure. It is possible for this device to communicate with other devices in a simple way, to realize data input by using buttons and keyboard, and to display information on LED, LCD displays, etc.

Keywords – **switching converter, digital control, pulse width modulation, digital signal processors.**

I INTRODUCTION

A switching converter transforms an one voltage level into another for a given load by switching action of semiconductor devices. In the past, most of power electronic converters employed analog control methods. The reason is that digital controllers of the previous era had bandwidth problems. In the recent years the situation has changed significantly. The speed and functionality performance of the DSPs has improved. They are also available at a much lower cost. The advantage of the digital controller is that it is programmable and offers more functionality to the system compared to the analog controllers. Novel control algorithms and methods with DSP can be realized.

Interleaving control schemes are widely used in converter applications [1, 3, 5]. Merits of such control methods are reduction of input/output current or voltage ripples and volume, and increase in the processed power capacity of converters. In discontinuous conduction mode (DCM) the reverse-recovery losses of the boost diode are eliminated and switching losses can be reduced. Current in choke only depends on the on-time of transistor but does not depend on the current in the previous periods. This allows to improve dynamic and stability of converter even without current sensors in each phase.

Compared to DCM with constant switching frequency variable frequency mode yields lower total harmonic distortion (THD) of the input current and smaller peak inductor currents and results in lower switching and conduction losses. It is easier to achieve interleaving control of converters with constant frequency of operation [2, 4, 6, 8]. It is more difficult

to realize interleaving features of a converter with variable frequency operation. This will be the focus of the article.
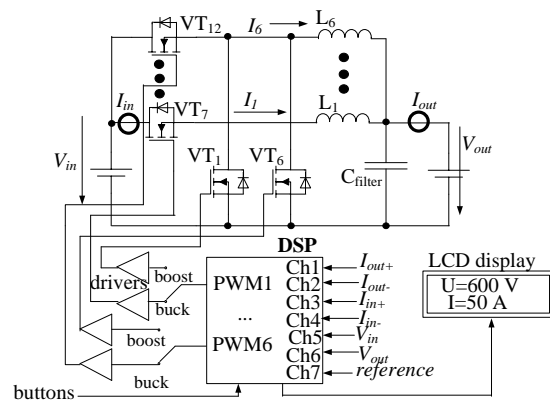

Fig. 1. DSP controlled DC-DC converter structure

Figure 1 shows the structure of DC-DC converter. It has six phases and is bi-directional as it can work in both buck and boost mode. If boost mode is selected, transistors VT1...VT6 are being switched on and off but VT7...VT12 remain turned off and vice versa. In order to calculate new period and pulse length values seven analog values are measured and converted into digital signals. Buttons and LCD display provide user interface. At present it is used to charge and discharge accumulator or ultracapacitor with maximal power 10 kW. Soft start must be realized in order to feed a resistive load or an electric drive.

Using the inductance as well as the input and output voltage the required on-time and off-time are calculated to ensure operation in boundary conduction mode (BCM). It is shown in figure 2. The required

phase shift value is determined by using the calculated switching period to guarantee optimal ripple cancelation. The current tracking can be done via open-loop control and no current sensing is necessary.
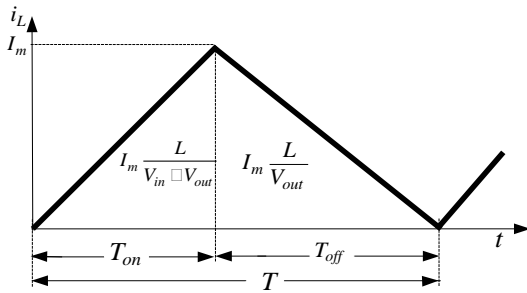

Fig. 2. Inductor current at boundary conduction mode

In BCM the peak current in choke is twice the average current [5]. The summary output current I_{out} of n phase converter is sum of all choke currents. Peak current in choke can be expressed as shown below.

$$I_m = \frac{2 \cdot I_{out}}{n} \tag{1}$$

I_m can be used not only to maintain the desirable output current but also to control input current and output voltage. It can be done if I_m is output of proportional-integral (PI) regulator that is shown in figure 3.
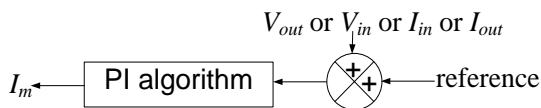

Fig. 3. Calculation of I_m by PI regulator

An error in the voltage measurement could cause a drop out of the BCM. In such a case entering into continuous conduction mode (CCM) has to be avoided to prevent overcurrent. Therefore it is beneficial to move slightly into DCM. Inductance is multiplied by the coefficient to get the a little enlarged DCM switching period and to stay into DCM.

II MATERIALS AND METHODS

In order to control the DC-DC converter the STM32F407VGT6 microcontroller (MCU) is used. This ARM Cortex-M4 32 bit MCU with floating-point unit has 210 DMIPS, up to 1MB Flash, 194 KB RAM, 17 timers (including the general purpose ones), 3 analog to digital converters (ADC), 15 communication interfaces. MCU maximal operating frequency is 168 MHz. It also includes a full set of digital signal processor (DSP) instructions and a memory protection unit (MPU).

The program code was written in C language and IAR Embedded Workbench for ARM integrated development environment (IDE) was used. The IAR Embedded Workbench for ARM is a window-based software development platform that combines a robust and modern editor with a project manager. It integrates all the tools needed to develop embedded applications including a C/C++ compiler, a macro assembler, a linker/locator and a HEX file generator. The IAR Embedded Workbench helps to expedite the development process of embedded applications by providing the IDE with project management tools and editor, highly optimizing C and C++ compiler for ARM, automatic checking of C rules, CMSIS (Cortex Microcontroller Software Interface Standard) compliance, linker and librarian tools, JTAG support.

To measure signals the Tektronix TPS 2024 digital oscilloscope was used. The oscilloscope has 200 MHz bandwidth and 2 GS/s real time sample rate. The TPS2024 input connector shells are isolated from each other and from earth ground.

The general-purpose timers (that are a part of a MCU) consist of a 16-bit auto-reload counter driven by a programmable prescaler. They may be used for a variety of purposes, including measuring the pulse lengths of input signals (input capture) and generating output waveforms (output compare and PWM). Pulse lengths and waveform periods can be modulated from a few microseconds to several milliseconds. The timers are completely independent and do not share any resources. They can be synchronized together.
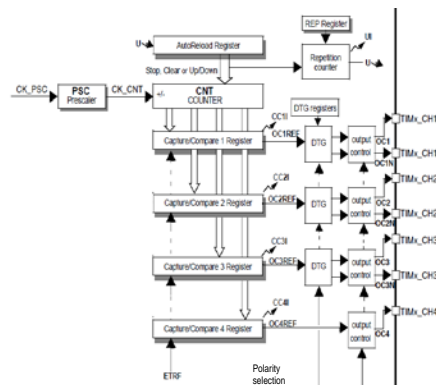

Fig. 4.   Fragment of timer's block diagram [7]

Figure 4 shows PWM generation part of timer's block diagram. Each timer has four capture/compare registers. The counter and the auto-reload register can be written and read by software. The content of the preload register is transferred into the shadow register permanently or at each update event. The update event is generated when the counter reaches an overflow. It can also be generated by a software. PWM signal frequency is determined by the value of the auto-reload register and a pulse length is determined by the value of capture/compare register in timer's PWM mode.

A 12-bit ADC has up to 19 multiplexed channels allowing it to measure signals from 16 external sources. The analog to digital conversion of the channels can be performed in single, continuous, scan or discontinuous mode. The main features of ADC are interrupt generation at the end of conversation and

dual and triple mode with configurable direct memory access (DMA) to data storage.
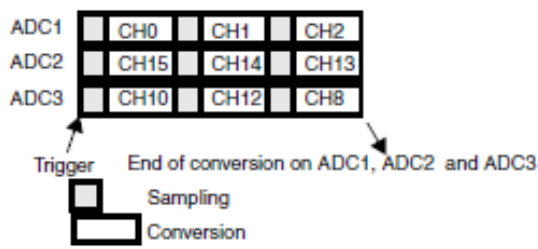

Fig. 5.   Triple ADC mode of 9 channels

To provide control, protection and user interface of DC-DC converter it is necessary to measure 7 analog signals. In this case ADC's triple mode (Fig. 5) was selected to provide conversation of these signals as fast as possible. Maximal frequency of ADC clock is 36 MHz. Three ADC's clock cycles are required for signal sampling and 12 for conversation. The time required for analog to digital conversation can be calculated:

$$t_{ADC} = \frac{N_{cycle}}{f_{CLOCK_{ADC}}} = \frac{15}{36 \cdot 10^6} = 417ns \qquad (2)$$

At the end of conversation three DMA transfer requests are generated. Then, the three transfers from the ADC register to SRAM take place: first, the ADC1 converted data, then the ADC2 converted data and finally the ADC3 converted data. This process is repeated for each three new conversations to avoid loss of the data already stored in the ADC register.

III RESULTS AND DISCUSSION

A.   ADC starting time

The Interrupt Service Routine (ISR) of a timer is the heart of the control software. The ISR has the highest priority of execution. During the interrupt of overflow of the timer's counter (IRQ1) the new period and pulse length values are set for each of six timers. In the capture/compare ISR of the timer (IRQ2) ADC is started and the new period and pulse length values are calculated.

Two major sources of electromagnetic interference (EMI) in DC-DC converter are dv/dt and di/dt during the switching times of the power transistors. EMI affects the accuracy of ADC. Therefore, it is important to measure current and voltage at a moment switching of transistors does not take place. Switching off the transistors interrupts current for a short time and produces significant EMI.
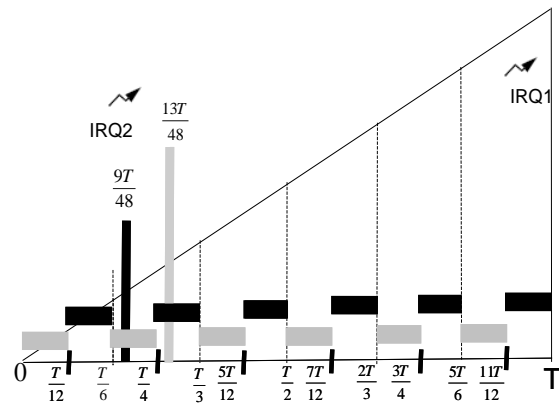

Fig . 6.   Selection of ADC's starting time

The transistors are controlled by microcontroller and it is possible to calculate the starting time of closing of the transistors. The transistor has the same pulse length in each phase. The pulses are only shifted in phase by 60 degrees or by sixth of the period (T). Figure 6 shows how to choose ADC conversion time without transistor switching off. The period is divided into 12 parts and it is determined in which part first channel's transistor switching off moment is. Switching moments of the transistors in other channels are in the other areas of the figure in the same color. So ADC conversion can be made in any area of a different color. To leave more time for calculation the ADC starting time is chosen in the beginning of period - 9T/48 in one case and 13T/48 in the other.
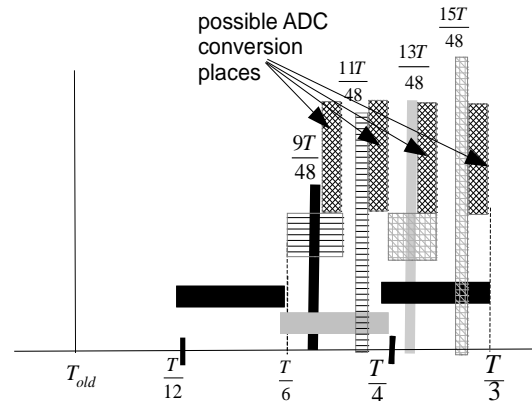

Fig. 7.   Selection of ADC conversation time

The transistor is controlled by PWM and the pulse length is determined by the timer's value stored in the capture/compare second register. This value is calculated in the IRQ2 program, which can be extended in order to find the position of value of the pulse length (CCR) and calculate new ADC starting time (p):

```
[12]    if (CCR<=(T/6))
[13]       {   if (CCR<=(T/12))
[14]           p=9T/48;        //ADC starting
    time 1
[15]           else
[16]             p=13T/48;}
       //ADC starting time 2
[17]    else if (((T/6)<CCR)&&(CCR<=(T/3)))
[18]       {   if (CCR<=(T/4))
[19]               p=9T/48;
[20]               else
[21]               p=13T/48;}
[22]
               ...............
```

The PWM signals from the previous period with length more than T/6 can also cause EMI. If the sum of the pulse time and the phase shift time exceeds T/6, then the phase with switch-off time of the transistor closest to the above calculated ADC starting time can be calculated with number up rounding to the nearest whole number as in (4). And then the switch-off time of the transistor of this phase can be calculated by using (5).

$$t_{pulse\_old} + n \cdot \frac{T_{old}}{6} \geq \frac{T}{6} \qquad (3)$$

$$n \geq \approx \frac{6 \cdot \left(\frac{T}{6} - t_{pulse\_old}\right)}{T_{old}} \qquad (4)$$

$$p_1 = t_{pulse\_old} + n \cdot \frac{T_{old}}{6} \qquad (5)$$

The program addition checks whether the switch-off time of transistor does not match the previously calculated ADC conversation time. If it does, a different ADC starting time is selected. Figure 7 shows the final algorithm of selection of the ADC starting time.

```
[23]    if((p1>=(T/6))&&(p1<(5*T/48))&&(p==(9*
    T/48))
[24]       {   p=11T/48; }       //ADC
    starting time 1a
[25]    else if
    ((p1>=(14*T/6))&&(p1<(T/4))&&(p==(13*T/48)
    )
[26]       {   p=15*T/68;}       //ADC
    starting time 2a
```

The previously calculated time required to perform ADC conversion is 417ns. The maximum time without EMI is T/48. It means that the minimum period of timer must be 20 µs or maximum frequency of impulse in each phase must be 50 kHz.

Figure 8 shows oscillogram of first channel PWM signal and one DSP output pin that is set when IRQ2 starts and that is reset when IRQ2 ends. It shows how much time is necessary for calculation of I_m, new period, pulse-time and new ADC starting time and so on. This time is less than the critical one.
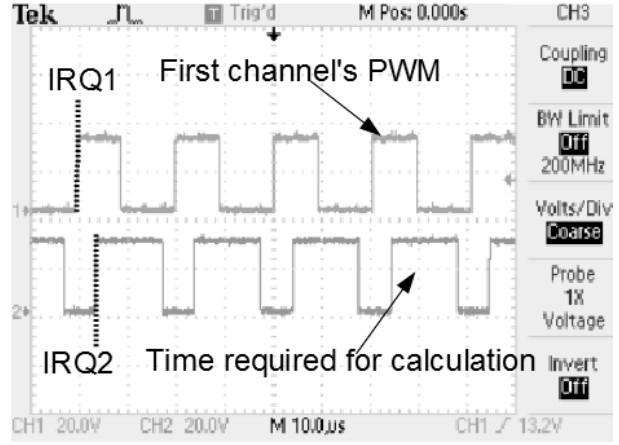

Fig. 8. Oscillogram of ADC's starting time

B. Digital filtering

The period value is calculated by using the (6) were I_m is feedback error calculated by using the proportional-integral (PI) algorithm, L is the inductance of choke, V_{in} is the input voltage and V_{out} is the output voltage. The equation shows that a small measurement error or noise induced error in sampled V_{out} value causes big error in period value.

$$T = I_m L \frac{V_{in}}{(V_{in} - V_{out}) \cdot V_{out}} \qquad (6)$$
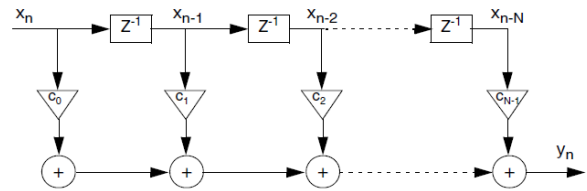

Fig. 9.   Block diagram of FIR filter

In order to improve the stability of the converter the finite response filter (FIR) for V_{out} was used. The figure 9 shows the block diagram of the FIR filter: x_n is the input signal, y_n is the output signal, c_i are the filter coefficients, also known as tap weights and N is the filter order. An Nth-order filter has N+1 terms on the right-hand side. The output value of filter is calculated by using (7).

$$y[n] = \left(c_0 x[i] + c_1 x[i-1] + c_N x[i-N]\right)$$

$$V_{out} = \left(\frac{1}{4}V_{outi} + \frac{1}{4}V_{out(i-1)} + \frac{1}{4}V_{out(i-2)} + \frac{1}{8}V_{out(i-3)} + \frac{1}{8}V_{out(i-4)}\right)$$

(7)

Four previously measured V_{out} values are stored in memory and when current ADC value is read, the filtered V_{out} value is calculated by (7). The filter coefficients are set equal to $1/2^n$ because shifting is faster then dividing. Older values have less influence on the filtered value if the coefficients are smaller. After calculation all the historical values are overwritten, the newest value is stored in memory and

127

the oldest value is erased. The circular buffer is shown in a fragment of the program.

```
[27]           Vout4=Vout3;
[28]           Vout3=Vout2;
[29]           Vout2=Vout1;
[30]           Vout1=Vout0;
       Vout0=ADCTripleConvertedValue[5];
```

The ripple of output voltage is not large but ADC's starting time varies as discussed above and it can lead to measurement error. The digital filtering of voltage value reduces this error and eliminates it's influence on stability of the interleaved converter.

C. Phase-shifted impulses generating

Six gate signals are needed to control the six-phase DC-DC converter. The phase shift between phases of converter in N-phase converter system can be calculated as in (8).

$$\varphi = \frac{360°}{N} = \frac{360°}{6} = 60° \tag{8}$$

The power transistors are controlled by PWM signal of microcontroller. Frequency and pulse length are calculated in each period. In overload ISR of the counter of the first channel's timer the new period and pulse width values of all timers are recorded in corresponding register but they are updated when an update event occurs. This event is generated when counter overload of corresponding timer occurs.
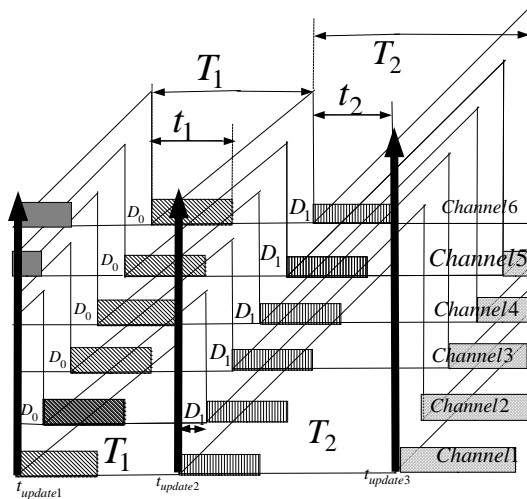

Fig. 10.   PWM signals

As interleaved DC-DC converter has 6 phases, PWM pulses must be shifted by 60 electrical degrees. As can be seen in figure 10 the phase shift ($D_0 = D_1$) does not change together with frequency, which is not correct. This problem can be solved.

Rapid decrease of the period causes duplication of PWM pulses and consequently the malfunction of the DC-DC converter. The maximum speed of decrease in period for the pulses not to overlap is one sixth of the value of the previous period if the pulse width is less

than 5/6 of the period as shown in figure 11. The converter does not have a current sensor in each phase. So it is necessary to increase a period a little in order not to get into uncontrollable continuous conduction mode. So the pulse length never exceeds 5/6 of the period.
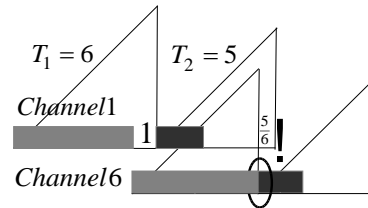

Fig. 11.   Determination of maximum speed of period change

50 kHz was chosen as the minimum switching frequency. The maximum value of a period is set to be equal to 1 ms so the frequency is 1 kHz. Further increase in the period creates very short PWM signals that produce big noise. It is possible to calculate the number of periods (n) in order to change the frequency from the lowest one to the highest one. It follows from (9) and (10) that 21 period is necessary to reach the minimum frequency. Such a time allows to respond to the load change.

$$\left(\frac{5}{6}\right)^n = \frac{f_{lowest}}{f_{highest}} = \frac{1}{50} = 0,02 \tag{9}$$

$$n = \log_{\frac{5}{6}} 0,02 \approx 21 \tag{10}$$
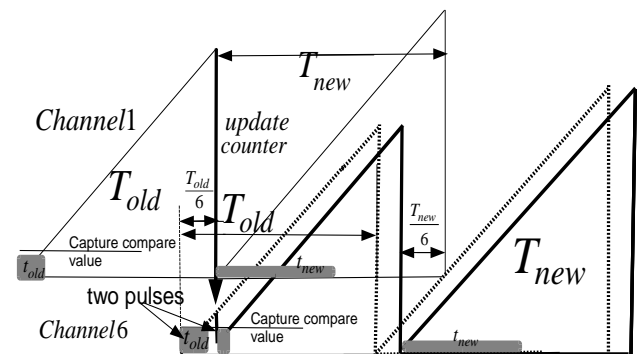
Fig. 12.   Realization of phase shift with counter update

Phase shift can be done by setting a counter value when the IRQ1 occurs. This counter value is calculated so that timer's period of the corresponding channel ends at point that provides right phase shift of new pulses. Figure 12 shows the implementation of the phase shift with a counter update. As can be seen in the figure the counter value can be calculated from the isosceles triangles by (11) where n is the number of channel from 2 to 6 can be written. The disadvantage of this method is that an extraneous pulse can be generated when changing the counter's value.

$$CNT = \frac{(n-7)\cdot T_{old}}{6} + \frac{(n-1)\cdot(T_{old} - T_{new})}{6} \quad (11)$$
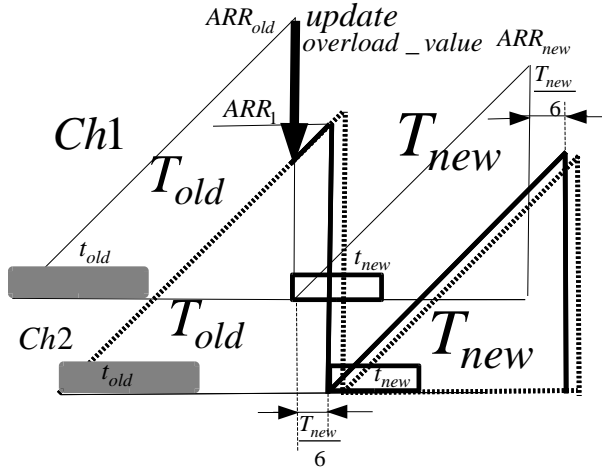

Fig. 13.   Realization of phase shift with overload value update

The phase shift can be implemented by updating the overload value of the timer which is value of the auto-reload register (ARR). In this case the period value is either prolonged or shortened. As discussed above the increase in period can not exceed 1/6 of it's length. This means that changing the period by updating it only affects the last sixth of the period where there is no impulse. As demonstrated in figure 13 the new value of ARR is set in the IRQ1. This value is selected so that it ensures the overload of the n-channel's timer in time that corresponds to required phase shift. The ARR value that must be set to provide a correct phase shift can be easily calculated by using the (12).

$$ARR_1 = ARR_{old} - \frac{(n-1)\cdot ARR_{old}}{6} + \frac{(n-1)\cdot ARR_{new}}{6} \quad (12)$$

D.   Hardware implementation

The figure 14 shows hardware implementation of DSP controlled 6 phase interleaved DC-DC converter. It is possible to realize communication with a device via USB, CAN, I2C, UART, SPI, touch screen, digital microphone, etc. LCD display (1), LEDs (5) and buttons are selected in this case as cheapest solution. The power transistors (4) are placed on the radiator plate. DSP board (3) is connected via the cable (2) to the buttons.
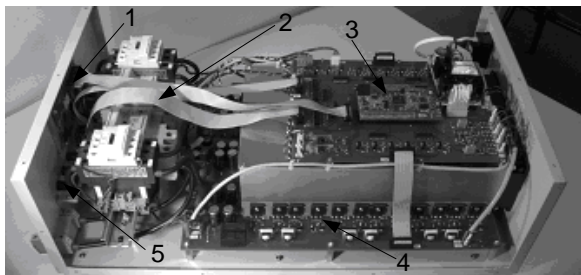

Fig. 14.   Hardware of interleaved DC-DC converter

IV CONCLUSION

It is possible to design interleaved DC-DC converter without measuring current in each phase. So it is necessary to implement digital control to implement the open-loop control.

In order to ensure that the measured values do not contain disturbances and to improve the system stability the simple FIR digital filter is implemented.

The analog to digital converter's starting time must not coincide with the power transistor's switching time, therefore the ADC starting time calculation and algorithm is used.

Six gate signals are needed to control the six-phase DC-DC converter. This paper describes the algorithm for phase shifting of signals from calculated values. This algorithm was implemented with some limitations and requires future investigations.

Digital control of the DC-DC converter makes it easy and quickly to configure. Such implementation of the hardware of the converter needs a smaller number of components and is less costly. The input of data is realized simply by using buttons and potentiometer, while output of data - by using LEDs and the LCD display.

V REFERENCES

[1] Ashur A. S., Thorn, R. Modeling and Simulation of Automotive Interleaved Buck Converter. Universities Power Engineering Conference, 2009, pp. 1-6.

[2] Chattopadhyay S., Das S. A Digital Current-Mode Control Technique for DC-DC Converters. *IEEE* Transactions on Power Electronics, 21(6), 2006, pp. 1718–1726.

[3] Chunliu C., Chenghua W. Research of an Interleaved Boost Converter with four Interleaved Boost Convert Cells. Microelectronics & Electronics, 2009, pp. 396–399.

[4] Grote T., Figge H., Fröhleke N., Böcker J. Digital Control Strategy for Multi-Phase Interleaved Boundary Mode and DCM Boost PFC Converters. Power Electronic & Electric Drives, 2011, pp. 3186 - 3192.

[5] Huber L., Irving B. T., Jovanovic M. M. Open-Loop Control Methods for Interleaved DCM/CCM Boundary Boost PFC Converters. IEEE Transactions on Power Electronics, *23*(4), 2008, pp. 1649–1657.

[6] Kim J., Lim J., Chung S., Song Y. DSP-Based Digital Controller for Multi-Phase Synchronous Buck Converters, Journal of Power Electronic, *9*(3). 2009, pp. 410–417.

[7] STM32F40x, STM32F41x, STM32F42x, STM32F43x advanced ARM-based 32-bit MCUs reference manual, 2012, pp 1416.

[8] Tsai J., Wu T., Chen Y., Lee M. Interleaving Phase Shifters for Critical Mode Boost PFC. *IEEE* Transactions on Power Electronics, *23*(3), 2008, pp. 1348–1357.

Selection of Parameters of Current Collection Systems of Turbo-Generators to be Monitored by Means of Technical Diagnostics

Alexander Markov, *Pskov State University*, **Yuri Rodionov**, *Ecotech Ltd, Pskov*

Abstract. In this article the choice of parameters of the current collection systems is substantiates, which must be monitored by technical means. It is shown that such parameters are the intensity of the sparking under brushes, uniformity of current distribution on parallel brushes, vibrations and runout slip rings and the state of their surface.

For monitoring these parameters Ecotech Ltd (Pskov) develops a hardware-software complex.

Complex consists of the following devices: - device to monitor the intensity of sparking, - device for measuring the current of brushes, - device for measuring vibrations and runout, - device for exploring the surface of rotating slip rings.

Development of hardware-software complex is supported by the Foundation for Assistance to Small Innovative Enterprises in the scientific and technical field.

Keywords – turbo-generator, current collection system, current distribution, sparking, vibrations, hardware-software complex.

I INTRODUCTION

It is known that current collection system of turbo-generator is the least reliable. For example according to the Department of general inspection of operation (Russia) current collection system takes the first place by accident, on its share is more than 25% of all accidents turbo-generators.

The reason of the unsatisfactory situation with the reliability of the current collection system is that monitoring tools in power plants are absent.

This article is devoted to justifying the choice of the parameters of current collection systems, which are subject to mandatory monitoring by the hardware-software complex for a permanent monitoring of current collection systems. Also a block scheme of hardware-software complex and technical specifications of devices are presented.

And finally the article contains the results of testing the devices.

Now the operation of current collection systems of turbo-generators is carried out in accordance with the operating instructions of JSC «Electrosila» and the firm ORGRES. The instruction of the JSC «Electrosila» [1] provides for monitoring of 12 specific problems. The ORGRES instruction [2] contains a list of 64 causes of violations in the operation of the current collection systems, it also shows the 38 signs of violations in the operation.

Obviously such a long list of monitored parameters using a hardware-software complex is not possible and it is not necessary for several reasons.

First, a significant part of the settings more easily and efficiently controlled visually. For example brush damages, the presence of discoloration on pressure springs, mechanical damages of various elements of the current collection system and others damages are easy to control by visually.

Second, many irregularities in the current collection system appear in the same way. For example in the form of sparking may occur deterioration turbine vibration condition, incorrect pressure on the brush, the deterioration of the profile or contaminated surfaces of slip rings, uneven current distribution on the brushes, the lack of humidity in the engine room, poor quality brushes, uneven brush wear.

Third, the number of parameters does not make sense to control by hardware-software complex, as they are caused by natural factors of production of power stations such as turbine start, the critical frequency at turbine start, works for rotor balancing, no isolation between the brush holder and the traverse.

Thus, from the above it follows that monitoring through the hardware-software complex to be fairly limited set of parameters.

The rationale for its selection is as follows.

II JUSTIFICATION OF THE NECESSITY TO MONITOR THE INTENSITY OF SPARKING

The instruction of the JSC «Electrosila» requires regularly (at least once a day) to inspect the current collection system and visually evaluate its work in sparking, as the sparks of carbon brushes is the indicator of the current collection system, and it is necessary to monitor its intensity.

According to this instruction should distinguish three types of brush sparking:

1. Sparking a large number of brushes, having the form of sparks flying away, the path which ends with an asterisk. This type of sparking is the combustion of small ferroparticles in oxygen air. Sparking cause is the lack of contact pressure of brushes or its high vibration.

To reduce or eliminate sparking you should increase the contact pressure at all brushes of sparkling slip rings. If this measure does not give the

desired effect then you need to check or improve the shape of the contact surface of the slip rings by machining or balancing to reduce the vibrations. In urgent cases you can resort to manual polishing of slip rings surface without turning off the turbo-generator.

2. Sparking a small number of brushes, accompanied by the destruction of the brush material. This type of sparking due to sharp violation of the current distribution between the parallel brushes. It should reduce the contact pressure of the overloaded brushes.

Sparking between the side surfaces of brushes and the inner walls of brush holders. The reason for this sparking is the violation of contact between the brush and conductor. Defective brushes should be replaced by new ones, preferably of one plant with similar physical and mechanical properties. The contact pressure of new brushes should be at 30 - 40% less than the old, fully lapped. In all cases the intermediate pressure on the brush should be set in proportion to its degree of grinding.

Daily visual control of operation of the current collection system aims to determine timely the beginning of the sparking gain. Purpose - manual grinding of contact rings, a temporary reduction in the current load of the rotor or otherwise.

When the circular fire appears turbo-generator must be immediately disconnected from the network.

The instruction of JSC «Electrosila» allows 1 ¼ sparking of brushes according to «Rotating electrical machines. General specifications».

Instruction ORGRES [2] contains similar requirements for monitoring sparking and also notes the importance of monitoring of this parameter. For example paragraph 3.1.1 of this instruction indicates that the turbine must be disabled in emergency, removed the excitement and the turbo-generator is disconnected from the network when a circular fire at one or both poles appears and in intensive sparking.

Instruction ORGRES admits sparking of degrees 1 and 1 ¼. When sparking degree is more than 1 ¼ it is necessary to take special precautions to reduce it. Namely you must relieve the turbo-generator reactive power and produce extraordinary vibration measurement of slip rings. If the allowable vibration values (300 microns) is exceed you should take steps to eliminate it.

Thus the intensity of sparking is a subject of mandatory monitoring. However the instructions require to control it visually and very rarely (once a day). This makes it impossible to detect timely the sparking began. The consequence of this is the development of sparking up the circular fire with a turbo-generator emergency stop.

Consequently there is a need to monitor the intensity of sparking under brushes **constantly** using the hardware-software complex.

III JUSTIFICATION OF THE NECESSITY TO MONITOR THE UNIFORMITY OF THE CURRENT DISTRIBUTION

Instructions JSC "Electrosila" indicates that the monitoring of current collection system and its adjustment are to ensure similar meaning of currents of parallel brushes. However, the instructions do not have any indications of the instruments with which to measure the current of brushes.

Current of brush is proposed to determine indirectly, by temperature of brush wire. Brush with more hot conductors require relieving the pressure, with more cold - increasing. Conductor temperature should be determined by hand. Obviously that this method cannot measure the current brushes.

The instructions ORGRES also indicates that the adjustment of current collection system is to provide as uniform loading of each brush. Current measurement should be made with the help of indicators DC. In other words, devices specifically designed for the measurement of currents brush does not exist.

As a result the number of failures of turbo-generators is maintained at a high level. The situation is aggravated by the fact that there is a decrease in the qualification of the staff, falling technical education.

Thus monitoring of uniformity of the current distribution between brushes with the use of hardware-software complex is necessary.

IV JUSTIFICATION OF THE NECESSITY TO MONITOR VIBRATIONS OF SLIP RINGS

Vibrations and runout of slip rings are an important parameter of the current collection system. It characterizes the quality of the surface of slip rings. According to the instructions of JSC "Electrpsila" vibrations and runout are measured by a special indicator. The value of vibration should not exceed 300 microns, runout – 50 microns.

Vibrations measurements should be made once a month at least. Measurements are carry out under steady-state mode of turbo-generator and at the same rotor current. If the vibrations are more than 300 microns it is necessary to take steps to eliminate it.

The instruction allows the operation of turbo-generator with the vibrations of more than 300 microns. In this case there should be no unacceptable sparking, destruction of brushes, large heating. If it is impossible to ensure these conditions it is necessary to stop the turbo-generator. The negative consequences of high vibrations are high mechanical wear of slip rings and brushes.

V JUSTIFICATION OF THE NECESSITY TO MONITOR THE STATE OF THE SURFACE OF SLIP RINGS

The instructions need to pay special attention to the surface state of the slip rings. It should not have defects. The surface state should be evaluated once a day visually. Obviously that you can evaluate the surface state visually only slip rings are fixed.

Thus the state of the surface of contact rings determines the state and quality of current collection system.

Therefore, this parameter should be monitored. It should be monitored not visually but using a special device and when the rings are rotating with an angular speed of 3000 rev / min.

VI HARDWARE-SOFTWARE COMPLEX

So there is a necessity to monitor sparking brushes, uniform current distribution, vibrations of slip rings, state of the surface of the rings.

Today the company Ecotech Ltd (Pskov, Russia) develops hardware-software complex for monitoring these four parameters. The complex consists the following devices [3]:

- device for monitoring the intensity of sparking under brushes,
- device for measuring current of brushes,
- device for measuring vibrations and runout,
- device for exploring the surface of the rotating slip rings. This device will be auxiliary.

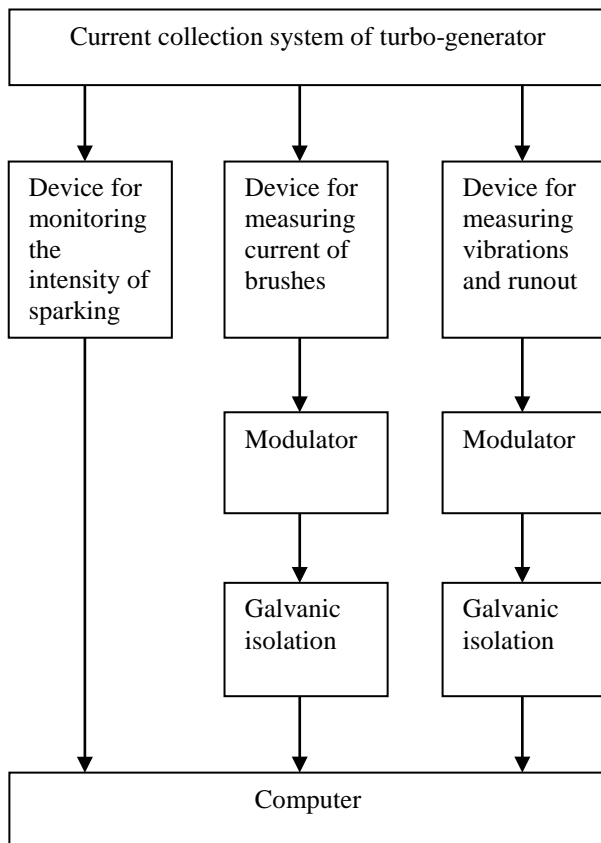The block scheme of the hardware-software complex is shown in Fig. 1.

Fig. 1. Block scheme of hardware-software complex

Device for monitoring the intensity of sparking has two identical channels of measurement. This allows to use them to monitor sparking of both positive and negative polarities.

Information about the intensity of sparking appears in three forms:

- three-color alarm («red», «yellow», «green»), which characterizes the degree of sincerity;
- sound alarm, buzzer sounds in large sparking case. Buzzer locates where the staff is always present;
- analog form of alarm, on the front panel there is an indicator, the scale of which is divided into 4 zones:

a) lack of sparking or sparking level is equal 1;

b) poor sparking or sparking level is equal 1¼ or 1½;

c) strong sparking or sparking level is equal 2;

d) invalid sparking (circular fire) or sparking level is equal 3 and more.

This device has two receiving antennas, one for each slip ring. Each antenna is placed in a protective screen and fixed under the cover of current collection system near its ring. Galvanic connection between the antennas and current collection system is absent.

Technical specifications of this device are:

voltage	220 V, 50 Hz,
power	60 W,
mode of operation	continuous.

When adjusting the current collection system you should strive for setting up the same currents of all brushes. Practice of operation shows that current of one brush rarely exceeds 100 A. Therefore when developing the device for measuring currents of brushes it was decided to establish the limits of measurement of brush from 0 A to 100 A.

The device has a sensor of the «hook» to cover the funicle brushes. As each brush has two current carrying funicle, the measurements are performed separately for each of them.

Another device of the complex measures vibrations and runout of slip rings at all speeds of rotation. Resolution of this device is 0,5 microns. Ranges of the measured vibrations are 0-50, 0-100, 0-150, 0-200, 0-250, 0-300, 0-350, 0-400, 0-450, 0-500 microns.

VII TESTING OF THE DEVICE FOR MEASURING CURRENT OF BRUSHES

Testing of this device was performed on the experimental stand of Ecotech Ltd. It is based on the current collection system (Fig. 2).
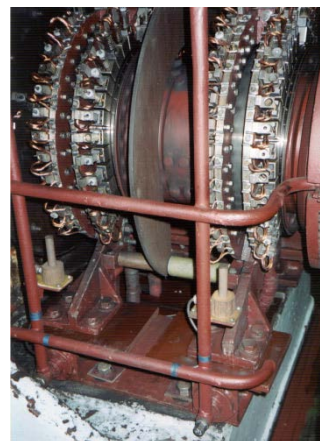

Fig. 2.   Current collection system of experimental stand

The results of measurements of currents of brushes are presented in Table I. The numerator gives the values of the currents measured by the device, the denominator gives the exact values of the currents. The exact value is obtained by using shunts. You can see that the exact value is very close coincides with the measured by the device.

TABLE I

THE RESULTS OF MEASUREMENTS OF CURRENT

Brackets	Negative ring (brushes EG-2AF)					Positive ring (brushes 611 OM)				
	Number of brush					Number of brush				
	1	2	3	4	5	1	2	3	4	5
1	30/30	37/30	28/28	31/30	30/33	40/38	37/38	23/28	55/50	25/31
2	25/28	25/28	43/35	16/20	61/73	30/26	27/34	42/37	40/33	65/72
3	48/45	52/45	60/48	40/35	32/36	56/58	43/38	84/78	46/41	34/31
4	24/30	33/35	54/41	56/50	85/91	80/97	50/42	63/58	47/46	77/72
5	33/34	39/31	47/49	76/68	23/34	16/17	25/30	22/18	85/87	26/35
6	74/68	38/35	70/68	25/30	14/20	28/30	36/32	31/30	41/38	33/27
7	22/27	51/46	66/61	60/55	47/40	17/20	27/31	74/81	17/20	30/27
8	74/68	79/60	37/30	20/25	21/25	43/40	26/30	24/28	36/41	31/40
9	22/27	16/25	35/30	29/30	16/22	44/46	23/26	40/38	21/26	32/30
10	74/68	24/30	18/21	30/35	44/40	68/80	19/23	23/33	35/31	14/19
11	22/27	32/30	33/33	0/0	55/50	24/25	30/25	25/30	32/32	16/20
12	74/68	44/30	12/8	32/25	25/27	39/37	15/14	35/31	20/26	29/27
13	22/27	22/27	36/33	22/28	20/18	18/22	24/28	8/6	30/33	45/40
14	74/68	22/20	55/45	19/14	30/27	24/22	30/29	33/37	16/21	65/53
15	21/25	32/27	63/53	17/18	40/38	78/72	44/42	0/0	21/23	15/20
16	47/52	33/28	45/45	41/47	27/22	25/22	3/2	50/47	56/51	35/33

VIII TESTING OF THE DEVICE FOR MEASURING VIBRATIONS AND RUNOUT

Testing of this device was performed on the
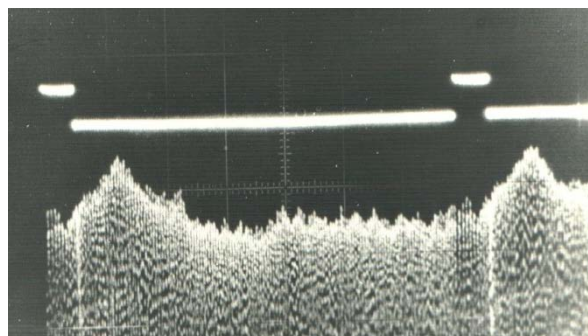
experimental collector. Tests were carried out at the rotation speed of 3000 rev / min. The results are shown on Fig. 3.

On the oscilloscope screen we can see every collector plate, the runout of collector, protrusion of individual plates.

IX CONCLUSION

So the most important parameters of the current collection systems are the intensity of the sparking under brushes, uniformity of current distribution on parallel brushes, vibrations and runout slip rings and the state of their surface.

For monitoring these parameters Ecotech Ltd (Pskov) develops a hardware-software complex. The complex consists the following basic devices:

- device for monitoring the intensity of sparking under brushes,

- device for measuring current of brushes,

- device for measuring vibrations and runout of slip rings or collectors.

These all devices were successfully tested on the experimental stand Ecotech Ltd.

X ACKNOWLEDGMENTS

XI REFERENCES

[1] Brush-contact device of TVV and TVF types turbo-generators. Operating instruction. - 1988.

[2] Typical instruction for operation and maintenance of slip rings unit of turbo-generators of 63 MW and above. - 2000.

[3] Y. Rodionov, "Design, manufacture and testing of the model of a hardware-software complex of continuous monitoring of the current collection systems of turbo-generators," Ecotech Ltd, Pskov, Russia, Tech. Rep. 01201271200, 2012.

Technology for Obtaining Cu₂ZnSnSe₄ Thin Films

Pāvels Narica[1], Vjačeslavs Gerbreders[2], Velga Akmene[2], Irēna Mihailova[2]

1 - Rezeknes Augstskola, Address: Atbrivosanas aleja 76, Rezekne, LV-4601, Latvia
2 - Daugavpils University, Parades 1, Daugavpils LV-5401, Latvia.

Abstract. **Cu₂ZnSnSe₄ thin films were obtained by sequential deposition of basic elements (Sn, Se, Zn, Cu) on a glass substrate. The thickness of each layer was selected to achieve 2:1:1:4 stoichiometric ratio for copper, zinc, tin and selenium, respectively. To obtain compound Cu₂ZnSnSe₄ samples were annealed at temperature range of 150⁰C to 400⁰C. Surface of samples were investigated using scanning electron microscope. Analysis of chemical composition and x-ray diffractometry was performed before and after annealing of samples.**

Keywords – **semiconductor, Cu₂ZnSnSe₄, thermal annealing.**

I INTRODUCTION

Copper zinc tin selenide $Cu_2ZnSnSe_4$ (CZTSe) is among perspective materials for solar energy harvesting due to its optical and electrical properties. $Cu_2ZnSnSe_4$ has a narrow bandgap, high absorption and long-term stability. From the ecological point of view it is important that $Cu_2ZnSnSe_4$ is a non-toxic («Cd-free») material because of the lack of heavy metals in it. It consists of widespread and therefore relatively cheap elements. Still, efficiency of material is low and it is necessary to invest in further research to optimize technological processes of $Cu_2ZnSnSe_4$ production.

The aim of the research was to obtain $Cu_2ZnSnSe_4$ compound by sequential sputtering on glass substrate and annealing the samples afterwards. Influence of annealing temperature on forming of compound was investigated as well as influence of layer sputtering sequence on optical and electrical properties of $Cu_2ZnSnSe_4$ samples.

II MATERIALS AND METHODS

A. Synthesis of Cu₂ZnSnSe₄ (CZTSe) films

To provide interaction between the initial compounds (copper selenide, zinc and tin) most effective technology for obtaining thin films was selected. CZTSe films were obtained on glass substrate using vacuum evaporation system EMC 150T ES (Quorum Technologies Ltd.), which is a combined system with interchangeable inserts for sputter coating or carbon/metal evaporation.

For application of selenium (Se) thermal evaporation method was used. Thickness of applied layers was controlled by quartz resonator while evaporation rate was maintained in required range by regulating current in evaporator. Evaporator is a metallic plate shaped as boat which contains selenium tablets.

Evaporation time was 10 minutes. Cu, Zn and Sn were applied by magnetron sputtering device EMC 150T ES (Quorum Technologies Ltd). The effect of compound application sequence was studied and optimal parameters were selected on the basis of experimental data (Table 1). Table 1 shows the sequence of sputtered layers as well as thickness of each layer.

TABLE 1.

Layer N⁰	Compound	Layer thickness (mm)
1.	Cu	20
2.	Zn	20
3.	Sn	30
4.	Se	360
5.	Sn	60
6.	Cu	30
7.	Se	800
8.	Zn	25
9.	Cu	45

To determine the optimal conditions for obtaining $Cu_2ZnSnSe_4$, samples were annealed in furnace at different temperatures. Temperature was varied from 150⁰C to 400⁰C by step of 50⁰C. It was investigated if there is a correlation between annealing temperature and formation of compound $Cu_2ZnSnSe_4$.

B. Methods of investigation

Surface of thin films was investigated, using scanning electron microscope (SEM) TESCAN-VEGA LMU II. Investigation of thin films structure was performed on x-ray difractometer SmartLab RIGAKU with Cu-Kα radiation (λ = 1.543 Å) operated at an acceleration voltage of 40 kV and an emission current of 150 mA. Bragg - Brentano focusing optic wavelength with a primary monochromator was used.

The phase structure analysis of films was performed by comparing distances between crystal lattice planes of samples with those of etalon samples according to

JCPDS data. Relative intensity of x-ray diffractogram (XRD) peaks was also compared to etalon samples.

To acquire precise values of crystal lattice constant, Nelson-Riley extrapolation method was applied. Linear approximation of obtained values was carried out with a method of least squares.

III RESULTS AND DISCUSSION

Figures 1 and 2 show SEM images of $Cu_2ZnSnSe_4$ films annealed at different temperatures. At annealing temperature of 200^0C film has a finely dispersed structure. With a temperature growth, an increase of crystallite size can be observed (Fig.1).
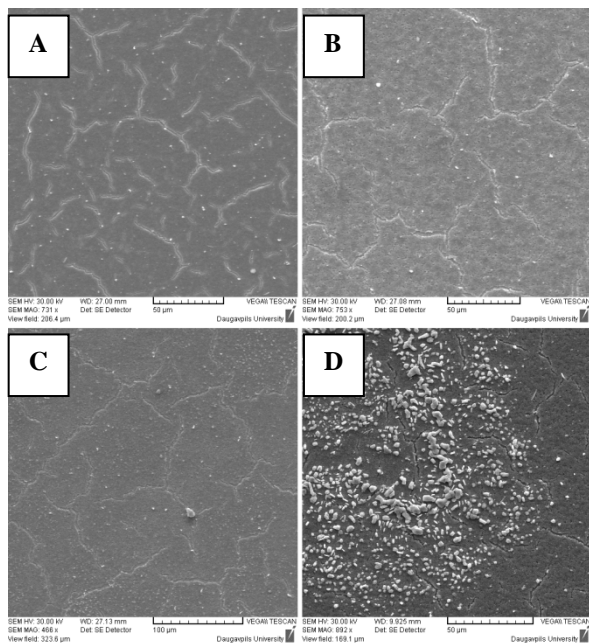

Fig. 1. SEM images of $Cu_2ZnSnSe_4$ films annealed at a) 250 ^0C; b) 300^0C; c) 350^0C; d) 400^0C.

Structural analysis of crystallites of the sample annealed at 400^0C (Fig.1,d) showed that they consist of copper oxide. That means that further increase of annealing temperature is not recommended because of increase of metal oxide in sample. Besides, in the annealing process amount of Se in sample decreases due to its evaporation.

Investigation of thin films structure was performed on x-ray difractometer. Since the multi-layer structures were evaporated on glass substrates coated with an ITO layer, there are peaks corresponding to In_2O_3 on all XRD patterns. In samples annealed at 250^0C, the required CZTSe compound wasn't obtained. In that case thin films are composed of CuSe, ZnSe and SnSe. At annealing temperature of 300^0C CZTSe compound appears and peaks relevant to simple selenides CuSe, ZnSe and SnSe disappear. When increasing temperature to 350^0C, improvement of CZTSe crystalline structure is observed. Further increase of temperature to 400^0C, Cu_8O peaks appears on XRD pattern together with CZTSe peaks.
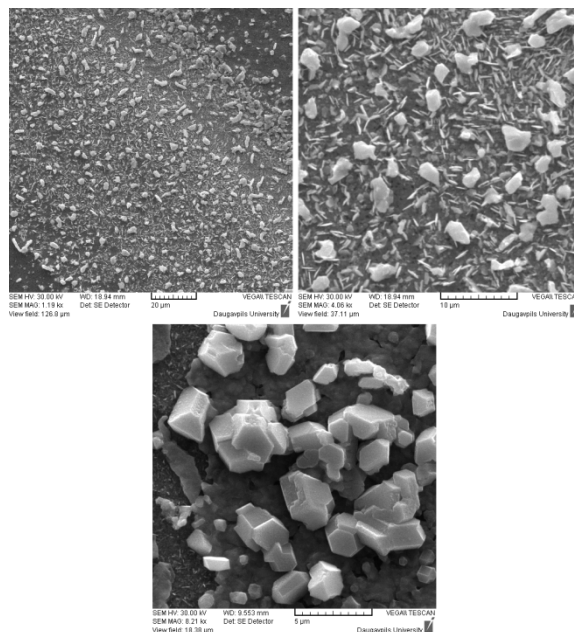

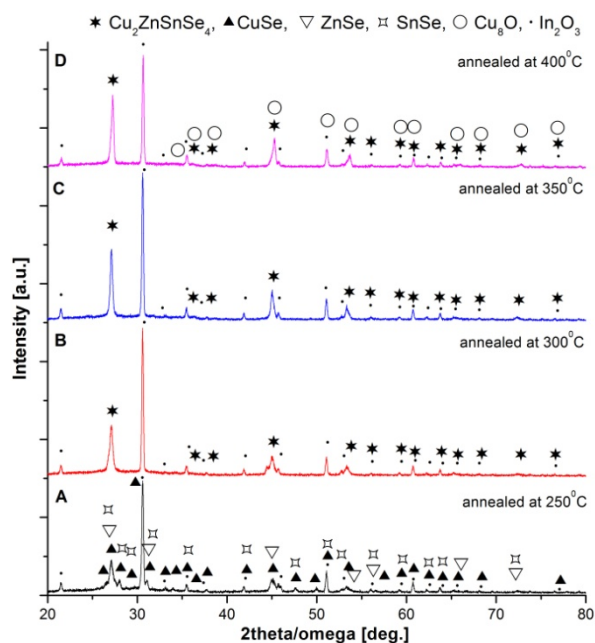Fig. 2. SEM images of CZTSe film annealed at 400^0C at different scale.

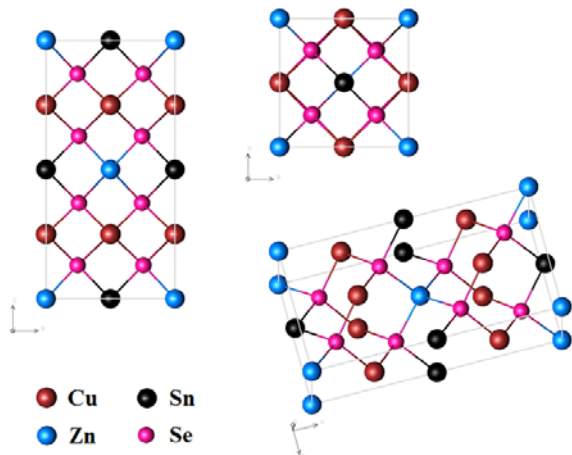Fig. 3. X-ray diffractometry data of $Cu_2ZnSnSe_4$ films annealed at: a) 250 ^0C; b) 300^0C; c) 350^0C; d) 400^0C.

Fig. 4. Structure of $Cu_2ZnSnSe_4$ crystal lattice according to x-ray diffractometry data of thin film annealed at 350 ^{0}C.

From the experimental data it was concluded that optimal conditions for annealing of compounds is temperature of 300 - 350^{0}C for 30 minutes.

IV Conclusion

Method for obtaining $Cu_2ZnSnSe_4$ compound was developed. Potential of obtaining extra-pure thin films using thermal and magnetron sputtering was investigated. Surface morphology and structure of $Cu_2ZnSnSe_4$ films was explores after annealing at different temperatures. Minimal temperature of transition from amorphous to crystalline phase was determined.

V References

[1] Altomare A., J. Appl. Crystallogr. 42 119. 2009.
[2] Chaliha S., Borah M.N., Sarmah P.C., Rahman A.. *J. Optoelectron. Advanc. Mater.* 10, 427. 2008.
[3] Deshpande M.P., Chaki S.H., Patel N.H., *J. Nano- Electron. Phys.* 1, 193. 2011.
[4] Green M.A., Emery K., Hishikawa Y., Warta W., *Prog.Photovolt.: Res. Appl.,* 18, 346. 2010.
[5] Hariskos D., Spiering S., Powalla M., *J. Thin Solid Films*. 480, 99. 2005.
[6] Kauk-Kuusik M., Altosaar M., Muska K., Pilvet M., Raudoja J., Timmo K., Varema T., Grossberg M.,. Mellikov E, Volobujeva O. Post-growth annealing effect on the performance of $Cu_2ZnSnSe_4$ monograin layer solar cells. *J. Thin Solid Films*, Tallin 2013.
[7] Poortmans J., Arkhipov V., *Thin Film Solar Cells: Fabrication, Characterization and Application*. Leuven, Belgium:John Wiley & Sons, Ltd. IMEC: 2006.
[8] Rusu G.I., Popa M.E., Rusu G.G., Iulia Salaoru, *Appl. Surf. Sci.* 218, 223. 2003.
[9] Venkatachalam S., Mangalaraj D., Narayandass Sa.K., *Vacuum* 81, 928. 2007.

Study of the Ion Radiation Influence on the Parameters of Unijunction Transistors

Nikolaj Nenov[1] ,Petar Tomchev[2] , Rayna Ivanova[3]

Technical University of Gabrovo, BULGARIA,

1 - e-mail: nenovtugabrovo@gmail.com, 2 - e-mail: tomchev@edasat.com, 3 - e-mail: ivanova@tugab.bg

Abstract. **The object of this report is study the influence of gamma quanta on some parameters of the unijunction transistors to synthesize radioisotope equipment.**

Keywords **- ionizing radiation, gamma quanta, unijunction transistor, volt-ampere characteristic.**

I INTRODUCTION

Radioactive elements and radioactive radiation are widely used in modern science. Scientists, engineers and physicians studied the movement of substances with small amounts of radioactive elements in a variety of systems. By measuring the absorption of radioactive radiation in the substance can be established other their properties, and it can be possible to monitor and study the various technological processes.

Exclusively used in practise are gamma irradiation facalities, electron accelerators and other elementary particles.

Radioactive sources together with appropriate radiation detectors are used to control a variety of automated industrial processes, such as radioactive level gauges and switches for gases, liquids and bulk materials. With their help determine the thickness of the coating density of liquids, powders or solids. Radioactive sources and radiation detectors in priority are used in hard to reach places and conditions in which direct application of other methods is difficult, such as at high temperatures and pressures, poisonous and corrosive environments, etc.

II DISCUSSION

It is known, that irradiation with ionizing radiation is associated with the transmission of the additional energy of the substance contained in the irradiation field. The device of unijunction (Fig.1) transistors characterized by a P - N transition suggesting greater susceptibility to irradiation due to the larger number of charge carriers, generated in the volume of the transition as a result of irradiation.
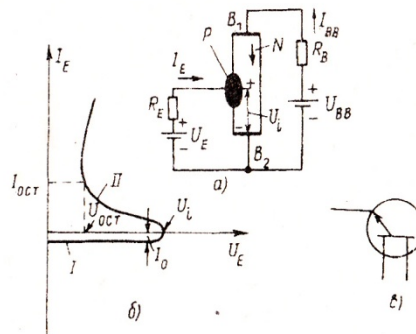

Fig.1 (a) unijunction transistors principle device; (b) volt - ampere characteristics; (c) circuit designation

There was transistor type 2N2646 studied, from which was removed some part from metal casing, which makes it possible to direct radiation. The static characteristics of the transistor shown in Fig. 2.
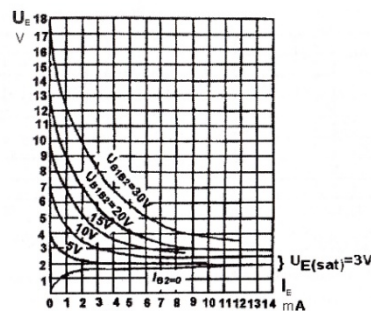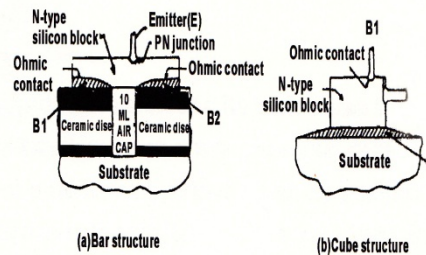

Fig.2 Structure and family static characteristics of the transistor 2N2646

In the beginning of the research there was performed experimental design shown in Fig. 3.
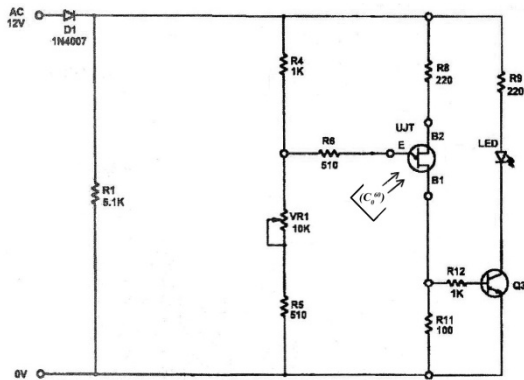

Fig.3 Schematic of the experimental set

Operating point of transistors is set by the active divider R4 - R5 and tuning precision potentiometer VR1. It allows examination of the impact of radiation with ionizing radiations at different operating points of unijunction transistor. For better visualization in scheme was added bipolar transistor (Q3) and low power holy diode (LED).

Bipolar transistor and led were added in the diagram for better visualization modes. Were captured waveforms without irradiation (Fig.4) and (Fig. 6) and after irradiation – (Fig.5) and (Fig.7).
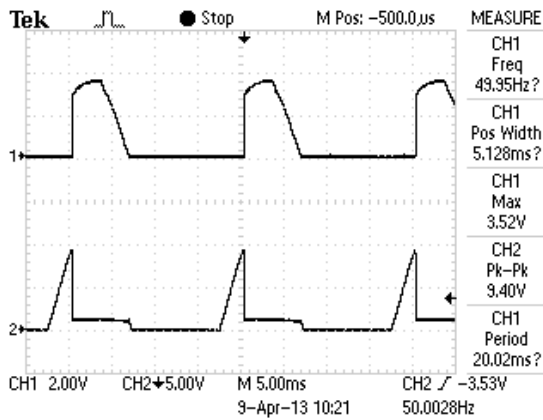

Fig.4 pulse voltage (CH2) and current (CH1)
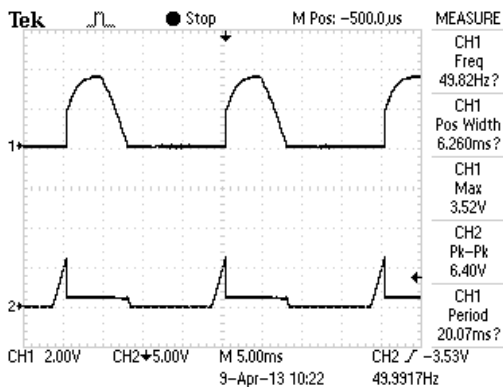
Fig.5 pulse voltage (CH2) and current(CH1) before irradiation after irradiation with gamma quanta
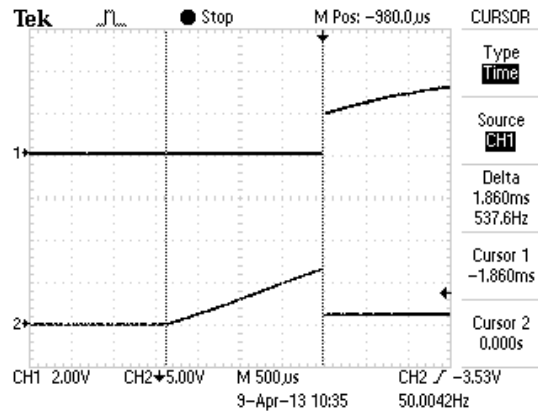
Fig.6 time interval before irradiation
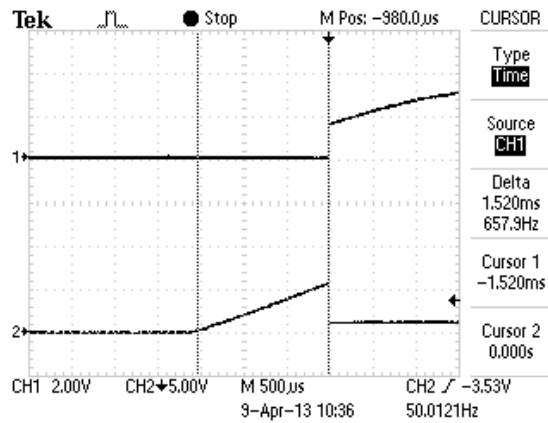
Fig.7 time interval change after irradiation

Irradiation was done using a low-power Co ^{60} source at the time of peak voltage of the transistor.

Waveforms were taken with a dual beam remembering oscilloscope "Tektronix TDS 1002".

Without exposure to the specific values on the elements of the scheme voltage at which the inflection point reaches the VAX e 9.4 V., (CH2, Pk-Pk) (Fig.4), but after irradiation, the voltage drops to 6.4 V., (CH2, Pk-Pk) (Fig.5).

It also feels the substantial difference in voltage amplitude V_{EB1} with and without exposure (~32%).

The first beam (CH1) of the same waveform is shown and the change of the current through the transistor. Without irradiation it is 1.55V/510 = 3.04mA, and then irradiation becomes 1/510 = 1.96mA.

From these diagrams can be seen that the current climate is of the same order. These changes are sufficiently large to allow construction of radioisotope relays for various applications.

On the other hand switching time of the transistor also significantly changes. This is clearly seen in both the duration of the current and voltage impuls.

The range of change of the switching time of unijunction transistor due to irradiation can be seen from the diagrams in Fig.6 and Fig.7. Without irradiation time is 1.86ms. (Fig.6), and in irradiation falls to 1.52ms.(Fig.7).

This length can easily be measured and serve to quantization of the frequency-independent series of

pulses. Thus, digital form of time measurement for change the current and voltage for proper calibration makes it possible to construct and measurement devices for various applications.

III CONCLUSION

Incurred from the initial experiments can be concluded that exposure with gamma quanta to unijunction transistors change their volt-ampere characteristic widely (VAX), which is a precondition for further more depth research in order to optimize some parameters variables to an extent sufficient for use in the construction of both radioisotope relays and precision measuring equipment.

There is going to be the study of this type of transistors, which are operating in generator mode.

The results of these studies will be published soon.

IV REFERENCES

[1] Пугачев А.В., Е.В.Сахаров. Справочник по радиоизотопной автоматике.”Энергия”, Москва, 1974г.

[2] Мишев И.Т. Основи на съвременната радиационна дозиметрия.”Техника”,София, 1971

[3] Ненов.Н.Х. Учебно-методично ръководство за лабораторни упражнения по индустриална електроника. „ЕКС-ПРЕС”,Габрово,2010г.

[4] Petrova D., Fabrication Technologies and Economic Aspects for Components in Microtechnology, VII International scientific conference "Management and engineering'09" Sozopol, 22-24.06 2009, TU - Sofia, XVII, 3/113, June 2009, ISSN–1310–3946, pp. 306-312.

Flowline with Resistive Electric Heating System

Alexander Pavlov, Igor Plohov

Pskov State University, Faculty of Electric drive and automation systems, Address: Lenin Square 2, Pskov, 180000, Russia

Abstract. **The article deals with electric heating systems applied in flowlines for providing their continued operation in wintertime. The problem of obtaining a given distribution of heat output along the length of the pipeline with electric heating system has been solved. It allows to maintain the same temperature sections being in different environments. As the object of investigation a polymer tube with an integrated electrical heating is chosen.**

Keywords **– flowline, electric heating, plastic pipe, hose-cord, equivalent circuit, four-pole.**

I INTRODUCTION

To transport natural gas or oil from production areas plants to places for complex preparation and then to the points of connection to the main pipeline flowlines are used [1]. To prevent freezing product (oil and / or gas mixtures) being transported during a cold season the pipelines need heating. The most widely used heating occurs with electric power [2].

Electric pipeline heating system (EPHS) doesn't undergo corrosion, stable to defrosting and can be powered by a common power supply system. Depending on the length of a pipe there are different EPHS (see Table 1). [3]

TABLE 1.

EPHS PIPELINES.

Length of the pipeline	Electric pipelines heating system	The distribution power network
up to 100 m	self-regulating and resistance cables	network is not needed
200-300 m		needed
up to 3-10 km	three-phase cables connected in star, including the self-regulating	network is not needed
more than 10 km	non-contact induction heating (skin-systems)	the power of one, two sides, with intermediate points

Nowdays steel and polymer pipelenes are used as flowlines. Flowlines are laid not only in the ground, but also on the surface, where they are aggressively affected by the environment. The use of a polymer pipeline with EPHS as a flowline would solve several problems: to ensure smooth operation of the flowlines at t° below 0°C, to reduce transportation costs on the pipeline delivery (polymer tube comes in large segments of the reels), to simplify the installation and to improve the protection against aggressive environment. [4]

II MATERIALS AND METHODS

The complex design of steel and plastic pipes has been developed: some pipes have a system of distributed heating, the other include thermal insulation layer, and the third group are provided with reinforcing elements (relevant for polymer pipes) [5, 6, 7, 8, 9].

III RESULTS AND DISCUSSION

We have developed a new construction of polymer pipeline, which combines the advantages of hose-cord (multilayer polymer tube with electrical and other conductors) and the original EPHS. The development objective was to obtain the given thermal distribution along the length of the pipeline.

Pipeline with EPHS is hose-cord (Fig. 1.), consisting of an inner working tube 1 (flexible polymer tube, for example of low pressure polyethylene HDPE), on the top of which there is a reinforcing layer 2. It consists of a steel belt 3 and a layer of the armoring steel wire 4. The reinforcing layer 2 is covered with an intermediate layer 5, which is surrounded by a high-temperature thermal insulation layer 6 (e.g., glass fiber), which also serves as additional reinforcement. Around the high-temperature thermal insulation layer 6 EPHS is laid 7, which is distributed over the entire length of the pipeline. EPHS 7 is made of high resistance conductor 8 (e.g., steel, nichrome, etc.), winded with a step h around the working tube 1 and nonintersecting isolated low-resistance conductors 9 and 10 (e.g., copper) with a step H, wherein H »h.
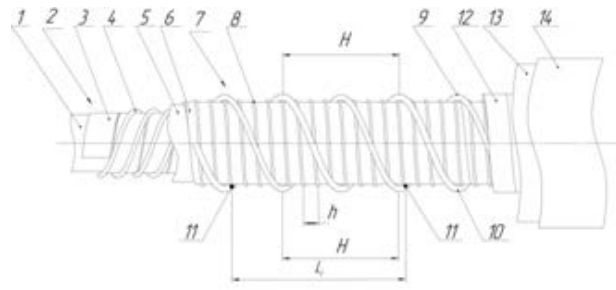

Fig. 1. Construction of the pipeline with electric heating

Low-resistance conductors 9 and 10 are turn is electrically connected (e.g., by soldering, welding) to the high resistance conductor 8 in individual points of their overlapping along the winding 11 spaced at different distances Li. EPHS 7 is surrounded by a high-temperature thermal insulation layer 12. Above

140

high temperature insulation layer 12 placed insulating layer 13 (for example, polyethylene foam). On which outer surface the polymeric waterproofing shell 14 (e.g., HDPE) [10].

By applying an electrical voltage to the low-resistance end of the isolated conductors 9 and 10 on EPHS 7 an electric current starts to flow and conductors 8, 9 and 10 are warm up. The electrical equivalent circuit of the EPHS is shown in Fig. 2.
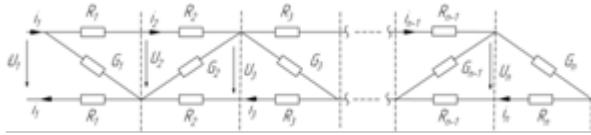

Fig. 2 The complete equivalent circuit of EPHS

EPHS parameter calculation is performed by applying the theory of quadripoles. In this case, the EPHS is given in the form of a chain system (Figure 3), consisting of series-connected sections with discrete longitudinal resistances Rk (low resistance conductor) and the transverse conductivity Gk (high-resistance wire), where k = 1,2 ..., n is a section number. The calculation consists in determining the parameters for each subsequent section using the parameters of the previous section by the transition matrix. [11]
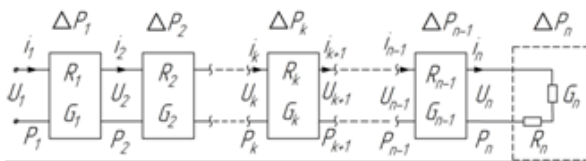
Fig. 3. Chain equivalent circuit of EPHS

IV CONCLUSIONS

The pipeline with EPHS is a complex technical solution to build a reliable system of transportation of petroleum products, ensuring trouble-free pumping of crude oil through the territory of the deposit. EPHS allows to get the required distribution of thermal power along the pipeline, which increases the reliability and provides energy saving when employing flowlines.

V REFERENCES

[1] F. Mustafin, L. Bykov, A. Gumerov etc, Flowlines and equipment. Moskow: Nedra , 2004.
[2] R. Aliev, V. Belousov, A. Nemudrov, etc, Pipeline transportation of crude oil and gas. Moskow: Nedra, 1988.
[3] N. Khrenkov, "Cable heating super-long pipeline: Select economical scheme," Territory neftegaz, vol. 6, pp. 94-95, 2007.
[4] A. Pavlov, I. Plohov, "Heated-pipe flowlines in the oil industry," Herald PskovGU, vol. 2, 2013
[5] N. Selivanov and V. Selivanov , "Pipe for transporting oil," RU patent 2,453,758 C2, November 27,2010.
[6] A. Robin, "Flexible load-carrying polymer tube and the method of its use," RU patent 2,315,223, Januar 20,2008.
[7] M. Gorilovsky, A. Shmeliov, V. Kovriga, S. Samoilov, I. Gvozdyov, S. Fisherman, I. Pyatin , "Insulated flexible multi-layer plastic pipe, not the spread of fire," RU patent 2010,141,068, April 20,2012.
[8] N. Joel, A. Tuan, "Hose with textile reinforcement," RU application for an invention 98,108,039 A, February 20, 2000.
[9] A. Robin, "The device and method of dewaxing oil and gas wells," RU patent 2,273,725 C2, , November 20.
[10] A. Robin, I. Plohov, A. Pavlov, "Pipeline with electric heating system," RU model application 2,013,107,874 A, February 21,2013.
[11] L. Bessonov , "Theory of Electrical: Electrical circuits", Moscow: Higher School, 1978.

Functional Safety of Power Plant's Technological Protections

Sergey Trashchenkov

Pskov State University, electromechanical faculty, Chair of Electric Power Industry.
Address: Lenin square 2, Pskov, Russian Federation.

Abstract. **Functional safety is an important component of safety in general, has received increasing attention in the petroleum and chemical industry, railway and other industries which used a complicated process, in case of failure can cause major damage and loss of life. Electric engineering is also among these industries. But quantitative analysis shows that the equipment of power plants does not satisfy stringent requirements of functional safety.**

Key words: **functional safety, safety related systems, technological protections.**

I Introduction

In the history of electric power can distinguish the individual stages of development, related to specific scientific and technological advances (the invention of the generator, the creation of a three-phase systems, nuclear energy, etc.). It is now one of the most actual areas of the industry is the introduction of power plants and substations digital multifunction systems automation technologies that could improve the efficiency of the plants and networks. But the application of such systems is possible only under strict safety requirements. It is considered from the standpoint of security the focus of this review of modern automation systems for the power industry.

II Materials and methods

The concept of security is extremely extensive. For complex continuous process using more specialized concept of functional safety (FS). FS is a part of an overall security, expressed in the absence of unacceptable risk to human health, their property, the environment from the functioning of the system. FS is provided by the so-called safety-related systems - systems that perform one or more specialized functions, to prevent the onset of dangerous failures. A dangerous failure meant crossing the equipment inoperable by an unpredictable or undesirable scenario. At power security systems are primarily technological protection.

Safety-related systems are interconnected by communication channels sensors that take readings of critical parameters, controllers that analyze the parameters and give commands, final elements that implement the controller's commands.

Initially, when the security-related systems were built on electromechanical relays, hardware protection functions were not associated with the functions of control. At present due to the development of automation systems safety functions are increasingly being integrated into a single framework automation, which, along with the safety function also performs:
- process control - local (actions performed by the controller without a command from the outside) and remote (commands come from the remote supervisory control);
- measurement - the collection and processing of sensor readings in real time;
- monitoring - recording of emergency processes and analysis of the current state;
- communication - the transfer of information between the field level and supervisory system, between the protection and monitoring for subsequent evaluation of emergency events.

The safety functin spite of the integration at the hardware and software levels, continues to be an isolateds, locals, because of its independent actions depend lives and health of personnel, damage to equipment during the failure. Other automatic functions should not affect the effectiveness of safety functions.

There are few tens of technological protections in thermal power plants (a specific amount depends on the schema and power of thermotechnical equipment). Traditionally, protections are divided into two groups - that trigger when exist danger for life of personnel and safety of equipment (group A) and trigger when exist danger for equipment damage or a reduction in its resource (group B). Below, for example, here is a list of boiler and turbine units protections group A for a drum boiler:
- extinction of the flame in the firebox;
- lowering the gas pressure after regulating valve;
- disable all smoke exhausts;
- disable all blasting ventilators;
- lowering the pressure in the lubrication system;
- increasing vibration bearing housings;
- lowering of the level in the damper oil tank;
- increase the pressure drop in the last stage pressure turbine;
- increasing the level of high pressure heater to the 2nd limit.

As described above, any power TK as a security system is analog and digital sensor data, thermocouples, thermistors, followed by communication with the input device (CPI) providing

a normalization signal preprocessing, the conversion of analog to digital values and their transfer to the controller. Modern programmable controllers perform many functions, logic operations, signal processing, control actuators, control, execution of commands from the user, etc. The controller provides signals to the final elements . The final elements of safety-related system on the block power plants with a drum boiler include:

– fuel supply device;
– ignition device;
– shut-off devices;
– valves;
– regulators;
– electric pumps.

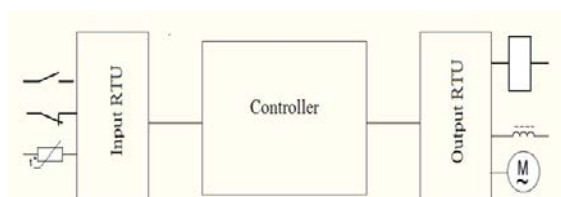General scheme of the security channel is shown on Fig. 1.

Fig. 1. Schematic diagram of the channel security system

To ensure safe and reliable safety-related systems use different architecture of this scheme, characterized by the redundancy. General architectures redundancy symbol is MooN, an M out of N. N - total number of redundant elements, M - the number of elements required to maintain the system in good working condition. Reserve are primarily controllers as the most critical elements of the systems that perform several functions, sensors to provide a system of reliable data, much less reserve final elements. According to the standard 61508 MooN concept applies to the channel - a full set of sensors, the controller and the final elements independently realizing safety function . Work if one of the channels is allowed only at the time of finding the cause and repair (18 hours).

There are several types of architectures:

– 1oo1 - the simplest not redundant architecture. Single failure results in failure of the entire system.
– 1oo2 - «one out of two». To perform the function of protection is sufficient to obtain a command from a single channel. In the event of failure of one of the channels, the work carried out on single-channel scheme, in 1oo1.
– 2oo2 - «two out of two». Circuit performs an operation to protect only when a command is received in two channels. Failure of one of the channels leading to the inability to carry out a protective function.
– 2oo3 - «two out of three» or majoritarian scheme. Made the implementation of thesafety function when receiving commands from any

two channels. The failure of two or three channels leads to unhealthy state of the system.

In addition to these common architectures modifications MooND, which are distinguished by the presence of special diagnostic modules that increase the safety of the protection systems.

In real technological protection schemes are often used combinations of architectures. Sensors are built on a "two out of three", controllers - "one of the two", and is located directly in the work of a single controller, and the second is in hot standby, and the only one final element (Figure 2). To assess the safety of the combined architecture needs to be assessed individually set of input sensors and communication devices, controllers, input and output remote terminal unit (RTU).
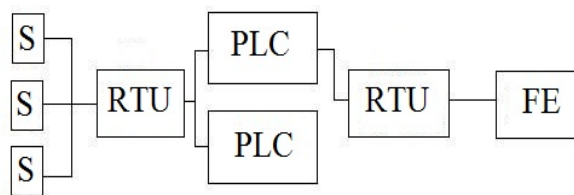

Fig. 2. The combined safety architecture

Such scheme is used in protection "increasing the level of high pressure heater to the 2nd limit", for example. Below is quantify assessment of functional safety for Fig. 2.

The main quantitative assessment of functional safety is the probability of failure on demand (PFD). It is probability of failure of the safety function when function should be triggered. The refusal of a failure is called a dangerous failure. The intensity of a dangerous failure is indicated λ_D. In contrast, there is a false alarm of a failure, called the safe failure, indicated λ_S. Dangerous and safe failures are divided into detectable internal diagnostics (λ_{DD} and λ_{SD}) and undetectable (λ_{DU} и λ_{SU}). Failures are divided into individual failures and common cause failures when the failure is more than one channel. Share of common cause failures is small, but it must be taken into account in the safety assessment, as the consequences of such failures are greatest. The shares of common cause failures are indicated β_D for detected and β_U for undetected.

Failure rate should be multiplied to their respective time intervals to find a probability.

These time intervals are:

– T – proof test interval;
– t – the time of appearance of undetectable failure in the system; equals t_{CE} –the average time a link failure;
– MTTR – Mean Time To Recovery;
– $t_{DU} = \frac{T}{2} + MTTR$ – time of undetectable dangerous failure;
– $t_{DD} = MTTR$ – time of dangerous detected failure;
– t_{GE} – average time of failure of all system.

143

Intervals are presented graphically in Figure 3.

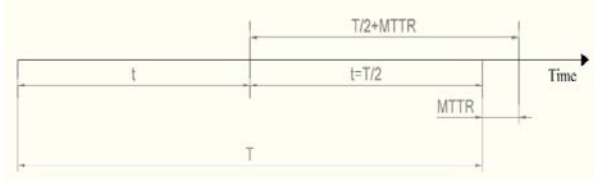
Figure 3. Graphical representation of appearance and detecting failures processes

The time t is assumed to be T/2 is taken as a uniform distribution of failure over time.

We define the rate for PFD sensor subsystem having architecture 2oo3.

$$PFD_s = 6[(1 - \beta_D) * \lambda_{DD} + (1 - \beta_U) * \lambda_{DU}]^2 * t_{CE} * t_{GE} + \beta_D * \lambda_{DD} * MTTR + \beta_U * \lambda_{DU} * \left(\frac{T}{2} + MTTR\right) \quad (1)$$

The expression $(1 - \beta_D) * \lambda_{DD} + (1 - \beta_U) * \lambda_{DU}$ in this formula is nothing else but the failure rate of a dangerous failure λ_D. Coefficient 6 is a result of taking into account the three channels and that the time T more time t_{CE} twice. The values of the time intervals t_{CE} and t_{GE} determined by the expressions:

$$t_{CE} = \frac{\lambda_{DU}}{\lambda_D} * \left(\frac{T}{2} + MTTR\right) + \frac{\lambda_{DD}}{\lambda_D} * MTTR \quad (2)$$

$$t_{GE} = \frac{\lambda_{DU}}{\lambda_D} * \left(\frac{T}{3} + MTTR\right) + \frac{\lambda_{DD}}{\lambda_D} * MTTR \quad (3)$$

Time of dangerous undetectable failure of the entire system in the last formula is accepted T/3 +MTTR, because the appearance of two faults during the proof test interval are also uniform, that is occurring every third proof test interval.

The probability of failure on demand for logic controller with architecture 1oo2 PFD_L is given by:

$$PFD_L = 2[(1 - \beta_U) * \lambda_{DU}]^2 * t_{CE} * t_{GE} + \beta_D * \lambda_{DD} * MTTR + \beta_U * \lambda_{DU} * (\frac{T}{2} + MTTR) \quad (4)$$

Values t_{CE} and t_{GE} for 1oo2 architecture are defined as well as for 2oo3.

For the subsystem of final elements, which has architecture 1oo1, PFD_{FE} is:

$$PFD_{FE} = (\lambda_{DD} + \lambda_{DU}) * t_{CE} \quad (5)$$

Failure of channel in this case is the failure of a subsystem itself and therefore takes into account only the time t_{CE}.

III RESULTS AND DISCUSSION

As an example, we take the controller TSXP572634M Shneider Electric. Its failure rate, as declared by the manufacturer is about $1.4 * 10^{-6}$ 1/hour. For convenience, it is assumed that $\lambda_D=\lambda_S=\lambda/2$.

The ratio of λ_{DD} and λ_{DU} determined by the diagnostic coverage:

$$DC = \frac{\sum \lambda_{DD}}{\sum \lambda_D} \quad (6)$$

Typically, DC takes 0%, 60%, 90%, 99%. For this calculation, we assume diagnostic coverage as 90%. Then $\lambda_{DD}=0,9\lambda_D=(0,9* \lambda)/2=0,63*10^{-6}$ 1/hour. For undetected failures $\lambda_{DU}=0,07*10^{-6}$ 1/hour.

Shares of detected and undetected common cause failures $\beta_D=1\%$ and $\beta_U=2\%$.

$$PFD_L = 2[(1 - 0,02) * 0,07 * 10^{-6}]^2 * 456 * 310 + 0,01 * 0,63 * 10^{-6} * 18 + 0,02 * 0,07 * 10^{-6} * \left(\frac{8760}{2} + 18\right) = 88,08 * 10^{-6} \quad (7)$$

$$t_{CE} = \frac{0,07 * 10^{-6}}{0,7 * 10^{-6}} * \left(\frac{8760}{2} + 18\right) + \frac{0,63 * 10^{-6}}{0,7 * 10^{-6}} * 18 = 456 \ hours \quad (8)$$

$$t_{GE} = \frac{0,07 * 10^{-6}}{0,7 * 10^{-6}} * \left(\frac{8760}{3} + 18\right) + \frac{0,63 * 10^{-6}}{0,7 * 10^{-6}} * 18 = 310 \ hours \quad (10)$$

As an final element of technological protection choose the main steam valve. It is known that its time between failures (MTBF) is approximately 5000 hours, then the failure rate $\lambda = 0,002$ 1/hr. The values of DC, β_D, β_U accept the same as for the controllers respectively time t_{CE} will remain the same, $\lambda_{DD}= 0,0009$ 1/hour, $\lambda_{DU}=0,0001$ 1/hour.

$$PFD_{FE} = (0,0009 + 0,0001) * 456 = 0,456 \quad (11)$$

Using the same values of DC, β_D, β_U for subsystems of sensors count the safety of architecture 2oo3. The sensors pick differential pressure gauges DM-3583M. The failure rate for these devices will take 0.35 * 10-6 1/hour. Obtain that $\lambda_{DD} = 0,1575*10^{-6}$ 1/hour, a $\lambda_{DU} = 0,035*10^{-6}$ 1/hour.

$$PFD_s = 6[(1 - 0,01) * 0,1575 * 10^{-6} + (1 - 0,02) * 0,035 * 10^{-6}]^2 * 456 * 310 + 0,01 * 0,1575 * 10^{-6} * 18 + 0,02 * 0,035 * 10^{-6} * \left(\frac{8760}{2} + 18\right) = 5,447 * 10^{-6} \quad (12)$$

Thus, the resulting safety indicator is the sum of the three components.

$$PFD = PFD_s + PFD_L + PFD_{FE} = 0,45 \quad (13)$$

IV CONCLUSION

The probability of failure on demand of sensors and controllers are insignificant compared to the PFD_{FE}. It turns out that the final element is the weakest point in the consideration of technological protection. The resulting figure PFD does not meet modern safety

requirements for safety systems of complex processes (PFD= 0,001..0,0001).

Technological protection usually gives commands to multiple final elements that perform different functions of safe shutdown of the process are not duplicating each other. Therefore, despite the active attention to digital automation equipment, a translation of all systems on the microcontroller to provide safety management will not be succeed.

V ACKNOWLEDGMENTS

VI REFERENCES

[1] IEC 61508-4:2010 Functional safety of electrical/ electronic/programmable electronic safety related systems. Part 4: Definitions and abbreviations.

[2] IEC 61508-6:2010 Functional safety of electrical/ electronic/programmable electronic safety related systems. Part 6: Guidelines on the application of IEC 61508-2 and IEC 61508-3.

[3] Fedorov Y. *Handbook for ICS Engineer: Design and Development*. Moscow: Infra-ingeneria, 2008.

[4] Strauss C. Practical Electrical Network Automation and Communication Systems. Milpitas, CA: IDC Technology, 2004.

LIST OF AUTHORS

Abrahamyan Hrayr	State Engineering University of Armenia Adress: Armenia, 0009, Yerevan, Teryan St., 105 Building; ph.: 37498109810; e-mail: ab_hrayr@yahoo.com	Armenia
Akmene Velga	Daugavpils University Adress: Parades 1, Daugavpils LV-5401	Latvia
Andreev Mikhail	Pskov State University, Faculty of Electrical Engineering, Department of Drive and automation systems. Address: 180760, Pskov, Lenin Square 2; e-mail: kane.lukas@gmail.com	Russia
Andrusich Andrei	Pskov State University, Faculty of Electrical Engineering, Department of Drive and automation systems. Address: 180760, Pskov, Lenin Square 2	Russia
Balashev Ivan	University Dunarea de jos of Galati- Romania Adress: Domneasca Street nr.47 Galati Romania	Romania
Balikova Vita	Riga Technical University. Adress: Azenes iela 12, Riga, LV1048, e-mail: vita.balikova@rtk.lv	Latvia
Davtyan David	State Engineering University of Armenia, Adress: Armenia, 0009, Yerevan, Teryan St., 105 Building; ph.: 37498109810	Armenia
Domracheva Yulia	Pskov State University, Faculty of Electrical Engineering, Department of Drive and automation systems. Address: 180760, Pskov, Lenin Square 2; e-mail: juli-politeh@yandex.ru	Russia
Fedotov Ilya	Pskov State University, Faculty of Electrical Engineering, Department of Drive and automation systems. Address: 180760, Pskov, Lenin Square 2; e-mail: fedotov1986@gmail.com	Russia
Gaile Līga	Riga Technical University Department of Structural Engineering 16/20 Azenes street, Riga LV 1048 e-mail: Liga.Gaile_1@rtu.lv	Latvia
Gerbreders Vjačeslavs	Daugavpils University Adress: Parades 1, Daugavpils LV-5401	Latvia
Grabusts Peter	Rezekne Higher Educational Institution Atbrivoshanas al. 90, Rezekne LV 4601, Latvia Phone: +(371)4625150; e-mail: peter@ru.lv	Latvia
Ilarionov Raycho	Technical University of Gabrovo BG 5300 Gabrovo Str. Hadji Dimitar 4	Bulgaria
Ilyin Alexander	Pskov State University, Faculty of Electrical Engineering, Department of Drive and Automation Systems. Address: Lenina 8, Pskov, 180000; e-mail: al.ilyin@yandex.ru	Russia
Isakov Andrei	Pskov State University, Faculty of Electrical Engineering, Department of Drive and Automation Systems. Address: 180760, Pskov, Lenin Square 2; e-mail: oceanrage@gmail.com	Russia
Ivanova Rayna	Technical University of Gabrovo e-mail: ivanova@tugab.bg	Bulgaria
Khitrov Alexander	Pskov State University, Electro mechanic Faculty. Address: 180760, Pskov, Lenin Square 2; e-mail: khitrov.aa@gmail.com	Russia
Khitrov Andrei	Pskov State University, Electro mechanic Faculty. Address: 180760, Pskov, Lenin Square 2	Russia
Khvattcev Aleksandr	Pskov State University, department of high mathematics, faculty of informatics. Address: 180680 Pskov, Leo Tolstoy Street 4; e-mail: a.hwattcev@yandex.ru	Russia
Kodors Sergejs	Rezekne Higher Educational Institution Atbrivoshanas al. 115, Rezekne LV 4601; e-mail: sk_7@inbox.lv	Latvia

Krasnikovs Andrejs	Riga Technical University, Institute of Mechanics and Concrete mechanics laboratory Address: 1 Kalku Street, Riga, LV-1658	Latvia
Krastev Krasimir	Technical University of Gabrovo BG 5300 Gabrovo Str. Hadji Dimitar 4	Bulgaria
Kroics Kaspars	Institute of Physical Energetic. Adress: Aizkraukles 21, Riga. LV-1006; e-mail: kaselt@inbox.lv	Latvia
Kuleshova Galina	Riga Technical University	Latvia
Loginov Sergey	Pskov State University, Faculty of Electrical Engineering, Department of Drive and automation systems. Address: 180760, Pskov, Lenin Square 2	Russia
Lukyanov Yuriy	Pskov State University, Faculty of Electrical Engineering, Department of Drive and automation systems. Address: 180760, Pskov, Lenin Square 2	Russia
Lusis Vitalijs	Riga Technical University, Concrete mechanics laboratory	Latvia
Lyokhin Sergey	FSG-fEIHPE "Pskov State University", Faculty of Informatics. Adress: pl. Lenin 2, Pskov, 180000	Russia
Macuta Silviu-Danuti	University Dunarea de jos of Galati- Romania Adress: Domneasca Street nr.47 Galati Romania; ph.: 0040722745272; fax: 0040236461353; e-mail: silviu.macuta@ugal.ro	Romania
Maltsev Pavel	Pskov state university, Faculty of Mechanical and machine building, Departament of Technology of machinebuilding. Address: Lenin square 2, Pskov, 180000; e-mail: inertan@gmail.com	Russia
Markov Alexander	Pskov State University	Russia
Mihailova Irēna	Daugavpils University Adress: Parades 1, Daugavpils LV-5401; e-mail: irena.mihailova@du.lv	Latvia
Minasyan Harutyun	State Engineering University of Armenia, Adress: Armenia, 0009, Yerevan, Teryan St., 105 Building; ph.: 37498109810	Armenia
Motaylenko Lilia	FSG-fEIHPE "Pskov State University", Faculty of Informatics. Adress: pl. Lenin 2, Pskov, 180000	Russia
Narica Pāvels	Rezekne Higher Education Institution Faculty of Engineering Atbrivoasanas aleja 90, Rezekne, Latvia Ph: +(371)26453990, fax: +(371)64625167; e-mail: pavels.narica@ru.lv	Latvia
Nenov Nikolaj	Technical University of Gabrovo; e-mail: nenovtugabrovo@gmail.com	Bulgaria
Nikiforov Igor	Pskov state university, Faculty of Mechanical and machine building, Departament of Technology of machinebuilding. Address: Lenin square 2, Pskov, 180000	Russia
Pakrastinsh Leonids	Riga Technical University, Department of Structural Engineering. Address: Azenes Street 16, Riga, LV-1048, ph.: +37129452138; e-mail: leonids.pakrastins@rtu.lv	Latvia
Pavlov Alexander	Pskov State University, Faculty of Electrical Engineering, Department of Drive and automation systems. Address: 180760, Pskov, Lenin Square 2; e-mail: alexander.pavlov.psk@gmail.com	Russia
Perminov Leonid	Pskov State University, Faculty of Electrical Engineering, Department of Drive and automation systems. Address: 180760, Pskov, Lenin Square 2	Russia
Plohov Igor	Pskov State University, Faculty of Electrical Engineering, Department of Drive and automation systems. Address: 180760, Pskov, Lenin Square 2	Russia

Plokhov Igor	Pskov State University, Faculty of Electrical Engineering, Department of Drive and Automation Systems. Address: Lenina 8, Pskov, 180000	Russia
Poletayeva Olga	FSG-fEIHPE "Pskov State University", Faculty of Informatics. Adress: pl. Lenin 2, Pskov, 180000	Russia
Rodionov Yuri	Pskov State University	Russia
Sargsyan Arevik	State Engineering University of Armenia, Adress: Armenia, 0009, Yerevan, Teryan St., 105 Building; ph.: 37498109810	Armenia
Savraev Igor	Pskov State University, Faculty of Electrical Engineering, Department of Drive and automation systems. Address: 180760, Pskov, Lenin Square 2	Russia
Sprince Andīne	Riga Technical University, Department of Structural Engineering. Address: Azenes Street 16, LV-1048, ph.: +37129452138	Latvia
Strochkov Ilja	Pskov State University, department of high mathematics, faculty of informatics. Address: 180680 Pskov, Leo Tolstoy Street 4; e-mail: strochkovPGUppi@yandex.ru	Russia
Tikhonov Vyacheslav	Pskov State University, Faculty of Electrical Engineering, Department of Drive and automation systems. Address: 180760, Pskov, Lenin Square 2	Russia
Tomchev Petar	Technical University of Gabrovo; e-mail: tomchev@edasat.com	Bulgaria
Trashchenkov Sergey	Pskov State University, electromechanical faculty, Chair of Electric Power Industry. Address: Lenin square 2, Pskov; e-mail: yogaformru@gmail.com	Russia
Uzhga-Rebrov Oleg	Rezekne Higher Educational Institution Atbrivoshanas al. 115, Rezekne LV 4601; e-mail: rebrovs@tvnet.lv	Latvia
Valbahs Edvards	Rezekne Higher Educational Institution Atbrivoshanas al. 115, Rezekne LV 4601; e-mail: err@inbox.lv	Latvia
Zarembo Imants	Rezekne Higher Educational Institution Atbrivoshanas al. 115, Rezekne LV 4601; e-mail: imants.zarembo@gmail.com	Latvia
Zhuravlev Yuriy	Pskov State University, Faculty of Electrical Engineering, Department of Drive and automation systems. Address: 180760, Pskov, Lenin Square 2	Russia